DEFECT-ENHANCED SILICON PHOTODIODES FOR PHOTONIC CIRCUITS

DEFECT-ENHANCED SILICON PHOTODIODES FOR PHOTONIC INTEGRATED CIRCUITS

By DYLAN LOGAN, B. Eng.

A Thesis Submitted to the School of Graduate Studies in Partial Fulfilment of the Requirements for the Degree

Doctor of Philosophy

McMaster University © Copyright of Dylan Logan, 2011

McMaster University (Engineering Physics)

DOCTOR OF PHILOSOPHY (2011)

Hamilton, ON

TITLE: Defect-Enhanced Silicon Photodiodes for Photonic Integrated Circuits

AUTHOR: Dylan Logan

SUPERVISORS: Dr. A. P. Knights & Dr. P. E. Jessop

NUMBER OF PAGES: xviii, 233

Abstract

The continuous reduction of feature size in silicon-based electronic integrated circuits (ICs) is accompanied by devastating propagation delay time and power consumption that have become known as the "Interconnect Bottleneck". Optical interconnection is a proposed solution that is poised to revolutionize the data transmission both within and between ICs. By forming the optical transmission and functional elements from silicon, they can be monolithically incorporated with standard ICs using the established CMOS (Complementary Metal Oxide Semiconductor) infrastructure with minimal incremental cost. A key required functional element is the photodetector, which provides optical-to-electrical conversion of signals. In this thesis, a method of achieving such conversion is explored, which uses the optical absorption at 1550 nm wavelengths provided by lattice defects.

The physics governing defect-enhanced silicon waveguide photodiode operation is described, and a device model is used to verify the posited detection process and propose design improvements. The model was used to design a novel photodetector structure using a waveguide formed by the LOCOS (LOCal Oxidation of Silicon) process with a poly-silicon self-aligned contact. The fabricated device exhibited a responsivity of 47 mA/W, providing an improvement over previous devices of similar dimensions, although were ultimately limited by the quality of the poly-silicon/silicon interface.

A sub-micron waveguide photodiode fabrication process using electron-beam lithography was developed, which produced photodiodes with responsivities of 490 mA/W. This process was used to integrate photodiodes onto micro-ring resonators, which exhibit resonant enhanced photocurrent. The physics of this enhancement were explored, and found to produce a 50 μm long resonant photodiode of responsivity equal to that of a 3 mm long non-resonant photodiode. Lastly, the integration of such sub-micron photodiodes as functioning power monitors throughout photonic circuits was demonstrated as a means to characterize and tune micro-rings during operation.

Acknowledgments

Academic experimental research is inherently collaborative, and the contained work would not have been possible without the support of several individuals.

Firstly, I must thank my thesis supervisors, Dr. Andrew Knights and Dr. Paul Jessop, for their patience and advice throughout my academic career.

The ideas and suggestions of other members of the research group were a significant benefit, as well as their assistance in fabrication and simulation. The help of Chris Brooks, Mike Bulk, Shabnam Homampour, Barry Stoute, Adam Prescott, Edgar Huante, Jon Doylend and Jason Ackert is much appreciated.

I would also like to thank Doris Stevanovic, Zhilin Peng, Doug Bruce and Graham Pearson for their help with fabrication and characterization processes. Also, I am indebted to Peter Jonasson for providing aluminum deposition and for recovering my laptop following a devastating incident involving a cup of coffee.

I also had the good fortune of conducting one year of the research towards this degree at the University of Glasgow. I'm grateful for that invaluable experience, made possible by Dr. Richard De La Rue and post-doctoral fellow Philippe Velha, as well as the countless other students and technicians operating within the James Watt Nanofabrication Centre.

Most importantly, I thank my parents and my future wife Lindsey for their support throughout this endeavour. I'm certain that I would not have written this were it not for them.

Contents

1. Introduction **1**

1.1 The Evolution of the Silicon IC Industry 1
1.2 An Overview of the Field of Photonics 4
1.3 The Silicon Photonics Solution to the Interconnect Bottleneck 8
1.4 Defect-Enhanced Silicon Photodetection 16

2. Background Theory **29**

2.1 Fundamentals of Guided Wave Optics 29
2.1.1 Overview of electromagnetic wave propagation 29
2.1.2 Description of guided waves 36
2.1.3 Methods of waveguide modeling 45
2.2 Optical Absorption in Silicon 46
2.3 Physics of p-i-n Photodiodes 56
2.3.1 Review of carrier transport and p-n junction operation 56
2.3.2 Electronic modeling in Silvaco's ATLAS software 59
2.3.3 Overview of p-i-n photodiode operation 60
2.4 Optical Resonators 66
2.4.1 The Fabry-Perot etalon 66
2.4.2 General characteristics of optical resonators and methods of simulation 69
2.4.3 Micro-ring resonators 71
2.5 Summary 80

3. Modeling Defect-Enhanced Photodetectors **85**

3.1 Overview 85
3.2 The Divacancy 86
3.3 Theory of Deep-Level Carrier Generation and Recombination 89
3.4 Single-Defect Model of Photodetection 92
3.5 Single-Defect Model Results 94
3.6 Evaluation of Device Designs 99
3.6.1 Performance dependence on reverse bias 99
3.6.2 Position of n^+ and p^+ regions and defect-forming implant mask width 100
3.6.3 Defect-forming implant depth 104
3.6.4 Adjusted defect implant mask profiles 105
3.6.5 Simulation of photodetector speed 107
3.7 Summary 107

4. Photodetectors formed via the LOCal Oxidation of Silicon (LOCOS) Process **111**
4.1 Overview 111
4.2 Device Design 112
4.2.1 Waveguide geometry 112
4.2.2 Poly-silicon contact design: Optical considerations 114
4.2.3 Poly-silicon contact design: Electrical considerations 116
4.2.4 Incorporation into the ATLAS simulation model 118
4.3 Fabrication of the LOCOS Photodetector 119
4.4 Optical and Electrical Characterization 122
4.5 Results and Discussion 124
4.5.1 Post-implantation annealing 124
4.5.2 Position of boron doped regions 126
4.5.3 Width of the Si^+ *implant window* 126
4.5.4 Influence of the amorphous silicon deposition method 127
4.5.5 Influence of the Si^+ *implantation dose* 129
4.6 Summary 130

5. Sub-micron Photodetector Structures **133**
5.1 Overview 133
5.2 Details of Device Fabrication 135
5.3 Electrical and Optical Characterization 143
5.4 Photodetector Characterization 145
5.4.1 Photodetector response vs. annealing 145
5.4.2 Dependence of length on photodiode response 148
5.4.3 Characterization of the noise properties 150
5.5 Summary 151

6. Resonant Photodiode Enhancement **153**
6.1 Overview 153
6.2 Design and Fabrication 155
6.2.1 Micro-ring design 155
6.2.2 Micro-ring p-i-n diode integration 160
6.3 Measured Resonant Enhancement of Photocurrent 162
6.3.1 Optical and electrical characterization of all-pass resonant photodiodes 162
6.3.2 Measured photodetection of all-pass resonant photodiodes 166
6.3.3 Discussion of resonant enhancement in all-pass resonant photodiodes 168
6.3.4 Resonant enhancement in an add-drop configuration 170
6.4 Summary 175

7. Demonstration of Integrated Power Monitor on Micro-ring Ports **177**

7.1 Overview 177

7.2 Characterization of Ring Resonant Power Monitors 178

7.3 Applications of Integrated Functionality 181

7.4 Summary 183

8. Summary, Conclusions, and Suggested Future Work **185**

8.1 Summary of Accomplished Work 185

8.2 Suggested Future Work 187

8.2.1 Modeling defect-enhanced photodetection 187

8.2.2 LOCOS-based photodetectors 188

8.2.3 Resonant enhanced photodiodes 188

8.2.4 Measurement of photodiode bandwidth 189

8.2.5 Integration of defect-enhanced photodiodes onto PICs 189

Appendices

A ATLAS Source Code Example for Photodetector Simulation 191

B Chronological Compilation of Published Work 199

List of Figures

1.1	a) NMOS device cross-section with interconnect levels, and b) Transistor count vs. date of introduction.	3
1.2	a) Schematic of a *p-i-n* photodiode and b) Absorption spectra of select semiconductors.	7
1.3	a) Schematic of SOI transmission waveguide, and b) illustration of a proposed optical interconnection scheme.	11
1.4	Illustration of several implementations of silicon photonic modulators.	13
1.5	Illustration of implementations of germanium-integrated SOI waveguide photodetection.	15
1.6	Schematic of a proposed optical transceiver.	16
1.7	a) Illustration of various lattice point defects, and b) Optical absorption in silicon following ion implantation of varying species and dose.	18
2.1	Schematic of propagation of transverse electromagnetic wave.	33
2.2	Illustration of the interaction of a light wave at the boundary between two dielectric media.	35
2.3	Illustration of ray propagation in a planar SOI waveguide.	37
2.4	a) Effective index and propagation angle of a slab mode vs. silicon film thickness d, b) mode intensity profile for several mode orders m.	40
2.5	a) A schematic of a silicon channel waveguide, b) mode intensity profiles of different mode orders p,q.	42
2.6	A schematic of a rib waveguide, and the equivalent structure used in the effective index method of approximating the mode solution.	43
2.7	a) Plot of the range of rib geometries that yield single-mode behaviour, and b) Illustration the butt-coupling process.	44
2.8	a) Illustration of the linear oscillator model of the atomic response to optical excitation, b) Response of the real and imaginary parts of the refractive index.	47
2.9	a) Schematic of band-to-band absorption process, and b) General absorption spectra including band-to-band absorption and free-carrier absorption.	50
2.10	Schematic of deep-level absorption mechanisms, including mid-gap levels and shallow acceptor and donor levels.	54
2.11	a) Schematic of a *p-n* junction and associated band structure, and b) general I-V characteristic curve of a *p-n* junction.	58
2.12	a) Schematic of a waveguide *p-i-n* junction and associated band structure, and b) general I-V characteristic illustrating dependence of reverse current on optical power.	60
2.13	a) Equivalent circuit of a *p-i-n* photodiode, and b) Illustration of the response of a photodiode to an optical pulse input.	63
2.14	a) Schematic of symmetric Fabry-Perot etalon, and b) transmitted intensity of a silicon etalon of varied reflectance and absorbance.	68
2.15	a) Schematic of a micro-ring resonator, and b) Schematic and intensity distribution in a waveguide coupler.	72
2.16	a) Schematic of a circular ring resonator, b) schematic of a racetrack ring resonator, and c) schematic of generalized coupler with coefficients κ and t.	74

2.17	a) Schematic of an add-drop ring resonator, and b) plot of its drop-port and through-port intensity spectra.	76
2.18	a) Schematic of an all-pass ring resonator, and b) plot of its resonant through-port intensity for different ring losses.	77
3.1	Divacancy charge state energies, a map of the Fermi level range for which the main characteristic divacancy absorption bands are present, and the absorption spectrum of *p*-doped silicon containing divacancies.	87
3.2	Schematic of free-carrier interaction with a defect level.	90
3.3	Schematic of a rib waveguide along with insertion of spatially dependent optical generation rate.	93
3.4	Schematic of the cross-sections of defect-enhanced photodiodes previously reported in literature.	95
3.5	Simulated and reported photocurrent vs. defect concentration of defect-enhanced photodiodes reported in literature.	96
3.6	Simulated effective quantum efficiency vs. defect concentration of defect-enhanced photodiodes reported in literature.	98
3.7	Simulated photocurrent of a large cross-section photodiode as a function of dopant separation.	101
3.8	Simulated photocurrent of a small cross-section photodiode as a function of sidewall dopant width.	102
3.9	Simulated photocurrent of the small cross-section photodiode vs. defect concentration for 1.2 µm and 450 nm wide Si^+ implant windows.	103
3.10	Simulated photocurrent and effective quantum efficiency of the large cross-section photodiode vs. Si^+ implant depth.	105
3.11	a) Schematic of a tailored Si^+ implant window mask, and b) simulated effective quantum efficiency vs. defect concentration for three tailored windows.	106
4.1	ATHENA output plots of a LOCOS waveguide photodiode following wet oxidation and poly-silicon deposition and etch.	112
4.2	a) cross-section of a LOCOS waveguide, and b) range of waveguide width and slab height for which the waveguide is single-mode.	113
4.3	Propagation loss of the LOCOS waveguide vs. width of the thermal oxide trench on either side of the waveguide.	114
4.4	Propagation loss vs. assumed poly-silicon optical absorption for several deposited film thicknesses.	116
4.5	a) ATLAS model of the built-in potential distribution of a LOCOS waveguide photodiode, and b) Simulated photocurrent vs. input optical power for LOCOS waveguide photodiode and previously reported devices.	119
4.6	Cross-section, SEM, and optical microscope images of the LOCOS waveguide photodiode at several stages in the fabrication process.	120
4.7	a) Schematic of photodiode characterization set-up, and b) measured current vs. on-chip optical power used to determine responsivity.	122
4.8	Simulated and measured I-V curve of LOCOS waveguide photodiode.	123
4.9	Measured and simulated photocurrent of LOCOS waveguide photodiode vs. defect concentration.	125
4.10	Measured and simulated photocurrent of LOCOS waveguide photodiode vs. p^+ region separation.	126
4.11	Simulated responsivity of LOCOS waveguide photodiode vs. defect concentration for several Si^+ implant window widths.	127
4.12	Measured dark current of a LOCOS waveguide photodiode vs. annealing temperature for two poly-silicon film deposition methods.	128
4.13	Photocurrent, dark current, and excess optical loss of a LOCOS waveguide photodiode vs. annealing temperature following a high dose Si^+ implantation.	129

5.1	Cross-section and ATLAS model output of a sub-micron photodiode with lightly doped sidewalls.	134
5.2	Cross-section and ATLAS model output of a sub-micron photodiode without lightly doped sidewalls.	134
5.3	Illustration of the electron beam writing process.	136
5.4	Schematic and SEM image of an etched silicon waveguide cross-section.	138
5.5	a) Diagram of the interferometry monitoring technique throughout the etch process, and b) sample monitor trace during an etch.	139
5.6	SEM image of the silicon waveguide cross-section following oxidation.	139
5.7	a) Optical microscope image of lithographically defined boron implantation window, and b) ATHENA model of device cross-section following boron implantation.	140
5.8	a) Optical microscope image of lithographically defined phosphorus implantation window, and b) ATHENA model of device cross-section following phosphorus implantation.	141
5.9	Schematic illustration of the 'lift-off' process used to define aluminum contacts	142
5.10	a) SEM image of the final silicon photodiode, and b) measured *I-V* characteristic curves.	143
5.11	a) *I-V* curve of a photodiode following several annealing stages, and b) variation in forward and reverse bias current throughout annealing stages.	144
5.12	Variation in measured photocurrent/responsivity of a 0.6 mm device as a function of annealing temperature.	146
5.13	a) Illustration of cut-back method to determine excess loss at various annealing stages, and b) Extracted excess loss vs. annealing temperature.	147
5.14	a) Measured photocurrent/responsivity of several device lengths as a function of annealing temperature; a) Measured photocurrent responsivity of several device lengths as a function of excess loss/defect concentration.	148
5.15	Measured photocurrent/responsivity following the 325 C annealing stage as a function of device length.	149
5.16	a) Reverse biased 0.6 mm long photodiode characteristic with and without optical excitation, and b) Noise-equivalent power (*NEP*) vs. bias.	150
6.1	Schematic implementations of resonant photodiodes.	154
6.2	Modeled and photographed optical waveguide mode, and a plot of effective and group index vs. curve radius.	156
6.3	a) Simulation of optical fields in a waveguide coupler, and b) cross-coupling coefficient vs. coupling gap.	158
6.4	SEM images of RIE etch lag test structures, and measured etch depth vs. gap width.	159
6.5	SEM images of an all-pass ring resonator and its evanescent point coupler.	160
6.6	Schematic of integrated *p-i-n* diodes on all-pass and add-drop ring resonators.	161
6.7	a) Optical microscope image of a phosphorus implant window defined on a ring resonator, and b) SEM image of final active ring resonator device.	161
6.8	Transmitted optical power of the all-pass ring resonator.	162
6.9	a) Measured optical resonance of the ring resonator following select annealing stages, and b) linewidth and extinction ratio as a function of annealing temperature.	163
6.10	a) Extracted parameters A^2 and t^2 as a function of annealing temperature, and b) Extracted absorption coefficient and cross-coupling coefficient vs. annealing temperature.	164
6.11	*I-V* characteristic of the ring resonator diode following select annealing temperatures.	166

6.12	Ring resonator photocurrent spectra, illustrating resonant enhancement in photocurrent.	167
6.13	a) Photocurrent resonance for select annealing temperatures, and b) Resonant photocurrent and electrical linewidth vs. annealing temperature.	168
6.14	a) Photocurrent vs. device length for non-resonant photodiodes, with the resonant enhancement overlaid, and b) Measured peak photocurrent/responsivity vs. excess absorption, as well as simulated resonant and non-resonant curves.	169
6.15	Waveguide transmission and build-up factor for two add-drop ring resonators.	171
6.16	a) Photocurrent resonance for several add-drop ring resonators, and b) Modeled and measured photocurrent enhancement vs. BUF ratio.	174
7.1	Schematic and optical microscope image of integrated power monitors on the bus waveguides of a ring resonator.	178
7.2	Optical resonance of two add-drop microrings and the associated current signals of the drop-port and through-port power monitors.	179
7.3	a) The optical resonance and drop-port monitor signal for several values of tuning power, and b) the wavelength shift of the ring vs. tuning power.	181
7.4	The drop-port monitor current for several wavelengths vs. tuning power.	183
A.1	ATLAS photodiode structure: material distribution.	192
A.2	ATLAS photodiode structure: dopant distribution.	193
A.3	ATLAS photodiode structure: potential distribution.	194
A.4	ATLAS photodiode structure: photogeneration rate distribution.	195
A.5	ATLAS photodiode structure: recombination rate distribution.	196

List of Tables

4.1	Phosphorus activation and reverse saturation diode current in poly-silicon films deposited on silicon for selected annealing temperatures.	117
6.1	Optical properties of implanted all-pass micro-ring resonators for selected annealing temperatures.	165
6.2	Optical properties of selected add-drop micro-ring resonator geometries and calculated resonant BUF and BUF ratio.	172

Chapter 1 Introduction

1.1 The Evolution of the Silicon IC Industry

The realization by Jack Kilby in 1958 that individual electronic device elements (diodes, resistors, capacitors, etc.) could be fabricated on a single semiconductor substrate, in a single process flow [1], may well be described as a defining moment in the history of technology. The subsequent formation of sophisticated electronic circuits onto the surface of a single wafer resulted in the Integrated Circuit (IC). Devices and products which depend on ICs have become ubiquitous in today's society.

For the last 50 years, silicon has been the dominant semiconducting substrate material in the Integrated Circuit industry. The reason that silicon is used as a standard substrate material, rather than other semiconductor materials such as germanium, is because of considerations of both cost and functionality. Silicon is one of the most common elements on earth, making up 25.7 % of the Earth's crust [2]. Silicon is refined from its oxidized form (SiO_2), in a multistage process to eventually produce high purity wafers of up to 12" diameter. Due to the low material cost, the starting silicon wafer accounts for a very small fraction of the final device cost [2]. Also, silicon has many ideal electrical properties. Compared to other Group IV semiconductors, such as germanium, silicon is less electrically conductive at room temperature and more importantly is less temperature-sensitive, enabling it to be used for more high-power applications. Perhaps the major benefit of silicon is the ability to thermally oxidize (i.e. grow SiO_2) on its surface. This oxide both smoothes and electrically passivates (i.e. reduces the influence of microscopic defects on) the silicon surface, producing a highly insulating layer. This layer can also be utilized throughout the fabrication process to mask ion implantation and etching steps.

The availability of cheap, high quality semiconductor material was but one factor necessary for the birth of the IC industry. The other was the development of planar processing. This refers to fabrication stages that alter the surface of the silicon wafer in a controlled and repeatable manner, including the oxide growth already described; the masked etching of silicon and oxide, masked diffusion, and dielectric and metallic deposition. Using these steps, it is possible to simultaneously fabricate different basic electronic elements on a wafer surface, as Jack Kilby demonstrated in 1958 when he fabricated the first IC composed of a resistor, capacitor and transistor on a silicon substrate [1].

The degree to which the process of integrating discrete elements monolithically on a single wafer has revolutionized the world cannot be overstated. The functionality, and consequently the density of elements, integrated onto a single chip have continued to grow since Kilby's initial demonstration. This is primarily driven by the need to improve overall IC functionality and speed, but also because individual devices tend to perform better when scaled down in dimension. Most importantly, the cost per function on an IC decreases in proportion to the device density, which has been the driving force of the microelectronics industry for the past several decades [3]. The technology that has dominated this industry is CMOS, or Complementary Metal-Oxide-Semiconductor. This is so-called because the MOSFET (or Metal-Oxide-Semiconductor Field Effect Transistor) is the fundamental device in ICs. All digital logic operations can be formed from combinations of two types of MOSFETs: *n channel* (or NMOS) and *p channel* (or PMOS), and these aggregate structures are referred to as Complementary MOS [2]. The fabrication technology must therefore be capable of forming both MOSFET types simultaneously on the same wafer, and these are referred to as CMOS Foundry Manufacturing lines. The MOSFETs are integrated onto the surface of the silicon wafer (along with electrical isolation regions), while several layers of metal and SiO_2 situated above the MOSFET provide the interconnection between individual devices as shown in Figure 1.1a.

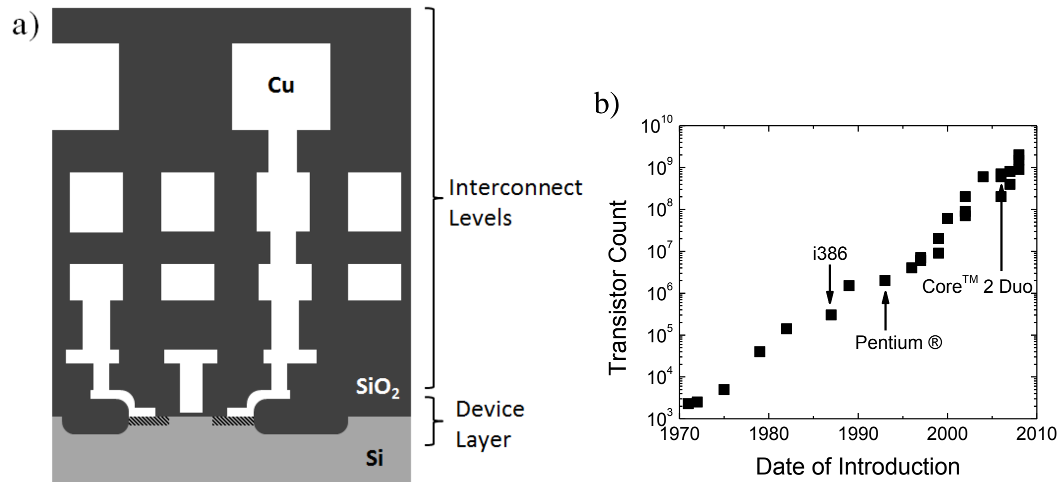

Figure 1.1: a) Illustration of an NMOS device integrated onto a silicon surface, with several levels of metal interconnects above [4]; b) A plot of number of MOSFETs in computer processors vs. the year they were brought to market, illustrating the validity of Moore's prediction of a doubling of transistor count every two years, explicitly labeling some Intel ® Processors [5].

The degree of device scaling was predicted somewhat successfully by Gordon Moore in 1962 in what has come to be known as Moore's Law, which states that the density of devices doubles every two years as shown in Figure 1.1b [6]. Today, common ICs have more than 1 billion transistors [7]. This is made possible by a steady evolution in CMOS processing technology, particularly optical lithography, in order to effect a continual reduction in the minimum feature size of devices. A document called the International Technology Roadmap for Semiconductors (ITRS) defines the progress of technology scaling, and coordinates the timing of future improvements. As of 2011 the microelectronic industry finds itself at the '*32 nm node*', which means the minimum feature size (the MOSFET gate length) is set at 32 nm. It is predicted, however, that by 2020 the inherent limits of CMOS devices will prevent further scaling, and a shift in paradigm will be required for any further improvements in IC performance [3].

Less than 1 μm of thickness of silicon is utilized in planar processing, with the remainder of a substrate simply providing structural support. An important development over the last twenty years has been to isolate this top (approximately) 1 μm from the remaining wafer thickness, in order to better isolate each component and eliminate the parasitic effects of the substrate [8]. Such wafers are called *Silicon-On-Insulator* (SOI), and consist of a thin silicon overlayer of 0.2- 5 μm thickness, a buried oxide (BOX) layer of 0.2-2 μm thickness, and the remaining (handle) silicon layer of several hundreds of μms thickness. There are a variety of methods of fabricating SOI, all of which greatly increase the price of the starting wafer, particularly if one desires a precise overlayer thickness and a good quality interface with the BOX [9]. SOI plays an important role in the work described in this thesis because it provides an ideal starting material for silicon photonic devices, as will be described in the following sections.

1.2 An Overview of the Field of Photonics

The quest for a comprehensive description of light has motivated physicists for centuries. In the field of photonics, one must alternate between two seemingly incompatible treatments of light as a wave and a collection of particles, depending on the physical situation. In more classical situations, for instance in describing the propagation of light through matter, light is treated as a wave. Specifically, the wave is formed of oscillating electric and magnetic fields, travelling at a speed c in the direction normal to their plane of oscillation. This 'Electro-Magnetic Spectrum' is made up of all the possible wavelengths λ of radiation, which is related to the frequency of oscillation ν through:

$$c = \lambda \nu \tag{1.1}$$

In other instances, such when light interacts with matter during absorption and emission processes, it becomes necessary to describe light as an ensemble of indivisible

quanta of radiation called *photons*, each travelling at speed c and having an distinct energy:

$$E = h\nu \qquad (1.2),$$

where h is Planck's constant (6.63 x 10^{-34} Js). A beam of light is thus in this picture comprised of a large number of photons, and its properties and interactions with matter become a statistical calculation. In this thesis, light propagation through silicon waveguides is treated as a wave; whereas light interaction with silicon through absorption is treated assuming the light is a distribution of photons [10].

The field of *Photonics* broadly refers to any technology that controls the flow of photons in a manner analogous to *electronic* devices that utilize the control of *electrons*. It encompasses the study of light emission in lasers or LEDs, light guiding, optical switching and modulation, nonlinear optics, light detection, and more [11]. What perhaps unifies this diverse field is the exploitation of light as a carrier of information. Although not popularly termed 'light', the radio-wave portion of the electromagnetic spectrum (comprising of frequencies v = 30 kHz -300 GHz) has been used to transmit information for nearly a century [12]. This is accomplished by using the radio wave as a 'carrier' of a transmitted signal, modulating the amplitude, phase or frequency of a carrier wave of frequency v at a rate $v_{sig} < v$. A series of waves of different appropriately spaced carrier frequencies may be transmitted through the atmosphere without interfering with one another, each sending data at a rate v_{sig}. The same approach has been utilized in the modern telecommunications industry to transfer data with much higher carrier frequencies, and consequently much higher data rates. These carrier frequencies are in the range of 220 -240 THz or 192-196 THz, corresponding to wavelengths of 1260-1360 nm (known as the *O* band) and 1530-1565 nm (known as the *C* band) [13]. These are in the 'near-infrared' portion of the spectrum, and are so chosen due to the properties of the means of their transportation: *optical fibre waveguides* [13].

An optical fibre is a cylindrical glass or plastic structure comprised of several shell/layers that is able to guide light over many kilometers with minimum loss (< 0.1 dB/km) [13]. It is the medium through which high bit-rate (> 1 Tb/s) signals are transmitted by optical networks [14]. In glass, scattering and the absorption caused by residue water defines two clear low-attenuation 'windows' in the optical spectrum ideal for fibre transmission: the aforementioned *O* and *C* bands. The most general optical point-to-point transmission link consists of a *modulator*, which encodes (or modulates) a bit-stream onto a light source carrier (such as laser emission), effectively converting a data signal from the electrical domain to the optical domain. This optical signal is then transferred over several kilometers via optical fibre, being periodically amplified if necessary. At the receiver, a *photodetector* converts the optical signal into a current signal which, after digital processing, recovers the original electrical domain signal [13].

A photodetector is any device that absorbs photons and produces a proportional current. There are a range of devices that fill this requirement, but this thesis will focus on the most common implementation: the *p-i-n photodiode*. This diode is formed of intrinsic semiconductor (*i*), doped with *p* type and *n* type regions as shown conceptually in Figure 1.2a. Under an applied reverse bias (i.e. when a negative voltage is applied to the *p* side with respect to the *n* side), an electric field will exist across the entire *i* region. Any photon incident on the *i* region with an energy $h\nu$ larger than the semiconductor bandgap energy E_g will generate electron hole pairs, which are swept out of the region by the electric field and form a current I_P. The ratio of generated charge carriers to the number of incident photons is called the *Quantum Efficiency* (η), and can be optimized by judicious selection of the *i* region geometry in relation to the absorption coefficient (α) of the semiconductor (expressed in dB/cm). An additional parameter used to characterize photodetectors is the *Responsivity* (R), which is the ratio of the generated current to the incident power, measured in units of A/W. When under reverse bias, the *p-i-n* junction exhibits a small current that flows independent of the number of incident photons, called the *reverse saturation current* or *dark current*. This is a significant parameter as it

determines the minimum number of photons that may be detected by the device; it is always desirable to minimize its value. The last important parameter in *p-i-n* photodiodes is the *Response Time* or *Bandwidth*, which indicate the fastest detectable optical signal. This can be limited by either the transit time of carriers (the time required for generated carriers to reach the doped regions), or the resistance-capacitance product (or RC constant) of the diode [15].

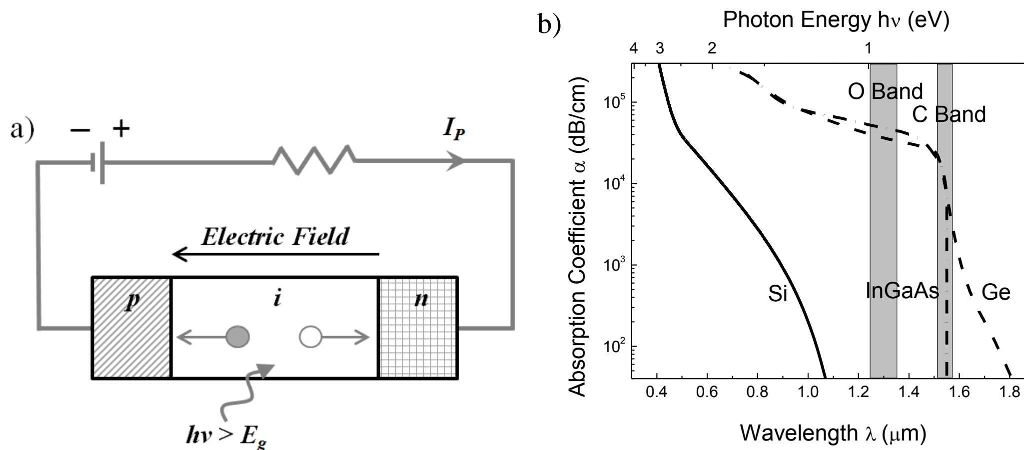

Figure 1.2: a) A schematic of a *p-i-n* photodiode with an incident photon of energy *hv* greater than the bandgap energy E_g; the absorption of the photon generates an electron-hole pair, which are swept to opposite ends of the device by the electric field, contributing to the photocurrent I_P (reproduced based on [15]); b) Absorption spectra of silicon [16], germanium [16] and $In_{0.47}Ga_{0.53}As$ (indium gallium arsenide) [17], plotted against both photon energy (top axis) and wavelength (μm); *O* and *C* Bands are indicated.

The values of both η and R will be strongly dependent on both the semiconductor used and the operating wavelength. The absorption coefficients of silicon, germanium and indium gallium arsenide (InGaAs) are plotted in Figure 1.2b as a function of wavelength. Above the ‘cut-off wavelength’, being the point at which the photon energy is equal to the semiconductor bandgap energy, the semiconductor will be transparent. Therefore, ideal choices for telecommunications applications would be germanium and

InGaAs, both of which have strong absorption at 1.3 and 1.55 μm. Silicon, on the other hand, is more commonly used in the detection of visible light. A more detailed analysis of *p-i-n* photodiodes is provided in chapter 2.

Perhaps the largest benefit of optical signalling is *Wavelength Division Multiplexing* (WDM), in which separate streams of data may be encoded on different carrier wavelengths, or 'channels', and transmitted without interfering along the same waveguide. The channels are combined and separated in passive optical devices called multiplexers and de-multiplexers, respectively [13]. Since the carrier frequencies are so large compared to common modulation frequencies of <50 GHz, the channels may be very closely spaced in wavelength, allowing simultaneous transmission of many channels. There is now an established grid of standard carrier frequencies, formalized by the International Telecommunications Union (ITU), which are spaced by 100 GHz (or 0.8 nm) [13]. However, recent advancements in filter and multiplexing technology have permitted the reduction of channel spacing to as low as 25 GHz, with consequential enhancement in data transfer speeds [14]

This well-established architecture for optical data transmission represents the paradigm which *silicon photonics* aims to scale to the wafer level, taking advantage of the fast bit-rates of optical communication with the low cost per function of ICs.

1.3 The Silicon Photonics Solution to the Interconnect Bottleneck

It was established in section 1.1, through a review of the trends in the IC industry, that the physical limits in device scaling will soon be reached. Having provided an overview of photonics in section 1.2, we are now in a position to describe the prospect of silicon photonics replacing some of these standard technologies.

One of the most devastating consequences of device scaling is the increased propagation delay and power consumption that is suffered in the traditional metal/dielectric based interconnects of ICs, popularly termed the '*Interconnect Bottleneck*'. Firstly, propagation delay is increased through an increase in the resistance-capacitance product (or *RC* constant) of a wire as it is reduced in dimension, due both to bulk geometry effects and increased surface scattering [18]. This has been alleviated to some degree through decreasing both the wire resistivity and the dielectric constant of the matrix it is embedded in. These are not sustainable measures, and have merely slowed the increase in propagation delay, which currently has values on the order of 25 ps/mm in copper [19]. Secondly, the copper wire becomes increasingly '*lossy'*, and hence more dissipative, at higher bandwidth densities [18]. The increasing bandwidth demands of ICs increase this loss to the point where several amplifiers are required along an interconnect path, each of which introduces uncertainty in signal timing. As a result of these factors, it is predicted that traditional copper interconnects will not be viable at speeds above 20 Gb/s [19].

The trend in modern computing has thus been to hold the processing speeds at their current level, and use multiple processor architectures to achieve increasing data transfer [20]. This simply shifts the interconnect problem from the chip-level to a bottleneck between cores, as data must be transferred between processors at Tb/s bitrates. What remains is still an interconnect bottleneck, but one that may be (and recently has been) addressed by silicon photonics.

It has been proposed that the scaling issues on ICs can be mediated by integrating the telecommunications architecture onto the chip-level to provide local optical transmission of data. This photonic solution offers reduced propagation delay and lower transmission loss (and less dependence of loss on bandwidth), at the expense of the large power requirements and cost of optical/electrical conversion. Recent years have witnessed a trend of optical transmission replacing copper cables for increasingly smaller distances: from rack-to-rack, to board-to-board, currently to chip-to-chip and likely to on-

chip in the near future [21]. Necessary for this development is integrated optics, which in a manner similar to ICs involves the monolithic integration of photonic devices (sources, modulators, detectors, etc.) onto a single substrate. Photonic Integrated Circuits (PICs) have been envisioned and fabricated, which perform functions of several discrete optical elements on a small semiconductor chip [22]. PICs designed to facilitate optical interconnection require the monolithic integration of photonic and electronic elements.

Using silicon for PICs has the advantage of exploiting the established CMOS infrastructure described in section 1.1, which minimizes the incremental cost of the transition between technologies. This infrastructure includes the design methods, fabrication facilities, and testing equipment for the electronic part of the chip [23]. With these obvious benefits comes the constraint that the photonic technology must be 'CMOS Compatible,' meaning that the layout and processing sequence of the photonic devices must be implemented in a way that does not jeopardize the function of these electronic components [23]. The key photonic element of a PIC is the waveguide, illustrated in Figure 1.3a: a silicon wire structure of cross-sectional area $< 25\ \mu m^2$ embedded in dielectric, commonly fabricated on an SOI substrate. Optical transmission on silicon waveguides is efficient in the *O* and *C* bands used in the telecom industry, as silicon is transparent at these wavelengths (see Figure 1.2b). Silicon also has a large refractive index with respect to that of SiO_2, which as we will see in the next chapter enables the confinement of light to small volumes during transmission. Currently, SOI transmission waveguides with cross-sectional area of $0.11\ \mu m^2$ have been demonstrated with loss of less than 1 dB/cm [24].

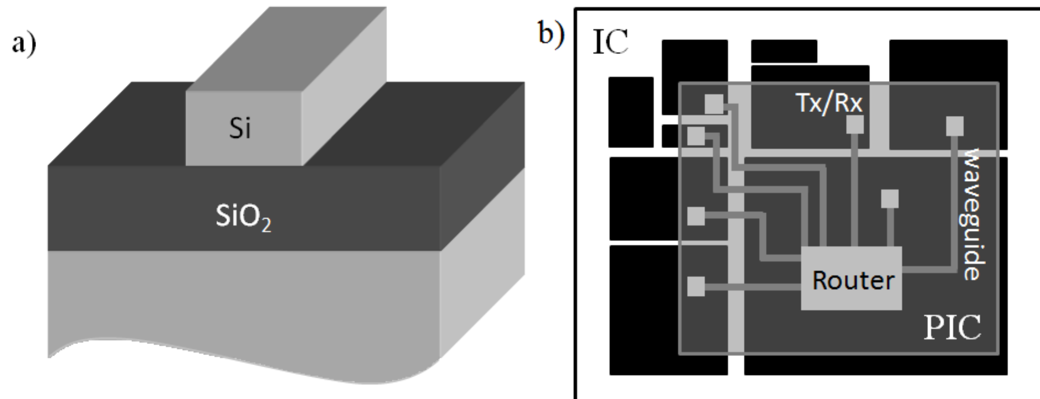

Figure 1.3: a) A schematic of a transmission waveguide formed on SOI, consisting of an etched channel (or 'wire') in the silicon overlayer; b) Schematic of IC with integrated PIC for interconnection (either monolithically integrated onto the top interconnect level or bonded); PIC consists of Router IC, transmission waveguides, and transmitter/receiver modules (Tx/Rx) (diagram reproduced from [23]).

A proposed integration scheme is illustrated in Figure 1.3b, where a PIC is integrated onto the top level of a standard IC to provide long-distance interconnection [23]. The router controls the transmission of signals to various parts of the chip, sent via silicon waveguides integrated onto the top level of the interconnect stack. Each portion of the chip must contain transmitter/receiver (Tx/Rx) modules, which provide conversion between the electrical and optical domain. In addition to the waveguide, the other photonic components necessary for such a scheme are the optical source, the optical modulator and the photodetector.

The ***optical source*** is problematic to implement, because silicon is not an efficient light-emitting material. There has been some success in the academic research arena, such as the demonstration of silicon lasers using the nonlinear Raman effect [25], achieving laser emission from strained silicon-germanium (SiGe) compound semiconductors [26], as well as a vast amount of work achieving light emission from silicon nanostructures embedded in dielectric [27]. However, the most promising solution

ignores silicon as the light generating material altogether and thus exploits a hybrid integration of light emitting III-V material with the PIC as a light source, either coupled in from off-chip [28] or on-chip via bonding [29].

Optical modulators, on the other hand, have been prototyped with increasingly successful results in recent years. The most common electro-optic effect utilized in silicon is the plasma-dispersion effect, which quantifies the change in refractive index when charge carriers are injected or removed from a waveguide (See section 2.2). Common device designs integrate a *p-n* [30] or *p-i-n* junction [31, 32] onto a silicon waveguide, as shown in Figure 1.4a and b for vertical [31] and horizontal [32] *p-i-n* junctions. Care is made to keep the *n* and *p* doped regions sufficiently far from the region of optical mode confinement, to avoid substantial passive loss. The induced refractive index change in the waveguide alters the phase of a mode, and therefore functions as a *phase modulator* (PM). The phase modulation is often converted into an amplitude modulation by embedding these diodes within an interferometer. Two common structures, shown in Figure 1.4c and d, are the Mach-Zehnder Interferometer [31] and a micro-ring resonator [32]. A fast electrical signal applied to the diode is encoded onto the intensity of the resulting mode by these structures, effectively producing conversion from the electrical to the optical domain. Modulation depths of 9 dB at 12.5 Gb/s have been demonstrated for micro-ring modulators [32] and of 2 dB at 40 GHz for Mach-Zehnder modulators [31].

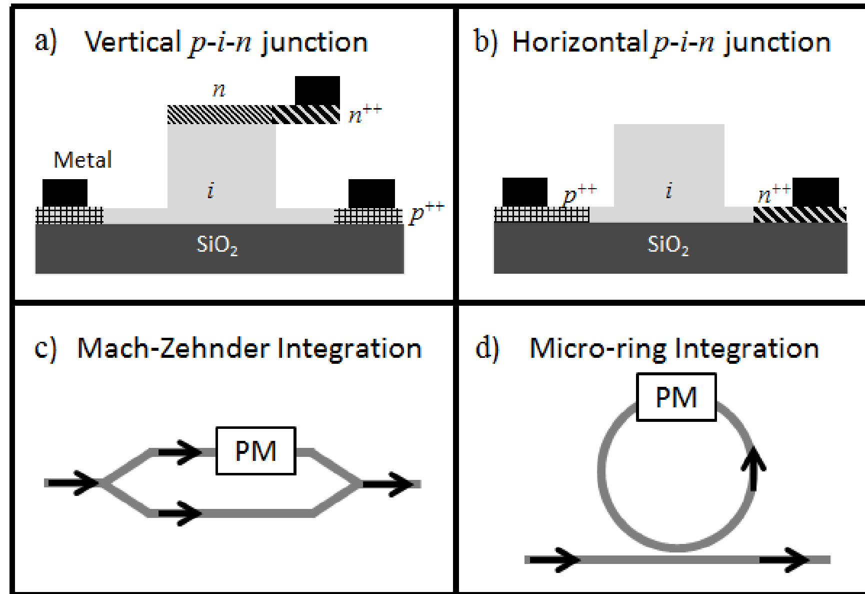

Figure 1.4: Silicon waveguide Phase Modulators (PM) formed of a) A vertical *p-i-n* junction [31], and b) a horizontal *p-i-n* junction [32]; To achieve intensity modulation in the silicon waveguide, these structures are embedded in an interference device, such as c) a Mach-Zehnder interferometer or d) a Micro-ring resonator [33].

The integrated ***photodetector*** often takes the form of a *p-i-n* photodiode (introduced in section 1.2) that is integrated onto the silicon waveguide in a similar way to the phase modulator. As silicon is virtually transparent throughout the *O* and *C* bands (see Figure 1.2b) as required for waveguide operation, there is no intrinsic absorption mechanism that can be used for optical to electrical conversion.

This has been similarly addressed through the integration of other material systems. It is evident from Figure 1.2b that the hybrid integration of either InGaAs compounds or germanium would provide the necessary absorption at 1.55 μm to enable photodetection. In a recent demonstration of this approach, multiple AlGaInAs quantum wells were bonded to the top of a silicon waveguide. Upon reaching this region, the optical mode leaks up into the quantum wells and is absorbed and extracted as photocurrent, providing responsivity of 0.31 A/W [34]. Another design involves grating-

coupling the light from a silicon waveguide vertically through a thick oxide cladding into a vertical InGaAsP *p-i-n* photodetector, alleviating the issues in bonding III-V material directly onto silicon [35].

There is a preference to use germanium over III-V materials, because germanium satisfies the requirement of being *'CMOS compatible'*, and can be grown epitaxially on silicon rather than having to resort to a complex bonding process [36]. Where the diode junction exists entirely within the III-V in the III-V hybrid example, germanium integration allows for the junction to be between the two materials (although this is not always taken advantage of). As shown in Figure 1.5, there are two ways in which a germanium photodiode is integrated onto the waveguide: in the *evanescently coupled design*, it is deposited on top of a waveguide section and absorbs the light leaking into it, while in the *butt-coupled design*, it is deposited at the end of a section of silicon waveguide [36]. In the first case, the electrical junction often occurs between germanium and silicon, while in the latter the *p-i-n* diode is entirely within germanium. Both integration methods result in similar responsivities on the order of 1 A/W (at 2 V bias) [37, 38]. Major silicon photonics companies such as Intel © [38] and Luxtera [39] have tended to favour the first design method, while Kotura © has explored both designs [37, 40]. The intrinsic germanium layer features a strong electric field, even when unbiased, which sweeps the charge carriers out of the waveguide at high velocity. As a result, these detectors are capable of high speed response, with the current record being a 3 dB bandwidth of 42 GHz [41].

The deposition of high quality germanium on silicon has been the focus of intense research for the past decade, and methods such as silicon-germanium buffer layers, multi-step depositions and post-deposition hydrogen annealing have been demonstrated to reduce the density of dislocations [36]. While germanium deposition exists in standard process flows of CMOS foundries, it occurs in the early stages of a device build (optical interconnects would ideally be integrated at the back-end) [36]. Germanium integrated photodetectors have now been fabricated in standard SOI CMOS manufacturing lines by

adding a second germanium deposition step immediately prior to metallization [28], although performance is limited because the deposition is not optimized for the photonic application [36].

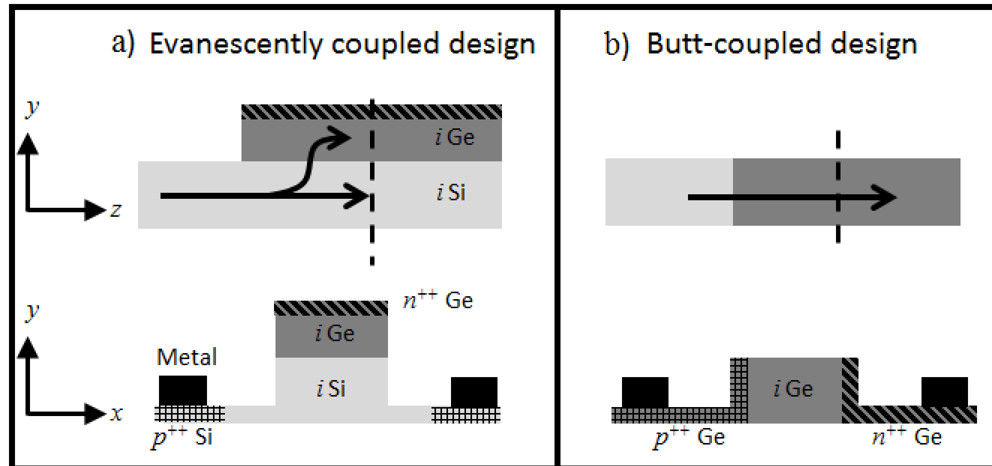

Figure 1.5: Schematic diagrams of the two integration methods used for germanium *p-i-n* photodetectors: a) The evanescently coupled design, where germanium is deposited on top of a section of silicon waveguide [38, 39, 40], and b) The butt-coupled design, where a *p-i-n* germanium structure is fabricated at the termination of the silicon waveguide [37, 41].

Optical sources, modulators and receivers have been combined to demonstrate ***Optical Transceivers***, which are PICs containing the necessary electronics and photonics to transmit and/or receive optical signals at high data rates. The basic structure is shown schematically in Figure 1.6, and is split into transmitter (TX) and receiver (RX) sections. In the transmitter section, a continuous wave (CW) laser source (either on-chip or coupled in) is modulated by the input electrical signal (shown as white lines). Several channels containing signals encoded onto different operating wavelengths are input into a multiplexer, and the resulting multiplexed signal is either coupled off-chip or transmitted to another portion of the chip via waveguides. Upon entering the receiver, the channels are de-multiplexed and each is input into a photodiode to produce a proportionate current

signal. This signal is input into a Trans-Impedance Amplifier (TIA) to convert it into a voltage signal, which is a reproduction of the input signal.

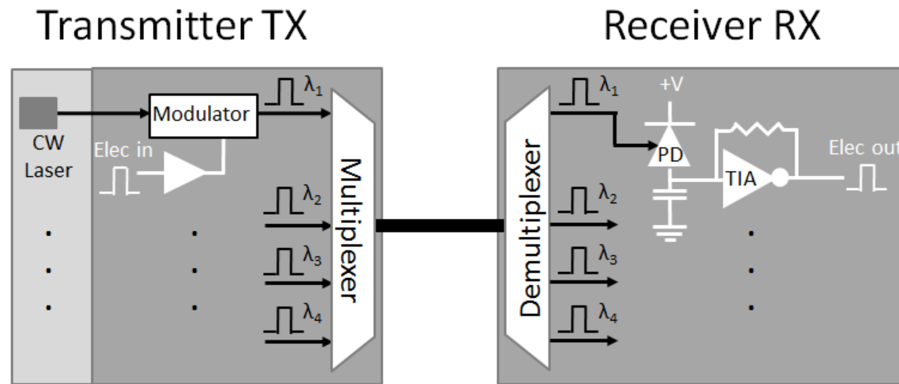

Figure 1.6: An optical transceiver consisting of transmitter and receiver modules: The transmitter modulates a CW laser with an input electrical signal for each channel, and multiplexes the modulated optical signals; the receiver demultiplexes the optical signals and through a photodiode (PD) and TransImpedance Amplifier (TIA), reproduces the electrical signal [28].

Luxtera have produced 10 Gb/s per channel transceiver models, which feature Mach-Zhender Modulators and germanium *p-i-n* photodetectors, with off-chip continuous wave laser sources. The bit-rate of the device may be scaled-up by adding more WDM channels, and currently four channels are used to produce a 40 Gb/s bit-rate [42]. Later work, in collaboration with Kotura © and Sun Labs (Oracle), featured micro-ring modulators and substantial decrease in power dissipation [43]. Intel ©, on the other hand, has recently demonstrated a four channel transceiver operating at 12.5 Gb/s per channel, providing a 50 Gb/s link. What was significant about this demonstration, however, was the integration of the (InP) laser directly onto the chip, forming the highest level of photonic integration to date [44]. These developments have sparked speculation about the possibility of the "macro-chip", a network of processors joined together with optical interconnects. It is expected to provide a 5-6 fold improvement in propagation delay reduction and a 6-300 fold reduced power dissipation over current ICs [20].

1.4 Defect-Enhanced Silicon Photodetection

Despite their widespread use in transceivers, there are a number of fundamental weaknesses with the approach of germanium integrated photodetectors. First, the integration of another material in a heterogeneous *p-i-n* structure as in Ref. 39 leads to significant dark current, which limits the minimum detectable optical power as discussed in section 1.2. The dark current is also found to continue to increase with applied reverse bias, limiting the operating voltage to 1-2 volts. Progress has been made in reducing the dark current to ~ 0.17 μA through optimization of the germanium deposition process [38]; however this is a complicated technique that has taken many years to develop and whose details are often proprietary. The second drawback with this approach is that it only permits end-line photodetection, meaning that the device structures absorb 100% of the light. The only way to facilitate power monitoring, whereby only a small fraction of the light is absorbed, is through coupling a fraction of light into a separate waveguide for detection, a process which results in a device with a relatively large footprint and is wavelength and polarization dependent.

A technology that addresses the above points uses the local enhancement in silicon absorption at 1550 nm through the incorporation of lattice defects. These defects are formed by inert ion implantation, a process in which silicon is bombarded with a small number of high energy ions, the majority of which pass entirely through the waveguide layer. While traveling through the silicon lattice, the ions collide with the host atoms and transfer energy, causing their ejection from the lattice and in turn colliding with other host atoms. These cascade processes leave a trail of damage in the silicon lattice, consisting for instance of single *vacancies* (sites where a silicon atom is missing) or *interstitials* (extra silicon atoms throughout the lattice) shown in Figure 1.7a. The silicon lattice is thus no longer perfectly ideal and periodic, and as a result its electronic and optical properties are changed.

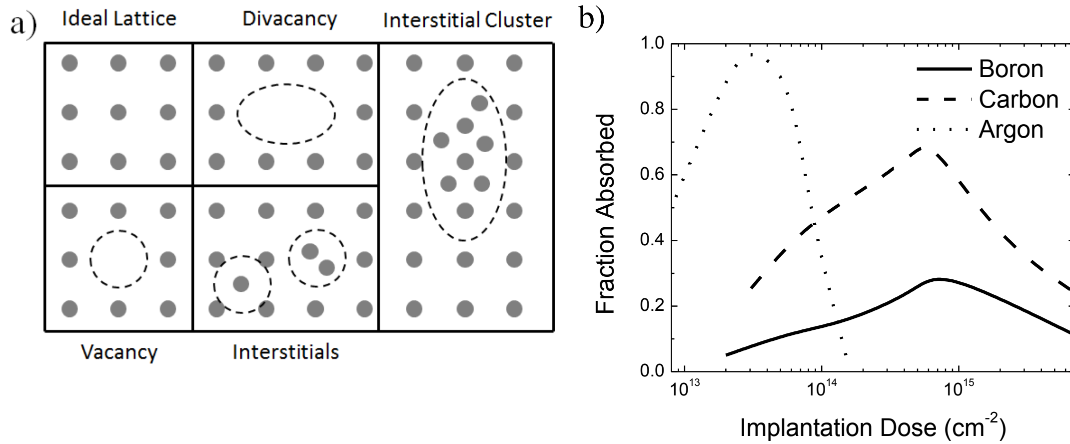

Figure 1.7: a) Schematic of two-dimensional square lattice with defects formed by inert ion implantation: the vacancy (a single missing host atom), the interstitial (a single extra host atom), the divacancy (two adjacent vacancies), and a interstitial cluster (redrawn from [2]); b) Measured excess absorption at 1.8 µm wavelength in silicon, following implantation at 80 keV of boron, carbon and argon ions [45].

Enhancement of optical absorption in silicon for photon energies less than the bandgap energy was reported in 1956 by Fan and Ramdas, following neutron implantation [46]. The resulting absorption spectrum is enhanced substantially (compared to unimplanted silicon) for wavelengths of greater than 1.1 µm, with a prominent peak at 1.8 µm. This peak was later associated with the divacancy, shown in Figure 1.7a as a pair of adjacent vacancies, a complex that is stable at room temperature. By increasing the implanted dose (i.e. number of ions per unit area incident on the surface), the absorption peak at 1.8 µm initially becomes larger as the number of divacancies increase, as shown in Figure 1.7b [45]. Beyond a certain dose, however, the number of divacancies is reduced as they agglomerate into larger cluster-type defects, such as the interstitial cluster in Figure 1.7a. If the dose is increased further, the silicon can be amorphized, meaning the crystalline order is lost entirely. This dose is dependent on the atomic mass of the implanted species: heavier atoms (e.g. argon) will generate more damage at a smaller

dose than a light atom (e.g. boron). Full details on the properties of the divacancy and a review of these early studies will be provided in chapter 3.

In defect-enhanced photodetectors, care is taken to implant with a dose close to that which maximizes the concentration of divacancies. One added benefit of this technology is that the defect chemistry is very sensitive to low temperature (> 200 C) thermal annealing. This allows for the absorption to be 'tuned' following the implantation, to bring it within a device operation specification. It is this feature, i.e. the variation of defect concentration, which facilitates applications in waveguide power monitoring. If a small concentration of defects is introduced the photodetector absorbs only a fraction of light and allows the rest to continue unperturbed.

The process is truly 'CMOS-compatible,' as it simply involves incorporating a lateral *p*-*i*-*n* photodiode onto a section of silicon waveguide, as well as a 'back-end' process consisting of the defect-forming implant. The implant is 'masked', meaning only a portion of the chip (the section of the waveguide containing the diode) is exposed to energetic ions. A variety of ion species may be used to form divacancies [45], as the species themselves do not remain in the waveguide in large numbers and are not involved in the detection process. In the devices described herein, Si^+ ions are used, although full 'CMOS-compatible' devices have been formed using B^+ implantation [47].

The defect-enhanced photodetector was first demonstrated by Bradley *et al.*, using relatively large (> 15 μm^2) waveguide cross-sections and diode lengths of several millimeters. The defects were formed initially by proton bombardment [48], but in later investigations by Si^+ implantation of dose 10^{12} cm^{-3} [49]. The authors observed a 13 dB/cm increase in waveguide absorption and a responsivity of 3 mA/W following implantation, with reduction in absorption and improvement in responsivity after an anneal at 300 C [49]. Because of the modest increase in optical absorption caused by this implant, the diodes were required to consume 6 mm of the device length in order to absorb 19% of the incoming light [48]. This places significant limitations on the

bandwidth, because the *RC* constant scales with device length. This is the main drawback of defect-enhanced detection with respect to germanium detectors, which feature effective absorption coefficients of up to 17 000 dB/cm and can therefore be made in lengths of 10 μm or less [37]. Further study of defect-enhanced photodetection using large cross-section waveguides was carried out by Liu *et al*. Using He^+ ions as the defect-generating implant species and exploring a wider range of annealing conditions, they were able to achieve a responsivity of 65 mA/W [50]. These early large cross-section devices were implanted such that the peak of the implanted species was within the overlayer of the SOI [49, 50].

In order to fully exploit the benefits of defect-enhancement, Geis *et al.* fabricated photodetectors on sub-micron silicon waveguides of 0.15 μm^2 cross-section, which greatly improved the extraction of optically generated carriers. In addition, the final 190 keV Si^+ implantation was sufficient to place the peak of the implanted species to be located in the buried oxide, causing defects to be located uniformly throughout the waveguide thickness. These two modifications provided a responsivity of 800 mA/W and operation at 20 GHz in a 0.25 mm diode, which was also limited by the device *RC* constant [51]. Later work using post-implantation thermal treatments at 475 C explored two stable defect states, characterized by different absorption coefficients, responsivities and leakage currents. These states were attributed to interstitial clusters rather than divacancies (which are known to be removed at temperatures ~ 300 C), and the second state was observed only after forward biasing the diode for several minutes [52]. The interstitial clusters were found to be more efficient than the divacancy, although the absorption coefficient was 8-18 dB/cm [52]. Currently, internal responsivities (i.e. photocurrent divided by the ***absorbed*** optical power) of 10 A/W have been obtained with simultaneous bandwidth of > 35 GHz using these defect structures [53].

Defect-enhanced photodetection is thus a relatively unexplored area, as a broad range of ion implantation and thermal treatments are available and evidently dramatically influence device performance. A systematic evaluation is certainly necessary, and may

well lead to the discovery of more efficient defect centres that can out-perform integrated germanium photodiodes. The purpose of the research summarized in this thesis, however, is to confine attention to the divacancy centre and to optimize device geometry and processing. A model of the detection process (the only proposed to date) is presented and used to provide improvement in the photodetector geometries. The improved efficiency may lead towards these devices' implementation as power monitors for diagnostic purposes throughout PICs. Such monitors, integrated on waveguides provide necessary feedback of optical power levels allowing these levels to be tuned to within desired specification. For example, in the transmitter device of Figure 1.6 in-line monitors could be placed on each optical channel to set the drive current of its on-chip laser. In addition to power monitoring, these photodetectors may be directly integrated onto small resonant structures, using their inherent enhancement in optical intensity to make the *p-i-n* diode 10-100 times smaller than previous generations without sacrificing responsivity. These resonant photodetectors are of a size and responsivity comparable to germanium photodiodes, but with a much smaller dark current.

Chapter 2 of this thesis will provide a description of the operating physics required for a complete understanding of the photodetectors, including descriptions of guided waves, silicon optical absorption, *p-i-n* photodiode physics, and resonator optics. **Chapter 3** will provide a review of the pertinent literature on the divacancy, describe a photodetector performance model implemented in commercial simulation software that is used to reproduce the performance of the photodetectors described above, and discuss some improvements in geometry. **Chapter 4** will introduce one such novel geometry designed using the model: an in-line power monitor fabricated using the LOCOS (Local Oxidation of Silicon) technique. **Chapter 5** will describe the process of fabricating sub-micron waveguide photodetectors using electron-beam lithography, and characterize the resulting structures. **Chapter 6** will detail the integration of these sub-micron photodetectors with micro-rings as resonant-enhanced detectors. **Chapter 7** will

demonstrate the integration of a photo-diode onto the drop-port of a micro-ring, to function as a power monitor used to tune the micro-ring onto resonance.

In summary, the novel contributions of this work are succinctly listed as follows:

1. Development of a model of the defect-enhanced photodetection process, and implementation in commercial software to design waveguide photodiode structures
2. Design of LOCOS-based photodetector and fabrication process, and execution of fabrication and device evaluation
3. Development of a process to fabricate *p-i-n* photodiodes on sub-micron waveguides using electron-beam lithography at the University of Glasgow
4. Design of micro-ring integrated photodiodes, and associated characterization and analysis of their performance
5. Demonstration of an integrated photodiode onto the waveguide ports of a micro-ring resonator, and application as a real-time monitor of resonance properties that provides feedback to a resonance tuner

References

[1] J. S. Kilby, "Invention of the integrated circuit," *IEEE Trans. Elec. Dev.,* vol. ED-23, pp. 648, 1976.

[2] J. D. Plummer, M. D. Deal, and P. B. Griffin, *Silicon VLSI Technology*, "Chapter 1: Introduction and Historical Perspective," Prentice Hall, 2000.

[3] "ITRS: International Technology Roadmap for Semiconductors 2010 Update Overview," Available Online: www.itrs.net

[4] M. J. Kobrinsky *et al.* "On-chip Optical Interconnects," *Intel Technology Journal: Optical Technologies and Applications* vol. 8, pp. 129-142, 2004.

[5] Reproduced from Wikipedia commons, user 'Oleg Alexandrov', under GNU Free Documentation License.

[6] G. Moore, "Cramming more components onto integrated circuits," *Electron.*, vol. 38, pp. 114-117, 1965.

[7] D. Liang and J. E. Bowers, "Photonic integration: Si or InP substrates?" *Electronic Letters,* vol. 45, p. 578-581, 2009.

[8] S. Cristoloveanu, "Silicon on insulator technologies and devices: from present to future," *Solid-State Electronics*, vol. 45, pp. 1403-1411, 2001.

[9] J. Colinge, *Silicon-On-Insulator Technology: Materials to VLSI: 3rd Ed.,* "Chapter 2: SOI Materials", Springer, 2004.

[10] B. E. A. Saleh and M. C. Teich, *Fundamentals of Photonics: 2nd Ed.,* "Chapter 12: Photon Optics", John Wiley & Sons, 2007.

[11] B. E. A. Saleh and M. C. Teich, *Fundamentals of Photonics: 2nd Ed.*, "Preface," John Wiley & Sons, 2007.

[12] G. Keiser, *Optical Fibre Communications: 3rd Ed.,* "Chapter 1: Overview of Optical Fibre Communications", McGraw Hill, 2001.

[13] H. J. R. Dutton, *Understanding Optical Communications*, IBM: International Technical Support Organization, Sept. 1998.

[14] "Infinera introduces new line system, sets new standard for capacity: 160 channels, longer reach and scalability to 8 Terabits on a fiber," Infinera Press Release, June 9, 2008 (www.infinera.com).

[15] G. Keiser, *Optical Fibre Communications: 3rd Ed.*, "Chapter 6: Photodetectors", McGraw Hill, 2001.

[16] B. E. A. Saleh and M. C. Teich, *Fundamentals of Photonics: 2nd Ed.*, "Chapter 3: Semiconductor Optics," John Wiley & Sons, 2007.

[17] M. S. Alam *et al.* "Refractive index, absorption coefficient, and photoelastic constant: key parameters of InGaAs material relevant to InGaAs-based device

performance," *Proc. Of 2007 International Conference on Indium Phosphide and Related Materials*, May 2007, Matsue, Japan. pp. 343-346, 2007.

[18] M. Moussavi, "Advanced Conventional Interconnects: State of the Art, Future Trends, and Limitations," in *Optical Interconnects: The Silicon Approach*, Edited by L. Pavesi and G. Guillot, Springer, 2006.

[19] G. Chen *et al.* "Predictions of CMOS compatible on-chip optical interconnect." *Integration: The VLSI Journal,* vol. 40, pp. 434-446, 2007.

[20] A. V. Krishnamoorthy, *et al*. "Computing systems based on silicon photonic interconnects," *Proc. Of the IEEE,* vol. 97, pp. 1337-1361, 2009.

[21] J. Bautista, "The Potential Benefits of Photonics in the Computing Platform." *Proc. of SPIE,* vol. 5729, Invited Paper, pp. 1-8.

[22] D. F. Welch, "Large-Scale InP Photonic Integrated Circuits: Enabling Efficient Scaling of Optical Transport Networks*." IEEE J. Sel. Top. Quan. Elec.,* vol. 13, pp. 22-31, 2007.

[23] A. Scandurra, "Silicon Photonics: The System on Chip Perspective," in *Silicon Photonics II: Components and Integration (Topics in Applied Physics Vol. 119),* Edited by David J. Lockwood and Lorenzo Pavesi, Springer, 2011.

[24] M. Gnan *et al.* "Fabrication of low-loss photonic wires in silicon-on-insulator using hydrogen silsesquioxane electron-beam resist," *Electronics Letters,* vol. 44, pp. 115-116, 2008.

[25] H. Rong, R. Jones, A. Liu, O. Cohen, D. Hak, A. Fang, and M. Paniccia, "A continuous-wave Raman silicon laser, " *Nature,* vol. 433, pp. 725-728, 2005.

[26] J. Liu, X. Sun, R. Camacho-Aguilera, L. C. Kimerling, and J. Michel, "Ge-on-Si laser operating at room temperature, " *Optics Letters,* vol. 35, pp. 679-681, 2010.

[27] P. R. J. Wilson, T. Roschuk, K. Dunn, E. N. Normand, E. Chelomentsev, O. H. Y. Zalloum, J. Wojcik, and P. Mascher, "Effect of thermal treatment on the growth, structure and luminescence of nitride-passivated silicon nanoclusters, " *Nanoscale Research Letters,* vol. 6, pp. 168-179, 2011.

[28] T. Pinguet *et al.* “Monolithically integrated high-speed CMOS photonic transceivers,” *Proc. Of IEEE: Group IV Photonics 2008, Cardiff, Wales*, pp. 362-364, 2008.

[29] A. W. Fang *et al.* “Electrically pumped hybrid AlGaInAs-silicon evanescent laser,” *Optics Express,* vol. 14, pp. 9203-9210, 2006.

[30] P. Dong *et al.* “Wavelength-tunable silicon microring modulator,” *Optics Express,* vol. 18, pp. 10941-10946, 2010.

[31] L. Liao *et al.* “40 Gbit/s silicon optical modulator for high-speed applications.” *Electron. Lett.,* vol. 43, pp. 1196-1197, 2007.

[32] Q. Xu *et al.* “12.5 Gb/s carrier-injection-based silicon micro-ring silicon modulators,” *Optics Express,* vol. 15, pp. 430-436, 2007.

[33] A. Mekis, “Lighting up the chip,” *Nature Photonics,* vol. 2**,** pp. 389-390, 2008.

[34] H. Park *et al.* “A hybrid AlGaInAs-silicon evanescent waveguide photodetector,” *Optics Express,* vol. 15, pp. 6044-6052, 2007.

[35] G. Roelkens *et al.* “Integration of InP/InGaAsP photodetectors onto silicon-on-insulator waveguide circuits,” *Optics Express*, vol. 13, pp. 10102-10108, 2005.

[36] J. Michel, J. Liu, and L. C. Kimerling, “High-performance Ge-on-Si photodetectors,” *Nature Photonics*, vol. 4, pp. 527-534, 2010.

[37] D. Feng *et al*. “High-speed Ge photodetector monolithically integrated with large cross-section silicon-on-insulator waveguide,” *Applied Physics Letters* vol. 95, p. 261105, 2009.

[38] T. Yin *et al*. “31 GHz Ge n-i-p waveguide photodetectors on Silicon-on-Insulator substrate,” *Optics Express,* vol. 15, pp. 13965-13971, 2007.

[39] G. Masini *et al.* “High-speed near infrared optical receivers based on Ge waveguide photodetectors integrated in a CMOS process,” *Advances in Optical Technologies*, vol. 2008, Art. ID 196472, 2008.

[40] N. Feng *et al.* “A compact high-performance germanium photodetector integrated on 0.25 μm thick silicon-on-insulator waveguide,” *Proc. Of SPIE Vol. 7607: Optoelectronic Interconnects and Component Integration IX,* p. 760704, 2010.

[41] L. Vivien *et al.* "42 GHz p.i.n germanium photodetector integrated in a silicon-on-insulator waveguide," *Optics Express,* vol. 17, pp. 6252-6257, 2009.

[42] J. Witzens *et al.* "10 Gb/s Transceiver on Silicon," *Proc. Of SPIE Vol. 6996*, pp. 699610-1-10, 2008.

[43] X. Zheng *et al.* "Low power silicon photonic transceivers," Proc. Of IEEE: Photonics Society Summer Topical Meetings Series 2010, Playa del Carmen, pp. 199-200, 2010.

[44] A. Alduino *et al.* "Demonstration of a high speed 4-channel integrated silicon photonics WDM link with hybrid silicon lasers," *Integrated Photonics Research, Silicon and Nanophotonics (IPRSN)* July 25, 2010, Postdeadline Session, Monterey, CA, 2010.

[45] E. C. Baranova, V. M. Gusev, Y. V. Martynenko, C. V. Starinin, and L. B. Haibullin, "On silicon amorphization during different mass ion implantation." *Radiation Effects*, vol. 18, pp. 21-26, 1973.

[46] H. Y. Fan and A. K. Ramdas, "Infrared Absorption and Photoconductivity in Irradiated Silicon," *Journal of Applied Physics*, vol. 30, pp. 1127-1134, 1959.

[47] J. K. Doylend, P. E. Jessop, and A. P. Knights, "Silicon photonic optical channel leveler with external feedback loop," *Optics Express,* vol. 18, pp. 13805-13812, 2010.

[48] J. D. B. Bradley, P. E. Jessop, and A. P. Knights, "Silicon waveguide-integrated optical power monitor with enhanced sensitivity at 1550 nm," *Applied Physics Letters,* vol. 86, pp. 241103, 2005.

[49] A. P. Knights, J. D. B. Bradley, S. H. Gou, and P. E. Jessop, "Silicon-on-insulator waveguide photodetector with self-ion-implantation-engineered-enhanced infrared response," *J. Vac. Sci. Technol.,* vol. A 24, pp. 783-786, 2006.

[50] Y. Liu *et al.*, "In-line channel power monitor based on Helium ion implantationin silicon-on-insulator waveguides," *IEEE Photon. Technol.Lett.*, vol. 18, pp. 1882–1884, Sep. 2006.

[51] M. W. Geis *et al.*, "CMOS-compatible all-Si high-speed waveguide photodiodes with high responsivity in near-infrared communication band," *IEEE Photon. Technol. Lett.*, vol. 19, pp. 152–154, Feb. 2007.

[52] M. W. Geis, S. J. Spector, M. E. Grein, R. T. Schulein, J. U. Yoon, D. M. Lennon, C. M. Wynn, S. T. Palmacci, F. Gan, F. X. Kärtner, and T. M. Lyszczarz, "All silicon infrared photodiodes: photo response and effects of processing temperature," *Optics Express,* vol. 15, pp. 16886-16895, 2007.

[53] M. W. Geis, S. J. Spector, M. E. Grein, J. U. Yoon, D. M. Lennon, and T. M. Lyszczarz, "Silicon waveguide infrared photodiodes with >35 GHz bandwidth and phototransistors with 50 AW^{-1}," *Optics Express,* vol. 17, pp. 5193-5204, 2009.

Chapter 2 Background Theory

2.1 Fundamentals of Guided Wave Optics

2.1.1 Overview of electromagnetic wave propagation

The equation governing the propagation of light in a dielectric medium containing no free charges and no current may be derived from Maxwell's Equations:

$$\nabla \times \vec{H} = \frac{\partial \vec{D}}{\partial t} \qquad \nabla \times \vec{E} = -\frac{\partial \vec{B}}{\partial t} \qquad \nabla \bullet \vec{D} = 0 \qquad \nabla \bullet \vec{B} = 0 \qquad \text{(2.1-2.4)},$$

where $\vec{H}$ is the *magnetic vector field*, $\vec{E}$ is the *electric vector field*, $\vec{B}$ is the *magnetic flux density*, and $\vec{D}$ is the *electric flux density* [1].

In non-magnetic materials, $\vec{B}$ is directly proportional to $\vec{H}$:

$$\vec{B} = \mu_0 \vec{H} \qquad \text{(2.5)},$$

where μ_0 is the *magnetic permeability of free-space*, and has a constant value of $4\pi \times 10^{-7}$ N/A^2 [1].

The relation between $\vec{D}$ and $\vec{E}$ is not as straight-forward, as it must incorporate the response of the dielectric to the applied field $\vec{E}$. Upon the application of $\vec{E}$, the bound charges within the dielectric deviate from their natural positions, forming *Dipole Moments*. By summing the contribution of each dipole in a bulk piece of material and dividing by the volume, one calculates the *Polarization Density* $\vec{P}$, also defined as:

$$\vec{P} = \varepsilon_0 \chi \vec{E} \qquad \text{(2.6)},$$

where χ is a bulk material parameter called the *dielectric susceptibility*, and ε_0 is the *electric permittivity of free-space*, which has a constant value of 8.85 x 10^{-12} F/m^2. Two assumptions have been made in Eq. (2.6), which are valid in all of the silicon photonic devices presented in this thesis. First, it was assumed that the material is isotropic, which means χ does not depend on the orientation of the material with respect to the incident electric field, and consequently $\vec{P}$ is always parallel to $\vec{E}$. Second, it was assumed that the material is a *Linear Dielectric*, which means $\vec{P}$ is linearly proportional to $\vec{E}$. More generally, χ has higher-order terms which depend on the electric field amplitude. In linear dielectrics, these higher order terms are insignificant (if not zero) for the electric field amplitudes that are typically encountered [1].

The Electric Flux Density $\vec{D}$ is formed of contributions from both the electric field $\vec{E}$ itself and the induced polarization density $\vec{P}$:

$$\vec{D} = \varepsilon_0 \vec{E} + \vec{P} = \varepsilon_0 (1+\chi)\vec{E} \quad (2.7)$$

This is often simplified to:

$$\vec{D} = \varepsilon \vec{E} \quad (2.8),$$

where $\varepsilon = \varepsilon_0(1+\chi)$ is defined to be the *electric permittivity of the material* [1].

The Maxwell's equations of Eq. (2.1-2.4) may now be rewritten for isotropic, homogeneous, and linear dielectrics in terms of $\vec{E}$ and $\vec{H}$ alone:

$$\nabla \times \vec{H} = \varepsilon \frac{\partial \vec{E}}{\partial t} \qquad \nabla \times \vec{E} = -\mu_0 \frac{\partial \vec{H}}{\partial t} \qquad \nabla \bullet \vec{E} = 0 \qquad \nabla \bullet \vec{H} = 0 \quad (2.9\text{-}2.12)$$

The wave equation is derived by taking $\nabla \times \nabla \times \vec{E}$ and using Eq. (2.10) and subsequently Eq. (2.9) to arrive at:

$$\nabla \times \nabla \times \vec{E} = -\mu_0 \varepsilon \frac{\partial^2 \vec{E}}{\partial t^2} \quad (2.13)$$

Invoking the following vector identity:

$$\nabla \times \nabla \times \vec{E} = \nabla\left(\nabla \bullet \vec{E}\right) - \nabla^2 \vec{E} \quad (2.14),$$

and combining Eq. (2.14) with Eqns. (2.11) and (2.13), the Electromagnetic wave equation is derived:

$$\nabla^2 \vec{E} = \mu_0 \varepsilon \frac{\partial^2 \vec{E}}{\partial t^2} = \frac{1}{c^2}\frac{\partial^2 \vec{E}}{\partial t^2} \quad (2.15),$$

where c is defined as the *speed of light* in the material. It is convenient to define it with respect to the *speed of light in vacuum* c_0:

$$c = \frac{1}{\sqrt{\varepsilon \mu_0}} = \frac{1}{\sqrt{\varepsilon_0 \mu_0}}\frac{1}{\sqrt{\varepsilon/\varepsilon_0}} = \frac{c_0}{n} \quad (2.16),$$

where c_0 has a constant value of 3 x 10^8 m/s, and $n = \sqrt{\varepsilon/\varepsilon_0}$ is called the *refractive index*, a material parameter used to describe the degree to which light propagation is slowed down from c_0 [1].

Similarly, if the same process were carried through for $\nabla \times \nabla \times \vec{H}$, the wave equation for the magnetic field $\vec{H}$ would result:

$$\nabla^2 \vec{H} = \frac{1}{c^2}\frac{\partial^2 \vec{H}}{\partial t^2} \quad (2.17)$$

In summary, Eq. (2.9) indicates that a time-varying electric field generates a magnetic field, while Eq. (2.10) indicates that a time-varying magnetic field generates an electric field. Then, from Eq. (2.15) and (2.16), the electric field and magnetic field may propagate together as a wave with speed c. If the form of one of $\vec{E}$ or $\vec{H}$ is known, the other can be deduced from Eq. (2.9-2.10). A general solution to Eq. (2.15) is:

$$\vec{E}(\vec{r},t) = \vec{E}_0(\vec{r})e^{i\left(\vec{k}\bullet\vec{r} - \omega t\right)} \quad (2.18),$$

where $\vec{E}_0(\vec{r})$ is the electric field, or the amplitude of the wave, $\vec{r}$ is a vector in Cartesian (x, y, z) coordinates, and t is time. The parameter ω is the *angular frequency* (measured in radians per second), although light waves are more commonly referred to by their optical

frequency $\nu = \omega/2\pi$ (measured in Hz) [1]. The solution of Eq. (2.18) is a *monochromatic wave*, as it contains only a single frequency. However, any practical polychromatic wave can be described as a linear combination of the waves of Eq. (2.18). While $\vec{E}_0(\vec{r})$ may also have time dependence, as it does in a modulated optical signal, it will be ignored in the present discussion since that variation is slow compared to ω.

The wavevector $\vec{k}$ describes the spatial periodic variation of electric field as a consequence of wave propagation. For propagation in isotropic materials, $\vec{k}$ is perpendicular to both $\vec{E}$ and $\vec{H}$, making the light wave transverse [1]. For instance, a particular solution would be a *plane wave* travelling in the z direction, made by setting $\vec{E}_0$ as a constant vector in the xy plane and setting $\vec{k}$ to be parallel to z with a magnitude of k:

$$\vec{E}(z,t) = \vec{E}_0 e^{i(kz-\omega t)} \tag{2.19}$$

At a given point on the z axis, the electric field oscillates with a frequency ω. Consequently, a wave is generated which travels at a speed c_0/n. If one were to follow a phase front in time and space, the phase of the wave would be constant:

$$\begin{gathered} kz - \omega t = \text{constant} \\ \therefore k\frac{\partial z}{\partial t} - \omega = 0 \end{gathered} \tag{2.20}$$

Therefore, the magnitude of the wavevector is determined from the speed of the wavefront (c_0/n) and the oscillation frequency ω:

$$k = \frac{\omega n}{c_0} = k_0 n \tag{2.21},$$

where k_0 is defined as the wavevector in free-space (i.e. the value it *would have* if it were propagating in a medium with n = 1). It is easier to conceptualize the wavelength λ, defined as:

$$\lambda = \frac{2\pi}{k} = \frac{\lambda_0}{n} \tag{2.22},$$

where again it is convenient to define a free-space optical wavelength λ_0. The wavelength refers to the distance in space (in this case along z) over which one oscillation cycle is completed, as illustrated in Figure 2.1. From Eq. (2.19), at a particular instant in time, the electric field amplitude is has a period of λ along z. The consequence of Eq. (2.22) is that, since $n \geq 1$, the wavelength of propagation is compressed in any material over its value in vacuum [1]. In this thesis, it will be λ_0 that is being referred to whenever wavelength is quoted.

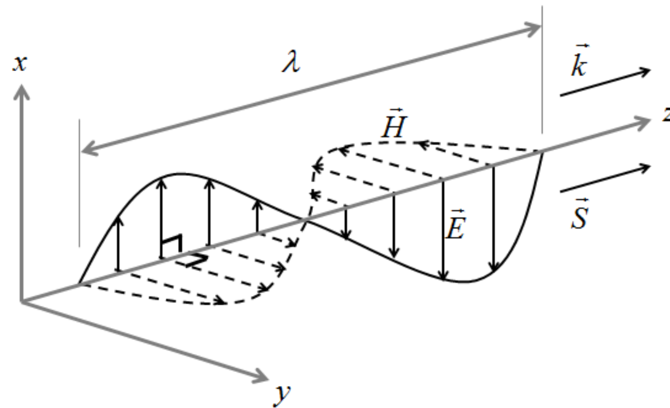

Figure 2.1: Propagation of a Transverse Electromagnetic Wave, shown at a single instant in time. The wave is linearly polarized, with the *electric field* $\vec{E}$ oscillating in the *x* direction, the *magnetic field* $\vec{H}$ oscillating in the *y* direction. The *wavevector* $\vec{k}$ and *Poynting Vector* $\vec{S}$, signifying the direction of propagation and energy transport respectively, are in the *z* direction. The *wavelength* λ signifies the nearest distance between two points of equal phase [1, 2].

The *Poynting Vector* is defined as:

$$\vec{S} = \vec{E} \times \vec{H} \tag{2.23}$$

This vector points in the direction perpendicular to both $\vec{E}$ and $\vec{H}$, as shown in Figure 2.1, and represents the instantaneous flux of energy transported by the wave [2]. In the case of isotropic materials, the Poynting vector and wavevector are parallel. The

intensity I of a light wave is equal to the time average of the magnitude of the Poynting vector [1]:

$$I = \left\langle \left| \vec{S} \right| \right\rangle = \frac{1}{2} n \varepsilon_0 c_0 \left| \vec{E}_0 \right|^2 \tag{2.24}$$

The intensity of light is measured units of power per unit area (W/cm^2), and so the optical power P is calculated by integrating the intensity over area. The plane wave of Eq. (2.19) is not physical, since it is infinite in extent in x and y and therefore carries infinite energy. However, any physical wave may be described as a linear combination of plane waves.

The orientation of $\vec{E}$ in a light wave is called *Polarization,* which determines how light interacts with an interface, as illustrated in Figure 2.2a. When light of any polarization is incident on a boundary between two materials of refractive index n_1 and n_2 at an angle θ_1, it must be written as the sum of two components: those with electric field oscillation normal to the plane of incidence[1] (Transverse Electric, or TE), and those having the electric field oscillation in the plane of incidence (Transverse Magnetic, or TM). The classification is required because the boundary conditions for the two cases are different. At the interface, the normal components of $\vec{D}$ and $\vec{B}$ (or equivalently the normal components of $\varepsilon\vec{E}$ and $\mu_0\vec{H}$) must be continuous, and the tangential components of $\vec{E}$ and $\vec{H}$ must be continuous [1].

The incident light is partially reflected and partially refracted at the interface. The boundary conditions provide the means to determine the fraction that is reflected (r_{TE} or r_{TM}) and the fraction that is transmitted (t_{TE} or t_{TM}). These coefficients are in general complex quantities, with a magnitude that indicates the fraction of the field that is reflected/transmitted and a phase that indicates the phase shift imparted to the reflected/ transmitted wave with respect to the incident wave. From Eq. (2.24), the fraction of the intensity that is reflected R is then [3]:

[1] The plane of incidence is defined as the plane formed by the wavevector of the incident light k_i and the normal to the interface (shown as a dotted line in Figure 2.1.2)

$$R_{TE} = |r_{TE}|^2 \quad \text{and} \quad R_{TM} = |r_{TM}|^2 \tag{2.25}$$

and the fraction of the intensity that is transmitted T is [3]:

$$T_{TE} = \left(\frac{n_2 \cos\theta_2}{n_1 \cos\theta_1} \right) |t_{TE}|^2 \quad \text{and} \quad T_{TM} = \left(\frac{n_2 \cos\theta_2}{n_1 \cos\theta_1} \right) |t_{TM}|^2 \tag{2.26}$$

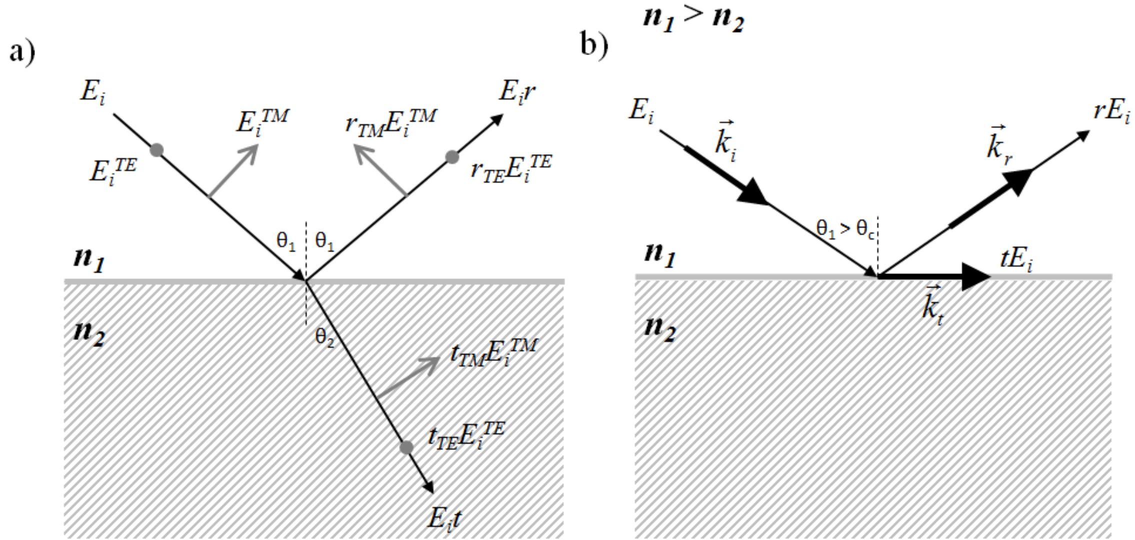

Figure 2.2: a) Interaction of light ray arriving at boundary between two materials of refractive index n_1 and n_2. The TE and TM components are reflected with respective coefficients r_{TE} and r_{TM} and transmitted with respective coefficients t_{TE} and t_{TM}. The reflected wave makes the same angle θ_1 with the normal to the boundary plane, while the transmitted wave makes an angle θ_2 with it; b) Total Internal Reflection occurring when $\theta_1 > \theta_c$ (defined in Eq. (2.18)), Illustrating incident, reflected and transmitted wavevectors (k_i, k_r, and k_z respectively), where k_t is along the interface and no power is transferred to the lower index material [1].

Note that $T + R = 1$ for both TE and TM polarizations, so energy is conserved. Also note that the coefficients become equal when $\theta_1 = 0$, as there is no plane of incidence and therefore no distinction between TE and TM.

The angle of reflection and refraction are also deduced from the boundary conditions, and in fact are the same for both TE and TM polarizations. The angle of

reflection is always equal to the angle of incidence, and the angle of refraction is given by *Snell's Law* [3]:

$$n_1 \sin\theta_1 = n_2 \sin\theta_2 \qquad (2.27)$$

When $n_2 > n_1$, the reflection of light is said to be external reflection; and when $n_1 > n_2$, the reflection of light is said to be internal reflection. For internal reflection, the reflection coefficient is complex with a magnitude of 1 for all incident angles:

$$\theta_1 > \theta_c = \sin^{-1}\left(\frac{n_2}{n_1}\right) \qquad (2.28),$$

where θ_c is defined as the critical angle, and light incident at an angle $\theta > \theta_c$ will have a reflected intensity of $R = 1$ and a transmitted intensity of $T = 0$ [3]. This situation is appropriately called *Total Internal Reflection*, and is depicted in Figure 2.2b. While there is no transmitted wave, an *Evanescent Field* penetrates into the lower index material with exponentially decaying amplitude [1]. Provided the lower index material remains homogeneous for a distance of several wavelengths, no energy is transmitted by the evanescent field.

2.1.2 Description of guided waves

A waveguide refers to any structure that confines light in one or two spatial dimensions. In silicon, this is achieved through the concept of total internal reflection. For instance, a thin silicon film sandwiched between two layers of lower refractive index is an example of a *planar waveguide,* shown in Figure 2.3. The silicon layer is referred to as the *slab*, the top (air) layer is called the *cladding*, and the bottom (SiO_2) layer is called the *substrate*. Light may undergo multiple reflections at both the slab/cladding and slab/substrate interfaces at an angle θ, as shown in Figure 2.3. Provided θ is greater than the critical angle for each interface, the light will be totally reflected indefinitely and therefore be confined to the slab region [4].

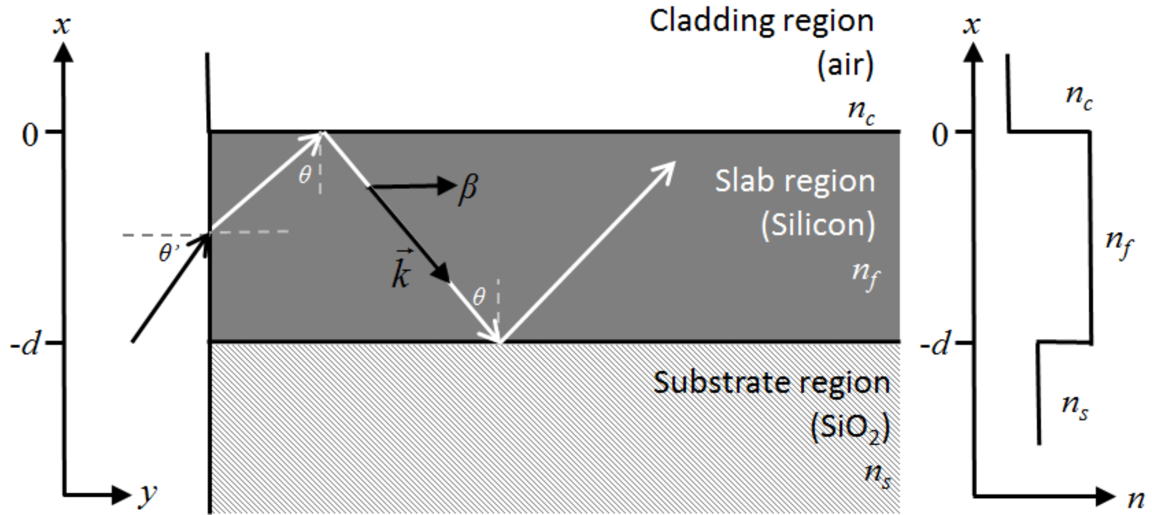

Figure 2.3: An asymmetric planar waveguide formed of a SiO_2 substrate, silicon film slab of thickness *d*, and an air cladding; light incident at an angle *θ'* will undergo multiple total internal reflections at an angle $\theta > \theta_c$ at each boundary, causing the light to be confined in the slab region and propagate in *y* with a propagation constant *β*.

Due to interference of the reflected waves, there exist only discrete angles θ_m for which a guided wave exists, each of which is called a *mode* of order *m* [5]. Each mode propagates in the *y-z* plane (here assumed to be in the *y* direction for simplicity) and has a unique intensity distribution in *x*. The propagation of mode *m* is governed by a propagation constant β_m, which are equal to the wavevector component k_y as defined in section 2.1.1, and defined as:

$$\beta_m = n_f k_0 \sin\theta_m = n_{eff}{}^m k_0 \qquad (2.29),$$

where $n_{eff}{}^{m,}$ is the effective index of the mth mode of the structure, which indicates the speed of overall mode propagation in *y* after taking into account the multiple reflections. The minimum value of *β* is set by the critical angle of the refractive index of the substrate to $\beta_{\min} = n_s k_0$ and the maximum value corresponds to direct propagation in *y* with no

reflections: $\beta_{\max} = n_f k_0$. As a result, the values of n_{eff} may range from n_s to n_f, and larger mode angles θ_m correspond to slower propagation and consequently larger n_{eff}^m [6].

The modes of a slab waveguide may be solved explicitly using Maxwell's equations along with the appropriate boundary conditions (being continuity of the tangential components of $\vec{E}$ and $\vec{H}$ and the normal components of $\varepsilon\vec{E}$ and $\vec{H}$ at each interface). The monochromatic solutions are of the form:

$$\vec{E}(x,y,t) = \left(E_x(x), E_y(x), E_z(x)\right)e^{i(\beta y-\omega t)} \tag{2.30}$$
$$\vec{H}(x,y,t) = \left(H_x(x), H_y(x), H_z(x)\right)e^{i(\beta y-\omega t)}$$

There are thus seven unknown parameters: $E_x(x)$, $E_y(x)$, $E_z(x)$, $H_x(x)$, $H_y(x)$, $H_z(x)$, and β. The solutions may be divided into TE and TM modes. TE modes will have $E_y = 0$ (since it is transverse electric, it must have no electric field component in the direction of propagation y), and it follows that $E_x = H_z = 0$ as well. Similarly, TM modes will have $H_y = 0$ and therefore $E_z = H_x = 0$. The TE modes of the structure of Figure 2.3 have the following solution:

$$E_x = E_y = H_z = 0$$

$$E_z = Ae^{-\gamma_c x} \qquad \text{for} \qquad x \geq 0$$

$$E_z = A\left[\cos\kappa x - \frac{\gamma_c}{\kappa}\sin\kappa x\right] \qquad \text{for} \qquad 0 \geq x \geq -d$$

$$E_z = A\left[\cos\kappa d + \frac{\gamma_c}{\kappa}\sin\kappa d\right]e^{\gamma_f(x+d)} \qquad \text{for} \qquad x \leq -d$$

$$H_x = -\left(\frac{\beta}{\omega\mu_0}\right)E_z$$

$$H_y = \left(\frac{i}{\omega\mu_0}\right)\frac{\partial E_z}{\partial x}$$

where:

$$\gamma_c^{\ 2} = \beta^2 - k_0^{\ 2} n_c^{\ 2}$$

$$\kappa^2 = k_0^{\ 2} n_f^{\ 2} - \beta^2$$

$$\gamma_s^{\ 2} = \beta^2 - k_0^{\ 2} n_s^{\ 2} \qquad (2.30),$$

and the boundary conditions have imposed the following on β:

$$\tan \kappa d = \frac{\kappa(\gamma_c + \gamma_s)}{\kappa^2 - \gamma_c \gamma_s} \qquad (2.31)$$

The solutions of this transcendental equation are plotted as the solid curve in Figure 2.4a for a wavelength of λ_0 = 1.55 μm, illustrating the variation in n_{eff} (or equivalently the internal reflection angle θ) with slab thickness d. It is evident that reducing d causes the number of guided modes to reduce, eventually to the point where no guided modes exist at all. Also plotted using a dashed curve is the result for a symmetric planar waveguide, where SiO_2 forms the cladding as well as the substrate. In this device, the waveguide will support at least one guided mode, regardless of the value of d. When a waveguide supports only the m = 0 mode, it is called a *Single Mode waveguide*; when it supports more, it is called a *Multi-mode Waveguide.* The thickness d at which the m = 1 mode disappears is called the *Cut-off*, and occurs when $n_{eff}^{m=1} = n_s$, which is equivalent to the loss of total internal reflection at that interface [4].

The result of Eq. (2.30) is then that the total internally reflected wavefront has field components that propagate with the same phase velocity as a wave in a homogeneous material of refractive index n_{eff}. The amplitude of these components has a sinusoidal variation within the slab, and exponentially decays into the substrate and cladding to a depth that is inversely proportional to n_{eff}. Indeed, the closer n_{eff} is to n_f, the more confined to the slab the guided wave is. Figure 2.4b illustrates the intensity distribution of the m = 0, 1, 2, and 3 mode for the structure in Figure 2.3. It is clear that the m = 0 mode is the most confined to the slab, since it has the largest n_{eff} [5].

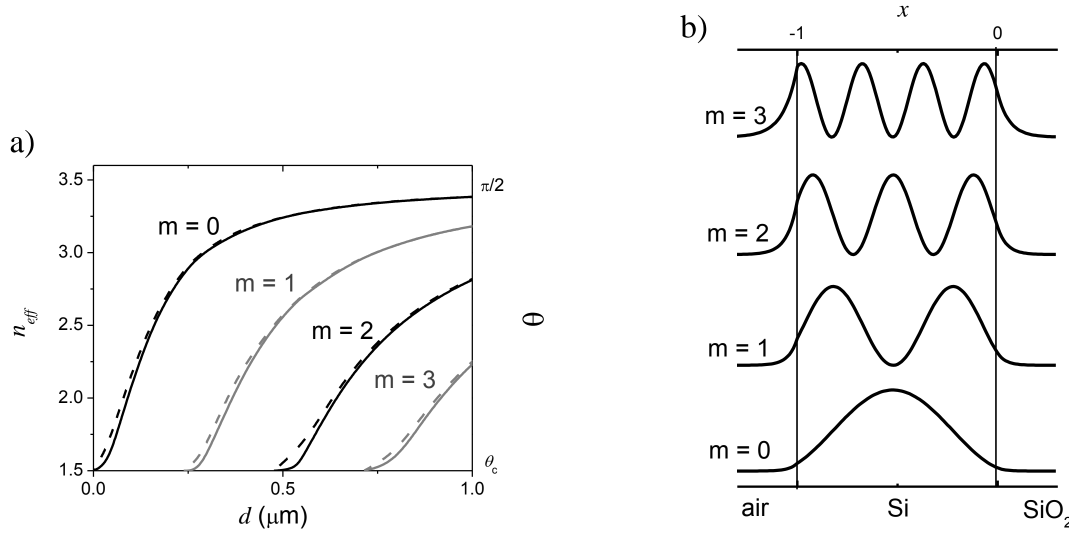

Figure 2.4: a) n_{eff} and θ vs. slab thickness *d* for SiO_2/Si/air (solid lines) and SiO_2/Si/SiO_2 (dashed lines) planar waveguides for a wavelength of λ_0 = 1.55 μm, calculated from Eq. (2.1.31), illustrating the variation of n_{eff} between n_s = 1.5 and n_f = 3.45, or equivalently in reflection angle from θ_c to π/2; b) TE mode intensity profile for SiO_2/Si/air planar waveguide modes *m* = 0, 1, 2, and 3, all with silicon thickness *d* = 1 μm.

There is a similar approach to finding the TM modes, which will not be described here. The resulting modes consist of field components E_x, E_y, and H_z, which have an amplitude variation in *x* that is similar to the TE mode.

In addition to the discrete mode solutions of Maxwell's equations for which $n_{eff} >$ n_s and n_c, there are an infinite number of *radiation mode* solutions for which n_{eff} is lower than one or both of n_s and n_c. These waves are not confined to the slab region [5]. Any light wave existing in the waveguide structure may be written as a linear combination of the allowed TE and TM guided modes and the radiation modes [4].

Waveguides that confine light in two dimensions are conceptually similar to the slab waveguide. A common two-dimensional waveguide is the channel waveguide shown in Figure 2.5a, which is formed of a high index material (silicon) of width *W* and height *H* embedded in a lower index dielectric. The effect of inhomogeneity in a second

dimension precludes the existence of pure TE or TM modes: they will generally have a small $\vec{H}$ and $\vec{E}$ vector in the direction of propagation, and are called hybrid modes. When the largest electric field component lies in the x direction, the hybrid mode is said to be quasi-TM and denoted by E^x, and when the largest electric field component is in the y direction, the hybrid mode is said to be quasi-TE and denoted by E^y.

The solutions of the channel waveguide of silicon are similar in nature to those for the planar waveguide, with sinusoidal variation in both x and y within the channel and evanescent decay into the surroundings. The wavevector components in the directions x (κ_x) and y (κ_y) are determined by the boundary conditions, and admit only discrete values (labelled by integers p and q). Once the κ_x and κ_y eigenvalues have been determined, the functional form of the mode $E^x{}_{pq}$ or $E^y{}_{pq}$ is established, with a propagation constant given by [5]:

$$\beta = \left[n_1{}^2 k_0{}^2 - \left(\kappa_x{}^2 + \kappa_y{}^2\right)\right]^{1/2} \tag{2.32}$$

The variation of β and n_{eff} with either waveguide height H or width W is similar to that of Figure 2.4a. The introduction of two mode numbers p and q increases the variety of intensity distributions, however. The lowest mode order is (p, q) = (0, 0), whose profile is shown in Figure 2.5b. Waveguides with small height H but wide extent W may be multimode in y, the first higher order mode being the pictured (p, q) = (0, 1) distribution. Alternatively, tall and narrow waveguides may be multimode in x, as shown in the distribution for (p, q) = (1, 0) [5]. For a silicon channel embedded in oxide, the waveguide must have $W < 600$ nm and $H < 450$ nm for single mode transmission at $\lambda_0 = 1.55$ µm.

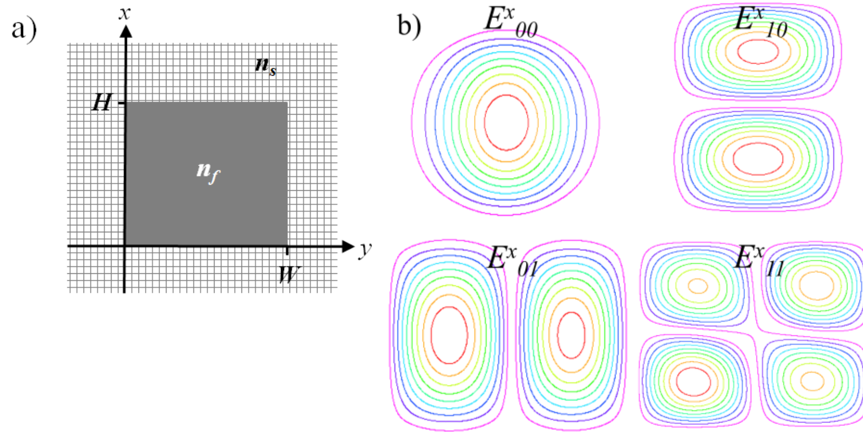

Figure 2.5: a) A silicon channel waveguide structure of height *H* and width *W*, surrounded by a uniform dielectric (SiO_2); b) $E^x{}_{00}$, $E^x{}_{01}$, $E^x{}_{10}$, and $E^x{}_{11}$ intensity distributions for the structure in a).

It is preferred to have single mode waveguides in integrated optics, as this means that all of the power in the waveguide is within the mode that is most confined to the channel. The more confined the mode is, the less susceptible to scattering losses from edge defects and cross-talk with other optical elements. More importantly, it is crucial for high-speed applications that the waveguide is single-mode. If multiple modes are present, the distribution of β leads to a broadening in the signal, known as intermodal dispersion.

An alternative two-dimensional waveguide structure is shown in Figure 2.6: a *rib waveguide* structure formed of a step in the silicon surface of height *H-h* and width *W*. The ability of this structure to confine light may be understood through the *effective index method*. Namely, a two-dimensional structure may be solved by considering each dimension individually. A planar waveguide of width *H* will yield a lowest order TM mode of effective index n_{eff1}, and a planar waveguide of width *h* will yield a lowest order TM mode of effective index n_{eff2}. The effective index of the two-dimensional structure is then the lowest order TE mode of the symmetric planar waveguide formed of a layer of refractive index n_{eff1} and thickness *W* sandwiched between layers of refractive index n_{eff2} as shown in Figure 2.6 [5].

One example of a rib waveguide used in this project is a W = 500 nm, H = 220 nm channel, with a h = 50 nm slab. From the effective index method, it is found that increasing h reduces the index contrast in y, and the mode will be less confined. At λ_0 =1.55 μm, it may be calculated that n_{eff1} = 2.87 and n_{eff2} = 1.74, and the estimated effective index of the structure is then n_{eff} = 2.62. The case of h = 0 (a channel structure) is similar to the above but with $n_{eff2} = n_s = 1.5$, which leads to the estimate n_{eff} = 2.65. It is therefore concluded that the presence of the thin h = 50 nm slab to the structure does not strongly influence the modal properties.

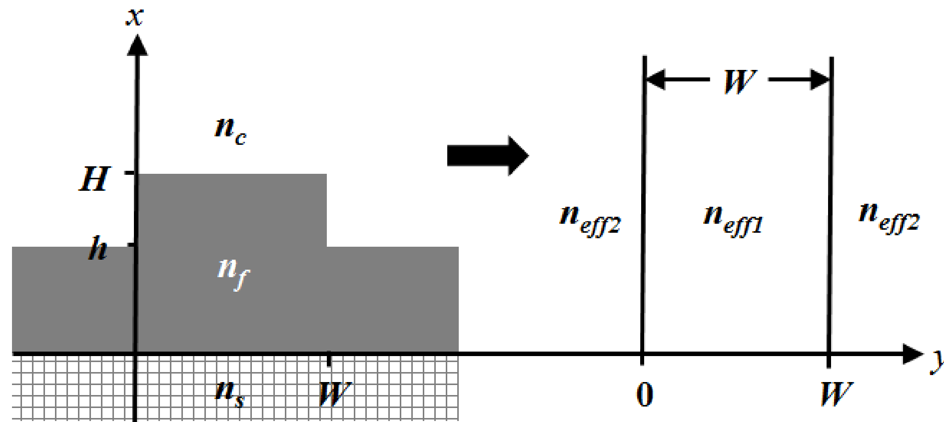

Figure 2.6: The structure of a rib waveguide, consisting of a silicon ridge of width *W* and height *H* surrounded by a silicon slab of height *h* (left); the effective index approximation for this structure involves solving the TM planar waveguides of thickness *h* and *H* to yield respective solutions n_{eff2} and n_{eff1}, and using as the film indices in the *effective* planar waveguide shown on the right to approximate the rib waveguide effective index.

The condition for single mode propagation has been solved by Soref and Bennett [7] to be:

$$\frac{W}{H} \leq 0.3 + \frac{\frac{h}{H}}{\sqrt{1-\left(\frac{h}{H}\right)^2}} \qquad \text{where} \qquad \frac{h}{H} \geq 0.5 \tag{2.33}$$

This condition is plotted as Figure 2.7a. It provides insight as to why rib waveguides are ubiquitous in silicon photonics: they may form single-mode structures with dimensions that are many times larger than the wavelength of the guided light. Larger cross-section waveguides are desirable because they are easier to fabricate with low propagation loss, and are much easier to couple light into. Channel waveguides are required to be sub-micron in dimension in order to be single-mode, while rib waveguides can be made with W and H up to 10 μm.

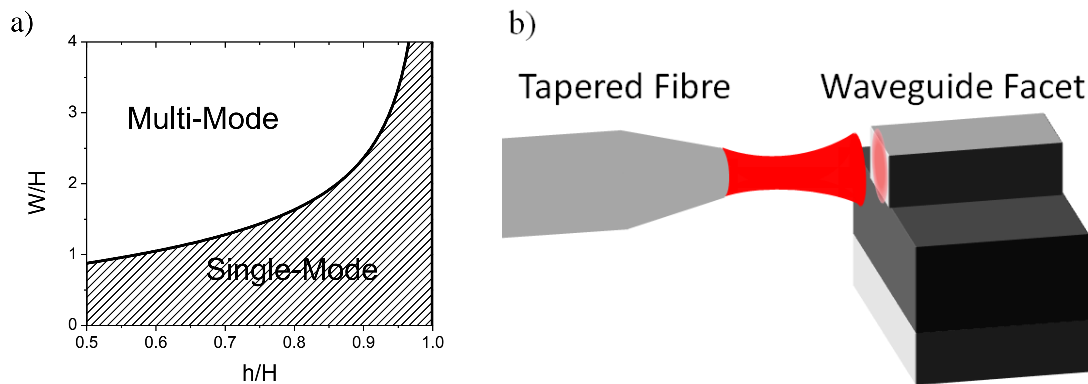

Figure 2.7: a) The single-mode cut-off of the rib waveguide of Figure 2.6, with the region of *h*/*H* and *W*/*H* for which the device is single-mode shaded [7]; b) Schematic diagram of the butt-coupling process from a tapered fibre onto an SOI waveguide facet, indicating the formation of the guided mode following a distance of propagation [8].

A waveguide mode is 'excited' by introducing an optical field that, when decomposed into a sum of the guided and radiation modes of the structure, contains a strong component of the desired guided mode [8]. The fraction of the incident power that does not contribute to the mode is referred to as *Insertion Loss*, and is used to as a measure of coupling efficiency. In this thesis, 'end-fire' or 'butt' coupling is used, which involves focusing light onto the polished end of a waveguide, as illustrated in Figure 2.7b. The light is focused on the facet using a tapered fibre, which produces a minimum spot size diameter of 2.5 μm [9]. While this process is quite inefficient, particularly for sub-micron waveguides, it has the advantage of simple preparation. In fact, all that is

required is to 'cleave' the SOI chip along the crystallographic plane normal to the waveguide, which naturally forms a smooth edge.

2.1.3 Methods of waveguide modeling

Two common approaches for modelling waveguides are the Beam Propagation Method (BPM) and the Finite Difference Time Domain (FDTD) method. Both are used in this project, specifically using the respective RSoft © simulation tools BeamPROP and FullWAVE. In the RSoft CAD environment, a two or three-dimensional structure is defined (with associated material parameters such as refractive indices), and an optical input is specified [10].

BPM operates by solving a simplified scalar wave equation using standard numerical methods at discrete points in the direction of propagation, and assuming only the first-order derivative of the field in the direction of propagation is non-zero [10]. This method offers a fast computation by factoring out the phase variation expected from the refractive index profile, leaving only a slowly varying envelope that can be solved with a large step size in the direction of propagation. The weaknesses in this method are that it cannot simulate back-reflections or scattering [10]. This technique was primarily used here to solve for waveguide modes, using the *iterative method* provided in the BeamPROP software. This sets coordinate in the propagation direction to be imaginary, causing the mode power to be amplified with propagation by a factor $e^{+\beta z}$. Of the contained guided and radiation modes, the $m = 0$ mode is amplified the strongest, as it has the highest value of β. Following a sufficiently long propagation, the intensity profile and n_{eff} are stable with further propagation and the simulation is terminated. By subtracting these field components and repeating, the higher order modes can be sequentially isolated.

Alternatively, FullWAVE performs a rigorous calculation of Maxwell's equations in arbitrary device geometries without using approximations. This is a much more extensive computation, as it involves solving the field components (E_x, E_y, E_z, H_x, H_y, and H_z) at each grid point in the structure, for every time step. The time step required for a stable solution becomes smaller as the spatial resolution is increased, and a spatial resolution of $\lambda/10$ is usually required [11]. This solution method should therefore be employed only when approximate methods such as BPM fail, for instance in resonant structures.

2.2 Optical Absorption in Silicon

The reaction of the constituent atoms of a material to an optical field is classically modeled as simple oscillators. The oscillating electric field $\vec{E}(t)$ drives the bound electron oscillation about the atomic cores, producing an oscillating dipole, as shown in Figure 2.8a. This oscillating dipole then radiates at the same frequency as $\vec{E}(t)$, and contributes to the propagating wave [12]. On a macroscopic scale, the total dipole moment per unit volume is equal to the *Polarization Density* $\vec{P}$ of Eq. (2.6). The frequency response of a material to a driving oscillation is therefore modeled by the linear dielectric susceptibility $\chi(\nu)$, which is a complex quantity. Following from Eqns. (2.7) and (2.16), the refractive index $n(\nu)$ is complex as well, and can be written in terms of its real n_r and imaginary n_i parts:

$$n(\nu)^2 = (1 + \chi(\nu)), \qquad n = n_r + in_i \tag{2.34}$$

This process does not conserve optical energy, as the radiated energy does not entirely compensate the energy coupled to driving the dipole oscillation. This is because the dipole oscillations are damped, and the optical energy lost is transferred to the lattice as heat in a process called *dissipative absorption.* The optical absorption loss of the

material is contained in n_i, as elucidated by replacing $k = nk_0$ with $(n_r + in_i)k_0$ in the plane wave of Eq. (2.19):

$$\vec{E}(z,t) = \vec{E}_0 e^{i(k_0 n_r z - \omega t)} e^{-n_i k_0 z} \tag{2.35}$$

From Eqns. (2.23-2.24), the intensity will then be of the form:

$$I(z) = I_0 e^{-2n_i k_0 z} = I_0 e^{-\alpha z} \tag{2.36}$$,

where α represents the material parameter called the *optical absorption coefficient*, which is defined to be:

$$\alpha = 2n_i k_0 = \frac{4\pi n_i}{\lambda} \tag{2.37}$$

When the dipoles oscillate at a frequency equal to their natural resonance frequency v_0, a large amount of energy of the oscillating field is coupled to the dipole oscillation. At this frequency, there is a maximum in dissipative absorption, and therefore a local maximum in n_i. This is illustrated in Figure 2.8b, which plots a typical spectrum of real and imaginary refractive indices. Note that, away from resonance frequencies, the real part of the refractive index n_r increases with frequency, which is called *Normal Dispersion* [13].

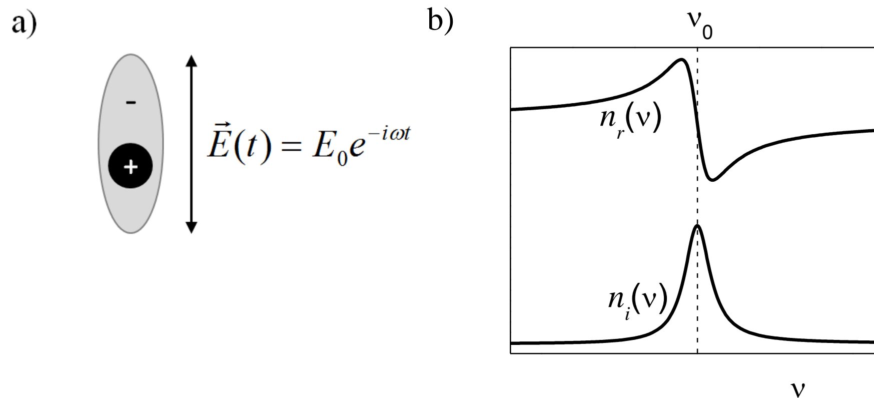

Figure 2.8: a) The linear oscillator model of an electron cloud surrounding a positive atomic core, being driven into oscillation by an electric field $\vec{E}(t)$; b) The frequency response of the atomic system's refractive index (real n_r and imaginary n_i parts) about a natural frequency ν_0 (on an arbitrary scale).

The total refractive index spectrum $n_r(\nu)$ and optical absorption spectrum $\alpha(\nu)$ of a material are formed of the superposition of the contributions of all its natural resonances. As the response function $\chi(t)$ of a material to an applied field is real, linear, causal and time-invariant, the real and imaginary parts of $\chi(\nu)$ satisfy the Kramer's-Kronig relations. As a result, the spectra of $n_r(\nu)$ and $\alpha(\nu)$ also obey this relationship, which means that the α of a material at any wavelength may be calculated from the n_r spectrum, and the n_r at any wavelength may be calculated from the absorption spectrum [12].

This linear oscillator model is a general description of material optical absorption, and is applicable to all materials. For instance, semiconductor optical absorption may be modeled as a superposition of many oscillators of closely separated frequencies. However, a more intuitive description is made by specifying the role of the photon: Optical absorption occurs when a photon interacts with a material such that its removal from the system causes the excitation of an electron to a higher energy state, where the energy difference between initial and final electron states is equal to the photon energy [14]. This is consistent with the predictions of the classical model, where the natural frequency ν_0 is indicative of the energy separation $h\nu_0$ between these two electronic states. There are several sources of optical absorption that are of concern to silicon photonics, and the most relevant to this thesis will presently be described.

1. Intrinsic band to band optical absorption

Band-to-band optical absorption occurs when the initial electron state is in the valence band and the final electron state is in the conduction band, and thus the process forms an electron-hole pair, as illustrated in Figure 2.9a. There may be multiple such

transitions induced for a given photon energy, as there may be several initial and final electron states with this energy separation. The absorption coefficient for a photon energy *hv* is directly proportional to the sum of the transition probability over all possible transitions with this energy separation[2]. The absorption spectrum of semiconductors thus has a sharp increase in the region of the band-gap energy, as photons having energy just above it may generate electron-hole pairs, and photons having energy just below it cannot [15, 16].

Silicon has a band gap energy of E_g = 1.12 eV which, as mentioned in the introduction, makes it transparent to photons of lower energy. The cut-off wavelength is expressed as:

$$\lambda_{cut-off} = \frac{hc}{E_g} \quad (2.38),$$

which for silicon has a value of approximately 1.1 μm.

The absorption spectrum of silicon is shown in Figure 2.9b. Silicon has a shallow absorption spectrum just beyond the cut-off, since it has an indirect bandgap and thus a phonon[3] must be involved in the electronic transition to facilitate a change in electron momentum. This has a lower transition probability compared to direct transitions, and thus has a smaller absorption coefficient [14].

[2] The transmission probability depends on the occupancy of the initial and final states, so the absorption coefficient is maximized when all of the initial valence band states are full and all of the final conduction band states are empty [14].
[3] A *phonon* is a quantized energy unit of the collective oscillation of atoms in a crystal lattice [17].

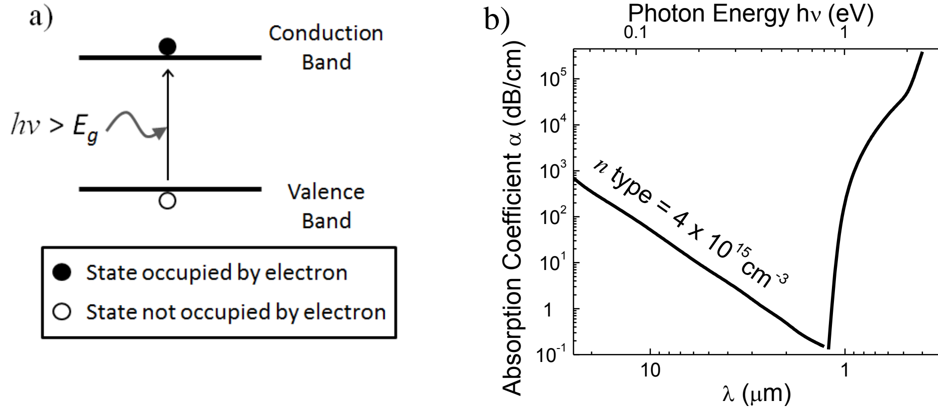

Figure 2.9: a) Schematic illustration of the band-to-band absorption process, showing the formation of an electron-hole pair through the absorption of a single photon; b) Absorption spectrum of silicon, featuring the sharp edge at the wavelength cut-off of 1.1 µm, and a tail from free-carrier absorption due to the background doping of the wafer [14].

In thermal equilibrium, the rate of thermal carrier generation *G* and recombination *U* are equal. Upon steady-state optical excitation of electron-hole pairs at a rate G_{opt}, the rate of thermal carrier recombination is increased to balance. However, if the device is connected to an external circuit and subjected to an electric field, the optical generation is balanced by thermal recombination and the removal of carriers as current density *J*. This is expressed in the *continuity equation* for electrons *n*:

$$\frac{\partial n}{\partial t} = G_{opt} + G_n - U_n + \frac{1}{q} \nabla \bullet J_n \qquad (2.39),$$

and for holes *p*:

$$\frac{\partial p}{\partial t} = G_{opt} + G_p - U_p - \frac{1}{q} \nabla \bullet J_p \qquad (2.40),$$

where the subscripts of *G*, *U*, and *J* refer to the contributions of electrons and holes to those quantities, and *q* refers to the elementary charge [18].

This is the principle behind the semiconductor photodetector, where band-to-band transitions are used to form a current in an external circuit. The efficiency is determined by the relative rates of J and U. The integrated germanium photodetectors described in section 1.3 operate through band-to-band absorption, which is the most efficient absorption mechanism for carrier generation.

2. Free-carrier optical absorption

As silicon is not a dielectric, but a semiconductor, the treatment of section 2.1 was not quite appropriate in assuming no free charges or currents. Through either doping or injection of current, electron and hole densities on the order of 10^{18}-10^{19} cm^{-3} can be present in the material. They are usually treated as perturbation to optical behaviour, by causing a refractive index shift Δn and optical absorption shift $\Delta\alpha$ in what is known as the *Plasma Dispersion Effect*. These effects can be approximated by modelling free carriers as a classical oscillator of Figure 2.8a but without a restoring force, which produces a Lorentzian resonance with $v_0 = 0$. From Figure 2.8a, the Δn due to free carriers is negative but approaches 0 as v increases and the $\Delta\alpha$ continuously decreases with v. This absorption tail is illustrated in Figure 2.9b, as a result of the n-type background doping in a silicon wafer [15]. Using the Lorentz oscillator model, the magnitude of Δn and $\Delta\alpha$ have been estimated by Soref *et al*. at $\lambda_0 = 1.55$ µm to be:

$$\Delta\alpha = \Delta\alpha_e + \Delta\alpha_h = 8.5\times10^{-18}e + 6.0\times10^{-18}h \qquad (\text{cm}^{-1})$$

$$\Delta n = \Delta n_e + \Delta n_h = -8.8\times10^{-22}e - 8.5\times10^{-18}h^{0.8} \qquad (2.41),$$

where e is the electron concentration and h is the hole concentration, and their differing contribution is a result of their different effective mass [19]. The physical interpretation of free-carrier absorption is that it causes electrons to be excited to higher energy levels in the conduction band, and holes to be excited to higher energy levels in the valence band [14]. The equations of Eq. (2.41) are important to silicon photonics for two reasons. First,

they allow designers to quantify the optical effects of doping in active devices, and provide a means of optimizing doping levels and their placement in the structure. Secondly, the absorption or refractive index change due to carrier injection or depletion is used widely in the modulation of light amplitude or phase respectively (see section 1.3).

3. Extrinsic (deep-level) optical absorption

The optical absorption above $\lambda_{cut\text{-}off}$ can be enhanced by using charge state levels located within the bandgap of silicon to act as intermediate states for optically excited carriers. These discrete energy levels are a product of the local perturbation in the silicon lattice at the site of either a defect or a substitutional dopant atom. An electron will have a localized wave state at this site that has a corresponding energy that falls within the band gap. For instance, when silicon is *n*-doped with phosphorus atoms, the excess electron is in a localized state at the phosphorus atom's location with an energy just below the conduction band edge. At room temperature, the excess electron of the phosphorus atom has a high probability of being thermally excited into the conduction band to function as a free electron, thus ionizing the phosphorus atom. Thus phosphorus is called a 'donor' impurity: it donates one electron per atom at room temperature. Similarly, *p*-type dopants like boron are called 'acceptors' because the localized electron charge state is just above the valence band, and thus a valence electron may be thermally excited into it at room temperature to form a free hole [20].

Other substitutional atoms that are much different from silicon in atomic mass will cause an even larger perturbation in the silicon lattice. These will form electronic states that are even more localized in space and therefore have energies far from both the conduction and valence band edges, called *deep levels*. Electronically, deep levels act as excess *carrier traps*, as electrons or holes captured by them do not have sufficient thermal energy to be excited back into the conduction or valence band. An electron

captured by a deep level may relax further into the valence band if the deep level captures a free hole (or vice versa). In this case, it functions as a *recombination center*, as it removes electron-hole pairs from the system. If the semiconductor has less than the equilibrium level of carriers (i.e. under depletion), the deep levels function as generation centers, which involves successive thermal generation of electron and holes [14]. The details of the electronic trapping process will be covered in section 3.3.

There are often more than one charge state associated with a defect, which means there are stable localized states for different number of occupying electrons, each having a unique energy level within the band-gap. The state that a defect is in is controlled by the doping level. For instance gold, a substitutional atom whose recombination properties is detrimental to CMOS electronics, has three deep level charge states associated with it. The lattice defects caused by inert ion implantation that were outlined in Figure 1.8 also have multiple deep level charge states within the band-gap of silicon, as the local damage to lattice periodicity permits local electron states.

The existence of a level within the bandgap of silicon may give rise to excess absorption above $\lambda_{cut\text{-}off}$. Figure 2.10 illustrates this process, where electrons (solid circles) and holes (empty circles) portrayed in several positions with respect to the conduction band, valence band, and deep level charge states (dashed lines). In the case of mid-gap levels, an electron from the valence band may be excited to an unoccupied deep level through the absorption of a photon. Alternatively, an electron occupying a deep level may be excited into the conduction band through the absorption of a photon. The presence of such a level would become apparent in the absorption spectrum, where a secondary absorption cut-off is present:

$$\lambda_{cut-off} = \frac{hc}{E_t - E_v} \quad (2.42),$$

for excitation from the valence band into a deep level, or:

$$\lambda_{cut-off} = \frac{hc}{E_c - E_t} \quad (2.43),$$

for excitation from a deep level into the conduction band, where E_c is the conduction band energy, E_v is the valence band energy and E_t is the defect level energy [14].

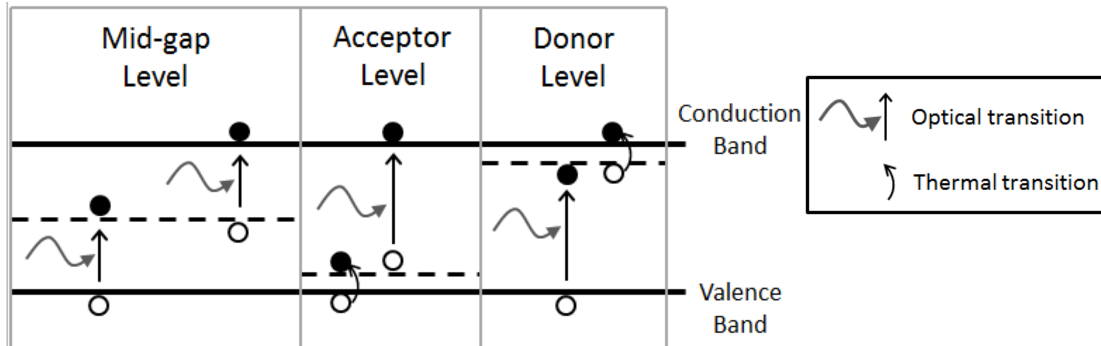

Figure 2.10: Schematic illustrating the possible forms of deep level absorption: when the level is in the middle of the band-gap, excitation either from the valence band to the deep level or from the deep level to the conduction band is possible (left); when the deep level is sufficiently close to one of the band edges, this absorption may lead to electron-hole pair formation through the emptying of excited carriers from the level into that band by thermal excitation (middle and right).

Transitions involving mid-gap states are not necessarily useful in photodetection, as each excitation process does not change the concentration of electrons and holes in the device. While the absorption process in the left diagram causes the generation of a hole, this process is not sustained unless a second process returns the deep level to its initial charge state. This second process can take the form of a thermal relaxation of the electron from the mid-gap state to back to the valence band (which removes the free hole), or an excitation by a second photon to the conduction band. Although the latter joint process does cause the formation of an electron-hole pair needed for photodetection, it is at the expense of two photons. Such a process would produce an intensity dependent responsivity, and will not be discussed further as it is not used in the devices of this thesis.

The instance of deep level absorption that is useful in linear sub-bandgap photodetection occurs when the level is close enough to the valence or conduction band edge to facilitate a secondary thermal excitation. For example, in the acceptor level shown in the center, the optical excitation of an electron from a defect level into the conduction band is followed by the thermal generation of a hole. Thus, the electron-hole pair has been formed with the absorption of a single photon. Alternatively, the third case illustrates the optical excitation of an electron from the valence band to the defect level, followed by a thermal excitation from this defect level into the conduction band. It is this process that forms the model of the defect-enhanced photodetectors described within this thesis, the specifics of which will be provided in chapter 3.

4. Scattering

The inhomogeneity in the refractive index distribution of a waveguide also contributes to an exponential decay in power, through the coupling of guided light into radiation modes [21]. For the purposes of this thesis, the main cause of scattering is roughness in the sidewalls of waveguides, resulting from the etch process. The scattering typically limits the propagation loss in SOI waveguides, which has motivated the proposal of novel waveguide structures such as the LOCOS structure described in chapter 4.

In general, absorption losses will affect the mode properties of a waveguide, however if they are sufficiently small they may be treated as a perturbation. Thus, the true value of β is then equal to the β calculated for the lossless case with an added imaginary term to account for losses. The waveguide mode shape is therefore the same, while the overall mode power decreases exponentially with propagation distance [21]. For instance, absorption mechanisms are modeled in BeamPROP by specifying an appropriate imaginary refractive index n_i for silicon.

The total intensity remaining after propagation in a silicon waveguide over a distance z is then written as:

$$I(z) = I_0 e^{-\alpha_{total} z} \qquad \alpha_{total} = \alpha_{b-b} + \alpha_{f-c} + \alpha_{d-l} + \alpha_p \qquad (2.44),$$

where α_{b-b} is the band-to-band absorption, which is negligible in silicon at 1550 nm,

α_{f-c} is the absorption due to free-carriers, usually present due to doping,

α_{d-l} is the absorption due to deep-levels, and

α_p is the propagation loss of the waveguide structure, dominated by light scattering.

2.3 Physics of *p-i-n* Photodiodes

This section combines the concept of optical absorption introduced in section 2.2 with the concept of carrier transport to describe the operation of a photodiode. A working knowledge of the band structure of semiconductors and the influence of Fermi statistics on carrier distribution are assumed. Inexperienced readers are directed to References 22 & 23 for a comprehensive introduction to these subjects.

2.3.1 Review of carrier transport and p-n junction operation

When an electric field ξ is applied across a section of silicon, electrons and holes are transported with an average *drift velocity* v_d:

$$v_d = \mu \xi \qquad (2.45)$$

in the direction of the applied field. The constant of proportionality μ is called the *mobility*, and describes the ability of a carrier to be transported by an electric field. It is primarily determined by the curvature of the conduction and valence bands, and the

frequency of collisions between the carriers and the lattice (which itself depends on the defect content and temperature). It therefore has different values for electrons and holes, called μ_n and μ_p respectively [18]. The drift velocity is small relative to their random thermal motion. Under high electric fields, this speed saturates as it approaches this thermal velocity v_{th}:

$$v_{th} = \sqrt{\frac{3kT}{m^*}} \qquad (2.46),$$

where m^* represents the effective mass of the electron or hole, k is Boltmann's constant and T is the temperature in degrees Kelvin [18]. The thermal velocity of electrons and holes in silicon is therefore approximately 10^7 cm/s at room temperature.

When an electric field is applied a section of silicon, a drift current J_{drift} results in the direction of the applied field:

$$J_{drift} = q\left(n\mu_n + p\mu_p\right)\xi = \sigma\xi \qquad (2.47),$$

where σ is defined as the conductivity of silicon. Therefore, the doping of silicon makes it more conductive through the increase of n and p in Eq. (2.47).

The other form of current that may exist in silicon is diffusion current J_{diff}, which arises from a concentration gradient in carriers, where carriers flow in the direction of a negative gradient [18].

A *p-n* junction, shown in Figure 2.11a, is formed of two a region of *n*-doped silicon adjacent to a region of *p*-doped silicon. Under equilibrium, the diffusion of holes into the *n*-type side and electrons into the *p*-type side is balanced by an opposing electric field formed by the opposite ion cores. This forms a contact potential V_0, and the region containing the ion cores is called the *depleted region*, as it has been 'depleted' of carriers. When a positive bias V is applied to the *p*-side with respect to the *n*-side, the barrier is reduced and carriers are free to diffuse to the opposite ends, forming a diffusion current.

When a negative bias is applied to the *p*-side with respect to the *n*-side, the barrier to carrier diffusion is further increased and the depleted region becomes wider. Only a small current remains, the reverse saturation current I_s, which is due to the drift of minority carriers[4] across the depleted region [24].

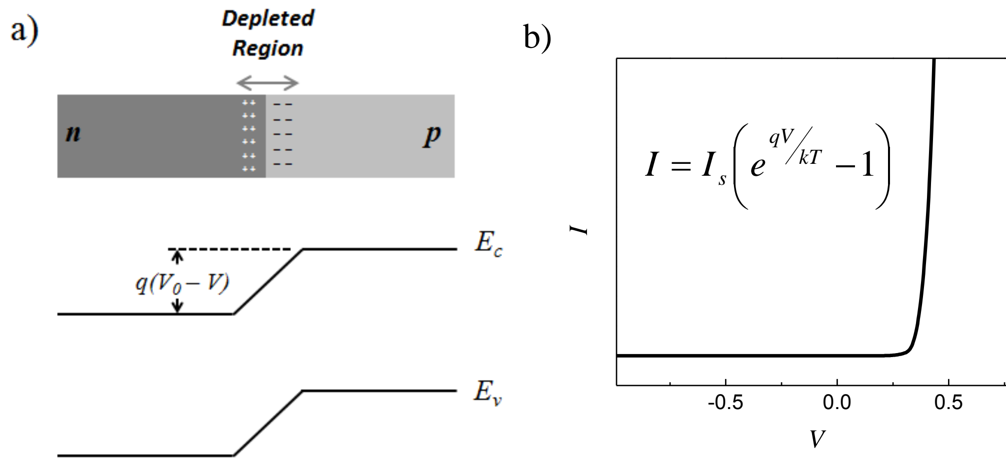

Figure 2.11: a) A schematic of a *p-n* junction and the respective conduction and valence band edges E_c and E_v, with a depleted region formed at the junction where an electric field exists [24]; b) Sample *I-V* characteristic of a *p-n* diode, along with the equation governing its operation.

The Equation of current as a function of applied bias, called an *I-V* characteristic, is shown as Figure 2.11b. The *p-n* junction thus provides rectification of current: offering large conductivity for *forward bias* (V > 0), and very little for *reverse bias* (V < 0). The *p-i-n* diode used for photodetection is a *p-n* junction with an intrinsic *i* silicon region located between the *p* and *n* regions, and also provides rectification of current similar to the *I-V* characteristic as in Figure 2.11. Under reverse bias, an electric field exists across the intrinsic region, so that it functions as a depleted region of a fixed width [25]. It is under reverse bias that the photodiode is operated, and it is designed such that the optical

[4] referring to electrons in the *p*-region and holes in the *n*-region that reach the depleted region and are swept across by the field as a drift current.

absorption takes place in the *i* region and the electric field is utilized to extract the generated carriers as a drift current.

2.3.2 *Electronic modeling in Silvaco's ATLAS software*

It is often necessary to solve the *I-V* characteristics and other performance parameters of complex two and three-dimensional silicon device structures. Silvaco © offers a full virtual wafer simulator, which incorporates wafer fabrication (ATHENA) and device testing (ATLAS). Both simulators were used in this project, the former to design fabrication process flows, and the latter to simulate photodiode performance. ATLAS may simulate a device structure that has either been imported from ATHENA or has been user defined. This geometric device structure includes a specific material and doping level associated with each grid point, as well as contacts defined for the connection of a user-defined external circuit. The material properties can be adjusted, for instance by specifying a carrier lifetime in silicon, or alternatively by defining carrier traps with particular capture properties. The simulator solves for a set of unknowns (for example hole concentration, electron concentration and potential) at each grid point through an iterative process by using an initial guess. The number of unknowns, and consequently the complexity of the simulation, increases with more comprehensive models. For instance, the Shockley-Read-Hall recombination model for carrier trapping used in this project also solves for the ionization level of the carrier traps at each point in the structure.

An *I-V* characteristic of a device is obtained by increasing the bias on one contact with a sufficiently small step size to ensure convergence. It is also possible to find transient solutions, by applying a bias at $t = 0$ and solving the structure at each time step Δt (using the solution at the previous time step as an initial guess). For each bias or time point, the total current is output into a log file, and structure files containing the distributions of potential, electron and hole carriers and trap ionization are created [26].

The utilization of this simulation package to model the response of a defect- enhanced photodiode will be described in chapter 3.

2.3.3 *Overview of p-i-n photodiode operation*

The *p-i-n* photodiode introduced in section 1.2 will now be described in more detail, with particular reference to a waveguide structure containing deep levels near in energy to the conduction band edge. Figure 2.12 illustrates an example of a *p-i-n* waveguide photodiode, with the band structure of the diode under reverse bias along a horizontal cutline. The intrinsic region has been fully depleted, as indicated by its sloped bands to indicate the presence of an electric field.

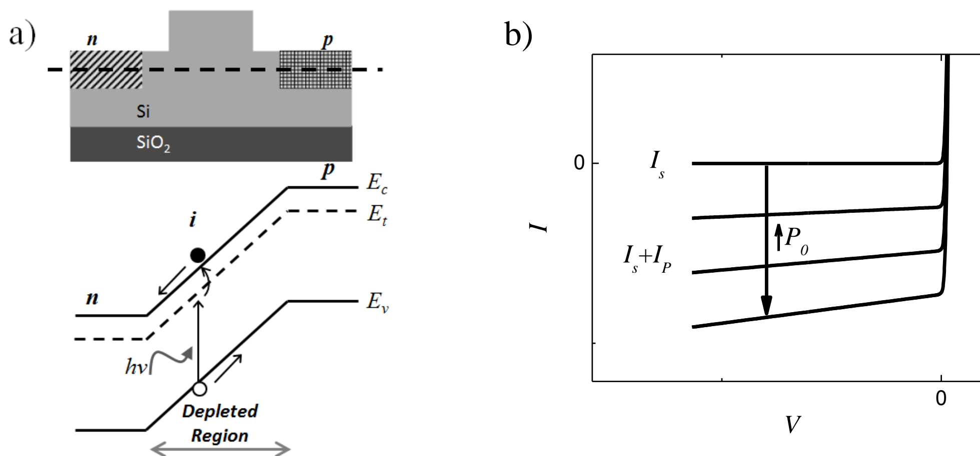

Figure 2.12: a) Cross-section of a *p-i-n* diode laterally integrated onto a silicon rib waveguide, with a cut-line illustrating the energy bands; a photon induced electron-hole pair generation within the depleted intrinsic *i* region, where the electric field causes the carriers to be swept to opposite sides of the device to form photocurrent (hv = photon energy, E_c = conduction band minimum, E_t = deep level energy, E_v = valence band maximum) [25]; b) Reverse bias portion of the IV- characteristic of a *p-i-n* photodiode upon increasing incident power, illustrating the increase in reverse saturation current I_s by an amount I_P.

When a photon is incident on the intrinsic region, an electron-hole pair is generated by the mechanism described in the right-most diagram of Figure 2.10. The electrons are swept by the electric field towards the *n* region and the holes are swept towards the *p* region using the mechanism of Eq. (2.45), as shown in Figure 2.12. The power in the optical mode of the waveguide decays exponentially with propagation distance according to Eq. (2.44). When an optical power P_0 is inserted, the power absorbed P_{abs} by a waveguide photodiode of length L is then:

$$P_{abs} = P_0\left(1 - e^{-\alpha_{total}L}\right) \tag{2.47}$$

Therefore, an efficient waveguide photodiode would need to be sufficiently long to absorb the majority of the input light. Under ideal conditions, the photocurrent obtained from this waveguide photodiode is:

$$I_P = P_{abs}\frac{q\lambda}{hc} \qquad (2.48),$$

where q is the elementary charge, and the ratio $\frac{q\lambda}{hc}$ represents the charge per unit energy obtained when a photon is absorbed to create an electron-hole pair [25]. This equation assumes that all generated carriers are extracted to form a photocurrent, which in the presence of recombination centers is not valid. Therefore, a carrier extraction efficiency term $\Im(\tau)$ must be added, which decreases from unity as the carrier lifetimes become comparable to the average carrier transit time (i.e. the time to travel from the center of the intrinsic region to the relevant doped region). In addition, the ideal case of Eq. (2.48) assumes that all optical loss leads to the generation of electron hole pairs. The fraction of absorption that leads to carrier generation (in this case deep level absorption, denoted by $\alpha_{d\text{-}l}$) with respect to the total loss α_{total} must be added as well. With these amendments, Eq. (2.48) becomes:

$$I_P = P_{abs}\frac{q\lambda}{hc}\frac{\alpha_{d-l}}{\alpha_{total}}\Im(\tau) \tag{2.49}$$

The *p-i-n* diode reverse saturation current I_s (more commonly referred to in photodiodes as the *dark current* I_D) is enhanced by an amount equal to the I_P, as shown in Figure 2.12b. The photodiode may therefore be operated under any negative bias. Increasing the bias may improve the carrier extraction efficiency by increasing the electric field strength in the *i* region.

The quantum efficiency η is defined to be [25]:

$$\eta = \frac{number\ of\ generated\ electron-hole\ pairs}{number\ of\ incident\ photons} = \frac{I_P / q}{P_0 / h\nu} = \left(1 - e^{-\alpha_{total}L}\right)\frac{\alpha_{d-l}}{\alpha_{total}}\Im(\tau) \tag{2.50}$$

Alternatively, the responsivity R is a proportional quantity that indicates the photocurrent obtained per unit optical power inserted (usually in mA/W) [25]:

$$R = \frac{I_P}{P_0} = \frac{\eta q}{h\nu} \tag{2.51}$$

While Eq. (2.50) reveals some of the practical limitations on photodiode efficiency, there are additional factors which are difficult to elucidate in an analytical formula. For instance, the two dimensional structure features a spatially dependent field throughout the waveguide cross-section, rather than the uniform field shown in Figure 2.12. Also, the spatial distribution of the optical mode leads to a spatially dependent carrier generation rate. Lastly, the efficiency of carrier extraction depends strongly on the rib waveguide geometry. For the above reasons, an electrical simulation package like ATLAS is required to model the photodetection process and evaluate the efficiency of device designs.

The equivalent circuit of the photodiode is shown in Figure 2.13. The photocurrent behaves as a current source in parallel with a capacitor and resistor. The capacitor is due to junction capacitance as well as the capacitances in the external circuit.

The resistance is due to the load resistor R_L, which is typically 50 Ω, and respective shunt and series resistances due to the diode: R_{sh} and R_s. The value of R_s is typically much smaller than the others and may be neglected from consideration. The photodiode signal is therefore passed through a low pass filter formed of the parallel C and R_L in the circuit. This places a limit on the speed of the optical signal that may be detected, referred to as the capacitance limit of the device bandwidth. As the capacitance increases with *p*-*i*-*n* diode area (and assuming R_s remains sufficiently small to be neglected), the bandwidth is reduced as the device length L increases [25].

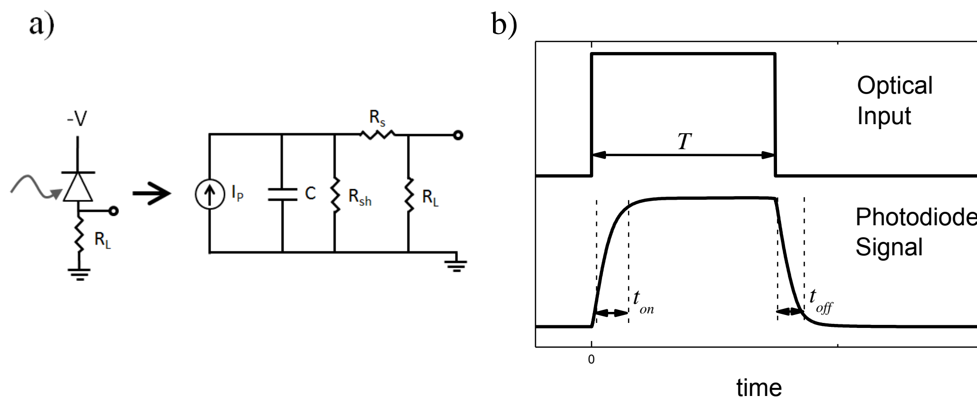

Figure 2.13: a) A reverse biased photodiode connected to a load resistance R_L and its equivalent circuit [25]; b) The response of a photodiode to an optical input of width T, with exponential delays t_{on} and t_{off} due to limits of the R_LC time constant and carrier transit time.

Alternatively, the speed may be limited by the transit time of carriers drifting through the depleted *i* region. Applying an increased electric field (i.e. increasing the reverse bias) may only improve carrier drift speeds up to the limit of their saturation velocity of Eq. (2.46). Therefore, this represents a fundamental limit to device bandwidth. It may be mediated by reducing the distance that carriers will have to travel (i.e. by reducing the intrinsic region size), although this will also increase the capacitance and thus reduce the RC bandwidth [25].

The total response of the waveguide photodiode to a periodic square-wave optical excitation is shown in Figure 2.13b. The presence of large *RC* constant or transit times that approach the period of the input have caused a filtering of the response, so the device responds to changes in optical signal with an exponential response function. The turn-on time t_{on} is defined as the time required for the current to rise from 10% to 90% of its maximum value, and the turn-off t_{off} time is defined as the time required for the current to fall from 90% to 10% of its maximum value [25]. Clearly, when either of these values exceeds the width of the optical input *T*, the ability of the photodiode to respond to the signal is lost.

Another limitation of *p-i-n* photodiode response is noise, which produces an uncertainty in the photodiode signal. This arises mainly from the probabilistic nature of the detection process, namely that the photons both arrive at the device and generate carriers with particular probability distributions, contributing a *photon noise* and *photoelectron noise*, respectively [28]. The photocurrent I_P referred to in Eq. (2.49) is therefore the *mean* photocurrent $\bar{I}_P$, and the deviation σ_{I_P} about this value is referred to as the noise power. The noise power associated with photon and photoelectron noise, for a detection bandwidth of *B*, is:

$$\sigma_P{}^2 = 2q\bar{I}_P B \tag{2.52}$$

This is a form of shot noise, which refers to the fluctuations in current arising from random generation and recombination events in the intrinsic region [26]. As discussed in section 2.2, the defects present in silicon act as generation centers within the depleted *i* region. As a result, photodiodes with defects present have a much larger dark current I_D and associated noise. The shot noise power arising from dark current is defined as:

$$\sigma_D{}^2 = 2qI_D B \tag{2.53}$$

The second contributing factor, the thermal noise, arises from the random thermal agitation of carriers in a resistor [27]. In this case, the thermal noise has the form:

$$\sigma_T{}^2 = 4kTB\left(\frac{1}{R_{sh}} + \frac{1}{R_L}\right) \quad (2.54),$$

where k is Boltmann's constant and T is the temperature in degrees Kelvin. The thermal noise is typically dominated by R_L, which is orders of magnitude smaller than the shunt resistance R_{sh} of a reverse biased photodiode. However, its contribution will be ignored in the following analysis, as this thesis is concerned only with the noise properties of the photodiode itself. The receiver architecture can be independently adjusted to reduce the thermal limitation posed by R_L.

The ratio of the rms signal power I_P^{RMS} and the noise power (or the *Signal to Noise Ratio*) is defined as [27]:

$$SNR = \frac{I_P^{RMS\,2}}{\sigma_P{}^2 + \sigma_D{}^2 + \sigma_T{}^2} = \frac{\bar{I}_P{}^2 / 2}{2q\left(\bar{I}_P / 2 + I_D\right)B + 4kTB / R_{sh}} \quad (2.55)$$

Alternatively, the noise properties of a photodiode may be written in terms of the *noise-equivalent power (NEP)*, which is the incident optical power that would provide an $SNR = 1$ with unit bandwidth $B = 1$ Hz [27, 28]:

$$NEP = \frac{2}{R}\sqrt{\left(I_D q + \frac{2kT}{R_{sh}}\right)} \quad (2.56)$$

Therefore, the *SNR* is maximized and the *NEP* is minimized mainly by minimizing diode area and dark current I_D.

2.4 Optical Resonators

The optical resonator is a ubiquitous device in optics that provides optical feedback and, through constructive interference, can 'store' light in a location for a finite period of time. Resonators are used in many passive and active integrated optical devices, including the silicon phase modulators of Figure 1.5. More importantly, resonators were used throughout the fabrication, characterization, and design of devices described in this thesis.

2.4.1 The Fabry-Perot etalon

The simplest resonator to conceptualize is the Fabry-Perot etalon, which is formed of two planar reflective surfaces separated by a distance *L* [29]. Equivalently, the device is formed of three layers: the top layer and bottom layer are semi-infinite and have a refractive index n_1, while the middle has a thickness *L* and a refractive index n_2, as shown in Figure 2.14a. Note that this is not the most general structure, as the bottom and top layer need not be the same material. Light of electric field amplitude E_i incident from above, at an angle of θ_1, will upon reaching the first interface be partially refracted into the middle layer, and partially reflected. The refracted light propagates through the material and be partially refracted and partially reflected at the second interface, and the reflected light will then propagate upwards back across the medium n_1 and be reflected and transmitted again, and so on. The total transmitted field E_t is the sum of the infinite partial waves transmitted through the bottom interface, which equates to:

$$E_t = E_i T\sqrt{A}e^{i\delta/2}\frac{1}{1-A\mathrm{R}e^{i\delta}} \quad (2.57),$$

where δ represents the phase shift after a single round trip of the film:

$$\delta = 2kn_2L\cos\theta_2, \qquad \text{where } k \text{ is the free-space wavenumber} \quad (2.58)$$

The T and R represent the transmittance and reflectance of the n_1/n_2 interface, and the round-trip loss of the material has been defined as:

$$A^2 = e^{-\alpha(2L\cos\theta)} \tag{2.59}$$

The fraction of the incident light intensity I_i that is transmitted is therefore:

$$\frac{I_t}{I_i} = \left|\frac{E_t}{E_i}\right|^2 = \frac{(1-R)^2 A}{(1-AR)^2 + 4AR\sin^2\left(\delta/2\right)} \tag{2.60}$$,

where the $T = 1 - R$ relation has been invoked to reduce the number of variables [28]. This relationship is plotted as a function of δ (bottom axis), or equivalently λ (top axis) in Figure 2.14b. The transmitted intensity therefore has maxima that are periodic in δ, since Eq. (2.4.4) gives $I_t/I_i = 1$ when $\sin^2\left(\delta/2\right) = 0$. We may assume that $\theta_2 = 0$, meaning the light is normally incident from the top of the device, as it is in all applications within this thesis. This condition is therefore valid when:

$$\delta/2 = m\pi = k_m n_2 L = \frac{2\pi n_2 L}{\lambda_m}, \text{ where } m = 1, 2, 3, \ldots \tag{2.61}$$

Therefore, the transmitted intensity reaches a maximum when:

$$\lambda_m = \frac{2n_2 L}{m} \text{ or equivalently } \nu_m = \frac{mc}{2n_2 L} \tag{2.62}$$

This is purely an artefact of the constructive interference of the partial waves, due to the phase difference δ being matched to their wavelength. Such wavelengths λ_m are called *resonant wavelengths*, and the corresponding ν_m are called *resonant frequencies* [28]. In selecting the top axis of Figure 2.14b, it was assumed that the etalon was formed of a silicon film (n_2 = 3.5) of L = 1 μm thickness (the refractive indices of the accompanying material are determined by the chosen reflectivity R).

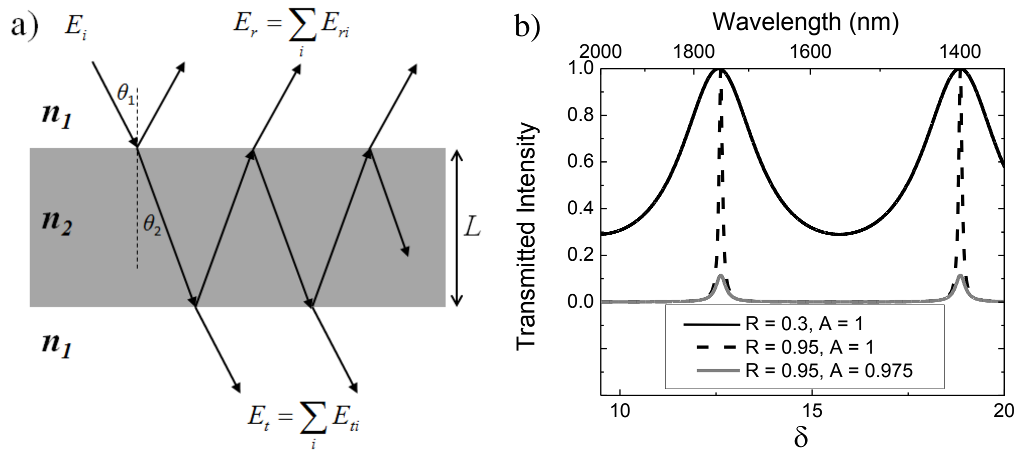

Figure 2.14: a) Diagram of a symmetric Fabry-Perot etalon, formed of a dielectric of thickness *L* and refractive index n_2 sandwiched between two semi-infinite dielectrics of refractive index n_1; Light is incident from above at an angle of θ_1, and proceeds to undergo multiple reflections at each interface, as described in the text [28]; b) Plot of the transmitted intensity, calculated from Eq. (2.60), for interface reflectivity *R* = 0.3 and *R* = 0.95 and absorbance of *A* = 1 and *A* = 0.975; The corresponding wavelength is plotted as the top axis, assuming that $\theta_2 = 0$, $n_2 = 3.5$, and *L* = 1 µm;

A similar analysis may be carried out with a summation of the partial waves emitted from the top, and forming a reflected intensity fraction I_r/I_i. The resulting function predicts a minimized reflected intensity at the resonant wavelength λ_m. The etalon is thus an optical filter, which transmits a narrow range of wavelengths centered on λ_m while strongly reflecting the neighbouring wavelengths.

The shape of the curve is strongly dependent on the resonator loss, due to both interface reflectivity *R* and absorbance *A*, as shown in Figure 2.14b. For a reflectivity *R*, the resonator incurs a loss of ln(*R*) upon every reflection. Therefore, the smaller the value of *R*, the less capable the resonator is of storing an optical field. As *R* is increased, the intensity maintained within the cavity after *m* reflections becomes greater. Therefore, in the field summation, there are more partial waves of similar amplitude contributing to the transmitted intensity by interfering with one another. This has the consequence of narrowing the transmission around the resonance wavelength. The full width at half

maximum (FWHM) of the resonance is commonly called its *linewidth*, which is an important characteristic parameter of optical resonators. When only reflection loss is present (i.e. $A = 1$), the total reflected intensity and total transmitted intensity of an etalon will sum to unity, regardless of the value of δ. Absorption loss, however, both decreases the resonant transmission and increases the linewidth. The former affects an oft-quoted parameter called the *Extinction Ratio*, which is the ratio of the resonant transmission and the off-resonant transmission, usually written in dB. From Figure 2.14b, it is clear that both the reflection loss and absorption loss influence the extinction ratio.

An SOI waveguide of finite length L and smooth facets forms a Fabry-Perot etalon. The facet reflectivity, due to the refractive index contrast between the silicon core and air, is $R = 0.31$. Therefore, the waveguide transmission has a spectral envelope from the interference effect. This effect is typically undesirable and inconsistent, as facet quality greatly influences the resulting spectrum. It is, however, of advantage in measuring waveguide transmission loss using the treatment outlined above, and will be utilized throughout this thesis. From the transmission spectrum of a waveguide, measuring the Extinction Ratio ER allows the transmission loss (in cm^{-1}) to be calculated as [30]:

$$\alpha = -\frac{1}{L}\ln\left(\frac{1}{R}\frac{\sqrt{ER}-1}{\sqrt{ER}+1}\right) \tag{2.63}$$

2.4.2 General characteristics of optical resonators and methods of simulation

An important characteristic of optical resonators is the *Free-Spectral Range* (FSR), which is defined as the separation between adjacent resonances. Since a resonance occurs when the round-trip phase difference is an integer multiple of 2π, the FSR is therefore defined as $\Delta\delta_{FSR} = 2\pi$. Or, written in terms of frequency, it is defined as:

$$\nu_{FSR} = \frac{c}{2n_2'L} \tag{2.64},$$

where $n_2' = n_2 + \nu \frac{dn}{d\nu}$ is the group index [28]. In cases of small dispersion $\frac{dn}{d\nu}$, the group velocity equates to n_2, and the FSR is then independent of frequency. Written in terms of wavelength, however, the FSR is always wavelength dependent:

$$\lambda_{FSR} = \frac{\lambda^2}{c}\nu_{FSR} = \frac{\lambda^2}{2n_2'L} \tag{2.65}$$

The resonant linewidth is reflected in two figures of merit used to describe resonators. The first is called the *Finesse*, which is the ratio of the free spectral range and the linewidth:

$$Finesse = \frac{\lambda_{FSR}}{\Delta\lambda} \tag{2.66}$$

The second figure of merit is called the *Q* (for Quality) Factor, and is proportional to the ratio of the optical energy ξ stored by the resonator to the rate of energy loss $d\xi/dt$:

$$Q = \omega \frac{\xi}{d\xi/dt} \tag{2.67}$$

Eq. (2.67) indicates that the decay of energy in a resonator is described exponentially:

$$\xi(t) = \xi_0 \exp\left(-\frac{t}{t_c}\right), \tag{2.68},$$

where $t_c = \frac{Q}{\omega}$ is referred to as the *Photon Lifetime* of the resonator [28].

From the Lorentzian form of the resonance, the FWHM can be shown to be equal to [28]:

$$\Delta\nu = \frac{1}{2\pi\, t_c} = \frac{\omega}{2\pi\, Q} \tag{2.69}$$

Therefore, an alternative representation of the *Q*-factor is:

$$Q = \frac{\nu}{\Delta\nu} \tag{2.70}$$

This is directly measurable from the transmission or reflection spectrum of a resonator. Again, an etalon with low total loss (R, A ~ 1) will have a narrow linewidth and therefore high Q. This demonstrates the association between loss and photon lifetime: low loss resonators store optical energy for long time periods characterized by t_c. This is explicitly evident in the variation of optical power within a resonator with time:

$$\frac{dP}{dt} = \frac{dP}{dz}\frac{dz}{dt} = \frac{dP}{dz}\frac{c_0}{n} = -\left(\alpha + \frac{1}{L}\ln(R)\right)\frac{c_0}{n}P \tag{2.71}$$

Therefore,

$$\frac{1}{t_c} = \left(\alpha + \frac{1}{L}\ln(R)\right)\frac{c_0}{n} \tag{2.72}$$

That is, the photon lifetime is inversely proportional to the total loss in the resonator [28]. While this discussion was presented for the etalon in particular, the concepts of Extinction Ratio, *Finesse* and the Q Factor are applied to all optical resonators, regardless of their construction.

A resonator can be modeled using FDTD programs such as RSOFTs FullWAVE using several methods. A common approach is to launch a pulse excitation into a structure and monitor the energy remaining as a function of time. By performing a fast Fourier transform (or *fft*) on this data, the stored energy vs. optical frequency is obtained, from which properties such as λ_m, $\Delta\lambda$, λ_{FSR}, and ER may be extracted [11].

2.4.3 Micro-ring resonators

Another form of resonator is a micro-ring, whose structure is shown in Figure 2.15a. Rather than undergoing multiple reflections in a planar structure, light undergoes multiple revolutions around a ring of radius R. Therefore, in this case, the round trip phase is given by:

$$\delta = kn_2(2\pi R) \tag{2.73}$$

The ring structure therefore behaves similarly to an etalon of length $L = \pi R$, with adjusted reflection and transmission coefficients to reflect the physics of coupling light into and out of the resonator from the 'bus' waveguides. The intensity reaching the *drop-port* is analogous to the transmitted intensity I_t of the etalon, where constructive interference within the ring at $\delta = 2m\pi$ leads to sharp peaks. The intensity reaching the *through-port* is analogous to the reflected intensity I_r of the etalon, and features resonant drops in intensity. The drop-port then functions as a narrow-pass optical filter, and the through-port functions as a narrow-stop filter.

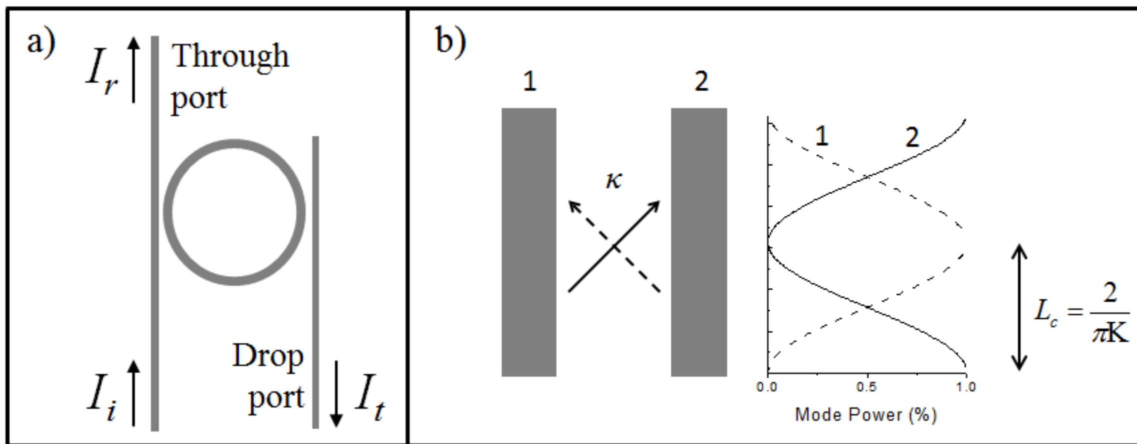

Figure 2.15: a) An illustration of a micro-ring resonator, formed of a ring waveguide sandwiched between two bus waveguides; the relevant analogue intensities of the etalon are shown for comparison; b) A diagram of two identical waveguides 1 and 2 having a coupling coefficient K. The coupled-mode equations predict that the optical power will be transferred periodically between 1 and 2 with a period given by L_c: the coupling length [31].

The interaction point between the ring and the bus waveguide is called a *waveguide coupler*, where energy is transferred between waveguides that have been brought into close proximity over a certain distance. Its operation is fundamental to the characteristics of waveguide modes. The single modes described in section 2.1.2 were calculated assuming the surrounding dielectric extended infinitely in all directions (or more practically up to a distance where the evanescent field is negligible). Were two waveguides separated by a distance on the order of their transmitting wavelength, the

mode of one waveguide would be perturbed by the presence of another, and energy would be transferred (or coupled) to it. This *coupling loss* or *cross-talk* is undesirable on optical chips, and sets the minimum separation between waveguides so that they may be considered isolated structures.

This effect is intentionally used in waveguide couplers, such as the one depicted in Figure 2.15b. Given the mode properties the individual waveguides 1 and 2, the amplitude of each propagating wave in the coupling region varies with propagation distance according to a pair of coupled first-order differential equations called the *Coupled Mode Equations*. The key parameter in these equations is the *coupling coefficient* K, which corresponds to the coupling strength (in m^{-1}) from waveguide 1 to 2 and from 2 to 1. While K depends on a multitude of factors, it generally decreases with increasing waveguide separation and mode confinement. Between the two parallel waveguides of Figure 2.15b, the energy is periodically transferred between them with a period given by the coupling length L_c, which is inversely proportional to K. In the case where waveguides 1 and 2 are identical, as in Figure 2.15b, it is possible to couple 100% of the modal intensity between them [31].

It is often preferred, when analyzing micro-ring resonators, to generalize the coupling physics to a ‘black box’ process. One reason is that, as in the micro-ring shown in Figure 2.15a, the coupler is not formed of two parallel waveguides, and the continuous curvature of a ring does not permit the decoupling of the length from the coefficient K. This type of coupler is referred to as an *evanescent point coupler*, and is used in the circular type of ring resonator, shown in Figure 2.16a. In another implementation, the ring does have straight sections in the coupling regions. This type is called a *racetrack resonator*, and is depicted in Figure 2.16b. By using a racetrack, it is possible to tune the coupling strength independently through both gap size and coupling length.

Both implementations are described using the model of Figure 2.16c, using two parameters: the *cross-coupling coefficient κ* and the *self-coupling coefficient t*. Assuming there is no loss in coupling, these parameters obey the following relationship:

$$\kappa^2 + t^2 = 1 \tag{2.74}$$

Given input fields X_1 and X_2, the fields output from the coupler Y_1 and Y_2 are determined by [28]:

$$\begin{bmatrix} Y_1 \\ Y_2 \end{bmatrix} = \begin{bmatrix} t & \kappa^* \\ \kappa & -t^* \end{bmatrix} \begin{bmatrix} X_1 \\ X_2 \end{bmatrix} \tag{2.75}$$

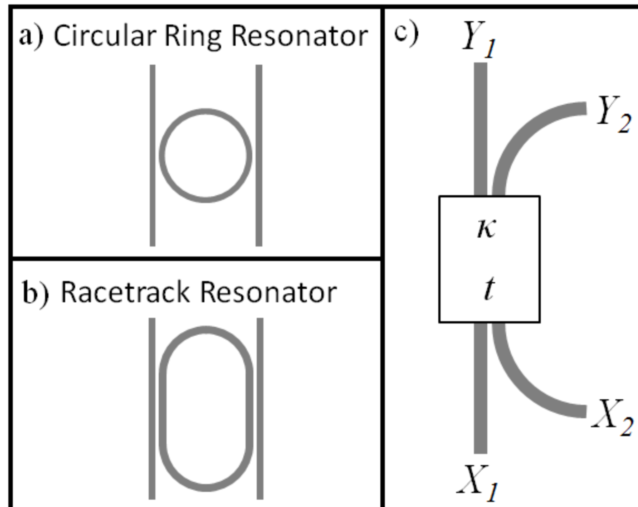

Figure 2.16: a) The circular ring resonator implementation, featuring a point-evanescent coupler; b) The racetrack ring resonator implementation, featuring straight waveguide coupling sections; c) 'black box' model of the coupler, used to describe the devices of a) and b) using the parameters *κ* (cross-coupling coefficient) and *t* (self-coupling coefficient) [28].

The type of ring resonator shown in Figures 2.15a and 2.16 is called an *add-drop ring resonator*, and is formed of a ring with two couplers to two bus waveguides, as shown in Figure 2.17. In this case, the coupler on either side is assumed to be identical,

making it directly analogous to the symmetrical etalon. The electric field that is transmitted into the drop port is:

$$\frac{E_{drop}}{E_i} = \frac{|\kappa|^2 \sqrt{A} e^{i\delta/2}}{1 - Att^* e^{i\delta}} \quad (2.76),$$

where $A^2 = e^{-\alpha(2\pi R)}$ is the intensity transmission in a single pass of the ring [32].

The proportion of the intensity arriving at the drop port is then:

$$\frac{I_{drop}}{I_i} = \left[\frac{E_{drop}}{E_i}\right]^* \left[\frac{E_{drop}}{E_i}\right] = \frac{|\kappa|^4 A}{\left(1 - A|t|^2\right)^2 + 4A|t|^2 \sin^2\left(\frac{\delta}{2}\right)} \quad (2.77)$$

This is simply the transmitted intensity of Eq. (2.60) for the etalon, if one substitutes $|\kappa|^2 = (1 - R)$ and $|t|^2 = R$.

Similarly, the electric field coupled to the through port is [32]:

$$\frac{E_{through}}{E_i} = \frac{t - t^* A e^{i\delta}}{1 - Att^* e^{i\delta}} \quad (2.78)$$

Therefore, the proportion of the intensity coupled to the through port is:

$$\frac{I_{through}}{I_i} = \left[\frac{E_{through}}{E_i}\right]^* \left[\frac{E_{through}}{E_i}\right] = \frac{|t|^2 \left[(1 - A)^2 + 4A \sin^2\left(\frac{\delta}{2}\right)\right]}{\left(1 - A|t|^2\right)^2 + 4A|t|^2 \sin^2\left(\frac{\delta}{2}\right)} \quad (2.79)$$

Assuming a coupling coefficient of $|\kappa|^2 = 0.1$, Eq.'s (2.77) and (2.79) are plotted in Figure 2.17b for a lossless ring (A = 1) and a moderately lossy ring (A = 0.95). For the lossless case, all of the input intensity is adequately coupled to the drop waveguide on resonance. Upon introduction of loss to the ring, however, the resonant intensity at reaching the drop port is significantly reduced.

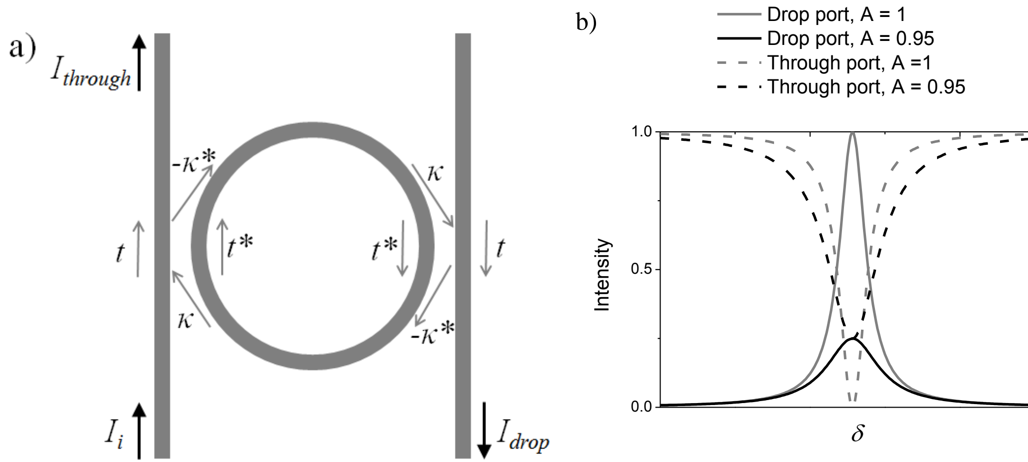

Figure 2.17: a) Schematic of an add-drop ring resonator structure, including two identical waveguide couplers with coefficients κ and t [32, 33]; b) Plot of I_{drop} and $I_{through}$ for the structure in a) assuming a coupling coefficient of $|\kappa|^2 = 0.1$ and loss of $A = 1$ and $A = 0.95$, obtained from Eq. (2.77) and (2.79).

Another implementation of the ring resonator is the *all-pass ring resonator* shown in Figure 2.18a, where the second bus waveguide is absent, and so no drop port exists. This structure is mathematically equivalent to the add-drop of Figure 2.17a, but with the self-coupling coefficient on the right side (t') set to 1 and the cross-coupling coefficient on the right (κ') set to zero. The electric field at the through port is then [32]:

$$\frac{E_{through}}{E_i} = \frac{t - Ae^{i\delta}}{1 - At^* e^{i\delta}} \tag{2.80}$$

Therefore, the intensity at the through-port is:

$$\frac{I_{through}}{I_i} = \left[\frac{E_{through}}{E_i}\right]^* \left[\frac{E_{through}}{E_i}\right] = \frac{|t|^2 + A^2 - 2At\cos\delta}{1 + A^2|t|^2 - 2At\cos\delta} \tag{2.81}$$

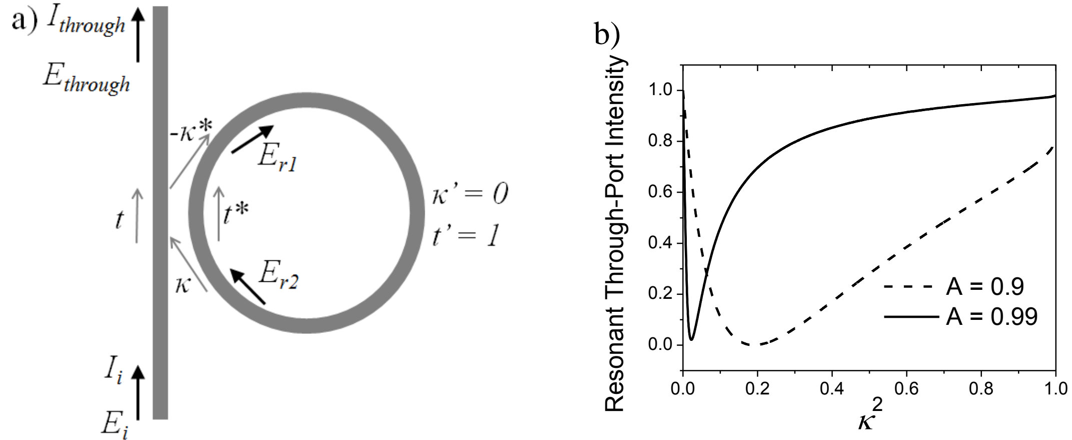

Figure 2.18: a) Schematic of the all-pass ring resonator, which is modelled as an asymmetric add-drop resonator with *κ'* = 0 and *t'* = 1 on one side [32, 33]; b) Plot of the resonant through-port intensity as a function of κ^2, illustrating the presence of 'critical coupling': the zero through-port intensity achieved for a particular value of *κ*.

In this structure, the only source of loss in the ring is A. This means that on resonance, all of the light coupled into the ring is absorbed or scattered, rather than being coupled into a drop port. At resonance, the intensity at the through-port is [33]:

$$\left(\frac{I_{through}}{I_i}\right)_{resonance} = \frac{|t|^2 + A^2 - 2At}{1 + A^2|t|^2 - 2At} = \frac{(t-A)^2}{(1-At)^2} \tag{2.82}$$

This provides a means of gauging how the coupling properties should be chosen to achieve the maximum power coupled into the ring on resonance. To illustrate this, Eq. (2.82) was plotted against $|\kappa|^2 = 1 - |t|^2$ in Figure 2.18b for $A = 0.9$ and $A = 0.99$.

It can be seen, both from Figure 2.18b and Eq. (2.82), that zero transmission is obtained when $t = A$, or $|\kappa|^2 = 1 - A^2$. This condition is called *Critical Coupling*, and is desired in devices that require a large Extinction Ratio. Clearly in Figure 2.18b the transmission curve becomes very steep when A and t are small, meaning that the

extinction ratio is dramatically altered by slight changes in coupling coefficient or loss [33]. The extinction ratio may be derived from Eq. (2.81) to be [34]:

$$ER = \left[\frac{I_{through}}{I_i}\right]_{\max} \Big/ \left[\frac{I_{through}}{I_i}\right]_{\min} = \frac{(|t|+A)^2(1-A|t|)^2}{(|t|-A)^2(1+A|t|)^2} \tag{2.83}$$

This also implies that it is theoretically possible to achieve critical coupling in any all-pass ring resonator, regardless of its loss, by properly selecting the coupler dimensions. On the other hand, it is not always possible to achieve 0% resonant transmission in the symmetric add-drop resonator of Figure 2.17. In fact, it is shown in Figure 2.17b that this is only achieved by having zero loss (A = 1), and is independent of κ entirely (although the intensity in the drop port off-resonance is dependent on κ). However, asymmetric add-drop ring resonators are capable of achieving critical coupling for non-zero loss.

The coupling domain to the left of the critical point is called *Under-Coupling*, and the domain to the right is called *Over-Coupling*. In addition to significantly affecting the extinction ratio, the coupling regime of operation influences the linewidth and therefore the resonator's *Finesse* and *Q*-Factor. The effect of coupling and loss is directly analogous to the etalon: both the cross-coupling coefficient and the ring loss must be minimized to maximize the linewidth. In an all-pass resonator, this means that while critical coupling may be achieved for a lossy ring by choosing an appropriately large coupling coefficient κ, this would result in a large linewidth. The linewidth is minimized by minimizing the coupling coefficient κ, and in some cases this means that an under-coupled resonator will have a smaller linewidth than a critically coupled one. In add-drop ring resonators, in fact, this is always the case.

The equation determining the *Finesse* of an all-pass resonator is derived from Eq. (2.81) to be:

$$\cos\left(\pi \big/ Finesse\right) = \frac{2A|t|}{1+A^2|t|^2} \tag{2.84}$$,

which indeed indicates an infinite *Finesse*, or an infinitely narrow linewidth $\Delta\lambda$, as A and $|t|$ approach unity [34].

One use of micro-rings in this project is to provide resonant enhancement of light intensity due to the confinement of energy in a structure. Referring to Figure 2.18a and Eq. (2.75) for an all-pass resonator structure, we have a relationship between E_i and $E_{through}$ on the bus waveguide and E_{r1} and E_{r2} on the ring.

$$\begin{bmatrix} E_{r1} \\ E_{through} \end{bmatrix} = \begin{bmatrix} t & \kappa^* \\ \kappa & -t^* \end{bmatrix} \begin{bmatrix} E_{r2} \\ E_i \end{bmatrix} \tag{2.85}$$

In addition, with knowledge of the ring loss alpha and the radius R, the relation between E_{r1} and E_{r2} can be expressed as:

$$E_{r2} = e^{-\alpha/2(2\pi R)} e^{ik(2\pi R)} E_{r1} = Ae^{i\delta} E_{r1} \tag{2.86}$$

Combining Eqns. (2.85) and (2.86) will lead to the following relationship between the field strength in the ring E_{r2} and the incident field strength on the bus waveguide E_i:

$$\frac{E_{r2}}{E_i} = \frac{Ae^{i\delta}\kappa^*}{1 - tAe^{i\delta}} \tag{2.87}$$

In terms of intensity, this is written as the Build-Up Factor (*BUF*):

$$BUF = \left| \frac{E_{r2}}{E_i} \right|^2 = \frac{A^2 \kappa^2}{1 - 2tA\cos\delta + t^2 A^2} \tag{2.88}$$

At resonance, the *BUF* is [32]:

$$BUF = \left| \frac{E_{r2}}{E_i} \right|^2 = \frac{A^2 \kappa^2}{(1 - tA)^2} \overset{t,A\to 1}{\approx} \frac{2}{\pi} \times Finesse \tag{2.89}$$

Therefore, the effect of storing energy in a ring on resonance causes the intensity to be enhanced over the incident value by a factor described by Eq. (2.89), which (assuming the ring is critically coupled and the loss is sufficiently low $A = t \sim 1$) is directly proportional to the *Finesse*. This is used in chapter 6 of this thesis, to enhance the photodetector response and thus implement them in much more compact structures.

Similarly, the *BUF* of an add-drop ring resonator is written as:

$$BUF = \left|\frac{E_{r2}}{E_i}\right|^2 = \frac{A^2\kappa^2 t^2}{1 - 2t^2 A\cos\delta + t^4 A^2} \tag{2.90}$$

On resonance, the *BUF* has a value:

$$BUF = \left|\frac{E_{r2}}{E_i}\right|^2 = \frac{A^2\kappa^2 t^2}{\left(1 - t^2 A\right)^2} \tag{2.91}$$

2.5 Summary

This chapter has provided the theoretical framework necessary for a complete understanding of the remaining chapters. The concepts and equations contained within will be referenced throughout the thesis. Having discussed the motivation and underlying theory, we are now in a position to present a device-based model of the photodetection process.

References

[1] G. Lifante, *Integrated Photonics Fundamentals,* "Chapter 2: Review of the Electromagnetic Theory of Light," Wiley, 2003.

[2] K. Kawano and T. Kitoh, *Introduction to Optical Waveguide Analysis: Solving Maxwell's Equations and the Schrödinger Equation,* "Chapter 1: Fundamental Equations," John Wiley & Sons, 2001.

[3] E. Hecht, *Optics (4th Ed.),* "Chapter 4: The Propagation of Light," Addison Wesley, 2002.

[4] D. Marcuse, *Theory of Dielectric Optical Waveguides,* "Chapter 1: The Asymmetric Slab Waveguide," Academic Press, 1974.

[5] G. Lifante, *Integrated Photonics Fundamentals,* "Chapter 3: Theory of Integrated Optic Waveguides," Wiley, 2003.

[6] K. Kawano and T. Kitoh, *Introduction to Optical Waveguide Analysis: Solving Maxwell's Equations and the Schrödinger Equation,* "Chapter 2: Analytical Methods," John Wiley & Sons, 2001.

[7] R. A. Soref, J. Schmidtchen, and K. Petermann, "Large single-mode rib waveguides in GeSi-Si and Si-on-SiO_2," *IEEE Journal of Quantum Electronics*, vol. 27, pp. 1971-1974, 1991.

[8] B. E. A. Saleh, M. C. Teich, *Fundamentals of Photonics: 2nd Ed.,* "Chapter 8: Guided Wave Optics," John Wiley & Sons, 2007.

[9] "OZ Optics: Tapered and Lensed Fibers," www.ozoptics.com, Ottawa, ON, Canada.

[10] "RSoft BeamPROP version 8.1 User Guide," www.rsoftdesign.com, RSoft Design Group, Inc., Ossining, NY.

[11] "RSoft FullWAVE version 6.1 User Guide," www.rsoftdesign.com, RSoft Design Group, Inc., Ossining, NY.

[12] J. Gowar, *Optical Communication Systems,* "Chapter 3: Material Dispersion," Prentice Hall International, 1984.

[13] E. Hecht, *Optics: 4th Ed.,* Addison Wesley, pp. 66-73, 2002.

[14] B. E. A. Saleh, M. C. Teich, *Fundamentals of Photonics: 2nd Ed.,* "Chapter 16: Semiconductor Optics," John Wiley & Sons, 2007.

[15] G. J. Burrell, B. Ellis, and T. S. Moss, *Semiconductor Opto-Electronics,* "Chapter 3: Absorption Processes in Semiconductors," Wiley, 1973.

[16] C. Hermann, and B. Sapoval. *Physics of Semiconductors,* "Chapter 6: Effects of Light," Springer-Verlag, 1995.

[17] C. Kittel, *Introduction to Solid State Physics: 8th Ed.,* "Chapter 4: Phonons I. Crystal Vibrations," John Wiley & Sons, 2005.

[18] S. M. Sze and K. K. Ng, *Physics of Semiconductor Devices: 3rd Ed.,* "Chapter 1: Semiconductor Physics," John Wiley & Sons, 2007.

[19] R. A. Soref and B. R. Bennett, "Electrooptical effects in silicon," *IEEE Journal of Quantum Electronics*, vol. QE-23, pp. 123-129, 1987.

[20] B. G. Streetman and S. K. Banerjee, *Solid State Electronic Devices: 6th Ed.,* Pearson: Prentice Hall, 2006.

[21] Chin-Lin Chen, *Foundations for Guided-Wave Optics,* "Chapter 4: Propagation Loss in Thin-film Waveguides," Wiley-Interscience, 2007.

[22] C. Kittel, *Introduction to Solid State Physics: 8th Ed.,* John Wiley & Sons, 2005.

[23] S. Wang, *Fundamentals of Semiconductor Theory and Device Physics,* Prentice Hall, 1989.

[18] S. M. Sze and K. K. Ng, *Physics of Semiconductor Devices: 3rd Ed.,* "Chapter 1: Semiconductor Physics," John Wiley & Sons, 2007.

[24] B. G. Streetman and S. K. Banerjee, *Solid State Electronic Devices: 6th Ed.,* "Chapter 5: Junctions," Prentice Hall, 2006.

[25] G. Keiser, *Optical Fiber Communications: 3rd Ed.,* "Chapter 6: Photodetectors," McGraw-Hill, 2000.

[26] "ATLAS User's Manual: Device Simulation Software," Silvaco International, Sept. 2004.

[27] S. M. Sze and K. K. Ng, *Physics of Semiconductor Devices: 3rd Ed.,* "Chapter 13: Photodetectors and Solar Cells," John Wiley & Sons, 2007.

[28] B. E. A. Saleh, M. C. Teich, *Fundamentals of Photonics: 2nd Ed.,* "Chapter 18: Semiconductor Photon Detectors," John Wiley & Sons, 2007.

[29] A. Yariv and P. Yeh, *Photonics: Optical Electronics in Modern Communications: 6th Ed.,* "Chapter 4: Optical Resonators," Oxford University Press, 2007.

[30] G. T. Reed and A. P. Knights, *Silicon Photonics: An Introduction,* "Chapter 4: Silicon-on-Insulator (SOI) Photonics," John Wiley & Sons, 2004.

[31] H. Nishihara, M. Haruna, and T. Suhara, *Optical Integrated Circuits,* McGraw-Hill, 1989.

[32] J. Heebner, R. Grover and T. Ibrahim, *Optical Microresonators: Theory, Fabrication, and Applications,* "Chapter 3: Optical Microresonator Theory," Springer, 2008.

[33] A. Yariv, "Universal relations for coupling of optical power between microresonators and dielectric waveguides," *Electronic Letters*, vol. 36, pp. 321-322, 2000.

[34] W. R. McKinnon, D.-X. Xu, C. Storey, E. Post, A. Densmore, A. Delâge, P. Waldron, J. H. Schmid, and S. Janz, "Extracting coupling and loss coefficients from a ring resonator," *Optics Express*, vol. 17, pp. 18971-18982, 2009.

Chapter 3: Modeling Defect-Enhanced Photodetectors

3.1 Overview

As discussed in section 1.4, the transparency of silicon to 1.55 μm light, required for waveguiding, precludes optical power detection using silicon band-to-band optical absorption. As a result, a means of locally increasing the absorption coefficient is required to integrate a photodetector onto the same chip as the high-transmission waveguides.

One method of local optical absorption coefficient enhancement utilizes point defects introduced by ion implantation. Point defects have charge state levels within the forbidden gap of silicon, which act as intermediate states in an absorption process, as described in section 2.2. For instance, the divacancy defect introduced in section 1.4 has a charge state located 0.4 eV below the conduction band [2, 3]. Photons at 1550 nm (which have an energy of 0.8 eV) are able to excite an electron from the valence band to this charge state, where it can then be further excited into the conduction band either thermally or by a second photon as in Figure 2.10. Therefore, an additional high energy ion implantation step at the end of a process is the sole requirement for the modification of silicon from a low absorption state needed for waveguides into a highly absorbing state needed for photodetection.

The device design is not straightforward, however. The nature of lattice defect formation prevents their incorporation with arbitrary depth profiles and concentrations. The defects created are highly dependent on the implanting species, dose and energy, as well as the subsequent thermal treatment. In addition, the deep centres provide an

enhancement in carrier trapping as well as that of carrier generation. This places severe restrictions on device geometry, as will be shown presently.

3.2 The Divacancy

For the purposes of evaluating the photodetector device designs, a single defect type was assumed to be present: the divacancy. This section will review the pertinent literature on irradiated silicon to provide a justification for this choice.

Deep levels tend to exhibit behaviour much different from shallow donors and acceptors: they distort the atoms in their vicinity to a large extent, and this distortion depends on the number of electrons occupying them (i.e. their charge state). For defects such as the divacancy, this is described by the *Jahn-Teller Distortion*, in which the transition from one charge state to another requires an additional investment of energy to move the neighbouring atoms to the new position. This was incorporated into a complex model of the divacancy by Corbett and Watkins [4]. There are six nearest neighbour atoms, and as electrons fill their orbitals, lattice distortion occurs and splits the transitional energies between charge states. When the divacancy has only a single electron, it is in the singly-positively charged state (+1); when it has two electrons, it is in the neutral state (0); when it has three electrons, it is in the singly-negatively charged state (-1); and when it has four electrons, it is in the doubly-negatively charged state (-2). Using this distorted model as a starting point, physicists correlated Electron Paramagnetic Resonance (EPR), optical absorption, and photoconductivity data with transitions between charge states.

Electron Paramagnetic Resonance is a spectroscopic method used to, amongst other things, identify defects in irradiated semiconductors [5]. The spin-down and spin-up states are split in the presence of a magnetic field, and electrons can be excited between these states by microwave photons. Further splitting (called 'hyperfine' splitting) results

from nuclear interactions and the resulting absorption spectrum peaks provide information on lattice structure. Combined with angular variation, it is possible to completely model the microscopic structure of the defect for each charge state [6]. In Figure 3.1a, the energy levels of the divacancy charge states are shown [4].

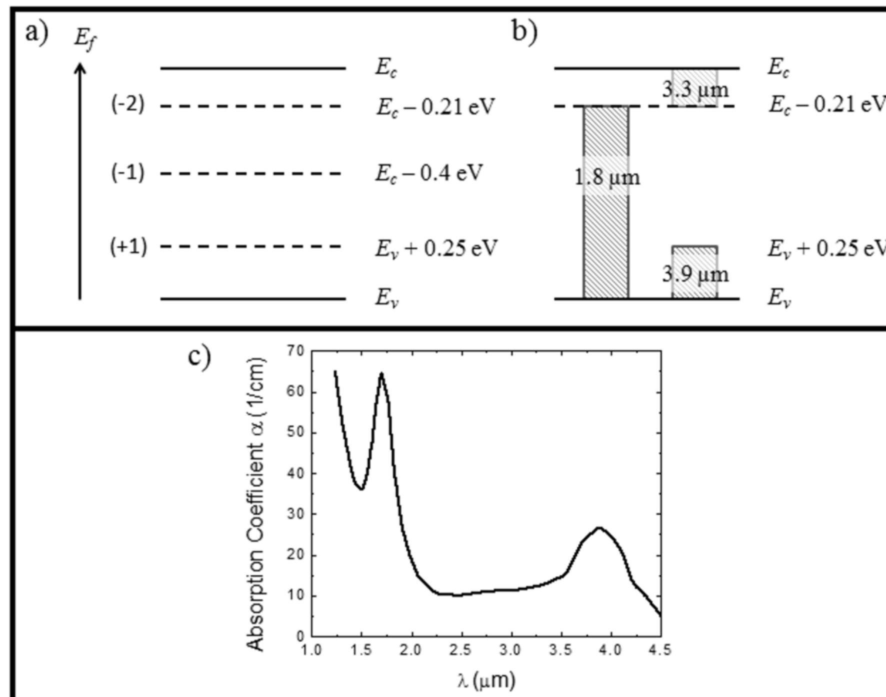

Figure 3.1: a) Map of divacancy charge state as a function of Fermi Level, deduced from EPR measurements [4, 7]; b) Map of existing absorption peaks as a function of Fermi level [8]; c) Sample absorption spectrum measured by Fan & Ramdas for a *p*-doped Si sample irradiated with electrons, showing the prominent 1.8 µm band [8].

Several absorption peaks in implantation-damaged silicon have been associated with the divacancy. The sample spectrum from lightly *p* doped silicon irradiated with electrons shown in Figure 3.1c exhibits the characteristic 1.8 µm peak [8]. This band has been independently observed to disappear in samples where the Fermi level is above E_c - 0.21 eV [8, 9] as in Figure 3.1b. For such highly *n* type silicon, a second absorption band centered upon 3.3 µm appears, coincident with the disappearance of the 1.8 µm [8,

10]. Since the two bands are not simultaneously observed, it was concluded that the final orbital state of the 1.8 μm band is the same as the initial orbital state of the 3.3 μm band [10].

The photoconductivity was measured as a function of photon energy [11-14], and the threshold wavelengths for photoconductivity provide the associated electronic transition energies. The change in photoconductivity when a sample undergoes uniaxial stress provides information on the microscopic structure [11], which through comparison with the results of EPR can identify a charge state. For example, the E_v + 0.32 eV threshold and the corresponding absorption band at 3.9 μm was correlated to the transition between the +1 and 0 charge state through interaction with the valence band (i.e. hole generation) [11]. Similarly, a photoconductivity threshold at E_c - 0.75 eV and the corresponding absorption band at 1.8 μm was correlated to the transition between the 0 and the -1 charge state through another hole generation in the valence band [13]. Once the -1 charge state is fully occupied (i.e. the Fermi level has risen above E_c - 0.21eV as in Figure 3.1a, the 1.8 μm absorption is removed and the 3.3 μm absorption occurs (and a photoconductivity threshold at E_c - 0.39 eV) for excitation of an electron from the divacancy into the conduction band [10, 14].

That the 1.8 μm absorption band and the corresponding photoconductivity level are present in lightly doped irradiated silicon at room temperature is an indication of the presence of divacancies in their neutral charge state. Fast neutron irradiation or ion implantation produce vacancy complexes in silicon, and the divacancy may be the dominant such complex at room temperature. In the case of oxygen implantation, for example, the divacancy is dominant for doses up to 10^{13} cm^{-2}, after which tetravacancies and, beyond a critical concentration, amorphous silicon regions appear [15, 16]. The corresponding critical dose becomes smaller for more massive ions, and the maximum 1.8 μm absorption was found to occur with doses which were smaller than this dose [16]. Positron Annihilation Spectroscopy has since been used to predict point defect concentration as a function of ion dose, adjusted for ion species [17]. The 1.55 μm

absorption in Si^+ implanted rib waveguides has shown good agreement with this dependence on dose, indicating that it is the tail of the 1.8 μm absorption band of the divacancy that is responsible [18].

The absorption and photoconductivity described above had a marked dependency on annealing conditions. This is an indication of the removal of the divacancies through recombination with interstitials and the agglomeration into larger clusters [19]. The disappearance of the 1.8 μm band following a 300-350 C anneal suggests the complete removal of the divacancies [3, 7, 9, 19]. The aforementioned Si^+ implanted rib waveguides were subjected to isochronous anneals, and exhibited a decreased propagation loss between 150 and 250 C annealing stages [18]. The recovery of the pre-implanted absorption level is an indication of the complete removal of the defect, and rules out the possibility of an impurity related center being responsible for the absorption.

In summary, the divacancy is a dominant defect at room temperature for a select range of ion implantation conditions. It has an associated absorption peak at 1.8 μm and photoconductivity which result from a transition from its neutral charge state to the singly-negatively charged state through the generation of a hole. The reduced absorption at 1.55 μm measured from ion implanted waveguides with annealing is consistent with the reported removal of divacancies at these temperatures. It is on this basis that the divacancy was selected as the relevant defect to be used in the single-defect model.

3.3 Theory of Deep-Level Carrier Generation and Recombination

A deep center in silicon interacts thermally with the conduction and valence bands according to Shockley-Read-Hall theory in the following ways as depicted in Figure 3.2: promotion of an electron from the defect level to the conduction band (occurring with a rate G_n), trapping of an electron from the conduction band by the defect level (occurring

with a rate U_n), promotion of an electron from the valence band to the defect level (i.e. hole generation, denoted by a rate G_p), and trapping of an hole by the defect level (denoted by a rate U_p) [20].

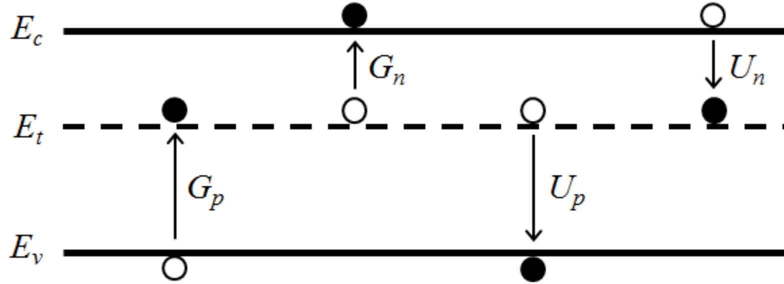

Figure 3.2: Schematic of defect level at energy E_t between the conduction band energy E_c and valence band energy E_v, along with the relevant transition rates G_n, U_n, G_p, and U_p [21, 27].

A piece of silicon material containing a uniform concentration of defects denoted by N_t will, in thermal equilibrium, have a value of each rate such that:

$$U_n - G_n = U_p - G_p \quad (3.1)$$

This ensures that the concentration of electrons occupying the defect state, denoted by n_t, is in steady state. The value of G_n is determined by the proximity of the defect level to the conduction band, the concentration of occupied defects n_t, and a defect property called the capture cross-section of electrons σ_n:

$$G_n = \sigma_n v_{th} n_t n_i \exp\left(\frac{E_t - E_i}{kT}\right) \quad (3.2),$$

where v_{th} is the thermal velocity of electrons at room temperature, E_t is the trap energy, E_i is the energy roughly in the center of the band gap of silicon, n_i is the intrinsic carrier concentration, k is the Boltzmann constant and T is the temperature.

The value of U_n depends on the concentration of electrons in the conduction band n, the concentration of unoccupied defects (N_t - n_t), and the capture cross-section of electrons:

$$U_n = \sigma_n v_{th} (N_t - n_t) n \quad (3.3)$$

Similarly, for holes:

$$G_p = \sigma_p v_{th} (N_t - n_t) n_i \exp\left(\frac{E_i - E_t}{kT}\right) \quad (3.4)$$

$$U_p = \sigma_p v_{th} n_t p \quad (3.5),$$

where σ_p is the capture cross-section of holes and p is the concentration of holes in the valence band.

To find the value of n_t in thermal equilibrium, Eqns. (3.2-3.5) are substituted into Eq. (3.1) to yield [21]:

$$n_t = N_t \frac{\sigma_n n + \sigma_p p'}{\sigma_n (n + n') + \sigma_p (p + p')}$$

where $$p' = n_i \exp\left(\frac{E_i - E_t}{kT}\right) \text{ and } n' = n_i \exp\left(\frac{E_t - E_i}{kT}\right) \quad (3.6)$$

Therefore, in thermal equilibrium the value of n_t depends on not only the defect characteristics (given by E_t, σ_n and σ_p) but also on the doping of the silicon. If the silicon is heavily n-doped, the large electron concentration n leads to a large trapping rate U_n and thus from Eq. (3.6) $n_t = N_t$. Alternatively, if the silicon is p-doped, Eq. (3.6) reduces to $n_t = 0$.

In the case of the divacancy, σ_n and σ_p are of similar magnitude but the defect level is closer to the conduction band than the valence band. Ion implantation produces defects with concentrations roughly in the range of 10^{16}-10^{18} cm^{-3}, whereas background doping is in the region of 10^{15} cm^{-3}. As a result, the value of n_t in thermal equilibrium is between 0 and 10^{15} cm^{-3}, depending on whether the wafer is n or p doped.

3.4 Single-Defect Model of Photodetection

Photodetection is possible by utilizing the optical transition of a free electron from the valence band to the divacancy level. The threshold energy of this transition is roughly 0.72 eV, and is therefore capable of being initiated by a 1550 nm photon. Similar to the rate G_p, this optical generation rate will be proportional to the concentration of unoccupied defect centers (N_t - n_t). In the case of the low doping conditions described above, $n_t \rightarrow 0$ and therefore the absorption rate is approximately proportional to N_t.

Since the excitation light is absorbed as it travels through the device, the generation term also has an exponential decay proportional to N_t. If the absorption coefficient corresponding to the divacancy is written in terms of its optical absorption cross-section β [22]:

$$\alpha_t = \frac{N_t}{\beta} \tag{3.7}$$

Then the generation rate in a waveguide drawn in Figure 3.3 may be written as [23]:

$$G_{opt}(x, y, z) = I(x, y)\frac{\lambda}{hc}\alpha_t \exp(-\alpha_t z) \quad (3.8),$$

where $I(x,y)$ is the intensity profile of the fundamental mode (normalized to total power), λ is the free-space wavelength of light launched, h is the Planck's constant and c is the speed of light in vacuum.

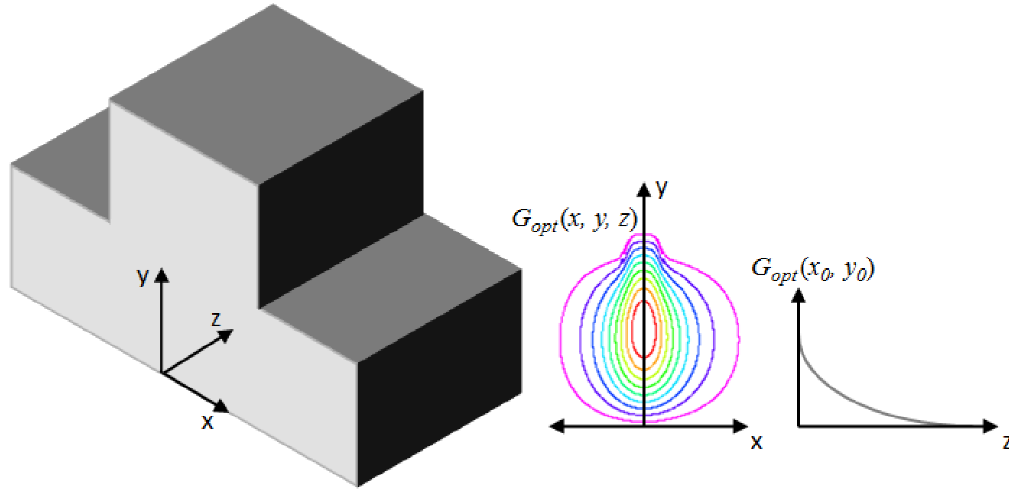

Figure 3.3: Rib waveguide structure used in the photodetector model; showing insertion point of optical generation rate G_{opt} (*x*, *y*, *z*) and the coordinate system used.

This three dimensional problem was solved in a two dimensional ATLAS simulation by utilizing several assumptions. First, following the optical transition from the valence band to the defect level, a relatively instantaneous thermal transition occurs from the defect level to the conduction band. This is justified by the fact that G_{opt} is less than the equilibrium value of G_n for reasonable (< 100 W) optical powers. Therefore, it is assumed that n_t does not significantly deviate from its thermal equilibrium value during optical excitation. Were it the case that $G_{opt} > G_n$, Eq. (3.8) would no longer be valid and each absorption event would not lead to the generation of an electron-hole pair. A saturation in the photodetector responsivity (meaning a loss in linear proportionality between photocurrent and injected light power) at high light intensities would be an indication that this is taking place.

Secondly, the simulation requires the de-coupling of the optical generation process and the electrical defect processes of Eq. (3.2-3.5). The former are simulated by adding acceptor carrier traps with the characteristics of the divacancy: E_t = 0.4 eV below the conduction band [2, 3], $\sigma_n = 3.65 \times 10^{-15}$ cm^2 [2, 3], and $\sigma_p = 3.6 \times 10^{-14}$ cm^2 [2]. The

latter is simulated by adding a separate spatially dependent electron-hole pair generation rate (in x and y), given by:

$$\int_0^L G_{opt}(x,y,z)dz = I(x,y)\frac{\lambda}{hc}\frac{\alpha_t}{\alpha_t+\alpha_i}\left[1-\exp\left(-(\alpha_t+\alpha_i)L\right)\right] \tag{3.9}$$

This represents the carrier generation rate of Eq. (3.8) integrated over the z coordinate, implicitly taking into account its length L and the associated absorption loss. The absorption loss will be a result of defect absorption α_t of Eq. (3.7) as well as loss from other mechanisms α_i (including free-carrier absorption). The x and y dependence is that of the optical mode used in $I(x,y)$ and is determined from a BeamPROP simulation.

The device cross-section is built in ATLAS, including the ridge waveguide of Figure 3.3, n^+ and p^+ doped regions, and aluminum contacts. The photocurrent can be measured as a function of applied bias, defect concentration, light intensity as well as other geometrical factors.

3.5 Single-Defect Model Results

The validity of this model was tested through a comparison against the reported results from three research groups described in section 1.4: McMaster University [24], The Chinese University of Hong Kong [25], and MIT Lincoln Laboratories [26]. All groups used the integration of *p-i-n* photodiode structures onto a silicon waveguide, and ion implantation followed by high temperature annealing to achieve a response at 1550 nm. The device design and implantation conditions, however, vary between the different groups. Figure 3.4 compares the design of the device fabricated at McMaster University to that fabricated by MIT Lincoln Labs.

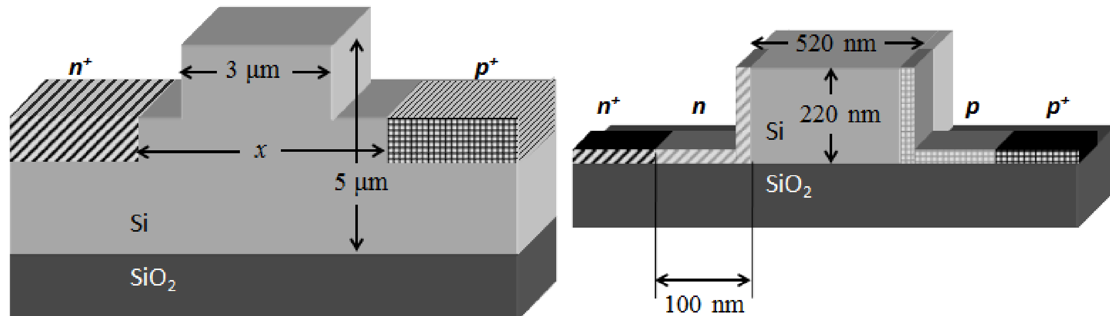

Figure 3.4: McMaster University device [24] (left) and MIT Lincoln Labs device [26] (right) (The Chinese University of Hong Kong device [25] is similar in structure to that of the McMaster University); parameters *x* and *y* reflect variable dopant geometry and are addressed in a later section, *L* represents the length of the *p-i-n* junction on the waveguide.

The devices of McMaster University and The Chinese University of Hong Kong are of similar dimension, having a cross-section of several micrometers. In contrast, the device from Lincoln Laboratories has a sub-micron cross-section. The McMaster University and Lincoln Laboratories groups both use Si^+ implantation species to generate the defects, although Lincoln Laboratories requires a lower energy (190 keV) than McMaster (1.2 MeV) due to its considerably smaller waveguide height [24, 26]. The Chinese University of Hong Kong use He^+ species to generate defects, at an energy of 800 keV [25]. Following implantation, all groups use high temperature annealing steps to repair the lattice and remove the defects, and therefore decrease the optical absorption. The absorption and photocurrent were measured after each annealing stage.

Each structure was built in the ATLAS environment as described in the previous section, and the integrated optical generation rate and acceptor trap concentration were simultaneously altered to reflect a changing N_t[5]. The calculated photocurrent is plotted for each device as curves in Figure 3.5. For the purpose of comparison, the measured photocurrent is plotted as data points. The corresponding values of N_t for the measured photocurrent were approximated from the reported loss values by using Eq. (3.7).

[5] Refer to Appendix A for a detailed ATLAS script used for such a simulation.

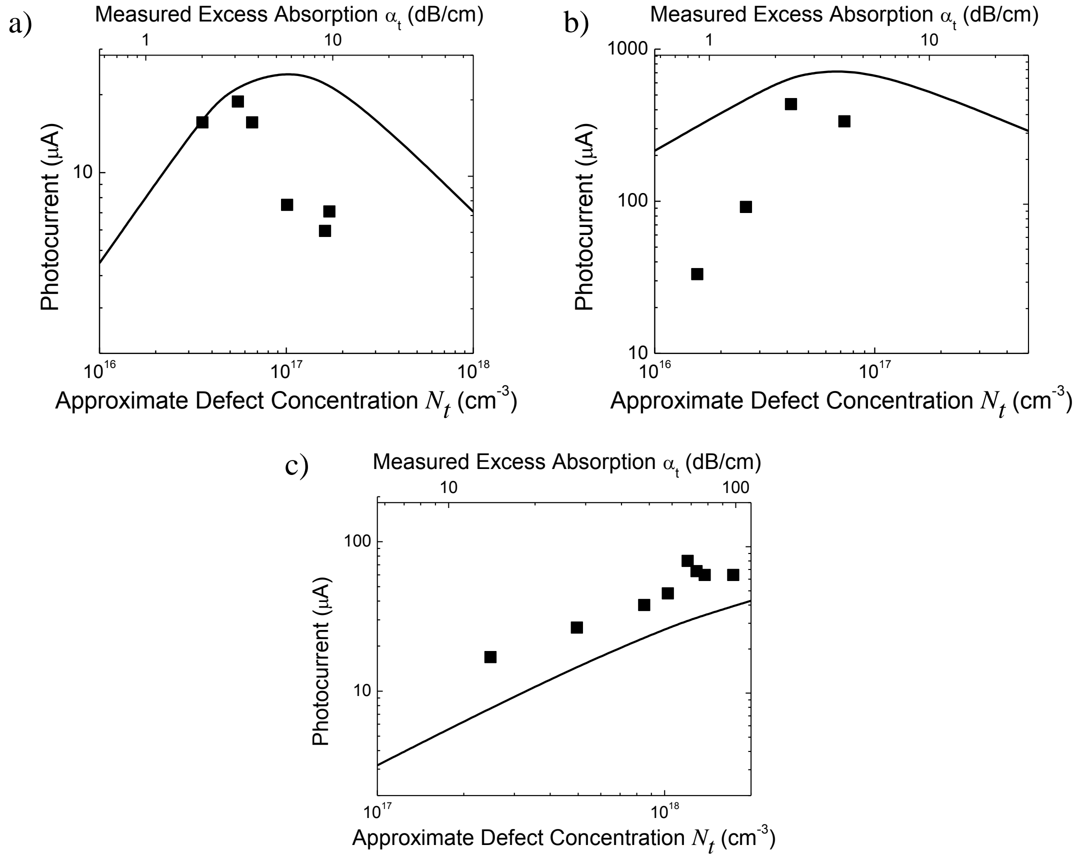

Figure 3.5: The simulated (solid lines) and reported (data points) photocurrent by (a) McMaster University [24] (with a device length L = 6 mm, x = 18 µm, biased at -2 V and 1 mW input power), (b) The Chinese University of Hong Kong [25] (with a device length of 17 mm, biased at -20 V and 25 mW input power), (c) MIT Lincoln Laboratories [26] (with a device length of 0.25 mm, biased at -5 V and 1 mW optical input power); Defect concentration N_t was approximated from the measured loss using Eq. (3.7) [27].

The observed trend in both simulation and experiment is an initial increase in photocurrent with N_t, a result of the increased carrier generation rate. However, above a particular value of N_t, the photocurrent begins to decrease. The main reason for this is that the recombination rate is linear with N_t (Eq. (3.3)), while the optical generation rate is sub-linear (Eq. (3.9)), and as a result the photocurrent begins to decrease when the

absorption length becomes comparable to the device length. The position of the peak in the curve is therefore strongly dependent on the length *L*. In addition, the optical generation occurs only in the region of strong optical power (i.e. within the mode), while carrier trapping occurs everywhere that defects are present. Therefore, introducing defects into the region outside of that occupied by the optical mode is detrimental to device performance. Larger values of N_t are tolerable in devices with short transit distances between a generation event and carrier extraction, or in the presence of large electric fields (large reverse bias). For instance, the Lincoln Laboratories device has a cross-sectional size that is an order of magnitude smaller than the other devices, allowing the p^+ and n^+ regions to be much nearer to one another. As a result, carriers have to travel at most 500 nm before extraction, in contrast to the McMaster device where they would have to travel 5 μm. Where carrier trapping would degrade the performance of the McMaster device for values of $N_t > 10^{17}$ cm^{-3}, it does not degrade the performance of the Lincoln Labs device until $N_t > 10^{18}$ cm^{-3}. Also, the close proximity of the p^+ and n^+ regions means that the Lincoln Labs device can be fully depleted under a reverse bias of 5 V, which further reduces the influence of carrier trapping.

In addition to absolute photocurrent, the defect-enhanced photodetectors may be analyzed with respect to an effective quantum efficiency η_{eff}, which is defined as:

$$\eta_{eff} = \frac{hc}{\lambda q}\frac{I_P}{P_{abs}} \quad (3.10),$$

where $q = 1.6 \times 10^{-19}$ C, I_P is the photocurrent and P_{abs} is the power absorbed by the photodetector. This is a useful metric for power monitoring applications, where it is only desired to absorb a fraction of the optical power. Figure 3.6a plots η_{eff} as a function of N_t for the McMaster device, both calculated values and those extracted from experimental results.

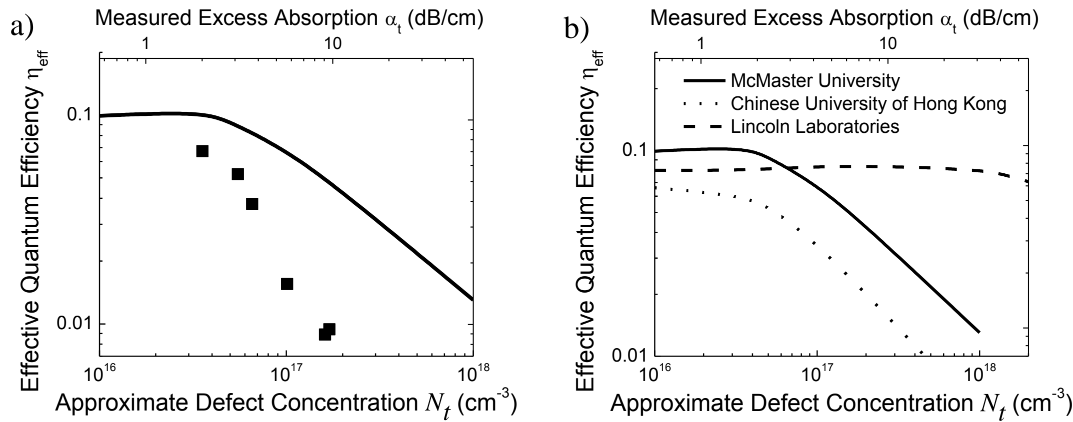

Figure 3.6: a) Simulated effective quantum efficiency η_{eff} of the McMaster University Device as a function of divacancy concentration N_t (solid curve), along with that extracted from experimental results (data points), b) Comparison of the simulated η_{eff} of the McMaster University device, The Chinese University of Hong Kong device, and the Lincoln Laboratories device; The McMaster University device was L = 6 mm in length, x = 6 µm, and biased at -2 V; The Chinese University of Hong Kong device was L = 17 mm in length and biased at -20 V; The Lincoln Laboratories device as 0.25 mm in length and biased at -5 V [27].

This indicates that larger cross-section devices become less efficient as N_t is increased, a consequence of the corresponding increase in carrier trapping reducing the efficiency of carrier removal. Figure 3.6b plots the calculated values of η_{eff} for the three devices. The degradation in efficiency of larger devices is not evident in the Lincoln Laboratories device, again a result of the ineffectiveness of the defects in trapping the carriers over the short distance available. It is also significant that the large absorption of the Lincoln Laboratories device limits its η_{eff} at low values of N_t to less than those of the McMaster University device.

While this single-defect model produces the correct physical result, its vast inherent inaccuracies should be noted. The implantation damage produces a multitude of defects, and while they may not all lead to carrier generation they are very likely to contribute to carrier trapping. Considering carrier trapping from divacancies alone is a simplification born out of the fact that any other defects are presently unidentified and

thus their trapping behaviour and its variation with thermal annealing are unknown. The carrier lifetimes are thus overestimated, meaning that accounting for any contribution of other defects to electrical trapping would shift the peak position of the photocurrent to smaller values of N_t. Indeed, this is believed to be the dominant reason why all simulated curves in Figure 3.5 have a peak photocurrent to the right of that obtained experimentally.

The value of the optical cross-section β of the divacancy at 1550 nm is also not well known. The assumed value is from earlier absorption investigations of the 1.8 μm absorption band, which is $\beta = 7.7 \times 10^{16}$ cm^{-2} [22]. This fixes the generation rate at an upper-most estimate, which will lead to larger simulated photocurrent than was measured.

The process of fitting the experimental curves is also flawed in that it was assumed that all reported loss was a result of divacancy absorption and generates carriers. The validity of this approximation will not only vary between devices but also between annealing stages within a single device (as secondary defects are introduced or removed).

That the correct trends can be described by assuming the presence of a single defect is a strong indication that we possess a sound understanding of the underlying physics, if not the subtle details. While the single-defect model is therefore only able to make concrete predictions of the optimized photocurrent with limited accuracy, it is able to evaluate device geometries and maximize the extracted photocurrent.

3.6 Evaluation of Device Designs

3.6.1 Performance dependence on reverse bias

The performance of a device may be improved by increasing the reverse bias, which increases the overlap between the carrier generation region (i.e. the optical mode) and the depleted area, thereby improving the carrier extraction. This enhancement is limited to complete overlap, which occurs in the Lincoln Laboratories device at a reverse

bias of 5 V. Experimentally, the authors reported a further increase in photocurrent beyond 10 V reverse biases that was attributed to carrier multiplication effects, which were not simulated in ATLAS [26]. Also, due to the presence of a depletion region at zero bias, all devices were simulated to have significant photocurrent in an unbiased mode.

3.6.2 Position of n^+ and p^+ regions and defect-forming implant mask width

1) McMaster University Device

One change in device structure that can be used to improve absolute photocurrent is the position of the p^+ and n^+ regions. The challenge lies in maximizing the overlap between the optical mode and the depleted region in order to maximize carrier extraction, without having the doped regions themselves strongly overlap with the optical mode and cause free-carrier absorption. A simulation was performed whereby the distance x between the p^+ and n^+ regions in the McMaster University device in Figure 3.4a was reduced under various conditions. The free carrier loss contribution was simulated using Eq. (2.41) and BeamPROP, and entered the model via the parameter α_i of Eq. (3.9). Figure 3.7a plots the photocurrent as function of x under light (10^{15} cm^{-3}) n and p doping conditions, and using a 50 µm wide defect-forming implant (i.e. defects occupy a 50 µm wide region centered on the ridge). Under both conditions, the photocurrent is gradually increased as x is decreased. For the n type case, the defect region is neutralized when the occupied defect concentration n_t matches the ionized donor concentration, leading to a large depletion width. Alternatively, a p type background has a net negative charge and is therefore not as well depleted. As a result, the model predicts a larger response from devices containing a light n type background. Note that it is possible that this simulation overestimates this effect, as the experimental points from a device with a lightly n type

background fit somewhere between the two curves. When x becomes smaller than the ridge width ($x < 3$ μm), the contribution of α_i begins to degrade the photocurrent.

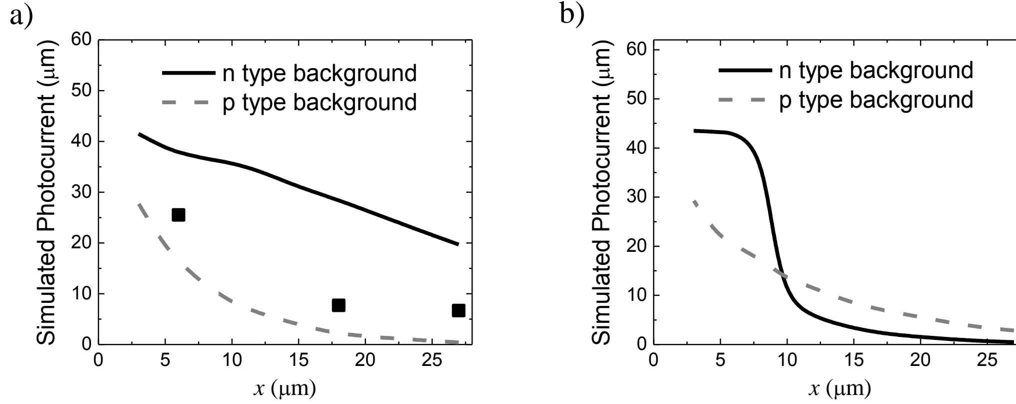

Figure 3.7: Simulated photocurrent of the McMaster University device plotted as a function of *x* (as defined in Figure 3.4), for defect implant mask widths of a) 50 μm and b) 5 μm; background doping is *n* type 10^{15} cm^{-3} (black curve) and *p* type 10^{15} cm^{-3} (grey dash curve), experimental data for *n* type 10^{15} cm^{-3} is shown for comparison (data points); devices were L = 6 mm in length and biased at -5 V with 1 mW optical input power [27].

It is also beneficial to reduce the width of the defect region to approximately the size of the optical mode, as other regions contribute to carrier trapping but not carrier generation. In Figure 3.7b, the implant width has been reduced to 5 μm. An improvement in the device with a *p* type background is evident for all values of x, whereas the improvement in the device with an *n* type background is only observed when the x becomes smaller than the implant width. When x becomes larger than the implant width, the enhancement in depletion described above no longer exists, and a drastic reduction in photocurrent is observed. Therefore, we can conclude that the maximum absolute photocurrent occurs in an *n* type background with x being similar to the ridge width, for an implant width slightly wider than x. Note that since the free-carrier absorption increases as x is decreased, this is not a configuration with a high η_{eff}.

2) Lincoln Laboratories Device

A similar study could be made using the Lincoln Laboratories device, by changing the depth of the sidewall implant on either side, labelled *y* in Figure 3.4b. The simulation accounts for this change through: a modification to the generation rate of Eq. (3.9) resulting from a changed value of α_i from free-carrier absorption, the electric field distribution in the waveguide, and the area of where carrier generation is possible. This last point reflects that the behaviour of the divacancy is not the same in heavily doped regions since its occupancy is altered, so no optical generation is simulated in them. The defects are still present there however, so the carrier trapping remains in this region.

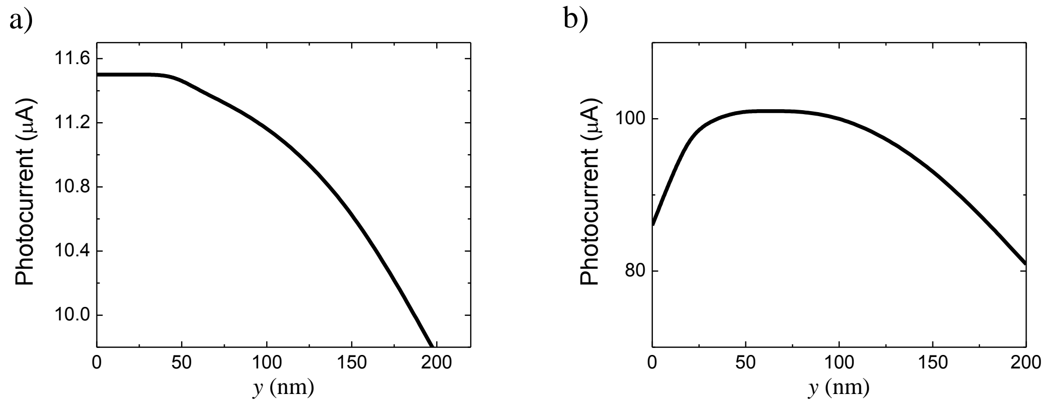

Figure 3.8: Photocurrent of the Lincoln Laboratories device vs. extent of doped regions on the side of the waveguide (*y*) for a) $N_t = 10^{17}$ cm^{-3} and b) $N_t = 10^{18}$ cm^{-3}; devices had length *L* = 100 μm and biased at -1 V.

For the case of $N_t = 10^{17}$ cm^{-3} in Figure 3.8a, the probability of trapping is small enough that all carriers can generally be removed from the device, even those generated in the center of the waveguide where the mode is strongest. Therefore, increasing the sidewall doping only increases free-carrier absorption and decreases the region of the waveguide where photogeneration is possible, both of which decrease the photocurrent. The situation changes for $N_t = 10^{18}$ cm^{-3}, where carrier trapping has reduced the lifetime

of the carriers to the point where those generated in the center of the waveguide cannot be swept out. Increasing the doped wall thickness improves the electric field in the center of the waveguide, allowing for better extraction efficiency. The influences of free-carrier absorption and reduced photogeneration eventually degrade the photocurrent for $y > 100$ nm. The optimum doped sidewall thickness is therefore between 50 nm and 100 nm.

Localizing the damage implant to the waveguide also provides changes to device operation, as shown in Figure 3.9. When the window is narrowed to be within the 500 nm wide waveguide, the carrier trapping is removed in those regions devoid of carrier generation. As a result, a much larger value of N_t becomes tolerable; the peak is shifted to the right and the maximum photocurrent is approximately doubled using this process improvement. Note that the achievement of $N_t = 10^{19}$ cm^{-3} has not been obtained in practice using the implant conditions described earlier in this section, so the total improvement may not be feasible.

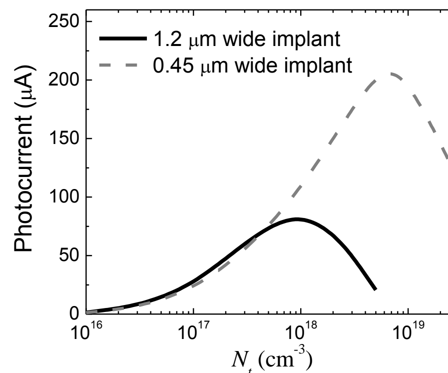

Figure 3.9: Photocurrent of the Lincoln Laboratories device vs. N_t for an implant width of 1.2 µm (black solid curve) and 450 nm (grey dashed curve); devices were L = 100 µm in length and biased at -1 V.

3.6.3 Defect-forming implant depth

The assumption that defects are formed in the entire silicon overlayer in equal concentration may be justified for the Lincoln Laboratories device, but is certainly not for the larger McMaster University device. Assuming a shallower damage implant complicates the calculation of α_t, not only because a fraction of the mode overlaps with the absorbing region, but also because the refractive index change in the damaged portion is significant enough to lead to radiation loss. The former is modeled by assuming a step-function defect distribution with an associated depth y_1, and integrating this distribution with the mode profile over the y coordinate:

$$\alpha_t' = \int_{y_1}^{\infty} I(0,y)dy \frac{N_t}{\beta} \tag{3.11}$$

Eq. (3.9) then becomes:

$$\int_0^L G_{opt}(x,y,z)dz = \int_0^L I(x,y)\frac{\lambda}{hc}\alpha_t \exp\left(-\left(\alpha_t' + \alpha_i\right)z\right)dz$$

$$\int_0^L G_{opt}(x,y,z)dz = I(x,y)\frac{\lambda}{hc}\frac{\alpha_t}{\alpha_t' + \alpha_i}\left[1 - \exp\left(-\left(\alpha_t' + \alpha_i\right)L\right)\right] \tag{3.12}$$

which represents the generation rate inserted only into a depth y_1; the remaining regions have a generation rate of zero and no carrier traps present. The only adjustment made to the generation rate inserted into this region is one that reflects that less attenuation will be sustained in its length L.

Figure 3.10 plots the photocurrent and η_{eff} of the McMaster University device as a function of the depth of the implant, for N_t = 10^{17} cm^{-3} and 10^{18} cm^{-3}. It is clear that for shallow implant depths, the maximum photocurrent occurs for larger values of N_t, since the N_t = 10^{18} cm^{-3} curve is above the N_t = 10^{17} cm^{-3} curve. As the depth is increased, the behaviour approaches that observed in Figure 3.5: a maximum response at N_t = 10^{17} cm^{-3}. This variation is a result of the implant depths influence on total loss: as the implant is

made shallower, the absorption length is made larger and the integrated generation rate of Eq. (3.12) increases.

The variation of the effective quantum efficiency reflects this effect as well. While the $N_t = 10^{18}$ cm^{-3} curve has a larger efficiency for a shallow implant and gradually decreases as the implant is made deeper, the $N_t = 10^{17}$ cm^{-3} has a maximum efficiency for mid-way implant depths. The lower loss associated with $N_t = 10^{17}$ cm^{-3} allows it to be implanted to this depth and only absorb 27% of the power, where $N_t = 10^{18}$ cm^{-3} absorbs 96% of the power. Since from Figure 3.10a the photocurrent of both concentrations is roughly the same, the $N_t = 10^{17}$ cm^{-3} device has four times the efficiency of the $N_t = 10^{18}$ cm^{-3} device.

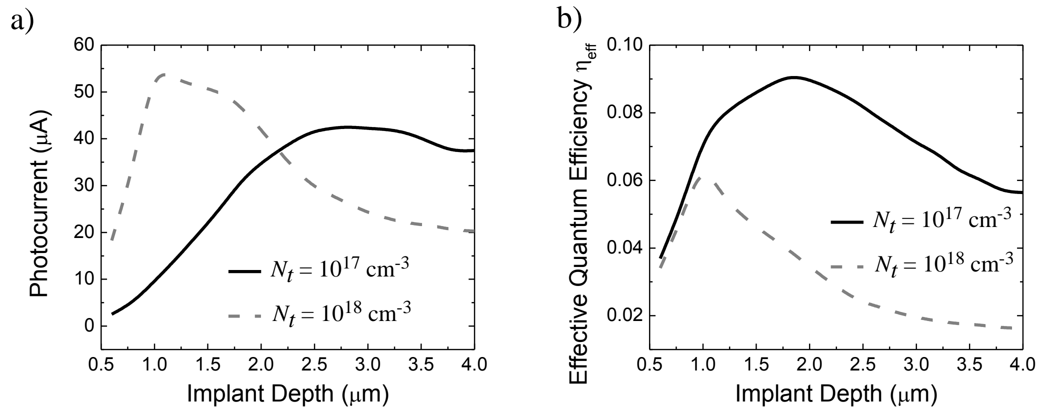

Figure 3.10: a) Absolute photocurrent and b) Effective quantum efficiency η_{eff} of the McMaster University device plotted as a function of implant depth for $N_t = 10^{17}$ cm^{-3} (solid black curve) and $N_t = 10^{18}$ cm^{-3} (dashed grey curve).

3.6.4 Adjusted defect implant mask profiles

The goal in the above analysis was to improve the removal of carriers from the center of the device to increase the absolute photocurrent, at the expense of effective quantum efficiency η_{eff}. The center of the waveguide is the least efficient region, so an improvement in η_{eff} may be envisioned by removing the defects there entirely. The

implant pattern shown in Figure 3.11a leads to a much smaller defect-induced absorption, and only allows carrier generation in the regions where they may be efficiently collected. This structure is ideal for power monitoring applications, where a fraction of the light is absorbed to provide a small photocurrent signal.

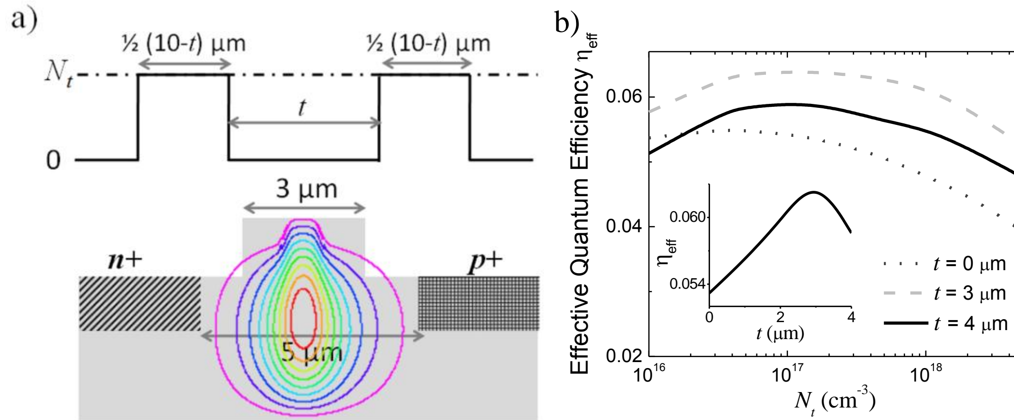

Figure 3.11: a) Implant mask pattern overlapped with device structure of the McMaster University device, b) Effective quantum efficiency η_{eff} vs. divacancy concentration N_t for different values of t defined in a) for a L = 6 mm device, x = 5 µm under a 2 V reverse bias.

Figure 3.11b plots the effective quantum efficiency for three values of t, calculated using Eqs. (3.11-3.12) (although in this case the integration of Eq. (3.11) is over the x coordinate), where the implant depth is assumed to be 5 µm. A small increase in efficiency is found at $N_t = 10^{17}$ cm^{-3} when t = 3 µm, meaning the defects are entirely outside of the rib. For this condition, only 0.71 dB of the signal is absorbed and 19 µA is obtained. In contrast, the t = 0 device absorbs 2.6 dB and produces 37 µA. Thus, if a smaller responsivity is tolerable, improvements in efficiency may be obtained by tailoring the defect implant mask. An inset plots the effective quantum efficiency vs. t for $N_t = 10^{17}$ cm^{-3}, showing that for $t > 3$ µm, the efficiency begins to decrease.

3.6.5 *Simulation of photodetector speed*

While the transit time difference between the larger and smaller cross-section devices has an influence on speed, it is not the dominant one. At their respective peak values of N_t, the transit time limits the speed of the McMaster University device to 1 GHz and the Lincoln Laboratories device to 50 GHz, which are much larger than the experimentally observed values of 3 MHz and 20 GHz [24, 26]. The speed of the photodetectors can be correlated with their capacitance. The McMaster University device has a simulated capacitance of 10-20 pF (depending on the n^+ and p^+ separation and length), while the Lincoln Laboratories device had a simulated capacitance of 0.1-1.5 pF, both of which are in good agreement with measured values [24, 26]. For the latter, connecting a 50 Ω load resistor (which was used in their measurement of bandwidth) produces a simulated 3-dB cut-off frequency of 30 GHz, consistent with their results [26]. Therefore, designs which minimize capacitance through either carefully designed contact structures or drastically reduced device length will have improved speed. The absorption coefficient achievable through the divacancy requires that the device length be larger than 100 μm however, which confines these designs to the regime of capacitance-limited speed.

3.7 Summary

This chapter has served to outline the device physics of defect-enhanced photodetectors and to practically evaluate different device structures. In particular, a model which assumed a single defect level was used to reproduce the behaviour of previously fabricated devices with some accuracy. The single defect was assumed to be the divacancy, based upon agreement between literature and waveguide absorption measurements. The model was implemented through ATLAS software, and used to suggest several novel device improvements.

References

[1] M. Gnan, S. Thoms, D. S. Macintyre, R. M. De La Rue, and M. Sorel, "Fabrication of low-loss photonic wires in silicon-on-insulator using hydrogen silsesquioxane electron-beam resist," *Electronics Letters*, vol. 44, pp. 115-116, 2008.

[2] E. Simoen *et al.*, "Impact of the divacancy on the generation-recombination properties of 10 MeV proton irradiated float-zone silicon diodes," *Nucl. Instrum. Methods in Phys. Res. A*, vol. 439, pp. 310–318, 2000.

[3] S. D. Brotherton and P. Bradley, "Defect production and lifetime control in electron and γ-irradiated silicon," *J. Appl. Phys.*, vol. 53, pp.5720–5732, 1982.

[4] G. D. Watkins and J. W. Corbett. "Defects in Irradiated Silicon: Electron Paramagnetic Resonance of the Divacancy," *Physical Review*, vol. 138, pp. A543-555, 1965.

[5] C. P. Poole Jr., *Electron Spin Resonance: A Comprehensive Treatise on Experimental Techniques,* Interscience, 1967.

[6] Watkins, G. D. "EPR of Defects in Semiconductors: Past, Present, Future," *Phys. Solid State*, vol. 41, pp. 746-50, 1999.

[7] A. O. Evwaraye, and E. Sun, "Electron-irradiation-induced divacancy in lightly doped silicon," *J. Appl. Phys*., vol. 47, pp. 3776-3780, 1976.

[8] H. Y. Fan & A. K. Ramdas, "Infrared Absorption and Photoconductivity in Irradiated Silicon," *Journal of Applied Physics*, vol. 30, pp. 1127-1134, 1959.

[9] L. J. Cheng, J. C. Corelli, J. W. Corbett and G. D. Watkins. "1.8-, 3.3-, and 3.9-μ Bands in Irradiated Silicon: Correlations with the Divacancy," *Physical Review*, vol. 122, pp. 761-774, 1966.

[10] C. S. Chen and J. C. Corelli "Infrared Spectroscopy of Divacancy-associated Radiation-Induced Absorption Bands in Silicon," *Physical Review B*, vol. 5, pp. 1505-1517, 1972.

[11] L. J. Cheng, "Effects of Uniaxial Stress on the Photoconductivity Spectra in Neutron-irradiated p-Type Si," in *Radiation Effects in Semiconductors,* Edited by F. L. Vook, Plenum Press, pp. 143-152, 1967.

[12] A. H. Kalma & J. C. Corelli, “Photoconductivity Studies of Defects in Silicon: Divacancy-Associated Energy Levels,” *Phys. Rev.* vol 173, pp. 734-745, 1968.

[13] R. C. Young & J. C. Corelli, “Photoconductivity Studies of Radiation-Induced Defects in Silicon,” *Phys. Rev. B*, vol. 5, pp. 1455-1467, 1972.

[14] A. H. Kalma, and J. C. Corelli, “Radiation-induced Photoconductivity of Silicon,” in *Radiation Effects in Semiconductors*, Edited by F. L. Vook, Plenum Press, pp. 153-161, 1967.

[15] V. S. Vavilov and A. R. Chelyadinskii, “Impurity ion implantation into silicon single crystals: efficiency and radiation damage,” *Physics-Uspekhi*, vol. 38, pp. 333-344, 1995.

[16] E. C. Baranova, V. M. Gusev, Y. V. Martynenko, C. V. Starinin, and L. B. Haibullin, “On silicon amorphization during different mass ion implantation,” *Radiation Effects*, vol. 18, pp. 21-26, 1973.

[17] P. G. Coleman, C. P. Burrows, and A. P. Knights. “Simple expression for vacancy concentrations at half ion range following MeV ion implantation of silicon,” *Appl. Phys. Lett*., vol. 80, pp. 947-949, 2002.

[18] P. J. Foster, “Optical attenuation in defect-engineered silicon rib waveguides,” *J. Appl. Phys.*, vol. 99, pp. 073101-1-7, 2006.

[19] J. Lalita, B. G. Svensson, C. Jagadish, and A. Hallén, “Annealing studies of point defects in low dose MeV ion implanted silicon,” *Nuclear Instruments and Methods in Physics Research B*, vol. 127/128, pp. 69-73, 1997.

[20] W. Schockley and W. T. Read, “Statistics of the recombination of holes and electrons,” *Phys. Rev.*, vol. 87, pp. 835–842, 1952.

[21] Details of theory of deep centers can be found in, for example: S.Wang, *Fundamentals of Semiconductor Theory and Device Physics*, “Chapter 7: Transport and Recombination of Excess Carriers,” Prentice-Hall, pp. 277–283, 1989.

[22] L. J. Cheng and L. Lori, “Characteristics of Neutron Damage in Silicon,” *Phys. Rev.,* vol. 171, pp. 856-862, 1968.

[23] S. M. Sze and K. K. Ng, *Physics of Semiconductor Devices: 3rd Ed.,* “Chapter 13: Photodetectors and Solar Cells,” Wiley, pp.674, 2007.

[24] A. P. Knights *et al.*, “Monolithically integrated photodetectors for optical signal monitoring in silicon waveguides,” *Proc. SPIE*, vol. 6125, pp. 61250J-1–12, 2006.

[25] Y. Liu *et al.*, “In-line channel power monitor based on Helium ion implantationin silicon-on-insulator waveguides,” *IEEE Photon. Technol. Lett.*, vol. 18, pp. 1882–1884, 2006.

[26] M. W. Geis *et al.*, “CMOS-compatible all-Si high-speed waveguide photodiodes with high responsivity in near-infrared communication band,” *IEEE Photon. Technol. Lett.*, vol. 19, pp. 152–154, 2007.

[27] D. F. Logan, P. E. Jessop, A. P. Knights, “Modeling defect enhanced detection at 1550 nm in integrated silicon waveguide photodetectors,” *J. Lightwave Tech.*, vol. 27, pp. 930-937, 2009.

Chapter 4: Photodetectors formed via the LOCal Oxidation of Silicon (LOCOS) Process

4.1 Overview

Relatively large cross-sectional area (> 1μm^2) waveguide photodetectors are limited in performance by the efficiency of carrier extraction. This can be improved by placing the junction within the waveguide ridge to achieve larger carrier depletion in the region of the optical mode. This is made possible by using the LOCal Oxidation of Silicon (LOCOS) method to form the waveguides. This is a standard CMOS process used for electrical isolation, where a patterned silicon dioxide/silicon nitride (SiO_2/Si_3N_4) stack is used to mask thermal oxidation. The silicon nitride provides a barrier to the diffusion of the oxidizing species and therefore prevents the oxidation of silicon beneath it. This results in extremely smooth trenches in the device surface. The edges of the trenches are angled, producing a "bird's beak" feature, as shown in the simulated ATHENA [1] output of Figure 4.1a. When two trenches are used to form a rib waveguide on SOI, the low sidewall roughness produces low propagation loss [2]. A poly-silicon contact can be self-aligned to the top of the ridge, as shown in Figure 4.1b. This symmetric device has a predicted enhanced responsivity over the asymmetric devices of similar cross-sectional area.

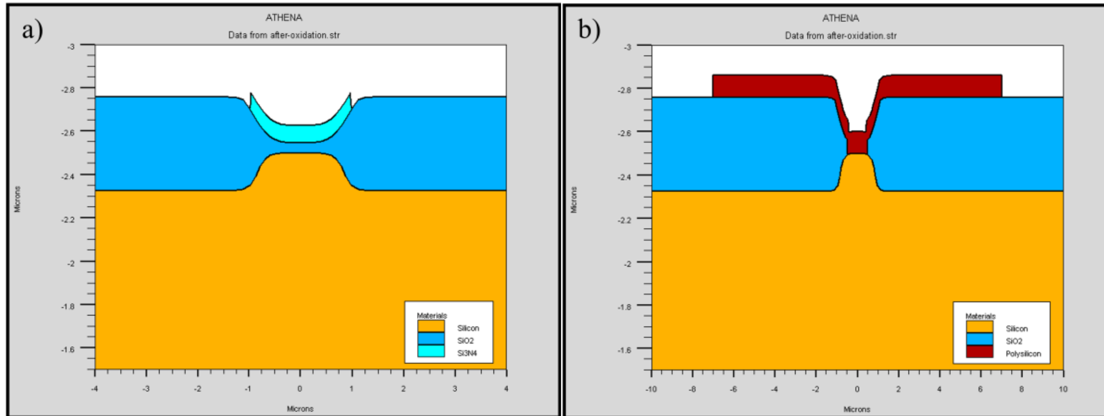

Figure 4.1 a) ATHENA output of two closely spaced oxidized trenches, illustrating the 'bird's beak' characteristic; b) ATHENA output following the poly-silicon deposition and etch, illustrating the self-aligned contact to the top of the rib.

4.2 Device Design

4.2.1 Waveguide geometry

A simplified geometry of the LOCOS waveguide is provided in Figure 4.2a. The values of H and h indicate the rib height and slab height respectively; their difference being determined by the degree of thermal oxidation. The parameter W_b represents the width of the bottom of the ridge, which is approximately equal to the width of the dielectric stack used to form the waveguide. The width of the top of the ridge W_t can be calculated using the characteristic 60° angle of the sidewall (with respect to the surface normal).

In any optical waveguide, it is desirable to ensure single-mode behaviour (as described in section 2.1.2) and strong optical confinement (i.e. large effective index n_{eff}). The mode cut-off condition may be calculated through manipulation of the following equation provided in Ref. 3 (which is itself derived from Eq. (2.33)):

$$\frac{W_b}{H} \leq 0.3 + \frac{h/H}{\sqrt{1-\left(\frac{h}{H}\right)^2 - \frac{(H-h)^2}{\sqrt{2}W_b H}}} \tag{4.1}$$

The assumed sidewall angle of 35° used for isotropic wet etched waveguides is replaced with that of 60° for the LOCOS waveguides. The resulting inequality provides, for given values of h and H, the maximum W_b for which single-mode behaviour will result:

$$\frac{W_b}{H} \leq 0.3 + \frac{h/H}{\sqrt{1-\left(\frac{h}{H}\right)^2 - \frac{\sqrt{3}(H-h)^2}{W_b H}}} \tag{4.2}$$

This inequality is plotted in Figure 4.2b for H = 1.5 μm (the thickness of the SOI overlayer), where the shaded region represents single-mode behaviour. This equation takes into account the simple relationship between W_t and W_b, and it should be noted that W_b must be sufficiently large so that W_t does not vanish.

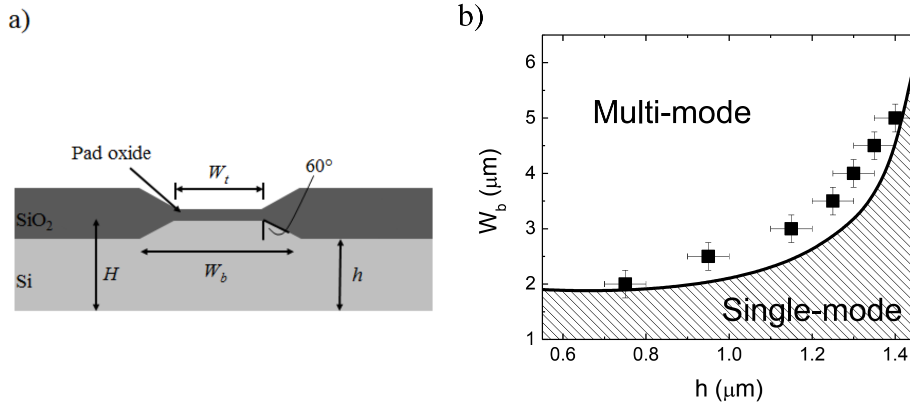

Figure 4.2: a) Cross-section of LOCOS waveguide (H = rib height, h = slab height, W_b = bottom rib width, W_t = top rib width), illustrating 60° sidewall angle; b) Region (shaded) of W_b and h for which the resulting waveguide will be single-mode, for H = 1.5 μm.

The data points of Figure 4.2b indicate the mode cut-off obtained through simulation using BeamPROP [4], the uncertainty being a result of the step size used in the simulation. In order to have a width W_t > 1 μm to contact with poly-silicon, a value of h = 1.3 μm was selected, and W_b was varied as 1.5, 2, and 2.5 μm. The width of the oxide trenches on either side of the rib were designed to minimize the mode leakage. Figure 4.3 plots the propagation loss of the fundamental mode as a function of this width, calculated using BeamPROP. It illustrates that for oxide trench widths below 6 μm, the structure can no longer support the optical mode. The final structure features a trench width of 14 μm to accommodate ohmic contacts to the poly-silicon, and so was safely beyond the 6μm limit.

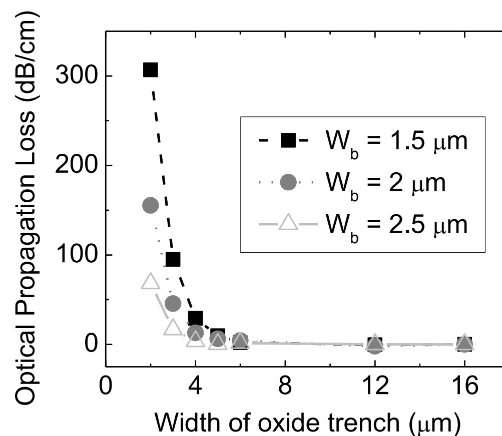

Figure 4.3: Simulated optical loss in a waveguide of H = 1.5 μm, h = 1.3 μm, and varying value of W_b, plotted as a function of the width of the thermal grown oxide trench surrounding the rib.

4.2.2 Poly-silicon contact design: Optical considerations

The optical loss in undoped Low Pressure Chemical Vapour Deposition (LPCVD) poly-silicon results from the presence of grain boundaries. At these long range crystalline defects, silicon dangling bonds produce electronic states within the band gap. These states have been approximated to exist 0.65 eV below the conduction band, and therefore

1550 nm light may excite electronic transitions between them and the band edges [5]. In addition to electronic absorption, the grain boundaries also behave as light scattering centers. In particular, the scattering due to surface roughness is a large concern in the formation of poly-silicon waveguides [6]. The absorption coefficient of poly-silicon films reported previously thus varies over several orders of magnitude, from 1-100/cm [7], depending strongly on the grain boundary density. It is desirable to maximize grain size, which is accomplished by a post-deposition thermal anneal. For example, a film deposited in the amorphous state and subsequently annealed at 900-1000 C produces poly-silicon with the large fraction of crystalline silicon, with a resulting optical loss that approaches that of crystalline silicon. In contrast, for a film deposited at higher temperatures (i.e. as polycrystalline silicon), a post-deposition high temperature anneal produces a much smaller improvement in optical loss, because the grain size is primarily determined at deposition [8, 9]. For this reason, the method of amorphous deposition followed by a high temperature anneal was selected for the devices reported in this thesis.

From the Soref formulae relating propagation loss to the doping concentration of silicon, Eq. (2.41), the loss due to a phosphorus concentration of 3×10^{17} cm^{-3} is approximately 11.1 dB/cm. It is assumed here that this is additive to the loss due to the presence of grain boundaries, while in reality the two contributing factors are not independent. Since phosphorus atoms segregate at the grain boundaries in electrically inactive forms [10, 11], they may change the electronic configuration of the defects there as well as the refractive index.

The propagation loss suffered by light in a LOCOS waveguide when a poly-silicon film is incorporated as shown in Figure 4.1b was modeled using BeamPROP, for various film thickness and dopant concentration. The poly-silicon refractive index was assumed to be 3.5, identical to that of the bulk silicon in the simulation. The refractive index deviates from this value only at the grain boundaries, and so averaged refractive indices are quoted in the research literature [7, 12]. However, the dependence of this average on grain size is weaker than that of the absorption coefficient [7], so the bulk

value was assumed. The results of the simulations are plotted in Figure 4.4, and indicate that for poly-silicon contact films less than 150 nm in thickness, the increase in propagation loss should be significantly less than 1 dB/cm, and possibly less than 0.1 dB/cm if the grain size is sufficiently large.

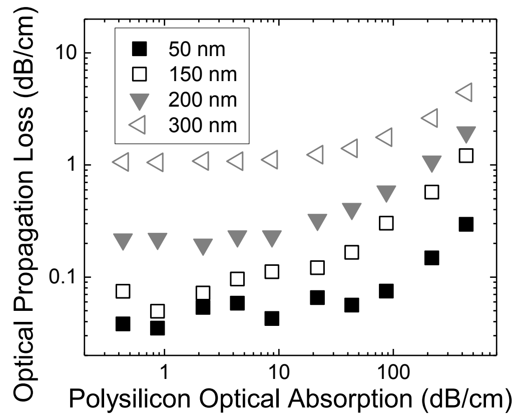

Figure 4.4: Propagation loss vs. assumed values of poly-silicon optical loss, assuming films of thickness 50 nm (black closed squares), 150 nm (black open squares), 200 nm (grey closed triangles) and 300 nm (grey open triangles) were deposited on a waveguide of dimensions H = 1.5 µm, h = 1.3 µm and W_b = 2 µm.

4.2.3 Poly-silicon contact design: Electrical considerations

The goal in the design of the poly-silicon contact was to form ideal rectifying behaviour with the silicon ridge (meaning a low forward resistance and a low reverse saturation current). This electrical property is dependent on both the poly-silicon/silicon interface quality as well as the properties of the film itself. In a similar manner to the optical absorption coefficient, poly-silicon resistivity is largely dependent on grain size, controlled by the deposition conditions and post-deposition anneal temperature [13].

Test samples were deposited with LPCVD amorphous silicon at 550 C, implanted with phosphorus at 25 keV and dose ranging from 2 x 10^{12} and 2 x 10^{13} cm^{-2}. The

deposited films underwent varying thermal treatments. They were measured using a Hall Effect set-up and a current-voltage (*IV*) probe station to determine the free-carrier concentration and the reverse bias dark current, respectively.

It was found that annealing the samples in an N_2 ambient provided a pathway for a significant out-diffusion of phosphorus. This is known to be mediated by the deposition of an oxide cap prior to the anneal or by annealing in an O_2 ambient [14]. However, the use of these techniques is not found to yield complete activation of the phosphorus, possibly due to the segregation of phosphorus into the crystalline silicon substrate [15]. As an O_2 ambient is undesirable in that it enhances the diffusion of dopants already present in the device, the N_2 ambient with a PECVD cap oxide was chosen as the method to crystallize the amorphous silicon layer. The thermal treatment produced mobilities in the region of 300–500 $cm^2/V/s$, which displayed no apparent trend with annealing temperature.

Utilizing a phosphorus dose of 2×10^{12} cm^{-2}, Table 4.1 provides the activated phosphorus concentration and dark current (from the poly-silicon/silicon junction) for 30 min anneals at various temperatures.

TABLE 4.1: Dopant activation and reverse saturation current (at -2 V) from a 100 nm LPCVD amorphous silicon film deposited on a silicon wafer. Films were deposited in LPCVD at 550 C and implanted with 25 keV phosphorus to a dose of 2×10^{12} cm^{-2}, and subsequently annealed for 30 min anneals at 800, 900 and 950 C.

Annealing Temperature (C)	Activated Phosphorus (cm^{-3})	Reverse Saturation Current ($\mu A/cm^2$) at -2 V
800	3.74×10^{17}	82
900	2.59×10^{17}	152
950	2.47×10^{17}	405

The activated phosphorus concentration was not found to change dramatically with annealing temperature for this dose, although this result was not consistent with published results [13]. The current-voltage (*I-V*) characteristic curve provides information on the quality of the poly-silicon/silicon interface. There is a thin native oxide region present on the silicon prior to the amorphous deposition, which is electrically broken down during the high temperature anneal [16]. An epitaxial realignment of the poly-silicon grains occurs at the interface, the degree of which is dependent on the annealing temperature [16]. As the temperature increases, these interfacial discontinuities lead to increased dark current. As a result, the annealing temperature was selected to be 900 C to simultaneously minimize dark current and maximize the activated phosphorus, while also minimizing the optical absorption for the reasons discussed in the previous sub-section.

4.2.4 Incorporation into the ATLAS simulation model

Using the selected waveguide dimensions of H = 1.5 µm, h = 1.3 µm, W_b = 2 µm, as well as the poly-silicon thickness of 100 nm doped with phosphorous to 3 x 10^{17} cm^{-3}, the device structure shown in Figure 4.5a results. This structure was incorporated into the ATLAS model described in chapter 3, which was used to simulate the photodetector performance in the manner described in the previous chapter. In Figure 4.5a, the built-in potential distribution is plotted illustrating strong electric field components in the upper half of the rib waveguide.

Figure 4.5b illustrates the predicted performance of this design (of 3 mm length), contrasted to the simulated performance of the three previously reported devices. All responsivities are labeled and represent optimum values for their device geometry (meaning that a defect concentration was chosen to produce the maximum responsivity), and all are simulated at a bias of -2 V. The theoretical performance of the LOCOS device is a three-fold improvement over previous large cross-section devices.

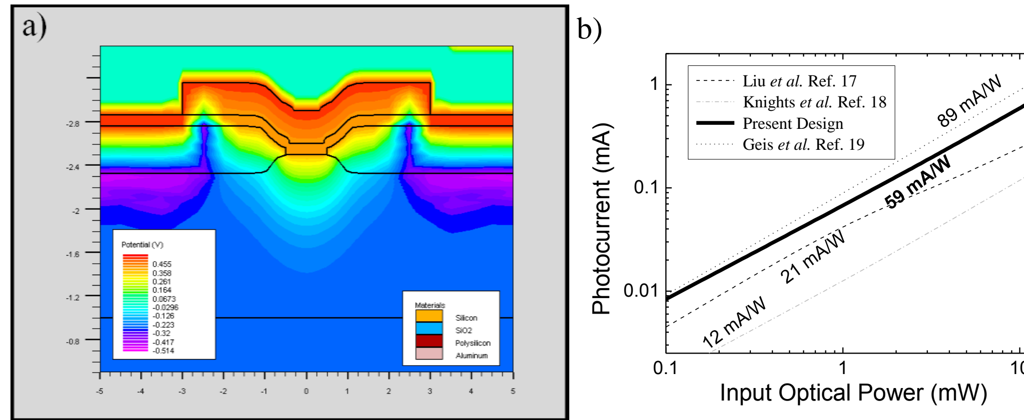

Figure 4.5: a) ATLAS model of device, displaying the built-in (unbiased) potential distribution within the rib; b) Comparison of device performance against the devices modeled in the previous chapter [17, 18, 19], simulated using the with an applied bias of -2 V.

4.3 Fabrication of the LOCOS Photodetector

The device was fabricated using a SmartCut™ SOI (Silicon on Insulator) substrate, with a 1.5 µm thick silicon overlayer and a 1 µm thick buried oxide. The dielectric stack was formed by a thermally grown 50 nm thick SiO_2 layer and a deposited 80 nm thick LPCVD Si_3N_4 film. Optical lithography was used to pattern strips of 1.5, 2 and 2.5 µm width onto photoresist on the surface of the sample. A CF_4/O_2 plasma RIE etch was used to transfer this pattern to the Si_3N_4 layer and a hydrofluoric acid (HF) wet etch was used to transfer the pattern onto the thermally grown SiO_2 layer, producing the structure of Figure 4.6a.

Following removal of the photoresist, the sample underwent a wet oxidation at 1100 C to grow 430 nm of SiO_2. This consumed approximately 190 nm of silicon and provided a ridge with slab height of h = 1.3 µm, as shown in Figure 4.6b. An SEM cross-sectional image of the LOCOS waveguide at this stage in the process is shown as Figure 4.6c. Phosphoric acid heated to 70 C was used to remove the Si_3N_4 oxidation mask, and 10:1 buffered HF acid was used to remove the 50 nm layer below it.

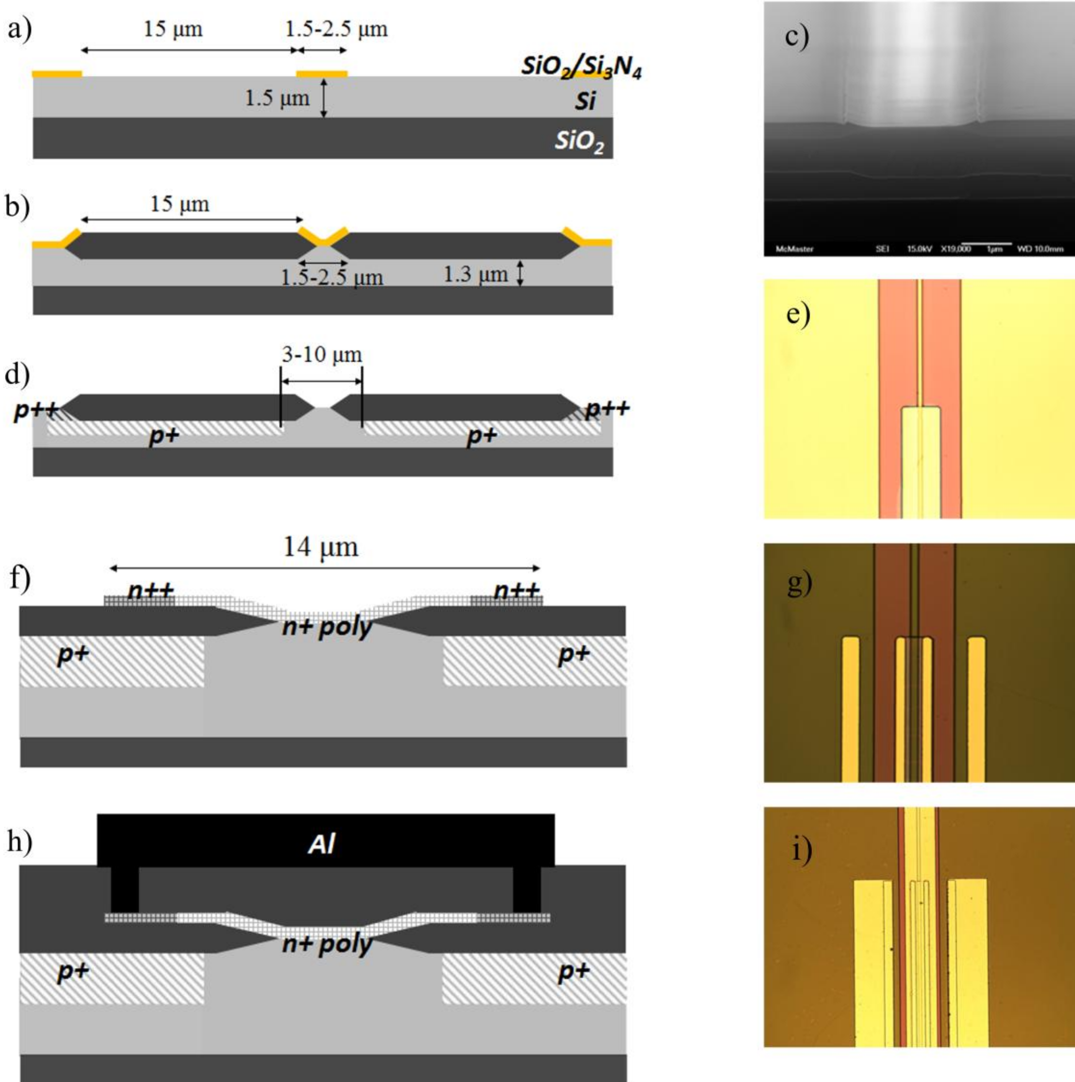

Figure 4.6: Cross-section and microscope images of photodiode at selected points in the process flow: a) following patterning of 50 nm SiO_2/80 nm Si_3N_4; b) following wet oxidation at 1100 C; c) SEM image of waveguide cross-section (with nitride remaining on top); d) following masked boron implant at 110 keV and 30 keV; e) following etch of amorphous silicon layer; f) following patterning and phosphorus implantation of LPCVD amorphous silicon; g) following etch of contact vias; h) and i) final device with aluminum contacts [20].

Photoresist windows for boron ion implantation were patterned using optical lithography, overlapping with the thermal oxide region and extending onto either side. An implantation of 110 keV boron ions at a dose of 4 x 10^{13} cm^{-2} doped the silicon region below the thermal oxide to a peak concentration of ~10^{18} cm^{-3}. A second shallow implantation of 30 keV boron ions with a dose of 10^{16} cm^{-2} doped only the silicon on the sides of the trench to a peak concentration of ~10^{20} cm^{-3}, forming the structure of Figure 4.6d.

The 100 nm amorphous silicon layer was then deposited using Low Pressure Chemical Vapour Deposition (LPCVD), and implanted with 25 keV phosphorus ions to a dose of 3 x 10^{12} cm^{-2}. Optical lithography was then used to pattern 14 μm strips centered on the waveguide, and an SF_6 plasma etch was used to transfer this pattern to the amorphous silicon layer. A microscope image of the device following the removal of the photoresist is shown as Figure 4.6e. A further photoresist mask was used to define a second phosphorus implant of 5 x 10^{14} cm^{-2} dose on the edges of the strip to provide a concentration of 5 x 10^{19} cm^{-3}, forming the structure of Figure 4.6f.

A 300 nm thick Plasma-Enhanced Chemical Vapour Deposition (PECVD) SiO_2 layer was deposited, and annealed in an N_2 ambient at 900 C for 30 minutes to crystallize the amorphous silicon and to break down the native oxide at the interface between the deposited silicon and the ridge. Optical lithography was used to open contact windows in photoresist to the poly-silicon on either side of the waveguide and to the p^{++} silicon on either side of the trench oxide. A CHF_3/Ar plasma was used to etch this pattern through the cap oxide, resulting in the device shown in Figure 4.6g. A 200 nm thick aluminum layer was deposited, and contacted the silicon in the regions where the oxide was etched. Photoresist was used to masked to define the contact pads, which were etched into the aluminum with standard aluminum wet etch (a commercial product having phosphoric acid as its main constituent), forming the final device structure of Figures 4.6h and 4.6i.

For the introduction of lattice defects, an implant of 4 MeV Si^{+} was used with a dose of 10^{13} cm^{-3}, masked by 4 μm thick photoresist.

4.4 Optical and Electrical Characterization

The devices were characterized in the method shown in the block diagram of Figure 4.7a. An ILX Lightwave laser (FOM system) operating at 1550 nm was end-fire coupled into the waveguide via a tapered fibre. The signal exiting the opposite waveguide facet was collected by a 40x objective and focused onto a Newport Fibre-optic detector, which provides a measure of the optical power.

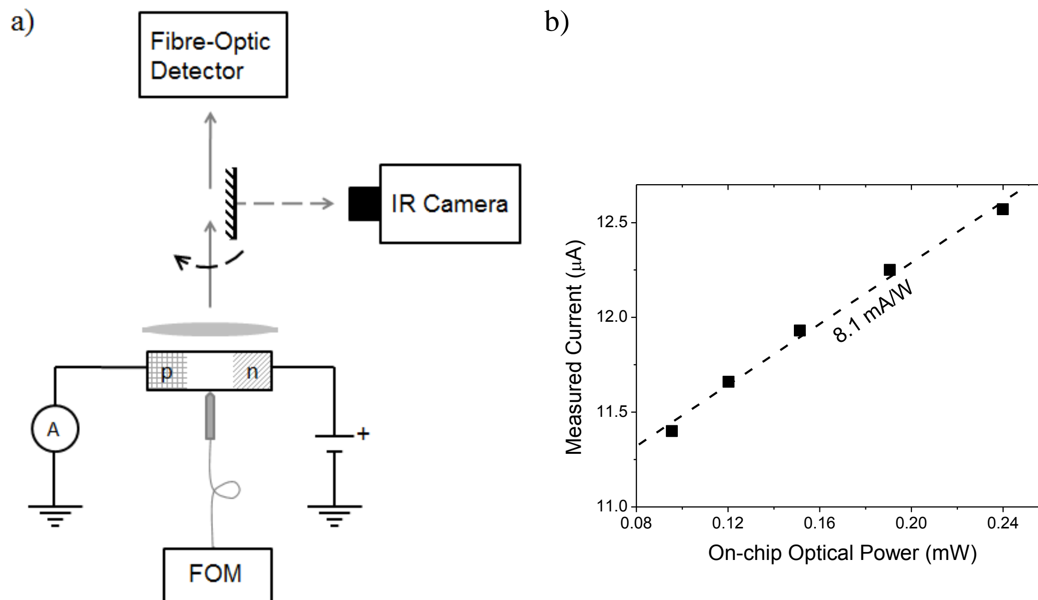

Figure 4.7: a) Schematic of set-up used to measure devices: 1550 nm CW source (FOM) is end-fire coupled into the reverse biased photodiode using a tapered fibre, the output is collected by an objective lens and focused on a fibre optic detector or (if the mirror is present) an IR camera, b) A typical plot of current vs. on-chip optical power, the slope of which is 8.1 mA/W (responsivity) and the intercept is 10.7 μA (the dark current).

From an analysis of the Fabry-Perot fringes of an un-implanted waveguide using a tuneable laser source, the transmission loss was extracted using Eq. (2.63) to be 2.9 ± 1.1 dB/cm (for the 2 μm waveguide width and TE polarization). The propagation loss was found to be largely dependent on polarization, consistent with previous work [21]. In this case, the propagation loss was 10.2 dB/cm larger for TM polarization.

By measuring the transmitted power from several undoped waveguides and subtracting the transmission loss, the total coupling loss was measured to be 20.4 ± 7.0 dB. Assuming symmetrical loss is sustained for in-coupling and out-coupling of light, the insertion loss was estimated to be 10.2 ± 3.5 dB. Thus, the on-chip optical power is approximated as being the laser output power less the insertion loss.

Tungsten probes of 1 μm tip radius probed the aluminum pads on the device, and were connected to a voltage supply and ammeter in series. The injected laser power and device bias were varied and the device current was measured on the ammeter. From a linear fit of measured current to injected optical power, the responsivity is obtained, as shown in Figure 4.7b.

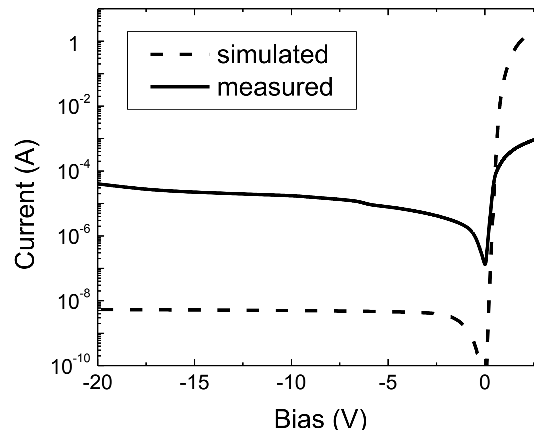

Figure 4.8: Simulated and measured IV curve of LOCOS device prior to Si^+ implantation [20].

The measured and simulated (by ATLAS) current-voltage (*I-V*) curve of the fabricated device is shown in Figure 4.8. The reverse saturation current is markedly larger in the fabricated device, and the forward bias characteristic is softened.

4.5 Results and Discussion

4.5.1 Post-implantation annealing

The responsivity and excess optical absorption were measured using the set-up of Figure 4.7a following isochronous anneals at temperatures between 200 and 450 C. The measured responsivity is plotted as a function of measured absorption in Figure 4.9 (data points) for a 6 mm long device, with a 1.5 μm wide waveguide, 10 μm separation between the edges of the boron implant, and 5 μm wide Si^+ implant window. As described in chapter 3, the excess optical absorption α_t was determined via Eq. (3.7) to estimate the defect concentration N_t at each annealing stage. This in turn was used to simulate the responsivity for this device geometry in ATLAS, which is also plotted as the solid curve in Figure 4.9. The characteristic curve described in chapter 3 is evident, and there is a general agreement on its shape between measurement and simulation. The peak responsivity is calculated to be approximately 47 mA/W, and occurs for an excess loss of 20 dB/cm (or 12 dB), or equivalently $N_t = 3.5 \times 10^{17}$ cm^{-3}.

Despite the reasonable prediction of the defect concentration that provides maximum response, the simulated photocurrent exceeds the measured values by nearly an order of magnitude. This is likely caused by the complexities associated with the poly-silicon contact. For instance, the defect states present in the grain boundaries and the interface with the silicon ridge have associated capture properties that were not taken into account in the simulation model. As a result, the measured diode characteristic of Figure 4.8 is much less ideal than the simulated curve. The defects in the poly-silicon both serve to capture carriers in forward bias and to generate carriers in reverse bias, as evidenced

by the low forward current and high reverse saturation current respectively. In addition, these centers inhibit the extraction of optically generated carriers and therefore reduce photocurrent.

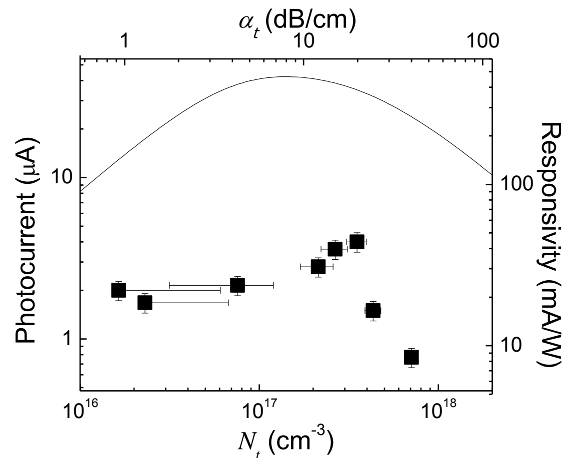

Figure 4.9: Measured (data points) photocurrent (left axis) and responsivity (right axis) vs. excess absorption (top axis) and N_t (bottom axis) for a device with W_b = 1.5 µm, p^+ separation = 10 µm, L = 6 mm and 5 µm wide Si^+ implant window; simulated result using methods of chapter 2 is shown as a curve [20].

A measurement of the influence of dark current on the noise properties of the photodiode is the noise equivalent power (*NEP*) defined by Eq. (2.56), which represents the minimum optical power that can be detected in 1 Hz of receiver bandwidth. From the simulated responsivity and reverse saturation (dark) current, an *NEP* of $2.3 \pm 0.6 \times 10^{-13}$ W/Hz$^{1/2}$ is calculated at -20 V bias following the 300 C anneal stage. In the fabricated device, the calculated *NEP* increases to $1.7 \pm 0.5 \times 10^{-10}$ W/Hz$^{1/2}$, for the same conditions. The combination of increased reverse saturation (dark) current and weakened carrier extraction limits therefore significantly degrades the noise performance of the photodetector.

4.5.2 *Position of boron doped regions*

The influence of the proximity of the doped regions to the optical mode was discussed in chapter 3 (Figure 3.7). Figure 4.10 plots the measured photocurrent as a function of p^+ region separation for waveguide widths of W_b = 1.5 and 2 μm, as well as a simulated responsivity assuming $N_t = 10^{17}$ cm^{-3}. For this device structure, there is a more modest increase in photocurrent as the p^+ region separation is reduced. The modeling predicts that the strongest electric field components are in the region of the poly-silicon/silicon interface, and therefore an enhanced depletion surrounding the p^+ regions is not strongly beneficial to the device performance. For separations below 5 μm, a decrease in photocurrent is observed, caused by the enhanced free-carrier absorption of the optical mode overlapping with the doped region.

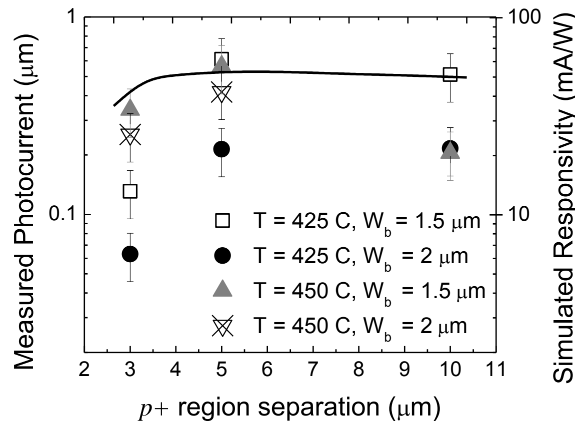

Figure 4.10: Measured photocurrent for several devices of similar geometry and annealing temperature and varying p^+ region separation (data points, left axis), and simulated responsivity for a device with W_b =1.5 μm and $N_t = 10^{17}$ cm^{-3} (right axis) [20].

4.5.3 *Width of the Si^+ implant window*

The predicted enhancement in photocurrent through the narrowing of the inert Si^+ implantation region described in chapter 3 (Figure 3.7) was also observed for the LOCOS

structure. The width of the implant, determined by the width of the window in the photoresist used to mask the implantation, was varied from 3 to 10 μm. Figure 4.11 plots the simulated responsivity curves for three implant widths. As the implant window is narrowed, the peak responsivity is shifted towards larger defect concentrations. This is caused by the removal of the recombination centers lying outside of the modal region that do not generate carriers but do limit their extraction. This causes the total photocurrent to increase, and allows for a larger concentration of generating centers to be present. The inset of Figure 4.11 plots the photocurrent for three nominally identical photodiodes at a single annealing stage, with three Si^{+} implant window widths. There is an evident enhancement in the performance of the device with a 3 μm wide implant window, which is comparable to the 3.4 μm FWHM of the optical mode distribution.

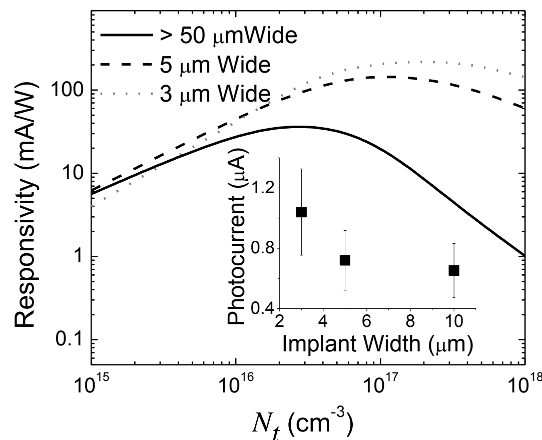

Figure 4.11: Simulated responsivity vs. defect concentration for implant window widths of 3 μm, 5 μm and > 50 μm; inset: measured photocurrent vs. implant window width for devices with L = 6 mm, 10 μm p^{+} region separation, bias = -10 V [20].

4.5.4 Influence of amorphous silicon deposition method

The excessive dark current (>1 μA) of the photodetectors, due mainly to the defects present in the poly-silicon, place a severe limit on the minimum detectable power. The effort to maximize the grain size in the design of the poly-silicon deposition process

was done with this in mind. To further study the importance of poly-silicon quality, a set of devices were fabricated using PECVD amorphous silicon rather than LPCVD amorphous silicon. The phosphorus dose required to dope the film to a uniform concentration of 3 x 10^{17} cm^{-3} was found to be a factor of 10 larger for the PECVD devices than it was for the LPCVD devices. The PECVD devices were observed to produce similar responsivities to the LPCVD devices of the previous sections. However, the dark current of the PECVD devices was much larger, as indicated in Figure 4.12. Here the dark current at -5 V bias is plotted as a function of annealing temperature for LPCVD and PECVD devices of the same geometry. The deposition conditions strongly affect the defect content, which is the principle cause of dark current from thermal carrier generation, as well as the density of grain boundaries. In particular, a PECVD film is known to have higher hydrogen content than LPCVD, which is retained in the crystallized film [22]. In both devices, the dark current is reduced by the Si^+ ion implantation, and approaches its pre-implanted value with annealing.

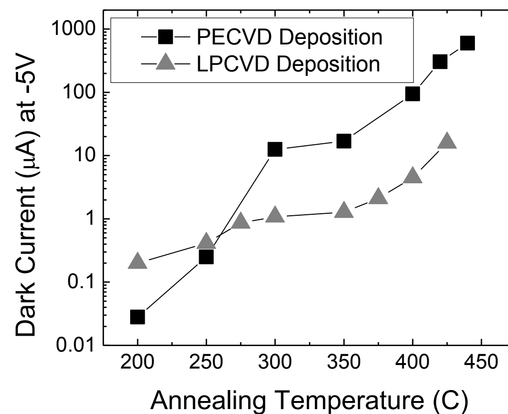

Figure 4.12: Dark current measured at -5 V bias for nominally identical samples (W_b = 2.5 µm, p^+ region separation = 10 µm, L = 3 mm, final Si^+ implant at 4 MeV and 10^{13} cm^{-2} dose in a 10 µm wide window), but having amorphous silicon deposited using different deposition techniques, measured following anneals at increasing temperature [20].

4.5.5 *Influence of the Si^+ implantation dose*

The reduction of dark current with ion implantation is incentive for the use of higher Si^+ implantation doses in the final processing stage. The presence of agglomerated interstitial defects that remain after anneals approaching 500 C has been shown to facilitate efficient photodetection, as described in section 1.4 [23]. Increasing the Si^+ dose leads to an increase in the concentration of such defects, leading to the anticipated decrease in dark current as well as a new mechanism for carrier generation.

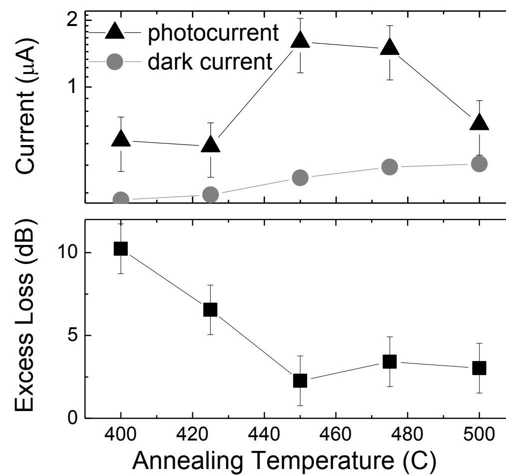

Figure 4.13: Photocurrent and Dark current at -20 V bias following anneals from 400 C to 500 C, for a waveguide with W_b = 1.5 μm, 10 μm p^+ separation, and a Si^+ implant window width of 10 μm [20].

The dose of the 4 MeV Si^+ implantation was increased to 5 x 10^{13} cm^{-2} for a LPCVD device, which was subsequently annealed at 400 – 500 C. Figure 4.13 plots the photocurrent, dark current and excess absorption for each annealing stage. The dark current was found to be greatly reduced over the values in Figure 4.12. However, the photocurrent was found to be much smaller, and a larger bias was required to achieve responsivities larger than 10 mA/W. It is significant, however, that the excess loss is also greatly reduced, which lends this design to power monitoring applications. For example,

the peak responsivity is 18 mA/W after the 450 C anneal, while the excess loss is 2.3 ± 1.5 dB. Thus, while the photocurrent has been sacrificed, the effective quantum efficiency of 3.5% is comparable with the previous devices, and has been achieved with a dark current of 400 nA.

4.6 Summary

This chapter described the application of the model of the chapter 3 to the design of a novel defect-enhanced photodetector structure. The photodiode was integrated onto a LOCOS-type waveguide, using a self-aligned thin polysilicon film to electrically contact the top of the waveguide. Consequently, this structure provides a geometry for photo-generated charge carrier extraction that is more efficient than the alternative designs described in chapter 3.

The formation of the device design and fabrication process using commercial software was described. The final device produced characteristic results that agreed well with the model, although it suffered from a large dark current and a low absolute responsivity. Several methods are suggested to improve the responsivity, including geometry modifications and larger Si^{+} implant dose.

References

[1] "ATHENA User's Manual," Silvaco International, March 2011.

[2] L. K. Rowe, M. Elsey, N. G. Tarr, A. P. Knights, and E. Post, "CMOS-compatible optical rib waveguides defined by local oxidation of silicon." *Electronics Letters*, vol. 43, pp. 392-393, 2007.

[3] O. Powell, "Single-mode condition for silicon rib waveguides." *J. Lightwave Tech.*, vol. 20, pp. 1851-1855, 2002.

[4] "RSoft BeamPROP version 8.1 User Guide," www.rsoftdesign.com, RSoft Design Group, Inc., Ossining, NY.

[5] W. B. Jackson, N. M. Johnson, and D. K. Biegelsen, "Density of gap states of silicon grain boundaries determined by optical absorption," *Appl. Phys. Lett*., vol. 43, pp. 195-197, 1983.

[6] A. Säynätjoki, J. Riikonen, H. Lipsanen, "Optical waveguides on polysilicon-on-insulator," *Journal of Materials Science: Materials in Electronics*, vol. 14, pp. 417-420, 2003.

[7]]Y. Laghla, and E. Scheid, "Optical study of undoped, B or P-doped polysilicon," *Thin Solid Films*, vol. 306, pp. 67-73, 1997.

[8] G. Harbeke, L. Krausbauer, E. F. Steigmeier, A. E. Widmer, H. F. Kappert, and G. Neugebauer, "Growth and physical properties of LPCVD polycrystalline silicon films," *J. Electrochem. Soc.: Solid-state Science and Technology*, vol. 131, pp. 657-682, 1984.

[9] M. Gartner, M. Modreanu, C. Cobianu, R. Gavrila, M. Danila, "Microstructural information from optical properties of LPCVD silicon films annealed at low temperature," *Sensors and Actuators A*, vol. 99, pp. 160-164, 2002.

[10] T. Matsuura, J. Murota, N. Mikoshiba, I. Kawashima, and T. Sawai. "Diffusion of As, P, and B from doped polysilicon through thin SiO_2 films into Si substrates," *J. Electrochem. Soc.*, vol. 138, pp. 3474-3480, 1991.

[11] D. Waechter and N. G. Tarr, "Low-temperature crystallization of *in situ* phosphorus-doped low-pressure chemical-vapour deposited amorphous silicon," *Canadian Journal of Applied Physics*, vol. 65, pp. 1030-1032, 1987.

[12] H. Y. Park, C. Park, B. Hwang, S. G. Lee, B. O, E. Lee, S. Park, "Transmittance characteristics of buckled fabry-perot tunable filter with membrane structure," *Optical Review*, vol. 12, pp. 472-475, 2005.

[13] G. F. MacKay, B. M. Manning, and N. G. Tarr "Rapid thermal annealing of in situ phosphorus-doped polysilicon emitters," *Can. J. Phys*., vol. 70, pp. 1109-1111, 1992.

[14] S. P. Murarka, "Phosphorus out-diffusion during high temperature anneal of phosphorus-doped polycrystalline silicon SiO_2," *J. Appl. Phys.*, vol. 56, pp. 2225-2230, 1984.

[15] D. Krüger, P. Gaworzewski, R. Kurps, and J. Schlote, "Phosphorus segregation at polysilicon-silicon interfaces from in situ P spike-doped silicon films," *Semicond. Sci. Technol.* vol. 10, pp. 326-331, 1995.

[16] G. L. Patton, J. C. Bravman, and J. D. Plummer, "Physics, Technology and Modeling of Polysilicon Emitter Contacts for VLSI Bipolar Transistors," *IEEE Transactions on Electron Devices*, vol. ED-33, pp. 1754-1768, 1986.

[17] Y. Liu *et al.*, "In-line channel power monitor based on Helium ion implantationin silicon-on-insulator waveguides," *IEEE Photon. Technol.Lett.*, vol. 18, pp. 1882–1884, Sep. 2006.

[18] A. P. Knights, J. D. B. Bradley, S. H. Gou, and P. E. Jessop, "Silicon-on-insulator waveguide photodetector with self-ion-implantation-engineered-enhanced infrared response," *J. Vac. Sci. Technol.,* vol. A 24, pp. 783-786, 2006.

[19] M. W. Geis *et al.*, "CMOS-compatible all-Si high-speed waveguide photodiodes with high responsivity in near-infrared communication band," *IEEE Photon. Technol. Lett.*, vol. 19, pp. 152–154, Feb. 2007.

[20] D. F. Logan, A. P. Knights, P. E. Jessop, and N. G. Tarr, "Defect-enhanced photo-detection at 1550 nm in a silicon waveguide formed via LOCOS," *Semicond. Sci. Technol.* vol. 26, p. 045009, 2011.

[21] R. Pafchek, R. Tummidi, J. Li, M. A. Webster, E. Chen, and T. L. Koch, "Low-loss silicon-on-insulator shallow-ridge TE and TM waveguides formed using thermal oxidation." *Applied Optics*, vol. 48, pp. 958-963, 2009.

[22] M. H. Brodsky, M. Cardona, and J. J. Cuomo, "Infrared and Raman spectra of the silicon-hydrogen bonds in amorphous silicon prepared by glow discharge and sputtering," *Phys. Rev. B*, vol. 16, pp. 3556-3571, 1977.

[23] M. W. Geis, S. J. Spector, M. E. Grein, R. T. Schulein, J. U. Yoon, D. M. Lennon, C. M. Wynn, S. T. Palmacci, F. Gan, F. X. Kärtner, and T. M. Lyszczarz, "All silicon infrared photodiodes: photo response and effects of processing temperature," *Optics Express,* vol. 15, pp. 16886-168895, 2007.

Chapter 5: Sub-micron Photodetector Structures

5.1 Overview

The efficient extraction of photo-generated charge carriers is best achieved by utilizing small waveguide structures, such as the design of Geis *et al*. described in chapter 3. That structure, shown in Figure 5.1a, features lightly doped regions along the waveguide sidewall, which ensure that the electric field formed in reverse bias is confined to the waveguide [1]. This is illustrated in the ATLAS model, pictured in Figure 5.1b, where the potential drop from a 5 V reverse bias occurs entirely over the intrinsic region of the waveguide. A simplified structure, shown in Figure 5.2a, does not include doping along the sidewall. The consequence of this is that moderate reverse bias primarily generates an electric field in the 50 nm thick slab region on either side of the waveguide, and much higher biases are required to generate a large electric field within the waveguide channel. This is again illustrated in Figure 5.2b using the ATLAS model, where of the 5 V reverse bias applied, only approximately 2 V of that potential is dropped across the waveguide. Using the photodetector model of chapter 3, it is predicted that the structure of Figure 5.1 has a peak responsivity[6] that is 2.75 times larger than the structure of Figure 5.2, at 5 V reverse bias and 1 mm length.

[6] Peak responsivity refers to that at the optimum defect concentration, which in this case is 10^{18} cm^{-3} for the device in Figure 5.1 and 5 x 10^{17} cm^{-3} for the device in Figure 5.2.

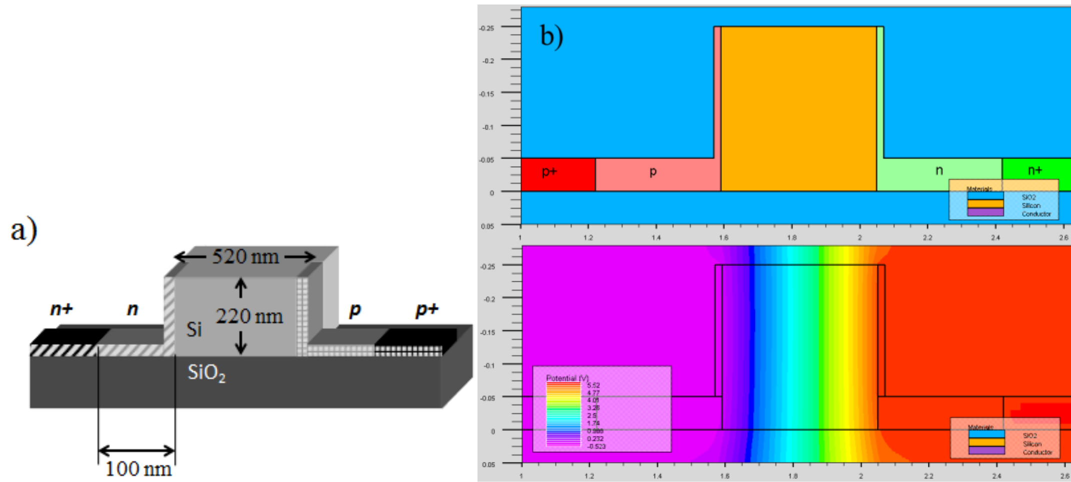

Figure 5.1: a) Cross-section of the sub-micron photodetector fabricated by Geis *et al.* [1], featuring a 520 nm wide waveguide with doped sidewalls, b) ATLAS model output illustrating the device structure layout (above) and the potential distribution upon the application of a 5 V reverse bias (below).

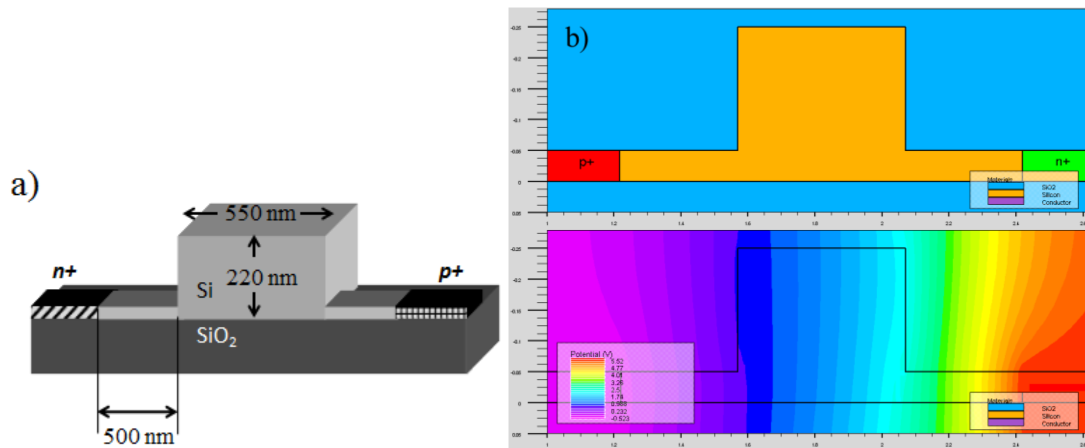

Figure 5.2: a) Cross-section of sub-micron photodetector whose fabrication is described within this chapter, b) ATLAS model output illustrating the device structure layout (above) and the potential distribution upon the application of a 5 V reverse bias (below).

Due to the complexities inherent to the fabrication the structure of Figure 5.1, it was decided that the first attempts at developing a sub-micron photodetector would follow the design of Figure 5.2. This chapter details the fabrication of this device structure using the tools at the James Watt Nanofabrication Centre and discusses its measured characteristics.

5.2 Details of Device Fabrication

The sub-micron feature sizes and alignment required by the structures in Figures 5.1 and 5.2 cannot be obtained using the optical lithography tools available in CEDT facilities at McMaster University. These requirements can be met using electron-beam (e-beam) lithography, which is a serial process where a focused electron beam scans the sample surface to expose a pattern into polymer resist. In the current case, this device fabrication was carried out at the James Watt Nanofabrication Centre at the University of Glasgow [2], using the Vistec VB6 E-beam lithography tool to define the waveguides and the dopant windows.

Electron-beam lithography provides pattern definition with much better resolution than traditional optical lithography, for which the minimum feature size is limited by diffraction effects [3]. On the other hand, the serial nature of the e-beam writing process makes it much more time-consuming than optical lithography, and therefore only feasible for low wafer throughput.

An input data file specifies the pattern layout as well as the beam spot size, the beam step size, and the dose. The VB6 tool has several calibrated beam diameters, the smallest of which is 4 nm [2]. The step size is selected to be slightly smaller than the beam spot size, so that as the beam is stepped in a line, the patterns overlap sufficiently to form smooth edges, as shown in Figure 5.3a. Similar to optical lithography, the exposure is controlled by a ‘dose’, which is a measure of the electrons arriving at the sample per

unit area. Being a serial process, as the beam size is reduced or the dose is increased, the time required for writing increases.

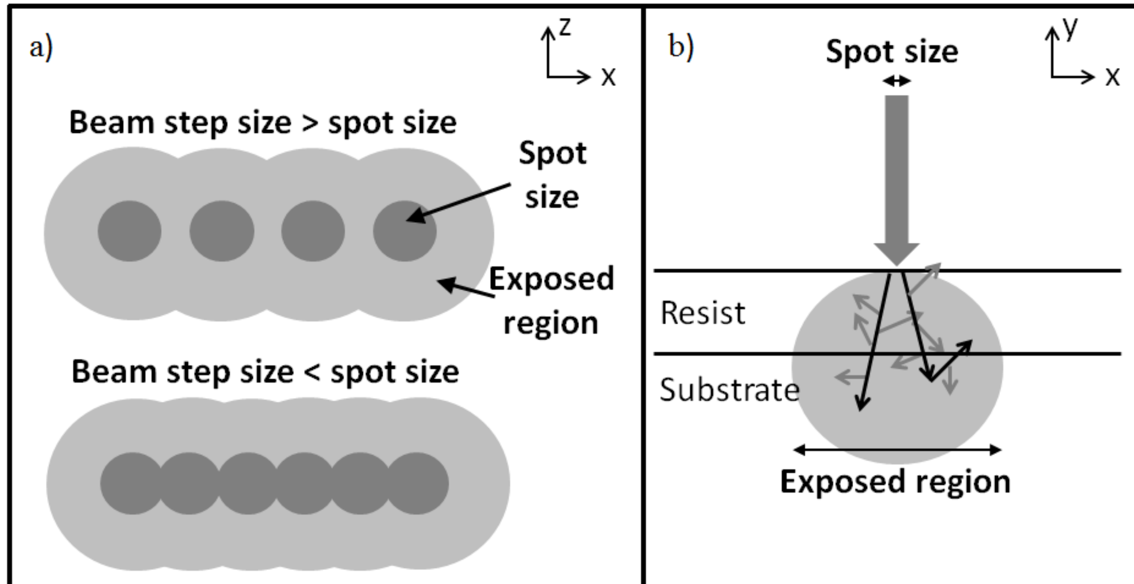

Figure 5.3: a) Illustration of serial process of stepping the electron beam along a line, where reducing the step size produces less rippled edges; b) Diagram of the electron scattering within electron beam resist during exposure, illustrating the primary electron scattering (black arrows) and secondary electrons (grey arrows) [4].

When an electron is incident on the resist, it deflects and causes the emission of secondary electrons which scatter within the resist as shown in Figure 5.3b. It is beneficial to use a high energy beam (the VB6 uses an electron beam energy of 100 keV) and thin resist layer, as this minimizes the lateral scattering of electrons. This lateral scattering of secondary electrons within the resist is the main determinant of resolution, as the exposed region is the convolution of the electron beam profile and the point spread function [4]. As a result, closely spaced features will be overexposed (and therefore larger or smaller than designed), a phenomenon known as the *Proximity Effect*. The dose may be adjusted to vary across the pattern to compensate for the expected overlap in exposure using methods called *Proximity Corrections* [4]. The beam writes one square 'field' of

the sample at a time before the stage must be moved, and it is typically at the edge of a field that discontinuities in patterns can occur. These resulting '*stitching errors'* are limited to approximately 20 nm in the VB6 [2]. It is therefore important to design the layout such that the critical features are contained within fields. In the present case, field sizes were 1.25 x 1.25 mm.

Similar to optical lithography, several different process layers of e-beam exposures can be aligned to one another using alignment markers defined in the first process stage. To provide high contrast in an electron beam image, these markers can be formed of deeply etched structures or with deposited material that has a large atomic number contrast with silicon. In this case, the markers were a series of deeply etched 50 x 50 μm squares located in four corners of the sample. The VB6 e-beam writer is automated to locate these markers and register the sample's position and orientation accordingly, a process that has demonstrated an alignment of features to 0.46 nm [2].

The waveguides were written in HSQ negative e-beam resist. The resist, formed of FOX 16 (Flowable Oxide) diluted with MIBK (Methyl Isobutyl Ketone) in a 1:1 mixture, was spun on at 3000 rpm for 30 seconds. It was then baked at 90 C for 2 minutes, forming a thickness of approximately 320 nm. The 550 nm wide waveguide pattern was then written by the VB6 using a beam spot size of 6 nm and a beam step size of 5 nm. The pattern was then developed in neat TMAH (Tetramethylammonium Hydroxide) held at 22 C for 30 seconds, followed by a rinse in DI water for 60 seconds, and Isopropanol for 30 seconds. The structure is then etched in an SF_6/C_4F_8 ICP-RIE plasma for approximately 90 seconds, to remove approximately 150 nm of the 220 nm Silicon overlayer thickness. The resulting structure is shown in both schematic and SEM form in Figure 5.4.

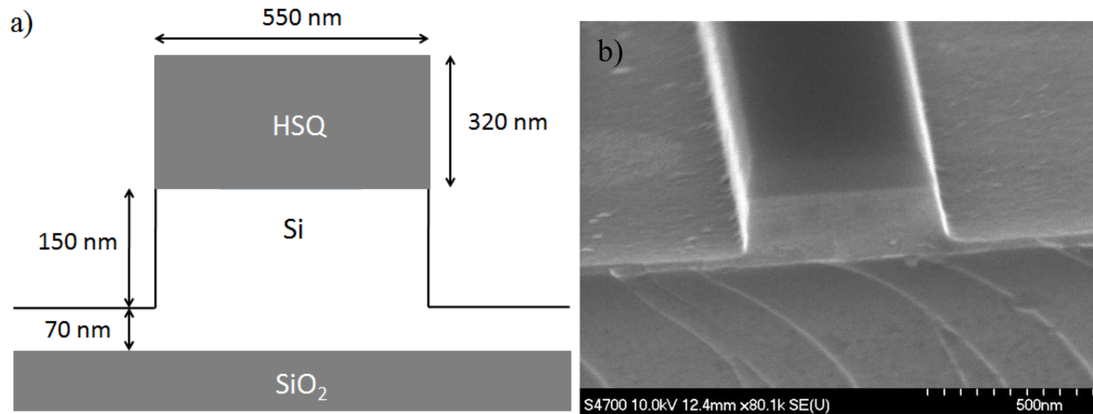

Figure 5.4: a) Schematic of etched waveguide cross-section; b) SEM of waveguide cross-section following the dry etch step.

To ensure the correct etch depth, an interferometer was used to monitor the silicon overlayer thickness throughout the etch process. This device consists of a camera and a HeNe (Helium-Neon) laser, which were directed downwards into the etch chamber and focused onto the sample surface. The reflected intensity of the laser was measured as a function of time, and the intensity varied due to interference from the silicon film etalon, as in Figure 5.5a. The reflection from the silicon film oscillates with a period which corresponds to a silicon layer thickness reduction of:

$$\Delta t = \frac{\lambda}{2n} \tag{5.1}$$,

where λ is the wavelength of the HeNe laser (633 nm) and n is the refractive index of silicon at this wavelength (approximately 3.9) [5].

As the silicon is etched, the thickness t decreases, and the reflected intensity forms the interference pattern of Figure 5.5b. One can terminate the etch process at the appropriate point on this pattern, in this case indicated as 150 nm, and be certain of a controlled etch depth. This is a crucial tool, since in practice the etch rate is not consistent between runs, and has been observed to vary by up to 15%.

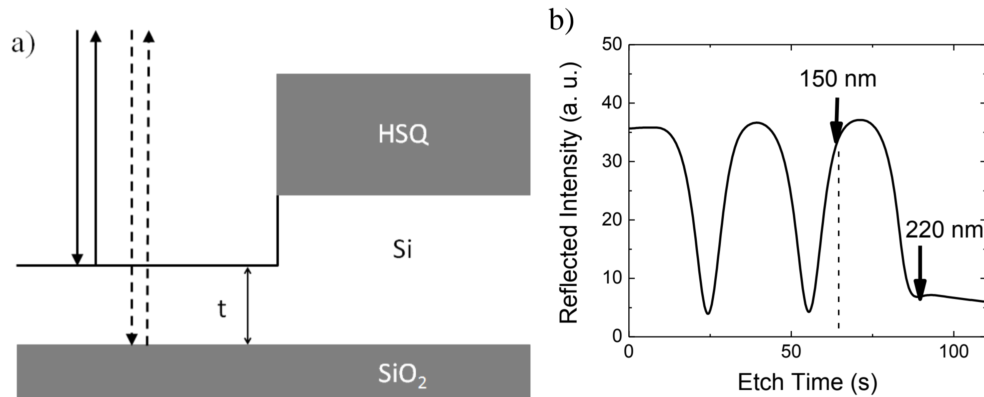

Figure 5.5: a) Diagram of masked SOI during the ICP-RIE etch process, with HeNe laser reflected off of thin film surface, b) The resulting fringe pattern measured throughout the etch process, indicating the point of etch termination required to leave a *t* = 70 nm slab region, and the point where the 220 nm overlayer is completely etched.

Following the etch process, the sample underwent a dry thermal oxidation at 1000 C for one hour to grow 50 nm of SiO_2, consuming roughly 22 nm of the Silicon slab region. The HSQ above the waveguide is baked in the process, forming the thick oxide cap shown in the cross-section of Figure 5.6.

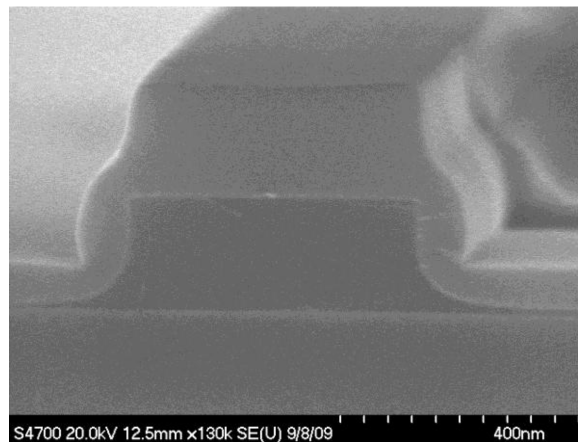

Figure 5.6: SEM image of the waveguide cross-section following oxidation.

The devices were then masked with a dual layer of PMMA (Poly(methyl methacrylate)) positive e-beam resist to form the boron implant window. The first layer of 535 nm thickness was formed by spinning 12% PMMA at 5000 rpm for 1 minute and baking for 20 minutes at 180 C. An additional 125 nm layer was formed by spinning 4% PMMA at 5000 rpm for 1 minute and baking for 40 minutes at 180 C. The VB6 was then used to write the boron implant window adjacent to the waveguide edge, with a beam size of 19 nm and a beam step size of 12.5 nm. The sample was then developed in MIBK (diluted with isopropanol in a 1:1 ratio) for 30 seconds, followed by an isopropanol rinse. The resulting implant window, aligned 500 nm from the waveguide edge, is shown in the optical microscope image of Figure 5.7a.

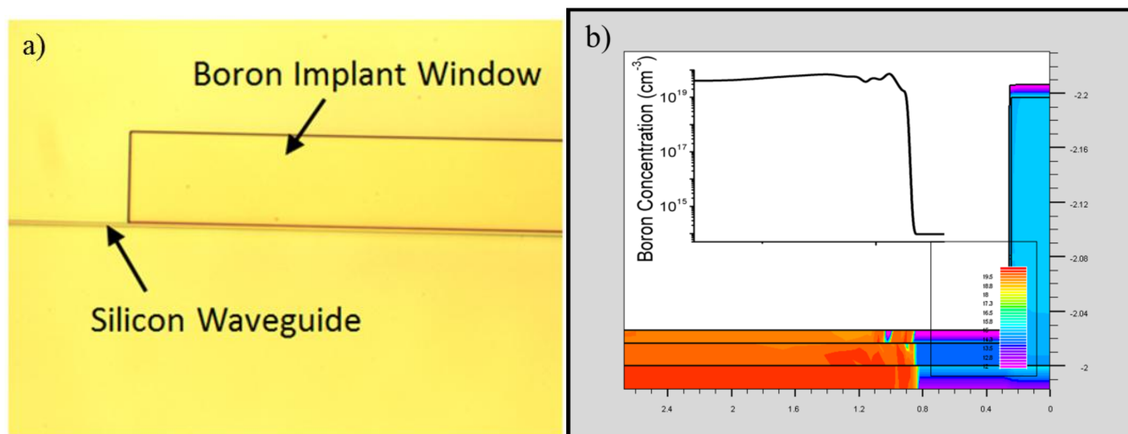

Figure 5.7: a) Optical microscope image of silicon waveguide after being masked for the boron implant; PMMA covers the entire sample save for the rectangular box labelled 'Boron Implant Window', b) ATHENA simulation of one half of the waveguide following the 10 keV boron implantation of 6 x 10^{14} cm^{-2} dose and removal of the PMMA.

The commercial simulation tool, ATHENA [6], was used to select the boron implant energy of 10 keV and dose of 6 x 10^{14} cm^{-2}, required to achieve a final concentration of 5 x 10^{19} cm^{-3} in the slab region, as pictured in Figure 5.7b. The 660 nm

thick PMMA layer is sufficient to block the ions in the other regions. Following implantation, the PMMA layer is removed in acetone.

Similarly, the phosphorus implant window was formed using the dual layer of PMMA, and was written and developed identically to the previous boron step. The resulting mask image is shown in Figure 5.8a, where the preceding boron implant has caused some visible discolouration on the other side of the waveguide, likely due to damage of the thin oxide. ATHENA was again used to select the phosphorus energy of 40 keV and dose of 3 x 10^{14} cm^{-2} required to achieve a final concentration of 5 x 10^{19} cm^{-3}. The resulting modeled structure is shown in Figure 5.8b.

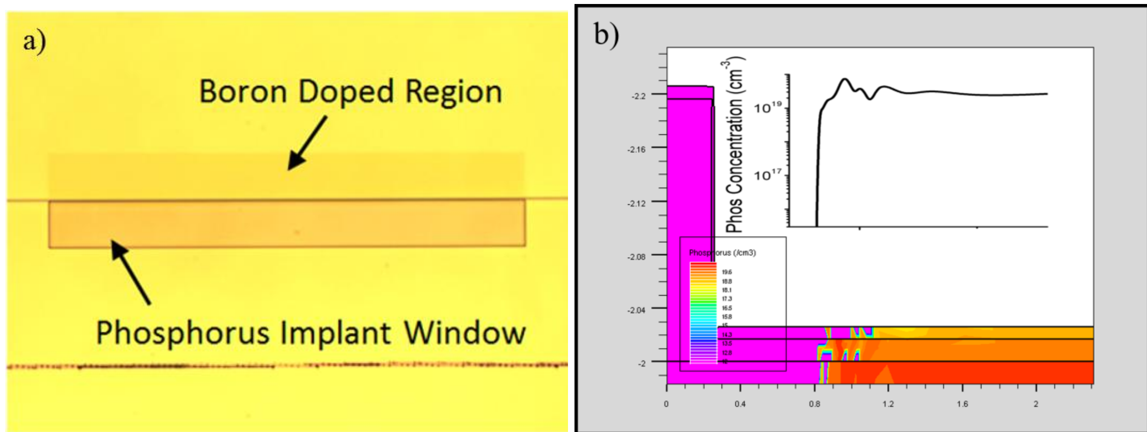

Figure 5.8: a) Optical microscope image the silicon waveguide after being masked for the phosphorus implant in PMMA, with some visible discolouration due to the previous boron implant visible on the opposite side of the waveguide, b) ATHENA simulation of one half of the waveguide following the 40 keV phosphorus implantation of 3 x 10^{14} cm^{-2} dose.

The devices were then covered with a 400 nm deposited oxide layer using Plasma-Enhanced Chemical Vapour Deposition (PECVD) and subjected to a 1000 C anneal in an N_2 ambient for 1 minute to activate the dopants. The ohmic contacts were then formed using optical lithography. Shipley S1818 photoresist was spun on at 4000 rpm for 30 seconds and baked at 100 C for 1 minute. The contact via pattern was exposed in a SuSS MA6 Mask Aligner at 30 mJ/cm^2, and developed in Microposit MF-319

developer for 70 seconds. This pattern was then etched through the oxide layer using a CHF_3 RIE process. The photoresist was then removed in acetone and the device was cleaned in isopropanol. A second layer of S1818 photoresist was spun on and baked identically to the first. The aluminum contact pattern was exposed and developed, forming the pattern indicated on the left of Figure 5.9. A 300 nm aluminum layer was evaporated onto the sample using a Plassys system, contacting the sample only in the regions where the photoresist was removed, as shown in the middle diagram of Figure 5.9. The sample was put into acetone held at 50 C for 3 hours to remove the S1818 photoresist, consequently causing the aluminum above it to 'lift-off'. This leaves the structure on the right of Figure 5.9, with a patterned aluminum contact formed without requiring an etch processing step.

Figure 5.9: 'Lift-off' process of forming patterned Aluminum contact on doped region adjacent to waveguide edge (half of the waveguide cross-section is shown here for illustration): Photoresist development of pattern (left), aluminum deposition (middle), and 'lift-off' of photoresist and Aluminum coating in warm acetone (right).

The aluminum contacts were then sintered with a 450 C anneal for 1 minute. The final via and aluminum pad position surrounding the waveguide is shown in Figure 5.10a. Photodiodes were fabricated in lengths of 0.2, 0.6, 1, 2, 3, 5, and 8 mm. The current-voltage (*I*-*V*) curves for all device lengths are shown in Figure 5.10b, indicating a forward

resistance of 6.5 ± 1.7 Ωcm (at a 1 V operating point) and a reverse saturation current of 27 ± 6 nA/cm (at -2 V).

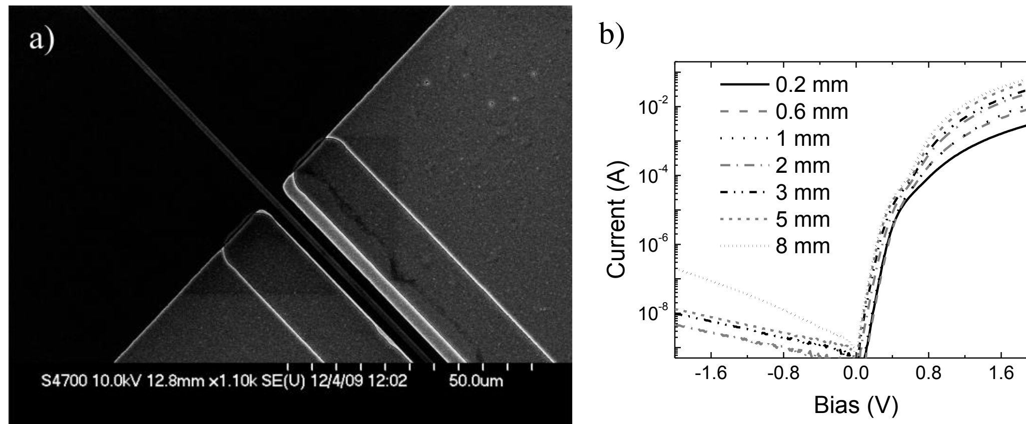

Figure 5.10: a) SEM of silicon waveguide at the end of a fabricated *p-i-n* junction, with vias patterned along each side and wide Al contacts on each side; b) Measured *I-V* curves of seven different *p-i-n* junction lengths following anneal at 450 C.

A final optical lithography stage was used to open windows in Shipley S1818 photoresist for a 200 keV Si^+ implant of 10^{13} cm^{-2} dose. These windows were 50 μm wide and had a length equal to that of the *p-i-n* diode.

5.3 Electrical and Optical Characterization

The *I-V* curve was measured for each device following the Si^+ implantation, and following 5 minute anneals at temperatures between 200 and 375 C. Figure 5.11a plots the *I-V* curve of a 3 mm device before and immediately after the 10^{13} cm^{-2} Si^+ implantation, and following 5 minute anneals at 275 C and 350 C. Following the implant but prior to annealing, both the forward bias resistance and the reverse saturation current are increased. This is largely improved as the device is annealed at temperatures approaching 375 C. Figure 5.11b plots the current at -2 V and 2 V following each

annealing stage. For temperatures in the range of 325-375 C, a significant recovery of the pre-implanted electrical characteristics is observed.

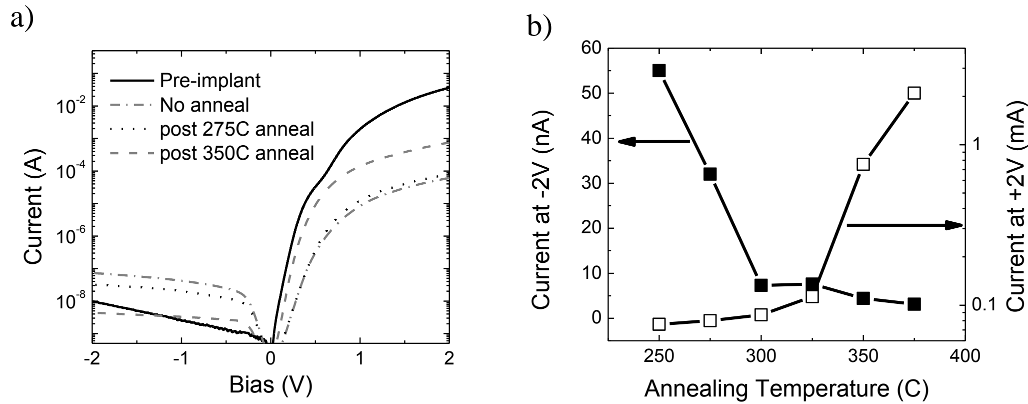

Figure 5.11: a) *I-V* curve of a 3 mm long *p-i-n* diode before implantation, following implantation, and following 5 minute anneals in N_2 at 275 C and 350 C; b) Evolution of current at -2 V (left axis) and +2 V (right axis) bias with annealing temperature.

In addition to the *I-V* curve, the capacitance was also measured. From measurements of capacitance from *p-i-n* diodes of length 0.6, 3, and 8 mm, the capacitance per unit length was measured to be 123 ± 29 pF/cm.

The waveguide facets were formed by thinning the substrate and cleaving as described in section 2.1.2. Light was coupled into the waveguide from an Anritsu Photonetics Tunable laser source using a single mode tapered fibre. The transmitted light was focused by an objective lens onto an Infra-Red (IR) camera or an InGaAs amplified photodiode. This focused light was modulated in free space at 300 Hz using a mechanical chopper wheel. The photodiode output was connected to a lock-in amplifier, using the chopper frequency as a reference. The lock-in signal therefore was a measure of the transmitted intensity, and was acquired by a LabVIEW program as a function of the input wavelength. In this way, the optical transmission spectra were measured, and featured the

Fabry-Perot effect described in section 2.4.1. From an analysis of the fringes, the propagation loss was estimated by Eq. (2.63) to be 2.6 ± 0.8 dB/cm.

To overcome the difficulties in coupling light into a 500 x 220 nm waveguide, 5 μm wide waveguides were fabricated between each device for testing purposes. The coupling procedure involves first aligning the tapered fibre to the wide waveguide, which produces a much more intense and easily visible optical mode, allowing for the fibre's height to be set. The fibre is then translated along the device edge to couple into the smaller 500 nm wide waveguide. Also, due to the inherent losses in butt-coupling to such a small waveguide cross-section, the coupling loss was estimated to be 14.8 ± 3.2 dB per facet. This was estimated by measuring the output optical power from several passive waveguides with an input of 1 mW, and halving the extracted loss (i.e. assuming each facet sustains equal loss).

5.4 Photodetector Characterization

5.4.1 Photodetector response vs. annealing

The photocurrent was measured for various applied reverse biases following 5 minute anneals at temperatures ranging from 200 C to 375 C. The unannealed sample was subjected to a 150 C ambient during the cleaving process, and so is associated with that temperature in the following data. A plot of photocurrent vs. annealing temperature for a 600 μm long device is shown in Figure 5.12, measured with an on-chip optical power of 115 ± 25 μW. The corresponding responsivity is plotted on the right axis, which has a peak value at 20 V reverse bias of approximately 490 mA/W. There is a clear enhancement of photocurrent with increasing reverse bias, as expected. Also observed is a shift of optimum response with increasing bias: the unbiased device has an optimum response in the region of a 300 C anneal, while under a -15 V bias the optimum response is around a 250-275 C anneal. This indicates that the application of large electric fields

enhances the extraction efficiency, and so a larger defect concentration can be tolerated by a device that is fully depleted. This result is consistent with and assists in the validation of the theoretical framework presented in chapter 3.

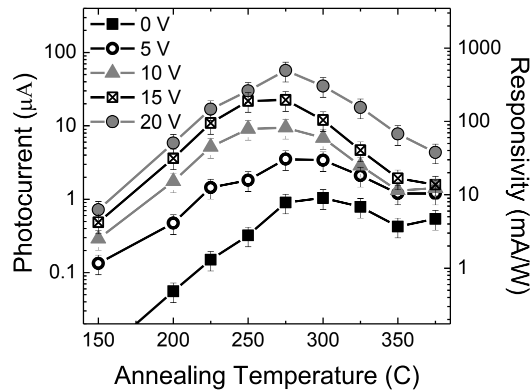

Figure 5.12: Measured photocurrent (left axis) and approximate responsivity (right axis) of a 600 μm long photodetector following 5 minute anneals at various temperatures ranging from 200 to 375 C, under the application of reverse biases of 0, 5, 10, 15 and 20 V.

The optical power transmitted through each waveguide was recorded following each annealing stage. A plot of the transmission loss vs. device length, shown in Figure 5.13a, was used to extract the excess loss (in dB/cm) as the slope of a linear fit. In the example shown, a loss of 165 dB/cm is measured following the 250 C annealing stage; and a loss of 35 dB/cm is measured following the 325 C annealing stage. Note, however, that the error in the slope is determined by the R^2 of the linear fit and the number of points used[7]. In the case of the 325 C anneal, the R^2 is 0.39 and 7 data points are used, which gives an error that overwhelms the measurement entirely. The error stems from facet quality variation between waveguides, and moreover the lack of precision in end-fire coupling alignment into such a small waveguide. It is therefore difficult to extract

[7] In a least-squares linear regression, the R^2 is a number calculated to determine the correlation between two sets of quantities, where the probability of a linear relationship between the two variables is indicated by how near R^2 is to unity [7].

accurate measures of absorption coefficient using this method, particularly after higher annealing temperatures.

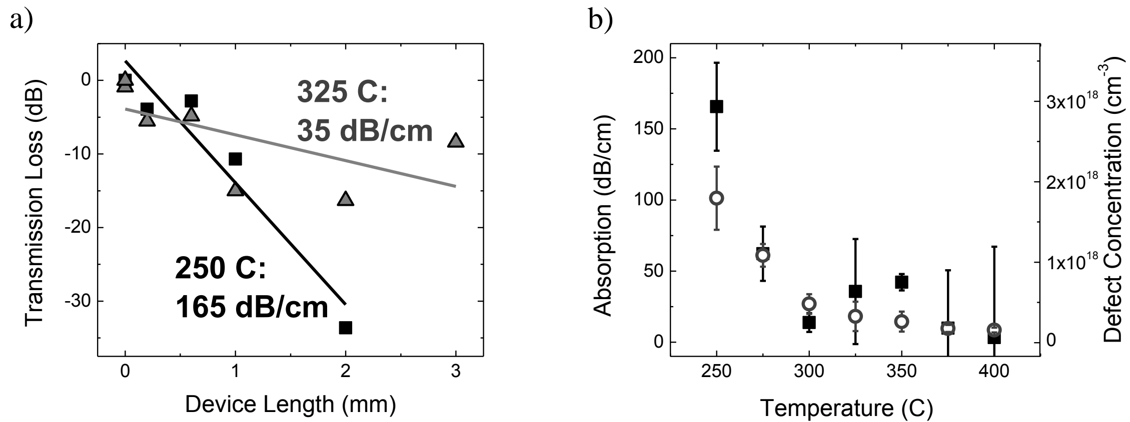

Figure 5.13: a) Measured transmission loss vs. Device length following 5 minute anneals at 250 C and 325 C, with the excess absorption loss extracted from the slope of a linear fit; b) Summary plot of extracted excess absorption as a function of annealing stage (black squares represent extracted values from method in a), while grey circles represent values extracted in chapter 6), with right axis indicating the estimated defect concentration using the method in Eq. (3.7).

The excess absorption calculated in this way is plotted as black square points in Figure 5.13b. The defect concentration is approximated using the optical cross-section of the divacancy using Eq. (3.7), and plotted on the right vertical axis of Figure 5.13b. In chapter 6, an alternative method of extracting excess absorption using implanted micro-rings is presented, the results of which are plotted as grey open circles in Figure 5.13b. The two methods are (for the most part) in agreement within uncertainty. As the data points obtained from the method described in chapter 6 have a much smaller uncertainty value, they are utilized instead throughout the remainder of this chapter.

5.4.2 Dependence of length on photodiode response

Figure 5.14a plots the extracted photocurrent vs. annealing temperature at 5 V reverse bias for four device lengths. As the device length is increased, the annealing temperature that produces the maximum photocurrent increases as well. This is a result of the loss in light intensity along the length of the device, where the total loss is proportional to the product of defect concentration and device length. For shorter devices, a larger defect concentration is needed to absorb the majority of light, and so lower annealing temperatures are favoured. This is illustrated for the 600 μm long device, whose response rolls off following the anneal at 350 C. The longer devices, on the other hand, can tolerate smaller defect concentrations, and so their response continues to increase with higher temperature anneals.

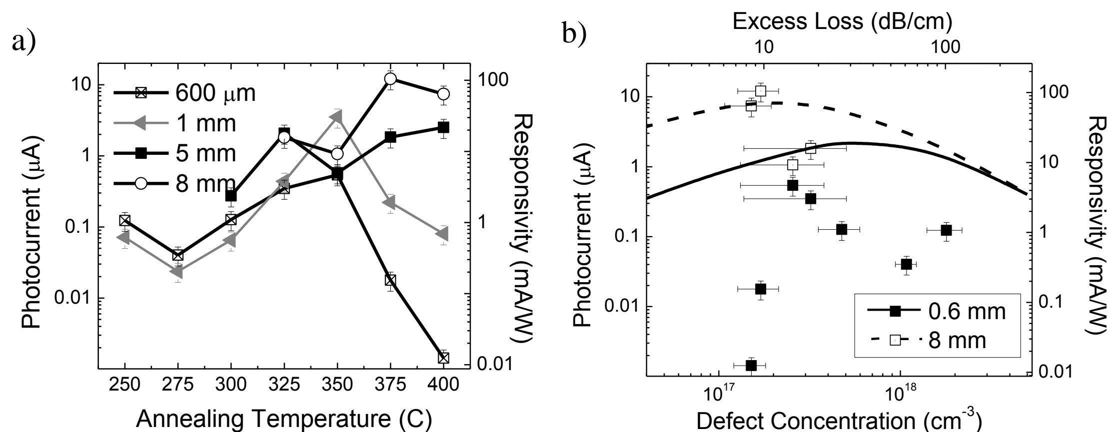

Figure 5.14: a) Measured photocurrent and approximate responsivity at 5 V reverse bias vs. annealing temperature for device lengths of 600 μm, 1 mm, 5 mm, and 8 mm; b) Measured photocurrent data points plotted as a function of defect concentration (bottom axis) and the measured excess loss (top axis) for 600 μm and 8 mm long devices. Solid curves corresponding to the photocurrent predicted by the ATLAS model described in chapter 3 are also included.

Figure 5.14b plots the photocurrent of the 600 μm and 8 mm device lengths as a function of estimated defect concentration and excess loss. The simulated responses,

obtained from the model described in chapter 3, are plotted also. The excess loss and defect concentration required to maximize photocurrent is larger in simulation than it is in measurement, for reasons outlined in section 3.5. The 600 μm long device is optimized for an excess loss of approximately 14.4 ± 7.0 dB/cm, corresponding to a defect concentration 2.6 ± 1.2 x 10^{17} cm^{-3} and an annealing temperature of 350 C. The 8 mm long device, on the other hand, is optimized for an excess loss of approximately 9.6 ± 2.4 dB/cm, corresponding to a defect concentration of 1.7 ± 0.4 x 10^{17} cm^{-3} and an annealing temperature of 375 C.

In Figure 5.15, the photocurrent is plotted as a function of device length following the 325 C anneal stage, for three applied biases. For comparison, the corresponding simulated photocurrents are plotted as curves. The saturation of photocurrent with device length is clearly observed in both simulation and measurement. Due to the exponential loss of the light intensity along the device, the benefit of increasing device length L becomes smaller as the L exceeds the $1/\alpha$ depth. Since at this stage the excess loss is approximately 23 dB/cm, this length is 2 mm, which is indeed where the response begins to saturate in the curve below.

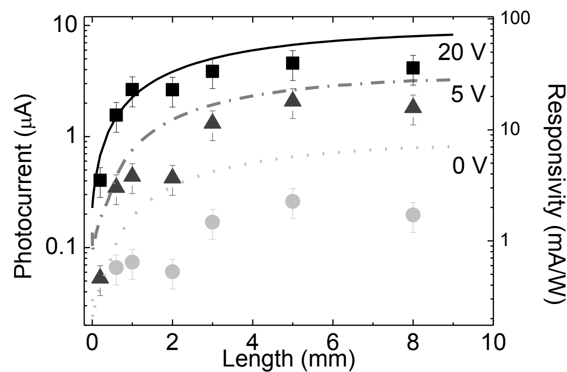

Figure 5.15: Measured photocurrent/responsivity (data points) following the 325 C annealing stage, plotted as a function of device length under reverse biases of 0, 5, and 20 V; the solid curves indicate the modeled performance using ATLAS.

The measured points agree reasonably well with the simulation results in Figure 5.15 under the larger reverse biases, although the model appears to overestimate the unbiased response. This is likely due to the built-in field not penetrating as far into the waveguide of the fabricated device as was modeled. When a bias is applied, the built-in field is a small component of the total electric field in the waveguide, and its miscalculation does not strongly affect the simulation results.

5.4.3 Characterization of the noise properties

In Figure 5.16a, the reverse saturation current of the 600 μm device is plotted both under dark conditions (dashed line) and with an on-chip optical power of 115 ± 25 μW (solid line). The grey curve provides the measurement following the 275 C anneal, and the black curve provides the measurement following the 325 C anneal.

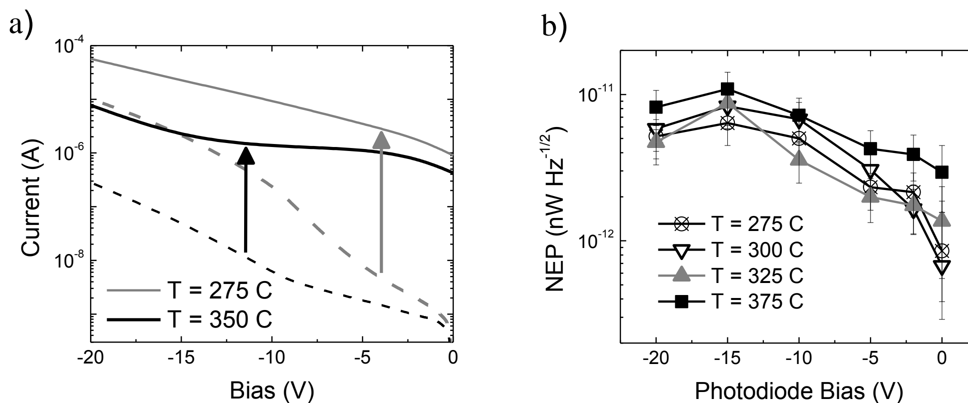

Figure 5.16: a) Reverse diode characteristic for a 600 μm long device, with the dashed curve indicating a measurement of dark current and the solid curve indicating a measurement under the insertion of 115 ± 25 μW of optical power (Grey curve: 275 C anneal, black curve: 350 C anneal); b) *NEP* measured following anneals at 250, 300, 325, and 375 C and plotted as a function of reverse bias.

Following the 275 C anneal, the shunt resistance R_{sh} is 4.0 ± 0.7 MΩ at -20 V. For the shot noise to be the dominant contribution to the total noise power, the average current in the photodiode must be larger than 10 nA. Since the dark current at -20 V bias is 10.2 μA, this condition is automatically satisfied. The shunt resistance R_{sh} is increased to 195 ± 33 MΩ following the 325 C anneal (at -20 V bias), and therefore the shot noise is the dominant contribution for average photodiode current larger than 0.3 nA. Similarly, the dark current at this bias is 283 nA, and so the shot noise remains the principle limitation on performance.

The information contained in Figure 5.16a was used to calculate the *NEP* (or Noise Equivalent Power, defined by Eq. (2.56)), which is plotted as Figure 5.16b for four annealing stages. An increase in *NEP* with increasing bias is observed, due to the increase in dark current. While the T = 275 C annealing stage has the largest responsivity, the T = 325 C stage offers the lowest *NEP* for several values of reverse bias as a result of the lowered dark current. Since the dark current increases with device length, the *NEP* is minimized by selecting a device length that is in the region of the $1/\alpha$ in Figure 5.15, so the dark current is minimized for the saturated (maximum) value of responsivity.

5.5 Summary

This section has described the process of fabricating sub-micron waveguide photodiodes using electron-beam lithography, and has discussed the properties of these photodiodes. In particular, the influence of defect concentration, applied bias and device length on responsivity and noise properties was explored. Moreover, the experimental results serve to validate the physical model provided in chapter 3.

References

[1] M. W. Geis *et al.*, "CMOS-compatible all-Si high-speed waveguide photodiodes with high responsivity in near-infrared communication band," *IEEE Photon. Technol. Lett.*, vol. 19, pp. 152–154, Feb. 2007.

[2] University of Glasgow: James Watt Nanofabrication Center. Online: http://www.jwnc.gla.ac.uk. (Accessed April, 2011).

[3] J. D. Plummer, M. D. Deal, and P. B. Griffin, *Silicon VLSI Technology*, "Chapter 5: Lithography," Prentice Hall, 2000.

[4] G. Wiederrecht (Ed.), *Handbook of Nanofabrication,* D. M. Tennant and A. R. Bleier "Chapter 4: Electron Beam Lithography of Nanostructures," Elsevier B. V., 2010.

[5] Robert Hull (Ed.), *Properties of Crystalline Silicon*, D. E. Aspnes "Optical Properties of Si," DataReviews Series No 20, INSPEC, 1999.

[6] "ATHENA User's Manual," Silvaco International, March 2011.

[7] P. R. Bevington, and D. K. Robinson, *Data Reduction and Error Analysis for the Physical Sciences: 3rd Ed.*, "Chapter 11: Testing the Fit," McGraw-Hill, 2003.

Chapter 6: Resonant Photodiode Enhancement

6.1 Overview

The improvement in speed with the reduction of the *p-i-n* junction area is a strong motivation towards structure lengths on the order of 10 µm. When the length of a photodiode is reduced below a critical point, the bandwidth is no longer limited by capacitance, but by the transit time of optically generated charge carriers. Using the ATLAS model described in chapter 3, this limit was found to be approximately 63 GHz, presuming the carrier lifetime is larger than 10 ps (or equivalently the defect concentration is less than 3 x 10^{17} cm^{-3}). From the measured capacitance of 123 ± 29 pF/cm quoted in section 5.3, it can be shown that the photodetector bandwidth is capacitance-limited for lengths greater than 5 µm[8]. In addition, since the reverse saturation current is proportional to the *p-i-n* junction area, the *NEP* (ignoring thermal circuit components) will be reduced as the device length is decreased. While the response does suffer somewhat as the length is reduced, this can be partially offset by increasing the defect concentration at which the device operates, as shown in Figure 5.14b. However, for lengths below 100 µm, the defect concentration required exceeds the levels practically introduced by high energy Si^+ ion implantation.

A way to reap the benefits associated with reducing photodiode length while avoiding the degradation in responsivity is to incorporate the photodetector into an optical resonator. These structures, which were described in detail in section 2.4, are generally composed of a feedback loop for select 'resonant' frequencies. Some possible waveguide resonator configurations are depicted in Figure 6.1: a 'slot' or 'hole' photonic crystal micro-cavity, and an add-drop or all-pass micro-ring resonator. The micro-cavities

[8] improved contact design may reduce this capacitance significantly [1], raising the cut-off length for capacitance-limited behaviour.

are simply Fabry-Perot etalons integrated onto a section of waveguide, with reflectors formed of either periodic slots or holes etched into the silicon. The slots have the benefit of electrical isolation (meaning that carriers are confined to the cavity) [2], while the holes cause minimal scattering loss and thus exhibit higher Q factors [3]. If the cavity is symmetric, as shown in the upper left, the device is simply a lossy transmission filter, which will partially absorb and partially transmit on resonance. If the cavity is made asymmetric as in the upper right, by adding several periods on the output side to make that mirror 100% reflecting, the transmission will be zero on resonance, and the cavity is 100% absorbing. This means that complete end-line detection is possible for an arbitrarily small cavity size.

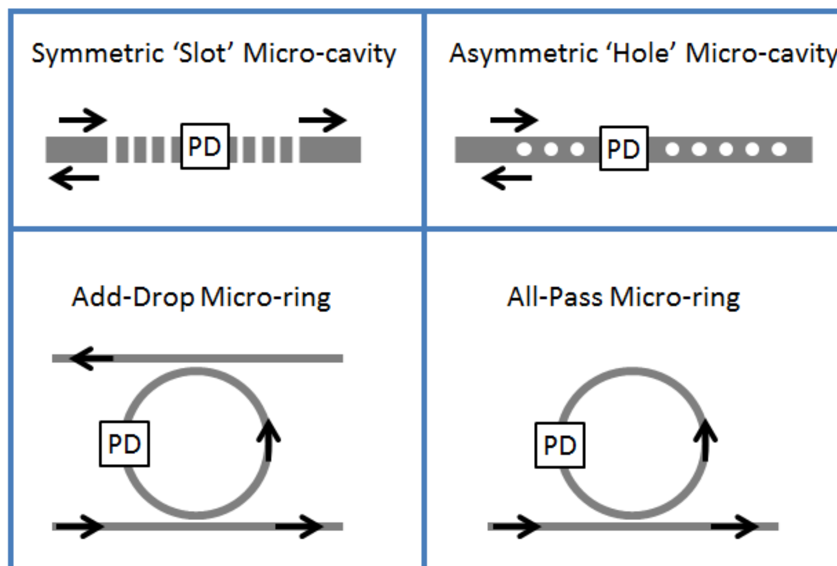

Figure 6.1: Potential implementations of resonant enhanced waveguide photodiodes (PD): Integrated onto a symmetric or asymmetric micro-cavity formed of periodically etched slots or holes to function as cavity mirrors, or integrated onto an add-drop or all-pass micro-ring.

Similarly, a photodiode integrated onto an add-drop micro-ring will have an enhanced but not total absorption on resonance, as the resonant light is partially transmitted to the drop-port and partially absorbed by the photodiode. On the other hand,

if the photodiode is integrated onto an all-pass micro-ring, all resonant light is absorbed or scattered. The photodiode thus absorbs a fraction of the input light equal to the ratio of the defect-enhanced absorption to the total ring loss.

The build-up factor (or *BUF*) given by Eqns. (2.89) and (2.91) provides the degree to which the αL product of the photodiode is effectively increased on resonance over a non-resonant device. As this factor is proportional to the finesse of the resonator, it may therefore be maximized by designing a resonator with narrow linewidth and large free-spectral range. The enhancement of other sources of absorption in silicon (namely those of surface states and two-photon absorption processes) has previously been reported in SOI micro-rings with integrated *p*-*i*-*n* junctions, although the low cross-sections of these absorption mechanisms limited the peak responsivity to 0.25 mA/W [4].

The design and fabrication of the above devices were attempted for this thesis and the micro-rings were found to be the only devices to yield successful *p*-*i*-*n* junction integration. This chapter will describe the design, fabrication and experimental results obtained from these devices.

6.2 Design and Fabrication

6.2.1 Micro-ring design

The first step in the micro-ring design is the selection of waveguide dimensions. Here, the same dimensions as chapter 5 were used, both for the bus waveguide and within the ring. The fundamental waveguide mode profile obtained from BeamPROP [5] is shown in Figure 6.2a, which has an effective index of $n_{eff} = 2.59$ at $\lambda = 1550$ nm (in good agreement with the approximation in section 2.1.2). For comparison, the mode spot-size from the bus waveguide at off-resonant wavelengths is shown in Figure 6.2b. In order to find the group index n_g, the effective index was solved for a series of input wavelengths

ranging from 1540 to 1560 nm. The waveguide dispersion was measured to be $\frac{dn_{eff}}{d\nu} = 2.7\times10^{-15}\,Hz^{-1}$, which from section 2.4.2 corresponds to a group index of n_g = 3.42 at λ = 1550 nm. This process was repeated for bent waveguides using the simulation feature in BeamPROP, and the overall n_{eff} and n_g is plotted as a function of bend radius R in Figure 6.2c. For R > 10 μm, the n_{eff} and n_g are saturated at their values for a straight waveguide.

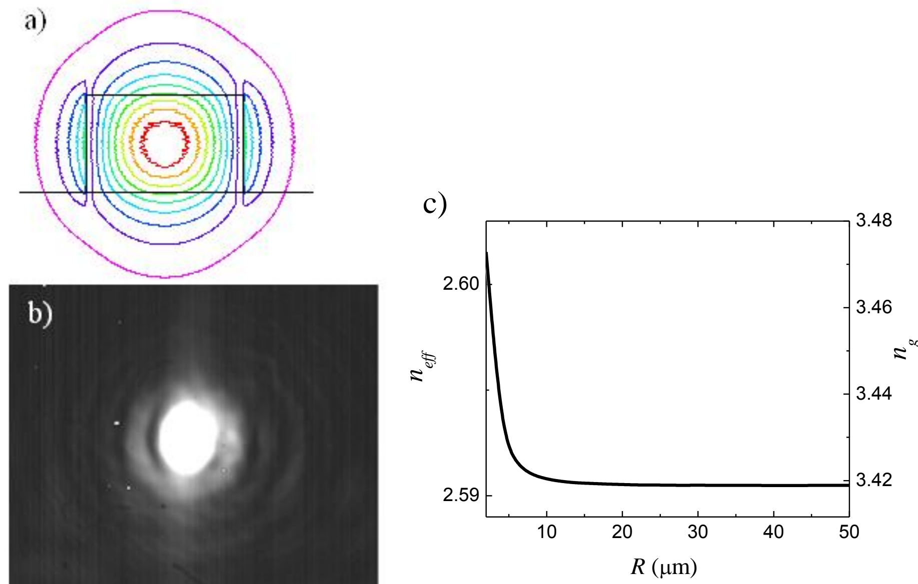

Figure 6.2: a) Calculated fundamental mode using BeamPROP; b) Mode spot size captured by the Infrared camera at the output of the waveguide; c) Plot of calculated n_{eff} and n_g as a function of waveguide bend radius R, measured at a λ =1550 nm operating point.

From the theory presented in section 2.4, the Q-Factor of an all-pass ring resonator becomes larger as the cross-coupling coefficient κ is decreased. Therefore, in order to achieve a narrow resonant linewidth, the κ is designed to be as small as possible. To simultaneously obtain a large extinction ratio, the ring must be critically coupled, which, as described in section 2.4.3, occurs when the coupled power equals the loss

incurred in one round trip of the ring. Therefore, the two design criteria are that the loss be minimized and the cross-coupling coefficient matches the loss ($\kappa^2 = 1 - A^2$).

The loss in the ring is dominated by two factors: the propagation loss and the bending loss. The propagation loss includes scattering loss due to sidewall roughness, and was extracted from passive waveguides to be 2.6 ± 0.8 dB/cm (see chapter 5). As the circumference of the ring is decreased, the total propagation loss decreases while the total bending loss increases. There exists then an ideal region in which the sum of the two contributions is minimized. A selected starting point was to ensure the bending loss does not exceed the propagation loss. From previously fabricated rings of similar waveguide dimensions, the bending loss was estimated to be < 2.5 dB/cm for $R > 10$ μm [6, 7]. On the other hand, a large free spectral range is desired for the resonant enhancement, meaning that the round-trip optical path length $2\pi R$ should not be made too large. Based upon these desires (and with the difficulties of *p*-*i*-*n* incorporation in mind), the ring radius was conservatively chosen to be $R = 20$ μm.

The coupler was modeled using a two-dimensional FullWAVE [8] simulation, using $R = 20$ μm and a variable coupling gap width. Power monitors were used on both the bus waveguide and ring to measure the cross-coupling coefficient κ^2, as shown in Figure 6.3a. The resulting values of κ^2 are plotted against coupling gap width in Figure 6.3b. Presuming a loss in the region of 2-5 dB/cm, the absorbance $A^2 = e^{-\alpha(2\pi R)}$ is 0.985-0.995. Therefore, the coupling strength $|\kappa|^2$ to the bus waveguide must be in the range 0.005-0.015 for the device to be critically coupled. From Figure 6.3b, this corresponds to a coupling gap in the region of 185 - 230 nm.

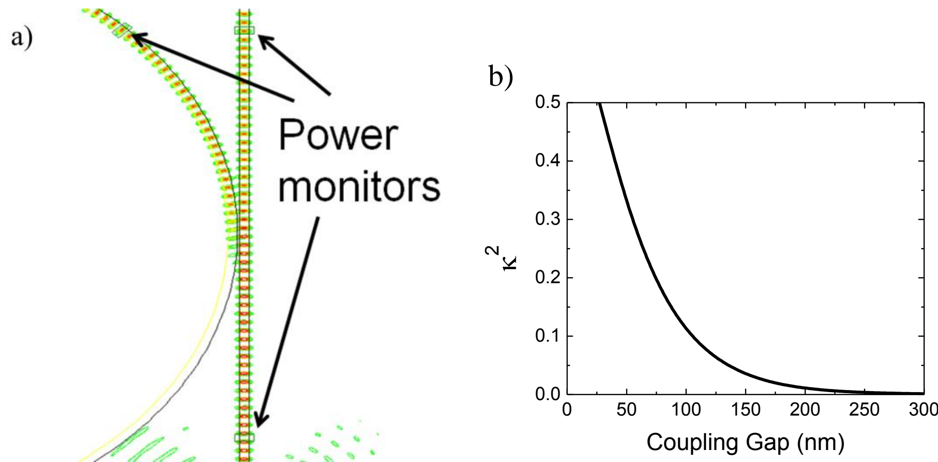

Figure 6.3: a) Capture of simulation window in FullWAVE, illustrating the coupling process between the bus waveguide and the ring, and the power monitors used to characterize it; b) Extracted cross-coupling coefficient κ^2 between a straight waveguide and a waveguide with radius R = 20 µm.

One additional practical consideration must be made when selecting gap size: the effects of *RIE etch lag*, which is the dependence of etch rate on the geometry of sub-micron features. In this case, the etch rate of silicon in the coupling region between waveguides will be smaller than other relatively open areas on the chip. This is not normally a concern when the silicon is fully etched to the buried oxide, as over-etching may mediate this problem. When a 50 nm slab must be left for electrical integration, this effect can lead to significant etch depth non-uniformity.

A test structure containing gratings of varying gap sizes was written by e-beam and etched to notionally leave a 50 nm slab of silicon. The etch depth within the gap was measured using SEM, as shown in Figure 6.4. There is a clear reduction of etch rate for gap sizes less than 190 nm, leading to the constraint that the designed gap should be larger than this value.

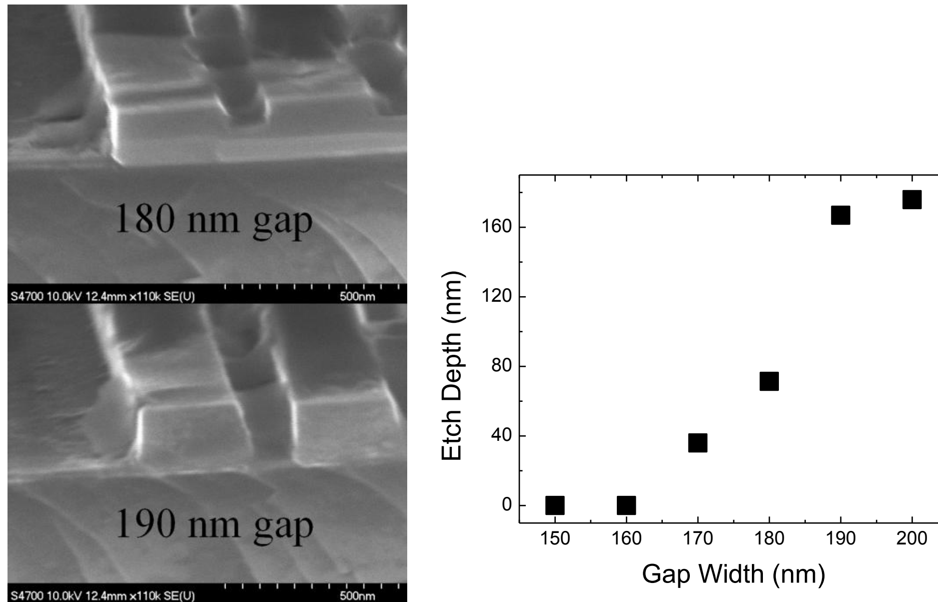

Figure 6.4: SEM images of test structure having varied gap sizes, illustrating a marked difference in etch depth between gap widths of 180 nm and 190 nm; The etch depth is plotted for each gap size on the right, indicating minimal etch lag about 190 nm gaps.

The e-beam process of chapter 5 was used in the fabrication of these waveguides, using the selected radius of 20 μm and designed gaps of 190-230 nm as a starting point. The e-beam writer dose was varied for several structures, resulting in a variation in waveguide width and consequently the coupler gap size – typically this variation is on the order of 10% around the designed nominal values. Passive, optical evaluation of the transmission spectrum of each structure indicated that a 200 nm gap produced the best combination of resonance extinction ratio and linewidth. SEM images of the corresponding etched micro-ring and coupler gap are provided in Figure 6.5.

In addition to this all-pass micro-ring resonator, several symmetric add-drop structure geometries were fabricated with varying radius and coupling gap width. The characterization of these devices will be described in section 6.3.4.

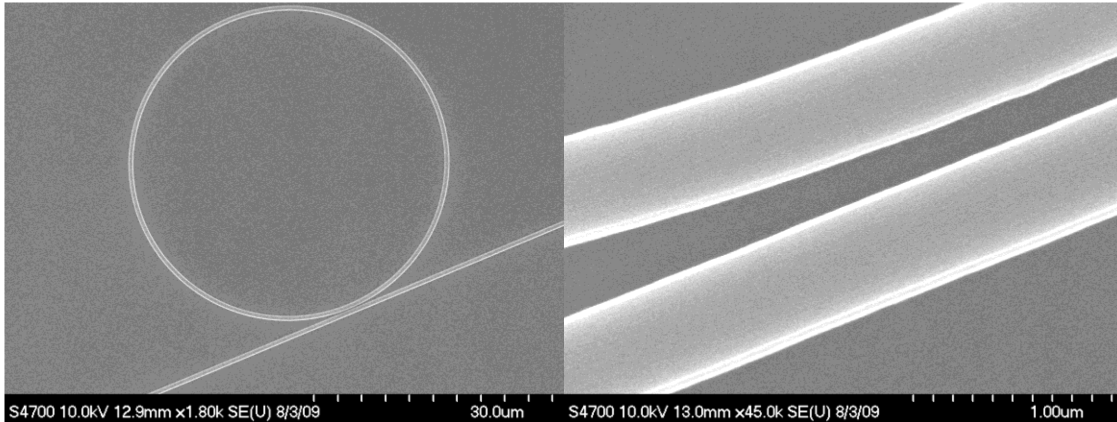

Figure 6.5: SEM image of full all-pass micro-ring resonator of *R* = 20 µm radius (left), and magnified image of the point coupler containing a 200 nm gap to the bus waveguide (right).

6.2.2 Micro-ring p-i-n diode integration

The integration of doped regions onto the micro-rings was also achieved in a similar way to the devices of chapter 5, and is illustrated schematically in Figure 6.6. Using PMMA positive e-beam resist, a circular concentric window was exposed for masking of a boron implant, extending up to 500 nm from the waveguide edge. Similarly, an arc-shaped window was opened in PMMA for the phosphorus implant mask. For the all-pass configuration of Figure 6.6a, the arc was 140° long and opposite the bus waveguide. For the add-drop configuration in Figure 6.6b, two 140° arcs extended at the top and bottom of the ring. The waveguide photodiode cross-sections are therefore identical to that shown in Figure 5.2a. The effective diode length for the 20 µm radius is therefore 50 µm for the all-pass configuration and ranges from 100 to 145 µm for the add-drop configuration.

The boron and phosphorus implantation conditions were likewise identical to the devices of chapter 5. A microscope image of a device following the e-beam lithography step to open the phosphorus implantation window is shown in Figure 6.7a. The center of the ring is discoloured due to the preceding boron implant, similar to Figure 5.8. An SEM

image of the same device is shown in Figure 6.7b following the lift-off of the aluminum contacts, where the contact pads and the oxide vias are clearly visible.

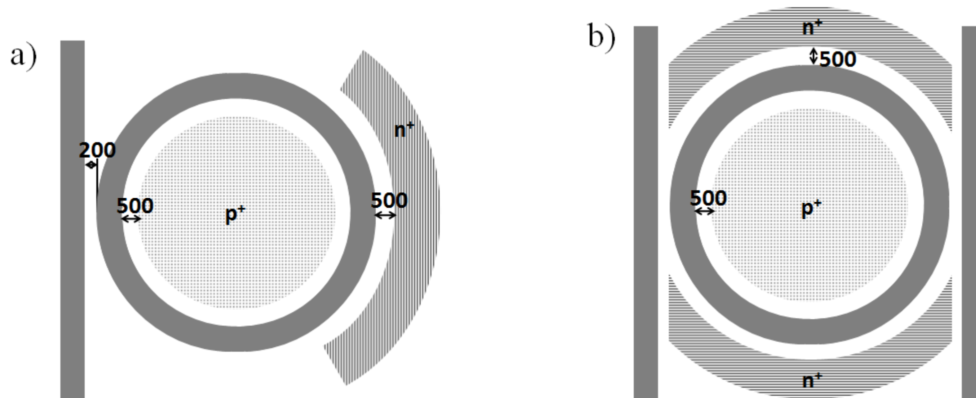

Figure 6.6: Schematic of p^+ and n^+ incorporation region onto a) all-pass and b) add-drop micro-ring resonators, both having a distance of 500 nm from the waveguide edge.

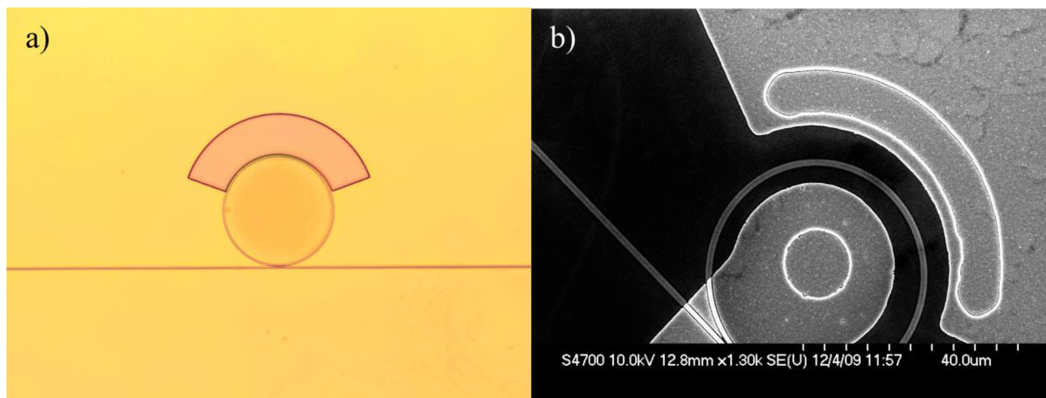

Figure 6.7: a) Optical Microscope image of the micro-ring following development of the phosphorus implant mask in PMMA, showing the arc-shaped window and a slight discolouration due to the previous boron implantation; b) SEM image of the micro-ring following aluminum lift-off, showing the large contact pads and the smaller contact vias to the boron and phosphorus doped regions.

The 200 keV Si^+ implantation of 10^{13} cm^{-2} dose was masked using photoresist such that the entire ring was implanted, including a small portion of the bus waveguide in the coupler region.

6.3 Measured Resonant Enhancement of Photocurrent

6.3.1 Optical and electrical characterization of all-pass resonant photodiodes

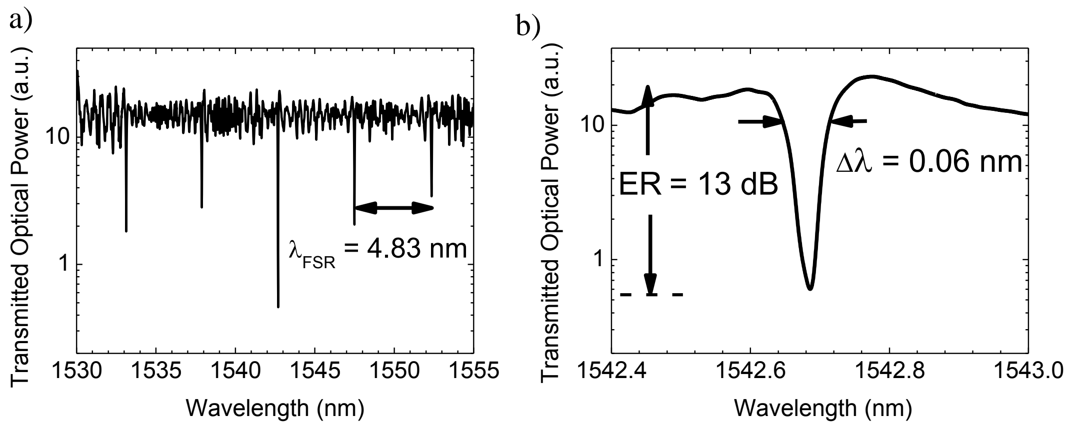

Figure 6.8: a) Transmission spectrum of bus waveguide, with periodic resonances of Free-spectral range λ_{FSR} = 4.83 ± 0.03 nm; b) Magnified view of single resonance, with linewidth $\Delta\lambda$ = 0.060 ± 0.006 nm and extinction ratio *ER* = 13 dB.

As in the characterization of the non-resonant devices of chapter 5, light from a Photonetics wavelength tunable laser was butt-coupled into the bus waveguide. The transmitted light was measured using an InGaAs amplified detector and lock-in amplifier as the tunable laser was scanned through wavelength with a step size of 0.005 nm. The transmission spectrum, measured prior to the Si^+ implantation, is presented in Figure 6.8a and exhibits resonance dips with a free-spectral range of λ_{FSR} = 4.83 ± 0.03 nm. From

Eq. (2.64), this corresponds to a group index of $n_g = 3.93 \pm 0.02$, which is larger than the simulated value of $n_g = 3.42$.

In the magnified resonance at λ = 1542.69 nm shown in Figure 6.8b, a linewidth of $\Delta\lambda$ = 0.060 ± 0.006 nm is observed, which corresponds to a *Q*-Factor of 26 000. Similarly, the *Finesse* is calculated from Eq. (2.66) to be 80.5 ± 8.1, and the extinction ratio has a value of approximately *ER* = 13 dB.

Following the Si^+ implantation, the resonance was altered significantly both in $\Delta\lambda$ and *ER*, indicating a change in absorption coefficient α. The free-spectral range did not vary from the value quoted above, and the resonant location varied randomly (presumably due to fluctuations in room temperature). A plot of the optical resonance following annealing is shown in Figure 6.9a, where the resonances have been aligned for illustrative purposes. Figure 6.9b plots the average extracted $\Delta\lambda$ and *ER* for each annealing stage, obtained through a Lorentzian fit to the measured data.

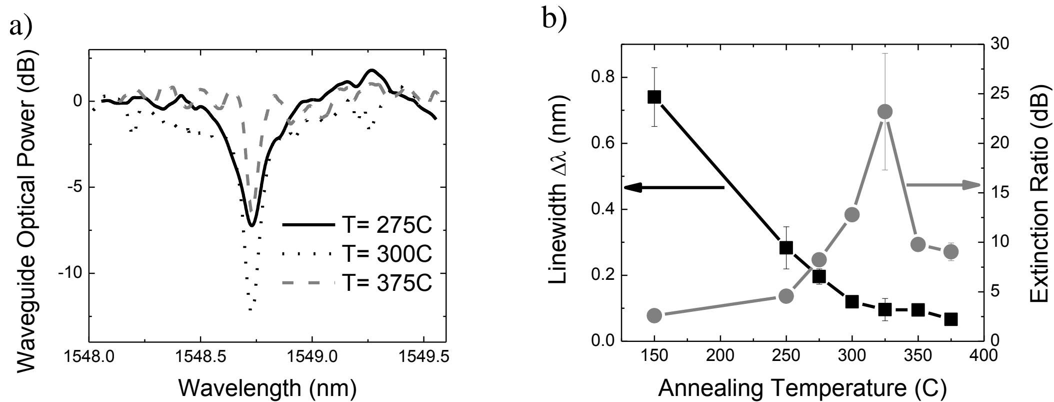

Figure 6.9: a) Plot of a single optical resonance following 5 minute anneals at T = 275 C, 300 C and 375 C; b) Extracted values of linewidth $\Delta\lambda$ and Extinction Ratio *ER* following each annealing stage (the unannealed stage is associated with a temperature of 150 C, as the device was subjected to this ambient during processing).

The extracted $\Delta\lambda$ and *ER* values may be used with Eqns. (2.83) and (2.84) to obtain the values of A^2 and $|t|^2 = (1 - |\kappa|^2)$ [9]. Due to the format of these coupled equations, there is no way to distinguish between these two roots. It is reasonable to assume, however, that the annealing affects the excess absorption (i.e. A^2) much more than it does the coupling coefficient ($|t|^2$), and use that to guide the selection of roots. The two roots are plotted in Figure 6.10a against the annealing temperature of the stage at which they were extracted. It is clear that one root significantly increases with annealing, while another has only a modest increase; the first root is assumed to be A^2 using the justification stated above, while the second is taken to be t^2. The T = 300 C annealing stage was ambiguous, as the roots were close in value, and so A^2 and t^2 were both equated to the average of the two values. The slight variation in coupling strength throughout annealing is expected, as the coupling region was implanted with Si^+ ions. Both roots therefore contain elements of coupling loss, which cannot be factored away using the present data [9].

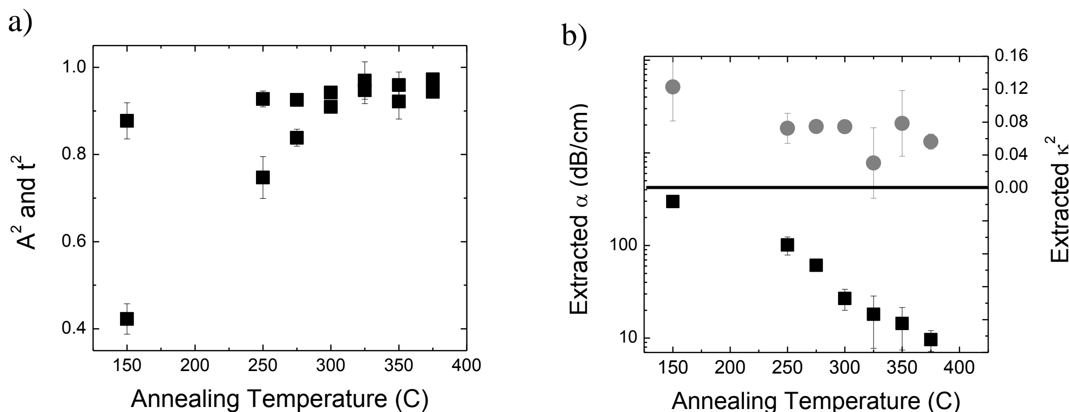

Figure 6.10: a) Extracted roots (A^2 and t^2) from the values of *ER* and $\Delta\lambda$ plotted in Figure 6.9b; b) Informed disentangling of the absorption coefficient α and cross-coupling coefficient κ^2 using the roots in a).

This method has thus independently calculated the absorption coefficient α due to defect introduction, with a smaller uncertainty than the cut-back method used for the non-resonant devices in chapter 5. The key values of Figure 6.9 and 6.10 are summarized in Table 6.1, and the defect concentration is approximated using Eq. (3.7), presuming that α is a result of defects. Note that for high temperature annealing stages (> 300 C), the absorption becomes comparable to the expected intrinsic micro-ring loss, and so the defect concentration is overestimated. It was these extracted values of absorption and defect concentration that were used in chapter 5 to compare to simulated results.

TABLE 6.1: Summary of optical properties of micro-ring resonator throughout thermal annealing treatment

Annealing Temperature (C)	Extinction Ratio (dB)	Linewidth $\Delta\lambda$ (nm)	Coupling Coefficient κ^2	Absorption Coefficient α (dB/cm)	Defect Concentration (cm^{-3})
150	2.58 ± 0.28	0.74 ± 0.09	0.123 ± 0.041	298.6 ± 28.6	5.29 ± 0.51 x 10^{18}
250	4.55 ± 0.20	0.28 ± 0.06	0.073 ± 0.018	101.2 ± 22.2	1.79 ± 0.39 x 10^{18}
275	8.24 ± 0.38	0.196 ± 0.023	0.075 ± 0.007	61.1 ± 8.0	1.08 ± 0.14 x 10^{18}
300	12.79 ± 0.92	0.120 ± 0.008	0.074 ± 0.004	26.9 ± 6.9	4.75 ± 0.12 x 10^{17}
325	23.19 ± 0.42	0.096 ± 0.034	0.030 ± 0.043	18.1 ± 10.4	3.21 ± 0.18 x 10^{17}
350	9.77 ± 0.41	0.095 ± 0.015	0.079 ± 0.040	14.4 ± 7.0	2.55 ± 0.12 x 10^{17}
375	9.04 ± 0.89	0.066 ± 0.013	0.056 ± 0.009	9.6 ± 2.4	1.70 ± 0.43 x 10^{17}

At annealing temperatures T > 250 C, the extracted values of κ^2 were 0.030-0.079, significantly larger than the designed range of 0.005-0.015 quoted above. This is may be caused by a change in waveguide width during the resist development or the dry oxidation, or due to a variation in the etch depth of the waveguide. As a result, the micro-rings were not critically coupled prior to the incorporation of defects by the Si^+ implantation. However, they were critically coupled when the ring loss had a value of A^2 = 0.92-0.97 (or equivalently α = 10-29 dB/cm), provided by the Si^+ implantation and subsequent annealing at T = 300-325 C. It is for this reason that the extinction ratio at the T = 325 C stage in Table 6.1 and Figure 6.9b is markedly increased over adjacent values;

it is at this stage that the ring loss is closest to matching the through-coupling coefficient ($A^2 = t^2$). This is beneficial in that the build-up factor is consequently maximized in a high efficiency photodetection regime.

The *I-V* characteristic of the integrated diode was measured following the 5 minute anneals at various elevated temperatures. The curves measured following 225, 275 and 375 C anneals are reproduced in Figure 6.11. Following low temperature anneals, the reverse-saturation current was in excess of 1 μA for reverse biases of 20 V. This was significantly reduced beyond the 275 C anneal, and following the 375 C anneal was below 3 nA at 20 V reverse bias.

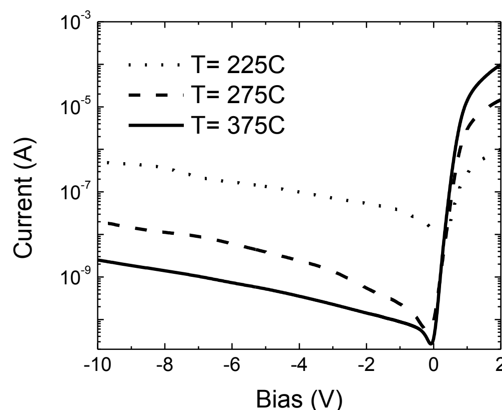

Figure 6.11: *I-V* curve of micro-ring *p-i-n* diode following Si^+ implantation and 5 minute anneals at 225 C, 275 C and 375 C in nitrogen.

6.3.2 Measured photodetection of all-pass resonant photodiode

The data acquisition was configured to measure current as well as the output of the lock-in amplifier as the laser wavelength was tuned. The current of the reverse biased micro-ring *p-i-n* diode featured marked increases on resonance, as illustrated in Figure 6.12a. This data was obtained following the 5 minute anneal at 325 C, and has resonances of free-spectral range equal to the optical resonances in Figure 6.8. In Figure 6.12b, the

photocurrent is plotted along with the bus waveguide transmission for a single resonance. The photocurrent is enhanced on resonance by more than 15 dB over the non-resonant photocurrent. Note that the off-resonance photocurrent is approximately 100 times larger than the dark current, which is believed to be due to both photodetection in the implanted coupler region and coupling of off-resonant light. Assuming an on-chip optical power of 115 μW, the highest measured resonant photocurrent of 7.65 μA (at -20 V bias) corresponds to a peak responsivity of 67 mA/W.

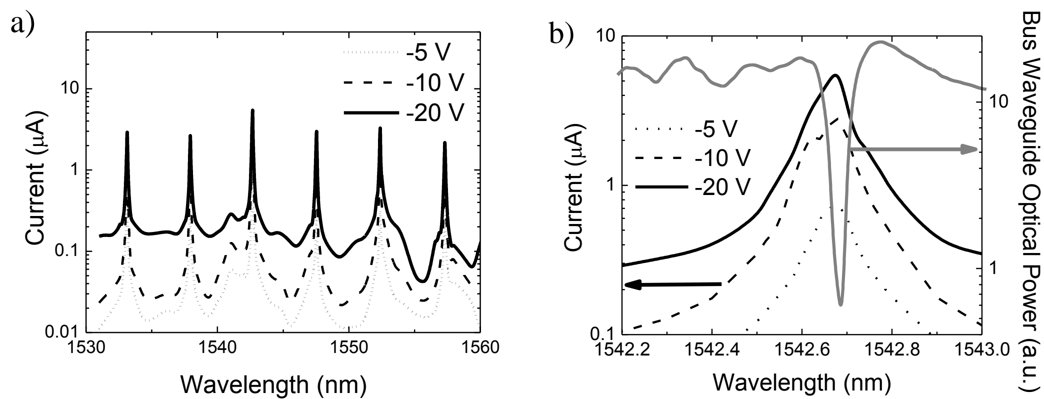

Figure 6.12: a) *P-i-n* diode current at 5, 10 and 20 V reverse bias vs. tunable laser wavelength, illustrating resonant enhancements matching the optical resonances of the micro-ring (following a 5 minute anneal at 325 C); b) magnification of the 1542.69 nm resonance, with the current and waveguide transmission plotted together on separate axes.

Similar to the non-resonant devices, the response of the resonant photodiodes demonstrates a variation with annealing. The electrical resonance measured following anneals at 250, 300 and 375 C is shown in Figure 6.13a, and the extracted peak photocurrent (which is the difference between the resonant current and the average off-resonance current) and resonant current linewidth are plotted in Figure 6.13b. The resonant linewidth becomes narrower as the device is annealed, as expected from the optical measurements of Figure 6.9b. However, the linewidth of the electrical resonance is larger

than the optical linewidth for all annealing stages, which is also attributed to the detection of light in the implanted coupler region.

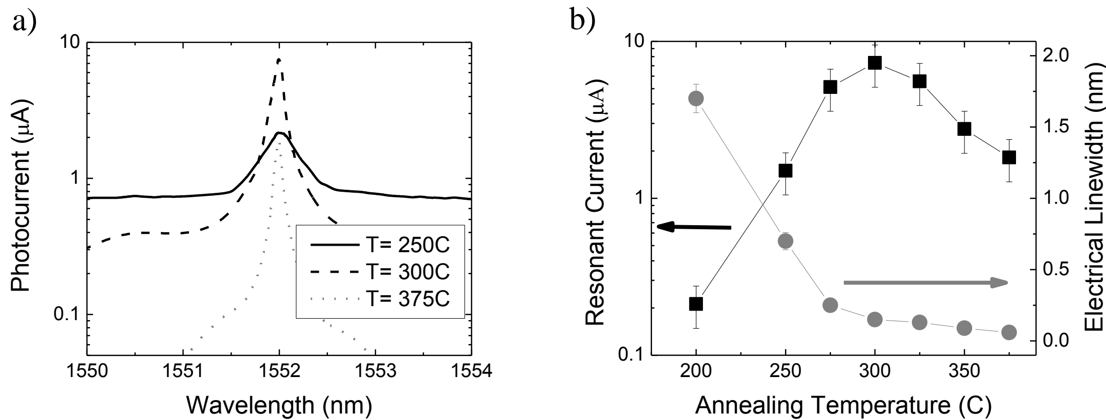

Figure 6.13: a) Wavelength variation in photocurrent following 5 minute anneals at 250 C, 300 C, and 375 C; b) Extracted values of maximum (resonant) photocurrent and linewidth of photocurrent resonance for each annealing stage.

6.3.3 Discussion of resonant enhancement in all-pass resonant photodiodes

The resonant enhancement in photocurrent may be quantified from the results of the previous section and Eq. (2.89). The photocurrent of the straight non-resonant photodiodes presented in chapter 5 is plotted in Figure 6.14a, following a 325 C anneal and biased at -20 V. As a comparison, the simulated results are plotted as a black curve, and the simulated responsivity of a 50 μm long (non-resonant) photodiode is emphasized by a grey dashed line. The measured photocurrent from the 50 μm resonant photodiode is plotted as a grey dotted line, indicating a photocurrent enhancement of 12 dB. Assuming the approximate form of the build-up factor in Eq. (2.89) and the non-implanted properties of the ring, the enhancement in αL would be expected to be:

$$BUF = \frac{2}{\pi}\frac{\lambda_{FSR}}{\Delta\lambda} = 51 = 17dB \tag{6.1}$$

This predicts that the 50 μm resonant photodiode would have a photocurrent equal to a 51 x 50 μm = 2.55 mm non-resonant photodiode at the same annealing stage. From Figure 6.14a, the measured resonant photocurrent intersects with the non-resonant curve at a length of approximately 4 mm, illustrating agreement (at least in order of magnitude) between expected and measured enhancement.

The *NEP* of this device is then reduced by a factor of 30 over the 4 mm long non-resonant device presented in chapter 5, as its dark current is reduced by a factor of 1000 while the responsivity is identical.

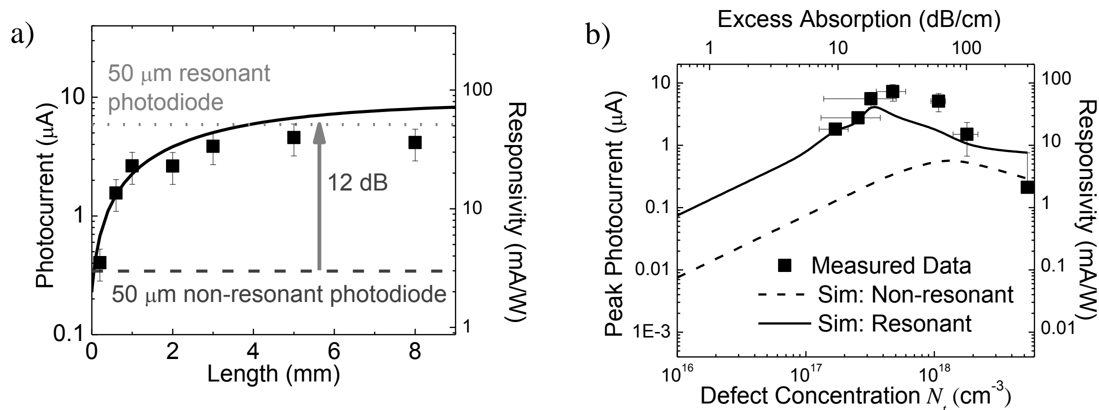

Figure 6.14: a) The measured (square points) and simulated (solid curve) photocurrent/responsivity of non-resonant photodiodes of different lengths presented in chapter 5, along with the simulated response of a non-resonant 50 μm photodiode (grey dashed line) and the measured response of the 50 μm resonant photodiode (grey dotted line) following a 325 C anneal, illustrating the resonant photocurrent enhancement of 12 dB; b) Measured peak photocurrent plotted against approximate defect concentration and excess loss, along with modeled results of non-resonant and resonant 50 μm photodiodes.

While using the *Finesse* as an order-of-magnitude approximation of the enhancement, note that it is only approximate for low loss conditions (A = 1) and critical coupling (t = A). In all but the highest annealing stages, this condition is not met. Therefore, the exact form of Eq. (2.89) must be used to calculate the resonant enhancement, using the extracted values of A and t of section 6.3.1. The simulated photocurrent of a 50 μm diode is plotted in Figure 6.14b as a function of defect concentration, both with and without the resonant enhancement expected from the parameters in Table 6.1. For comparison, the data points of Figure 6.13b are plotted as well. It is observed that the resonant enhancement in photocurrent shifts the peak response to lower defect concentrations in both the measurements and in simulation. The good agreement between the two curves provides evidence that the resonant build-up of intensity described in Eq. (2.89) is responsible for the enhanced photocurrent throughout annealing.

In addition to thermal annealing, the geometry of the micro-ring itself has a marked influence of the overall performance, as will presently be discussed.

6.3.4 Resonant enhancement in an add-drop configuration

As described in section 2.4.3, resonant enhancement may also be obtained in an add-drop configuration, characterized by a build-up in intensity described by Eq. (2.91). Such photodetectors would be needed in PICs to detect a wavelength channel that must also be simultaneously routed elsewhere. Several such micro-ring geometries were fabricated, with varying coupler geometries and ring radii. In particular, both circular ring structures (i.e. similar to the previous sections) and racetrack structures were fabricated with designs indicated in Figure 6.6b. They were subjected to a masked implant of Si^+ at 300 keV and 7 x 10^{12} cm^{-2} dose and annealed at T = 300 C for 5 minutes.

Figure 6.15a plots the sample optical transmission of a racetrack with 30 μm radius and a 10 μm length and 200 nm gap coupler section to the bus waveguide. The grey curve is a fit of Eq. (2.79) to this data, from which the values $A = 0.847 \pm 0.045$ and $t = 0.691 \pm 0.005$ are extracted. From this data, the *BUF* is calculated using Eq. (2.90), and is plotted as a function of wavelength on the right axis. Figure 6.15b plots the same information for a device with identical geometry but a 300 nm gap width. In this case, the self-coupling coefficient is increased to $t = 0.945 \pm 0.002$, which improves the *BUF* for reasons that will be described below. The extracted results from all of the fabricated devices are presented in Table 6.2.

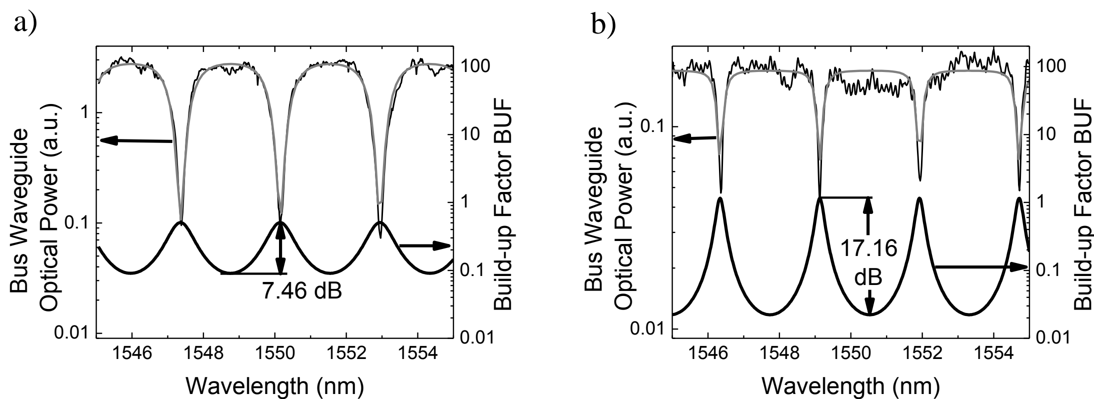

Figure 6.15: a) Waveguide transmission spectrum for symmetric add-drop racetrack resonators of 30 μm radius and 10 μm long coupling section (black curve, left axis) along with a fit of Eq. (2.79) (grey curve, left axis), and the corresponding variation in *BUF* described by Eq. (2.90) (black curve, right axis) for a) 200 nm coupling gap and b) 300 nm coupling gap.

TABLE 6.2: Extracted build-up factor of symmetric add-drop micro-rings of varying geometry following an anneal at T = 300 C.

Gap Distance (nm)	Radius (μm)	Coupling Length (μm)	*A*	*t*	*BUF* (on-resonance)	*BUF* ratio (dB)
200	20	10	0.890 ± 0.018	0.841 ± 0.005	1.19 ± 0.14	12.85 ± 5.11
250	20	10	0.890 ± 0.018	0.875 ± 0.006	1.40 ± 0.19	14.43 ± 6.81
300	20	10	0.890 ± 0.018	0.951 ± 0.004	1.81 ± 0.43	19.33 ± 13.33
200	25	10	0.868 ± 0.023	0.697 ± 0.021	0.56 ± 0.04	7.81 ± 1.61
250	25	10	0.868 ± 0.023	0.856 ± 0.009	1.11 ± 0.14	13.04 ± 5.38
300	25	10	0.868 ± 0.023	0.950 ± 0.010	1.42 ± 0.31	18.33 ± 12.00
200	30	10	0.847 ± 0.045	0.691 ± 0.040	0.51 ± 0.04	7.46 ± 1.50
250	30	10	0.847 ± 0.045	0.870 ± 0.015	1.02 ± 0.13	13.20 ± 5.62
300	30	10	0.847 ± 0.045	0.945 ± 0.005	1.15 ± 0.23	17.16 ± 10.48
200	20	0	0.905 ± 0.016	0.975 ± 0.002	1.95 ± 0.35	22.47 ± 7.30
250	20	0	0.905 ± 0.016	0.958 ± 0.002	2.14 ± 0.31	20.68 ± 8.11
300	20	0	0.905 ± 0.016	0.969 ± 0.002	2.07 ± 0.34	21.75 ± 7.64
200	25	0	0.882 ± 0.029	0.956 ± 0.003	1.63 ± 0.21	19.38 ± 8.55

The results of Table 6.2 pertaining to the racetrack device elucidate two geometrical influences on the build-up factor. First, as the coupling gap is increased, the coupling coefficient t is increased (or κ is decreased), and the *BUF* is enhanced. Since the coupling is symmetric, the ring is over-coupled for any value $A < 1$, and increasing either t or A brings it closer to a critically coupled state. This is indicated specifically in Figure 6.15, where increasing the gap width from 200 nm to 300 nm improves the *BUF* by a factor of two. Second, there is particular evidence that the build-up factor improves in proportion with the *Finesse*. As the ring radius is increased, the *Finesse* is reduced and consequently so is the *BUF*. Equivalently, for a given excess absorption coefficient α, the value of A will be smaller for a larger circumference ring, which decreases the *BUF*.

Also of interest is the device with similar geometry to the all-pass device discussed above (200 nm gap width, 20 μm radius, and 0 μm coupling length), save for the presence of a second waveguide bus. This device has a *BUF* of approximately 2,

which is more than an order of magnitude less than the corresponding all-pass device. Also, compared to the racetrack structures that feature a 10 μm long coupling region, the resonance of these devices is much less sensitive to variations in gap width.

Of note is the fact that the *BUF* falls below unity for several of these over-coupled devices, and they consequently perform poorer than a non-resonant device of similar geometry. The optimum symmetric all-pass devices are therefore those having a large coupling gap, small radius and large annealing temperature. Alternatively, designs featuring an asymmetric add-drop configuration could achieve critical coupling for a finite absorption strength *A*, similarly to the all-pass configuration.

In addition to the resonant *BUF* value, its ratio to the off-resonance *BUF* value is also of interest. This metric, indicated on Figure 6.16 and on the far right column of Table 6.2, provides a measure of the strength of the wavelength-selection of the photodetector. When used in de-multiplexing wavelength channels on a PIC, this is of critical importance.

The photodiode current spectra of the circular-type micro-ring resonators are plotted in Figure 6.16a. Due to variation in facet quality, it is difficult to make quantitative comparisons between the responsivity of these devices, as the on-chip optical power is not the same. It is, however, possible to compare the change in resonant current enhancement to that predicted by Table 6.2. The resonant current enhancement is measured from Figure 16.6a to range from 8.8 to 11.9 dB. The minimal variation is expected from the (almost) constant *BUF* ratio of these devices (19.4-22.5 dB).

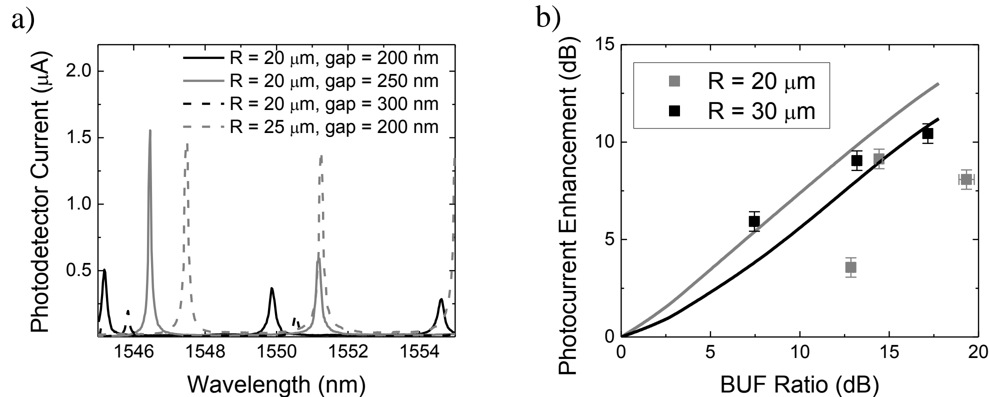

Figure 6.16: a) Photodetector current spectrum for circular-type add-drop micro-rings, measured at -20 V bias; b) plot of the measured (points) and simulated (curves) resonant enhancement of the racetrack type devices as a function of *BUF* ratio.

The resonant current enhancement is plotted against the *BUF* ratio in Figure 6.16b for racetracks of 20 μm and 30 μm radius. The simulated response is plotted as curves. There is a general increase in measured resonant photocurrent as the *BUF* is increased that is in relative agreement with the simulation, which is evidence of the role of resonant enhancement in the photodetection for the add-drop devices also. The 20 μm radius devices, having a smaller ring circumference, contain a smaller photodiode length than those of 30 μm radius. However, the 20 μm radius device also has a larger *Finesse*, and therefore a larger *BUF*. In the ATLAS simulation, this superior *BUF* was sufficient to provide the 20 μm radius device with a slightly larger photocurrent, as shown by the grey line. However, due to the poor performance of the two extreme 20 μm radius devices, the measured photocurrent of the 30 μm radius devices were found to be generally larger.

6.4 Summary

This chapter has described the design and fabrication of photodiodes integrated onto micro-rings to achieve a resonant-enhanced responsivity. In an all-pass configuration, a resonant enhancement of 12 dB was observed, producing a responsivity of 67 mA/W. A 50 µm long resonant photodiode was equal in responsivity to a 4 mm long non-resonant photodiode, while having a *NEP* that was smaller by a factor of 30. The nature of the photocurrent enhancement though the build-up factor was discussed, as well as the performance of the micro-rings when introduced with defects. The selection of device geometry and defect content to maximize resonant enhancement was described and shown to agree with theory. This demonstrates a method towards effecting reduction in photodiode size for end-line and in-line photodetection without sacrificing responsivity.

References

[1] M. W. Geis, S. J. Spector, M. E. Grein, J. U. Yoon, D. M. Lennon, and T. M. Lyszczarz, "Silicon waveguide infrared photodiodes with >35 GHz bandwidth and phototransistors with 50 AW^{-1}," *Optics Express,* vol. 17, pp. 5193-5204, 2009.

[2] C. A. Barrios, V. Rosa de Almeida, and M. Lipson, "Low-power-consumption short-length and high-modulation-depth silicon electrooptic modulator," *Journal of Lightwave Technology*, vol. 21, pp. 1089-1097, 2003.

[3] A. R. M. Zain, M. Gnan, H. M. H. Chong, M. Sorel, and R. M. De La Rue, "Tapered photonic crystal microcavities embedded in photonic wire waveguides with large resonance quality-factor and high transmission," *Photonics Technology Letters*, vol. 20, pp. 6-8, 2008.

[4] H. Chen, X. Luo, and A. W. Poon, "Cavity-enhanced photocurrent generation by 1.55 μm wavelengths linear absorption in a p-i-n diode embedded silicon microring resonator," *Applied Physics Letters*, vol. 95, pp. 171111-171113, 2009.

[5] "RSoft BeamPROP version 8.1 User Guide," www.rsoftdesign.com, RSoft Design Group, Inc., Ossining, NY.

[6] H. Qing-Zhong, Y. Jin-Zhong, C. Shao-Wu, X. Xue-Jun, H. Wei-Hua, and F. Zhong-Chao, "Design, fabrication and characterization of a high-performance micro-ring resonator in silicon-on-insulator," *Chinese Physics B,* vol. 17, pp. 2562-2566, 2008.

[7] S. Xiao, M. H. Khan, H. Shen, and M. Qi, "Compact silicon micro-ring resonators with ultra-low propagation loss in the C band," *Optics Express*, vol. 15, pp. 14467-14475, 2007.

[8] "RSoft FullWAVE version 6.1 User Guide," www.rsoftdesign.com, RSoft Design Group, Inc., Ossining, NY.

[9] W. R. McKinnon, D.-X. Xu, C. Storey, E. Post, A. Densmore, A. Delâge, P. Waldron, J. H. Schmid, and S. Janz, "Extracting coupling and loss coefficients from a ring resonator," *Optics Express*, vol. 17, pp. 18971-18982, 2009.

Chapter 7 Demonstration of Integrated Power Monitor on Micro-ring Ports

7.1 Overview

One of the greatest advantages of defect-enhanced photodetection is the facility for power monitoring. This involves the absorption of small fractions of the waveguide's optical power for detection while allowing the remainder to continue unperturbed. The variation in responsivity and excess absorption provided through either the implantation dose or post-implantation annealing permits precise engineering of the properties of such monitors, as devices annealed at higher temperatures (> 350 C), or with a relatively small dose (< 1×10^{11} cm^{-2}) have limited absorption levels. In the extreme case where monitoring is required for diagnostic purposes only (i.e. for wafer-scale testing), the absorption can be removed (almost) entirely by a post-implantation anneal at temperatures above 450 C.

This chapter describes a power monitoring application for the photodetector whose design is described in chapter 5, and whose operation is demonstrated through integration with the (un-implanted) micro-rings of chapter 6. Specifically, 250 μm long *p-i-n* photodiodes are integrated onto the bus waveguides of an add-drop micro-ring resonator as shown in Figure 7.1a. These devices, labeled as *through-port photodetector* and *drop-port photodetector*, reproduce the propagating optical power spectra of the signals in these respective bus waveguides. This provides the means to characterize the optical properties of the micro-ring without compromising the function of it, or the other elements on the chip. These monitor levels may be used to provide feedback to an ohmic heater on the ring, which tunes its resonance properties.

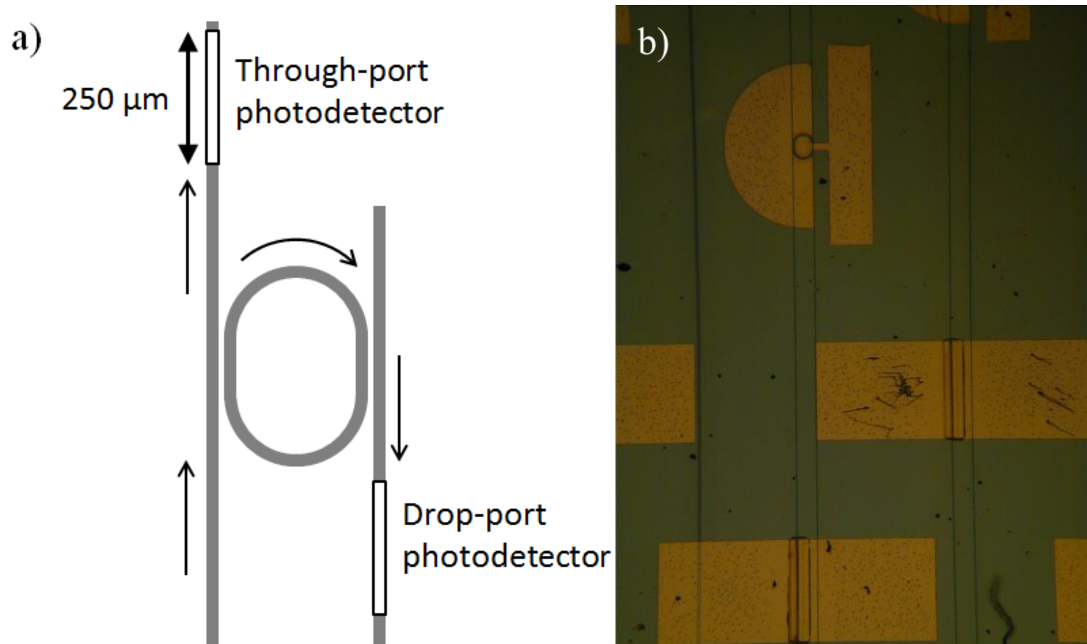

Figure 7.1: a) Schematic representation of integrated power monitors on the bus waveguides of an add-drop micro-ring, labelled 'through-port photodetector' and 'drop-port photodetector'; b) Optical microscope image of a chip during characterization, featuring a micro-ring (with an integrated *p-i-n* junction) and a power monitor integrated onto its left bus waveguide.

The power monitors have a cross-sectional geometry identical to those presented in chapter 5, and the micro-rings are similar to those presented in chapter 6. One type of micro-ring was a racetrack resonator with 25 µm semi-circular radius and 10 µm long coupling region with a 250 nm coupling gap. The second structure was a circular micro-ring with 20 µm radius and 200 nm evanescent point coupler gap.

7.2 Characterization of Ring Resonant Power Monitors

The 250 µm long power monitors induce excess optical absorption which was quantified and as shown in Figure 5.13b and tabulated in Table 6.1. The concentration of

defects is reduced following post-implantation annealing and consequently 30% of the incident power is absorbed as the signal passes through the 250 μm detector following a 275 C anneal; 14% is absorbed following the 300 C anneal; 8% is absorbed following the 350 C anneal; and 5% is absorbed following the 400 C anneal. These losses result in a peak detector responsivity (in mA/W) at 300 C; although the effective quantum efficiency (see Eq. (3.10)) is maximized at 350 C. There is thus some latitude in the necessary power absorbed by the monitor, depending on the electrical signal level required.

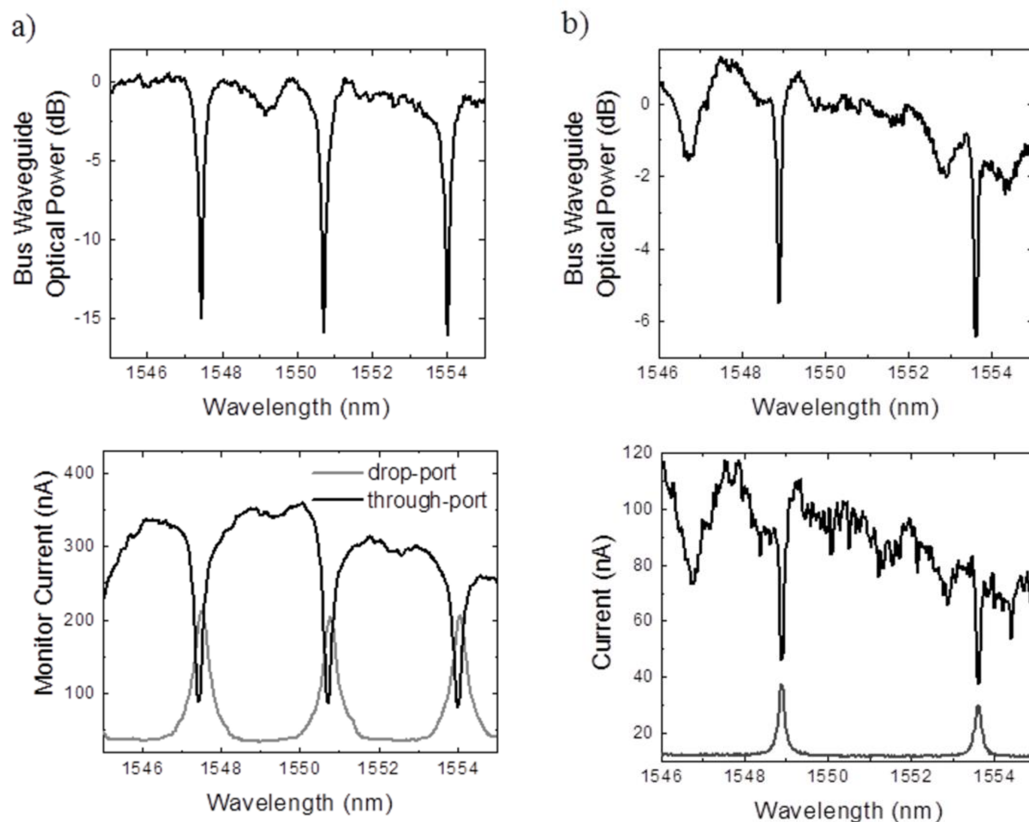

Figure 7.2: The optical resonance drop in the bus waveguide transmission (top), and current measured at -20 V bias from power monitors (bottom) integrated onto the drop-port (grey curve) and through-port (black curve) for a) the racetrack resonator design and b) the ring resonator design.

The bus waveguide transmission for each of the add-drop rings is plotted as the top portion of Figure 7.2a and b. The optical response of the racetrack type resonator, plotted in Figure 7.2a, features an extinction ratio of 15 dB, a free-spectral range of λ_{FSR} = 3.28 ± 0.03 nm, and a linewidth of $\Delta\lambda$ = 0.16 ± 0.03 nm. The optical response of the circular micro-ring resonator, plotted in Figure 7.2b, features an extinction ratio of 5.5 dB, a free spectral range of λ_{FSR} = 4.68 ± 0.03 nm, and a linewidth of $\Delta\lambda$ = 0.12 ± 0.04 nm.

The lower portion of Figure 7.2 plots the monitor current response as a function of wavelength, following a 5 minute 350 C anneal. The drop-port photodetector provides a clear low-noise signal of the resonance, with dark current conditions at off-resonance and an 8 dB and 5 dB resonant signal increase for the racetrack and circular rings, respectively. The through-port photodetector reproduces both the resonant transmission drop and other interference effects on the bus waveguide, similarly featuring a 6 dB and 3.4 dB signal decrease on resonance. The linewidth extracted from the through-port monitor current is in good agreement with that extracted from the optical transmission spectra.

The direct measurement of the monitor photocurrent (i.e. coupling directly onto the drop port) provides a measured monitor responsivity of 9.5 mA/W, or n_{eff} = 9.5% at 20 V reverse bias. It is noted that there should be loss in the optical coupling process, particularly since these add-drop micro-rings, being symmetric, are not critically coupled. The presence of loss is indicated clearly in Figure 7.2 through comparison of the off-resonance signal of the through-port monitor to the on-resonance signal of the drop-port monitor. The ‘racetrack type’ micro-ring is evidently the closer of the two to being critically coupled, as the drop-port and through-port signals are closest to mirror images at resonance.

The implementation of a power monitor that consumes 8% of the mode power to provide measurements of power levels, as well as linewidths and extinction ratios of micro-rings in the circuit, is thus demonstrated.

7.3 Applications of Integrated Functionality

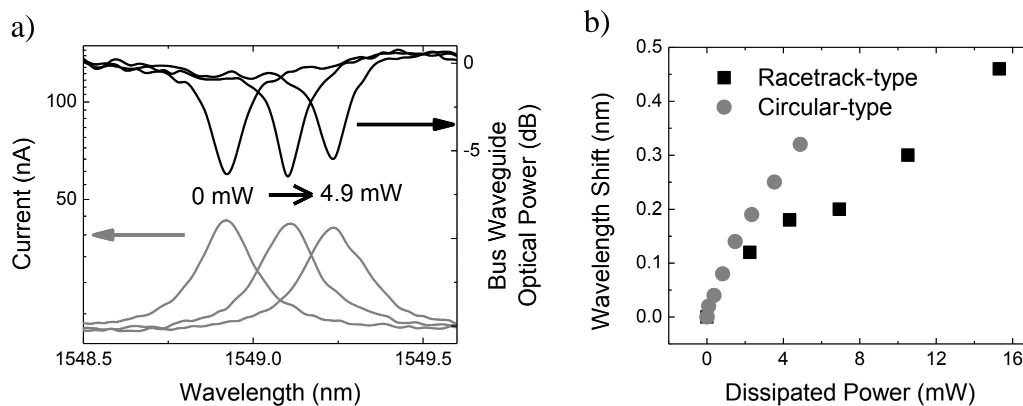

Figure 7.3: a) The Drop-port monitor current (left axis) and bus waveguide transmission (right axis) for applied ohmic heater power of 0 mW, 2.3 mW and 4.9 mW for the 'circular-type' micro-ring resonator; b) Wavelength shift observed in resonance vs. applied power to the *p-i-n* junction for each resonator type.

The advantage of these devices becomes greatest when the optical properties of the micro-ring resonators are able to be tuned, for example via ohmic heating. Integrated with these micro-rings were *p-i-n* junctions, as described in chapter 6, which when forward biased injected current, and thus heat into the device. For instance, Figure 7.3a plots the drop-port signal on the left axis and optical transmission on the right axis for the circular-type micro-ring, as the diode is forward biased at 0, 3, and 4 V. The dissipated power, calculated as the product of the bias and the current, causes the local temperature of the silicon waveguide to increase and consequently its refractive index to increase in a concomitant manner through the thermo-optic effect [1]. This modification in refractive

index causes a shift in resonance towards longer wavelengths, which is clearly detectable by the power monitors.

The wavelength shift of the circular-type and racetrack-type micro-rings is plotted against dissipated power in Figure 7.3b. As the *p*-*i*-*n* junction on the racetrack-type micro-ring is of a larger area, it has a larger dissipated power than the circular-type, when an equal bias is applied. Expressing the shift as a fraction of the free-spectral range (or a 2π phase shift), both devices provide similar shifts per unit dissipated power. Commonly, the power to shift by one-half free-spectral range (or a π phase shift) is provided as a figure of merit [2], which in this case is extrapolated to be $P_\pi = 35.4 \pm 0.3$ mW.

This is similar in efficiency ohmic resistor-type heaters formed of a thin high-resistance film deposited on top of the waveguide, which are more commonly used to thermally tune silicon photonic devices [2, 3]. It is, however, much less efficient than other designs that supply heat to silicon waveguides by passing current directly through it, which have reported efficiencies of $P_\pi = 6$ mW [4]. The weaker efficiency here is believed to be a result of both the low resistance and limited power range of a forward biased *p*-*i*-*n* junction, which is not an ideal device to provide local heating. These devices were in fact designed to provide a more efficient resonance shift to shorter wavelengths by the plasma dispersion effect (i.e. through a change in carrier concentration alone; see section 2.2). No such shift was observed, possibly due to a short carrier lifetime caused by surface states existing at the etched silicon/SiO_2 interface.

A stable wavelength was coupled into the bus waveguide, and the drop-port monitor signal was measured as the micro-ring *p*-*i*-*n* junction was swept in bias. The drop-port current for the ‘circular-type’ device is plotted in Figure 7.4a for two such input wavelengths, and the drop-port current for the ‘racetrack-type’ device is plotted in Figure 7.4b for another set of input wavelengths. Sweeping the bias on the *p*-*i*-*n* junction is equivalent to sweeping the injected wavelength, in that it provides a measure of the resonant width of the ring. In this case, however, this measurement is provided without

the requirement of a tunable laser, and can conceivably be made using the on-chip lasers available on the chip during wafer-scale testing.

For each wavelength in Figure 7.4, the monitor signal reaches a maximum level for a specific dissipated power level. On PICs, micro-rings designed to operate at (for example) 1551.1 nm will suffer variation due to fabrication non-uniformities or fluctuations in ambient temperature. The feedback from the drop-port monitor may be used to control the ohmic heater to tune these micro-rings to within specification, as shown in Figure 7.4.

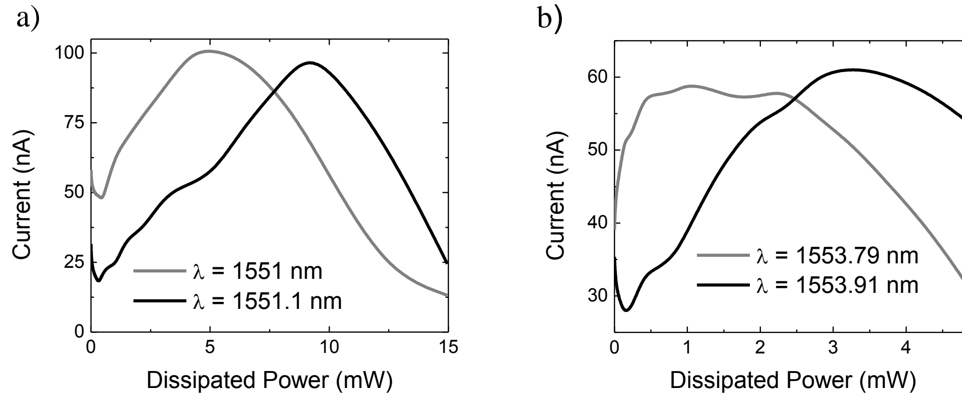

Figure 7.4: Drop-port monitor current plotted against micro-ring tuning power, using a constant wavelength input; a) on the racetrack-type device with 1551 and 1551.1 nm input, and b) on the circular-type device with 1553.79 and 1553.91 nm input.

7.4 Summary

This chapter served to provide a demonstration of the function of a defect-enhanced photodetector on a PIC. There are many suitable applications of power monitoring both during wafer-level testing and during the course of device operation. As has been shown here, these include measuring power levels and the optical characteristics of micro-rings, and these monitor signals can then be used to guide the adaptive tuning of

these elements throughout operation. Indeed, defect-enhanced photodetection provides the most straight-forward method of serving these functions in future silicon PICs.

References

[1] S. A. Clark, B. Culshaw, E. J. C. Dawney, and I. E. Day, "Thermo-optic phase modulators in SIMOX material," *Proc. of SPIE*, vol. 3936, pp. 16-24, 2000.

[2] I. Kiyat, A. Aydinli, and N. Dagli, "Low-power thermooptical tuning of SOI resonator switch," *IEEE Photonics Technology Letters*, vol. 18, pp. 364-366, 2006.

[3] X. Wang, J. A. Martinez, M. S. Nawrocka, and R. R. Panepucci, "Compact thermally tunable silicon wavelength switch: modeling and characterization," *IEEE Photonics Technology Letters,* vol. 20, pp. 936-938, 2008.

[4] M. W. Geis, S. J. Spector, R. C. Williamson, and T. M. Lyszczarz, "Submicrosecond submilliwatt silicon-on-insulator thermooptic switch," *IEEE Photonics Technology Letters*, vol. 16, pp. 2514-2516, 2004.

Chapter 8 Summary, Conclusions and Suggested Future Work

8.1 Summary of Accomplished Work

This thesis serves as an exploration of the capabilities of defect-enhanced photodetectors for use in photonic integrated circuits. The operating principles, design methods, fabrication, characterization, and application of these devices have been thoroughly reported herein.

The physics governing the operation of these devices was described in **Chapter 3**, where the use of a single-level model of the detection process was justified and implemented using the single negatively-charged level of the divacancy. This model was incorporated into an ATLAS simulation, and was utilized throughout the remainder of the thesis to design device structures with either improved responsivity for end-line detection or improved quantum efficiency for power monitoring. The later sections of chapter 3 proposed some improvements on current device structures, including the revised location of doped regions and tailoring the profile of the defect-forming implant window.

A novel device design was presented in **Chapter 4**, which featured a junction formed on the top of an SOI waveguide formed using the LOCOS method and a polysilicon film deposition. The details of the fabrication process were provided, which was carried out primarily by the author in the CEDT facilities at McMaster University, with selected process steps performed at Carleton University and the University of Western Ontario. The characterization of the photodetectors was also described in detail, and the results were compared to the values obtained from simulation. While there were some unresolved issues with the junction behaviour between the polysilicon and the

silicon ridge, there was a correlation between modeled and measured trends in photocurrent with changes in device geometry and defect content.

The design and fabrication of sub-micron waveguide photodetectors was described in **Chapter 5**. The fabrication was carried out by the author in the James Watt Nanofabrication Centre at the University of Glasgow, predominantly using the electron-beam lithography system. The measurement of the devices yielded excellent performance, with very strong agreement with modeled behaviour. A discussion of the main limitation of defect-enhancement was also included, being that the low absorption coefficient leads to the consumption of large lengths of waveguide by the photodiode.

The integration of defect-enhanced photodiodes with resonator structures was put forward in **Chapter 6** as a means of reducing the size of photodiodes. The design of an appropriate all-pass ring resonator structure was described, selected to maximize the resonant enhancement of absorption. This structure was fully characterized optically and electrically, and produced a responsivity which was enhanced by 12 dB on resonance. Moreover, the optical resonance properties were used to predict the enhancement factor for several annealing stages, and this was incorporated back into the model to predict the photocurrent with a high degree of accuracy. Also, the use of add-drop resonant structures was demonstrated, and results produced further agreement with the model's predictions.

Finally, the application of a sub-micron photodiode as a monitor of micro-ring performance was discussed in **Chapter 7**. These monitors, placed on both ports of an add-drop micro-ring, absorbed 8% of the waveguide power and produced a signal which was proportional to the micro-ring resonance. These are very useful in characterizing devices during wafer-scale testing and in monitoring ring performance during PIC operation. For the latter instance, it was shown that the monitor signal can be used as feedback to tune the micro-ring's resonance wavelength, to compensate thermal drift.

While this thesis effectively explored several aspects of defect-enhanced photodetectors, there remains a substantial amount of work to be undertaken with this relatively new device structure. The remainder of this chapter will suggest some areas ripe for investigation.

8.2 Suggested Future Work

8.2.1 Modeling defect-enhanced photodetection

The defect-enhanced photodiode is in position to become a key component of silicon PICs. Not only does it currently offer advantages over other more established technologies, the physical process governing its operation is general in that it can be extended to other defect types. Since the absorption provided by the divacancy is relatively modest, an exploration of other defect types may yield more strongly absorbing centers. This will permit the shortening of photodiode lengths to the point where they are competitive with integrated germanium photodiodes in end-line detection. Alternatively, a more efficient device center may be found, in that it provides strong optical generation with lower electrical capture cross-sections. The increase in device efficiency will be beneficial to power monitor applications, to produce a large signal per fraction of absorbed power. The simulation model is crucial in determining what the optimum defect parameters are for a given application.

To further increase the accuracy of the model for the current implantation-induced defects, it will become necessary to incorporate the influence of multiple defects. Before this can be started, it is first necessary to identify which defects are present in the device, and their concentration as a function of ion dose and annealing temperature.

8.2.2 LOCOS-based photodetectors

For the LOCOS-based design to be of use in applications, some investigation of alternative fabrication techniques is required. Particularly, the deposition and doping of the polysilicon film needs to be optimized by exploring a wider range of processes. In particular, the method of *in situ* doping of phosphorus in polysilicon deposition processes should be explored as a means to improve phosphorus dopant activation [1]. As well, a passivation of the dangling bonds in the grain boundaries in a hydrogen plasma would remove a large quantity of defects, thereby reducing the dark current [2].

Should these issues be adequately addressed, further development of these devices would involve scaling down to sub-micron dimensions. By forming symmetric p^+ contacts and a top *n*-type polysilicon contact onto a sub-micron waveguide design, the improved carrier extraction will become more pronounced. Additionally, forming a micro-ring photodiode from a low-loss LOCOS waveguide would enable a large Q-factor and therefore large photocurrent enhancement.

8.2.3 Resonant enhanced photodiodes

As the build-up factor generally scales with the Finesse, structures with a larger λ_{FSR} will exhibit a stronger resonant enhanced photocurrent. In a micro-ring architecture, this would be realized by decreasing the radius of the ring. A much more substantial improvement would be obtained by using the micro-cavity architecture illustrated in Figure 6.1. Since the cavity size is on the order of ~ 400 nm, the λ_{FSR} is on the order of 1 μm, so typically only one resonance is observed in the 350 nm wide reflection band [3]. Consequently, a resonant linewidth of 0.1 nm will have a corresponding ideal build-up factor of a microcavity on the order of 2500, two orders of magnitude larger than that achieved from a micro-ring configuration.

8.2.4 Measurement of photodiode bandwidth

This thesis has mentioned bandwidth as a motivation for reduction of photodiode length, as the capacitance currently limits their speed. The measurement of speeds above >200 MHz is outside of the capabilities of McMaster University, and therefore concrete evaluations of bandwidth have not been performed. The most necessary future work is the design of proper contact structures on the devices to allow for such measurements to be made. A characterization of the dependence of bandwidth on defect concentration is important at this stage, as it will guide the design of future devices.

As well, the bandwidth of the micro-ring resonant photodiodes must be determined. While they are expected from their capacitance to operate at higher speeds, they may become limited by the photon lifetime (see Eq. (2.69)). For the Q-factor of 26 000 measured in chapter 6, the expected photon lifetime is approximately 21 ps, and therefore the bandwidth is approximately 7.5 GHz. Direct quantification of this effect will also influence future designs, as a large Finesse is required for high responsivity but a modest Q-factor is required for high bandwidth. These requirements would be obtained by a resonator with a large $\lambda_{F\mathrm{SR}}$ but moderate linewidth.

8.2.5 Integration of defect-enhanced photodiodes onto PICs

As stated in chapter 7, the largest current application of defect-enhanced photodiodes is in-line power monitoring. These devices may be fabricated with low insertion loss and with short lengths, such that a small amount of optical power is removed from the optical mode. These are a valuable diagnostic tool, as they can be used throughout the circuit to ensure correct operation. It is reasonable to expect further demonstration of increasingly complex integrated functionality of power monitors in the near future.

In addition, the resonant photodetectors may be applied as compact de-multiplexers within receivers. This structure would consist of a bus waveguide that contains multiple ring resonators, each having a resonance tuned to a different channel wavelength. When a WDM signal is transmitted along the bus waveguide, it is decomposed in a serial fashion as each micro-ring couples a channel and converts it to an electrical signal using the integrated photodiode. If the complete optical-to-electrical conversion is required, the all-pass micro-ring architecture should be utilized. If, however, some optical signal is required to stay on the chip, the add-drop architecture should be used. Such a de-multiplexing architecture can potentially reduce the footprint of receivers, as no arrayed waveguide grating is required.

References

[1] D. Briand, M. Sarret, F. Le Bihan, O. Bonnaud, and L. Pichon, "Polysilicon *in situ* phosphorus doping control over large concentration range using low temperature, low pressure chemical vapour deposition growth process." *Materials Science and Technology*, vol. 11, pp. 1207-1209, 1995.

[2] I-W. Wu, T-Y. Huang, W. B. Jackson, A. G. Lewis, and A. Chiang, "Passivation kinetics of two types of defects in polysilicon TFT by plasma hydrogenation." *IEEE Elect. Dev. Lett*., vol 12, pp. 181-183, 1991.

[3] A. R. M. Zain, M. Gnan, H. M. H. Chong, M. Sorel, R. M. De La Rue, "Tapered photonic crystal microcavities embedded in photonic wire waveguides with large resonance quality-factor and high transmission," *Photonics Technology Letters*, vol. 20, pp. 6-8, 2008.

Appendices

A ATLAS Source Code Example for Photodetector Simulation

Below the ATLAS script defines the structure of the device described in Chapter 5.

```
go atlas

#Below, the mesh is formed for the simulation

mesh space.mult = 1
x.mesh location=0 spacing=0.01
x.mesh location=3.64 spacing=0.01
y.mesh location=-0.3 spacing=0.01
y.mesh location=0 spacing=0.01
y.mesh location=0.2 spacing=0.2

#The structure is built in ATLAS in this simulation. Alternatively, it
#could be fabricated in ATHENA and imported.

region number=1 material=oxide x.min=0 x.max=3.64 y.min=-0.3 y.max=0
region number=2 material=oxide x.min=0 x.max=3.64 y.min=0 y.max=0.2
region number=3 material=silicon x.min=0 x.max=1.07 y.min=-0.05 y.max=0
region number=4 material=silicon x.min=1.07 x.max=1.57 y.min=-0.05 y.max=0
region number=5 material=silicon x.min=1.57 x.max=2.07 y.min=-0.22 y.max=0
region number=6 material=silicon x.min=2.07 x.max=2.57 y.min=-0.05 y.max=0
region number=7 material=silicon x.min=2.57 x.max=3.64 y.min=-0.05 y.max=0

#The electrodes are now defined: the cathode (the n type region) and
#the anode (the p type region)

electrode number=1 name=cathode x.min=3.07 x.max=3.64 y.min=-0.25 y.max=-0.05
electrode number=2 name=anode x.min=0 x.max=0.57 y.min=-0.25 y.max=-0.05
```

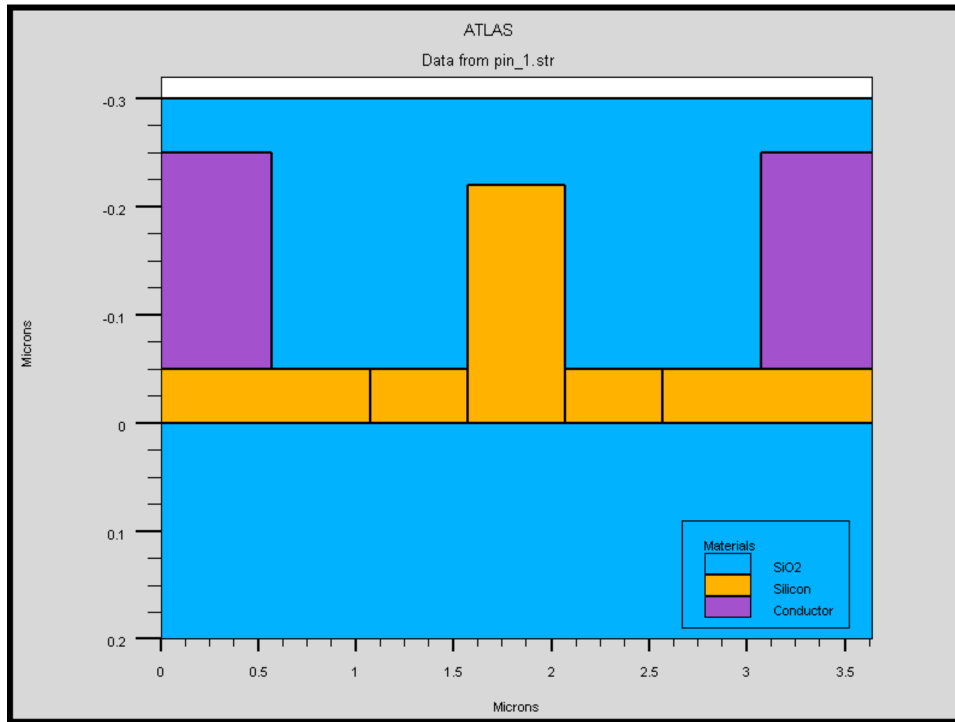

Figure A.1: ATLAS output of built silicon waveguide structure embedded in SiO_2 and contacted with aluminum.

The script next attributes doping levels and defect properties to the different regions of the device.

```
#The doping level for each region is now defined

doping uniform concentration=5e19 p.type region=3
doping uniform concentration=5e15 p.type region=4
doping uniform concentration=5e15 p.type region=5
doping uniform concentration=5e15 p.type region=6
doping uniform concentration=5e19 n.type region=7

#An intrinsic carrier lifetime is given for silicon, based on limits
#of surface recombination

material material=silicon taun=1e-8 taup=1e-8

#The carrier lifetime limitations provided by defects are handled by the
#following statements, which provide a trap level 0.4 eV below the conduction
#band with capture cross-section of electrons and holes of sign and sigp,
#respectively. The concentration of the defects in this case is set to be 2e17.
#They are introduced into several regions of the structure, which correspond
#to the implanted regions
```

```
trap e.level=0.4 acceptor density=2e17 degen=1 sign=3.65e-15 sigp=3.6e-14
region=4
trap e.level=0.4 acceptor density=2e17 degen=1 sign=3.65e-15 sigp=3.6e-14
region=5
trap e.level=0.4 acceptor density=2e17 degen=1 sign=3.65e-15 sigp=3.6e-14
region=6
```

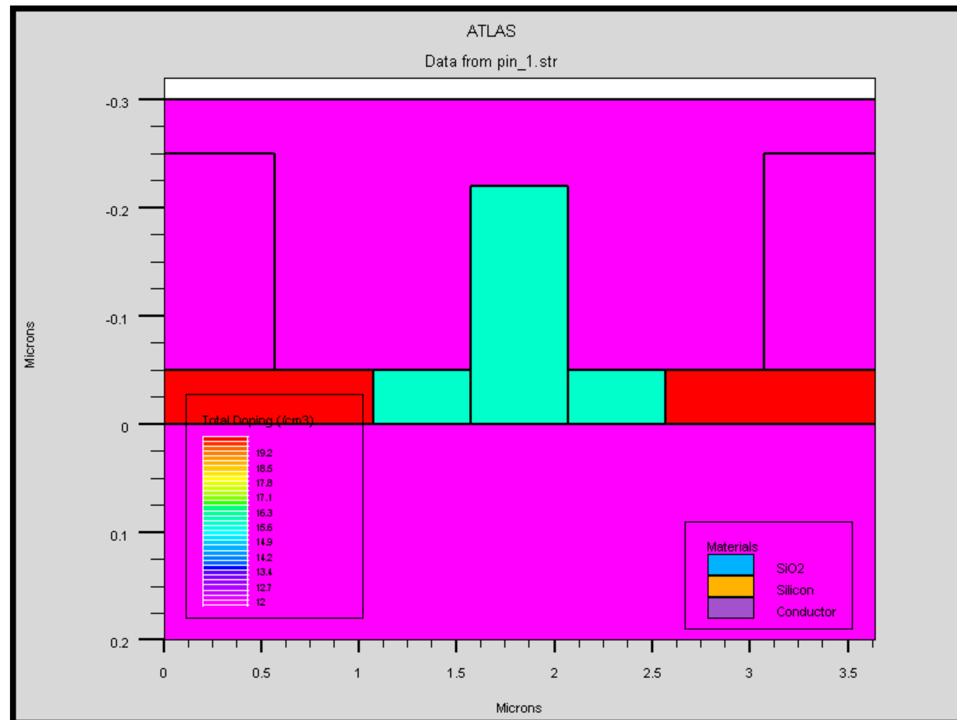

Figure A.2: ATLAS output of doping levels present in the device.

With the structure defined, the code goes on to solve the structure for a reverse bias of 5 V.

```
#Specify models to be used in ATLAS calculation: concentration and field
#dependent mobility, concentration dependent Shockley-Read-Hall recombination,
#Auger recombination, and Band-gap narrowing

model    conmob  fldmob  consrh  auger  bgn

#specify contact to be used in calculation

contact    name=cathode

#solve unbiased structure
```

```
solve    init outf=pin_0.str master

#call c file containing mode shape (see below) of optical generation rate

beam   num=1 F.RADIATE=submicron_mode.c

#specify solution method to be used, and ramp up positive bias on cathode

method  newton trap
solve    init
solve   vcathode=0.01
solve   vcathode=0.05
solve   vcathode=0.1
solve   vcathode=1.0
solve   vcathode=2
solve   vcathode=5
```

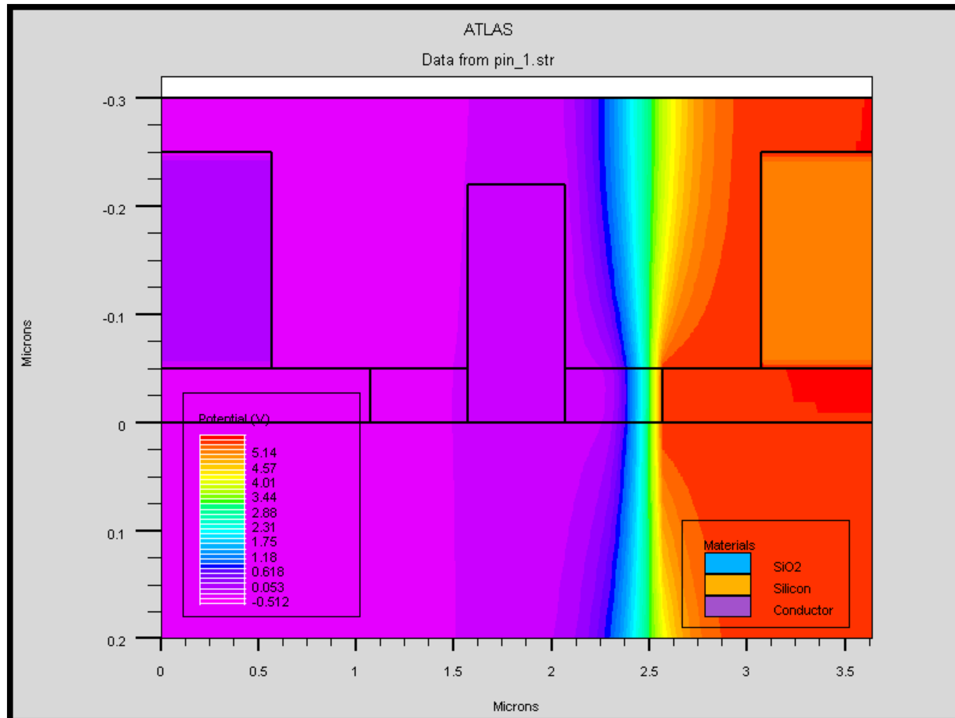

Figure A.3: ATLAS output of potential distribution in the device upon application of a 5 V reverse bias.

Lastly, the optical generation rate is applied, to reflect an injected power of 0.115 mW.

```
#ramp up intensity to optical generation rate, and save final structure as
pin_1.str

solve b1=1e2
solve b1=1e3
solve b1=5e3
solve b1=2e4
solve b1=3e4
solve b1=6e4
solve  b1=1e5 outf=pin_1.str master
```

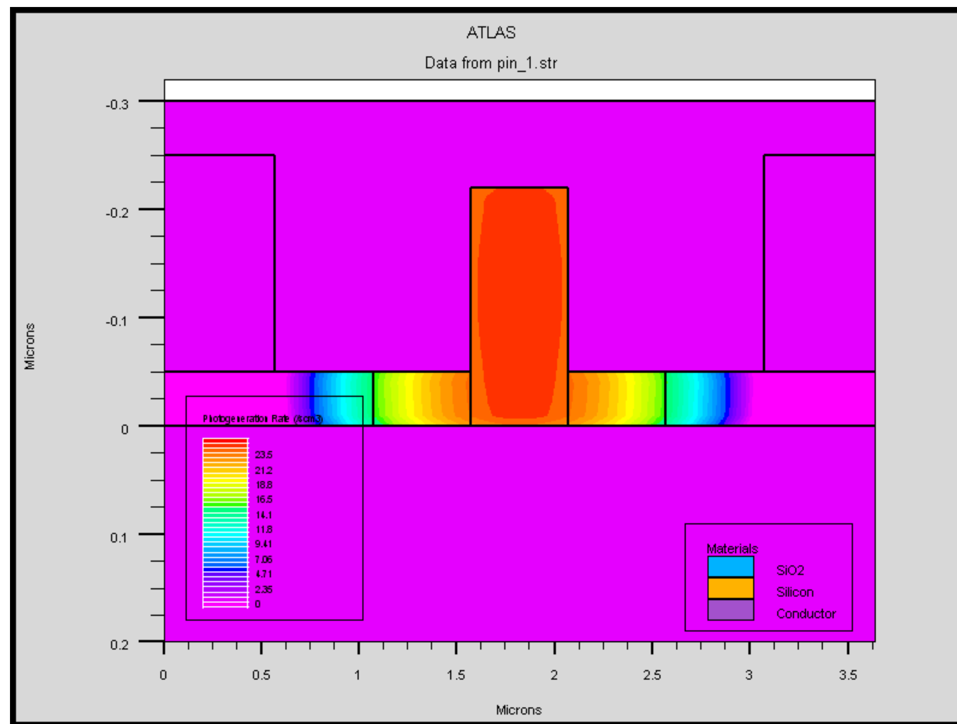

Figure A.4: ATLAS output of photogeneration rate in the device, upon launch of 0.115 mW optical power.

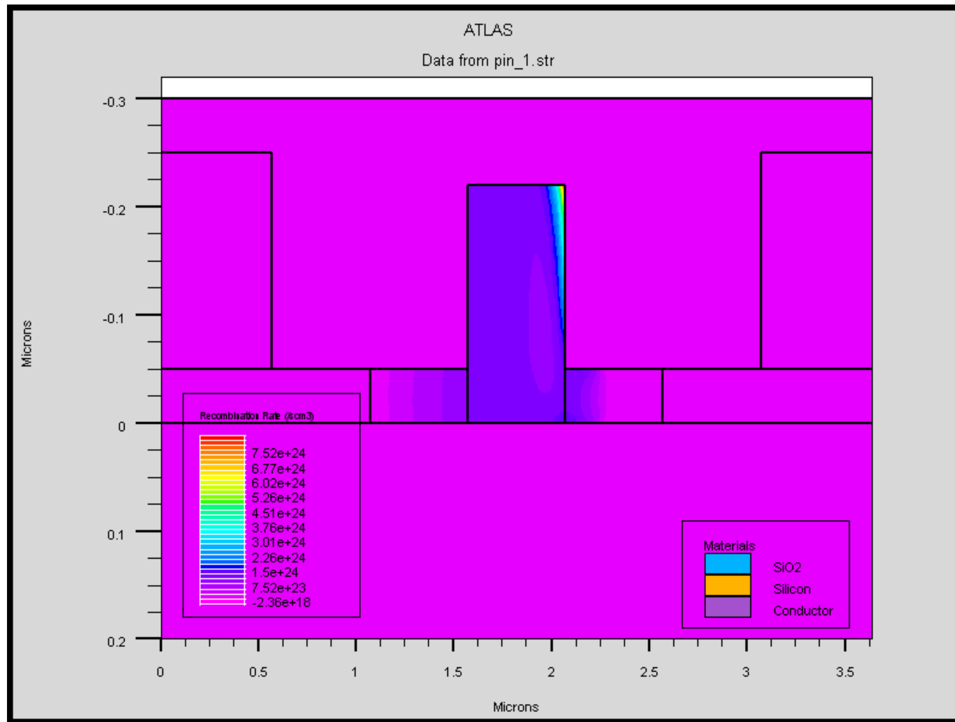

Figure A.5: ATLAS output of recombination rate in the device upon application of a 5 V reverse bias and launch of 0.115 mW optical power.

Below is the 'submicron_mode.c' file used in the ATLAS script:

```
#include <stdio.h>
#include <stdlib.h>
#include <math.h>

/*
 * Generation rate as a function of position
 * Statement: BEAM
 * Parameter: F.RADIATE
 * Arguments:
 * x           location x (microns)
 * y           location y (microns)
 * t           time (seconds )
 * *rat        generation rate per cc per sec.
 */

int radiate(double x,double y,double t,double *rat)
{
       double power;
       double x2;
       double y2;
```

```
        double sx;
        double sy;

        sx = 0.1571;
        sy = 0.11466;
        x2 = (x-1.82)/sx;
        y2 = (y + 0.11)/sy;

        power = exp(-pow(x2,2))*exp(-pow(y2,2))/(3.14*sx*sy);

                    *rat = power*7.21e18;

       return(0);
}
```

When called, this file returns an electron-hole pair generation rate for each (x, y) point in the mesh. It assumes a Gaussian mode shape, approximated from the shape produced in a BeamPROP simulation. The rate '*rat' is calculated based on Eq. (3.9), taking into account the device length L and the defect concentration N_t. When varying N_t in a simulation, it therefore must be adjusted both in the 'submicron_mode.c' file and the trap statements of the ATLAS script.

The ATLAS script weights '*rat' by a value b1 representing the intensity in Wcm^{-2} (b1 = 1 represents an intensity of 1 mW/cm^2).

Expressing the intensity launched into the waveguide as:

$$I(x, y) = A\exp\left(-\frac{x^2}{2\sigma_x^{\ 2}}\right)\exp\left(-\frac{y^2}{2\sigma_y^{\ 2}}\right) \tag{A.1}$$

The launched power in the waveguide is:

$$P = \iint_{x,y} I(x, y)dxdy = 2\pi A\sigma_x\sigma_y \tag{A.2}$$

Therefore, the generation rate is multiplied by the following weight (i.e. b1):

$$A = \frac{P}{2\pi\sigma_x\sigma_y} \tag{A.3}$$

The statement in the script specifies b1 = 1e5 (i.e. 10^5 Wcm^{-2}), which is equivalent to a total launched power of P = 0.115 mW. Due to the integration of Eq. (3.7), the final generation rate

introduced into the device (plotted above) is in units of $cm^{-2}s^{-1}$, not $cm^{-3}s^{-1}$ as indicated in Figure A.4.

Since the ATLAS simulation by default assumes a thickness of 1 μm, the current output is in units of A/μm. However, due to the altered units of the input generation rate, the integrated current results (in units of A). However, since the integration was done over units of cm, the resulting current needs to be weighted by a factor of 10^4. Alternatively, the simulation may be adjusted to assume a thickness of 1 cm, so no weighting of the results is required.

B Chronological Compilation of Published Work

B.1 D. F. Logan, P. E. Jessop, A. P. Knights, "Modeling Defect Enhanced Detection at 1550 nm in Integrated Silicon Waveguide Photodetectors," Journal of Lightwave Technology, vol. 27, p. 930, 2009.

This journal article describes the work completed within the first year of my Ph. D. research. A significant portion of the contained material has been represented within chapter 3. It provides a summary of the operating physics of defect-enhanced photodetectors, reviews existing demonstrations, and proposes a model using ATLAS to simulate them. It is presented in full in the following pages.

© 2009 IEEE. Reprinted, with permission, from D. F. Logan, P. E. Jessop, and A. P. Knights, "Modeling Defect Enhanced Detection at 1550 nm in Integrated Silicon Waveguide Photodetectors," IEEE Journal of Lightwave Technology, April 2009.

This material is posted here with permission of the IEEE. Such permission of the IEEE does not in any way imply IEEE endorsement of any of McMaster University's products or services. Internal or personal use of this material is permitted. However, permission to reprint/republish this material for advertising or promotional purposes or for creating new collective works for resale or redistribution must be obtained from the IEEE by writing to pubs-permissions@ieee.org .By choosing to view this material, you agree to all provisions of the copyright laws protecting it.

930 JOURNAL OF LIGHTWAVE TECHNOLOGY, VOL. 27, NO. 7, APRIL 1, 2009

Modeling Defect Enhanced Detection at 1550 nm in Integrated Silicon Waveguide Photodetectors

Dylan F. Logan, Paul E. Jessop, and Andrew P. Knights

***Abstract*—Recent attention has been attracted by photo-detectors integrated onto silicon-on-insulator (SOI) waveguides that exploit the enhanced sensitivity to subbandgap wavelengths resulting from absorption via point defects introduced by ion implantation. In this paper, we present the first model to describe the carrier generation process of such detectors, based upon modified Shockley-Read-Hall generation/recombination, and, thus, determine the influence of the device design on detection efficiency. We further describe how the model may be incorporated into commercial software, which then simulates the performance of previously reported devices by assuming a single midgap defect level (with properties commensurate with the single negatively charged divacancy). We describe the ability of the model to highlight the major limitations to responsivity, and thus suggest improvements which diminish the impact of such limitations.**

***Index Terms*—Ion implantation, integrated optics, p-i-n photodiodes, photodetectors, ridge waveguides, semiconductor defects, semiconductor device, silicon-on-insulator (SOI) technology.**

I. Introduction

A. The Requirement for Optical Detection in Silicon Photonics

THE detection of the optical signal via optical to electrical conversion is one of the essential functions required in any integrated optical circuit (IOC) [1]. In the case of silicon photonics this presents a contradiction in the specification of homogeneous waveguides where virtual transparency is demanded of the waveguide itself (hence, the suitability of subbandgap wavelengths in silicon photonics), thus, preventing the straightforward integration of efficient detectors. Because the most convenient carrier wavelengths in silicon-based optical devices reside close to 1550 nm, any solution to this detection paradox should thus be capable of fast and efficient detection of photons of no greater than ~0.78 eV in energy. Although hybrid solutions are available [2], [3], a monolithic complimentary-metal-oxide-semiconductor (CMOS) compatible process is preferred.

One successfully developed approach to the CMOS compatible integration of detectors is the incorporation of germanium via direct growth onto the silicon substrate [4]–[6]. Although high performance devices have been demonstrated it is recognized that careful process control must be maintained during Ge growth on Si to prevent the introduction of an unacceptable concentration of lattice defects which are known to create excess optical loss and unacceptable dark current. Further, where polarization insensitive monitoring of signals is required the asymmetric nature of the Ge/Si waveguide detector is often unsuitable. A wholly silicon-based approach to sub-band detection was introduced by Knights *et al.* [7]. In their report, they described the use of midgap levels, which were deliberately introduced in a straightforward manner via ion implantation, to detect an optical signal of 1550 nm while confined in a silicon-on-insulator (SOI) waveguide. The rather modest performance of this device (responsivity of ~3 mA/W and bandwidth of 2 MHz [8]) restricted its potential use to power monitoring. Indeed, the ability to control the fraction of signal "tapped" through the variation of the concentration of the midgap levels suggested this device might be ideally suited to this role. The idea of defect mediated detection has since been explored by other groups, notably Liu *et al.* [9] and Geis *et al.* [10], [11]. The results reported in [10] and [11] are of particular significance as they show that with suitable engineering of the device dimension and control of the defect morphology through postimplantation annealing, integrated detectors can be fabricated with performance comparable with those based on III-V materials. Specifically, the speed and responsivity of such devices may be > 20 GHz and ~1 A/W, respectively.

Despite the experimental demonstration of fast and efficient, defect-mediated detection, to date there has been no attempt to model the detection process in such devices. Indeed, only cursory attempts have been made by the three groups that have demonstrated these detectors to explain the physical process underpinning the detection process. In view of the impact of varying the device dimensions on detector performance it would appear important to develop such a model that might predict with confidence the responsivity and bandwidth of defect mediated waveguide detectors. In this paper, we present such a model and demonstrate its integration into the commercial simulation software "ATLAS."

The paper is divided into three sections. The introduction is first completed with a detailed description of the differences between the devices reported to date by the groups at McMaster University, The Chinese University of Hong Kong, and MIT Lincoln Laboratories. This is justified by the subsequent use of the reported results as a test of the presented model. The second section describes in detail the model itself, beginning with our simplest description of the physical basis of the detection process and concluding with an explanation of its incorporation into the ATLAS platform. The final section compares the previously reported experimental results with values for responsivity, effective quantum efficiency and device capacitance (the present limit to speed of operation). The model is found to reproduce the experimental trend for each device type (i.e.,

Manuscript received February 18, 2008; revised April 25, 2008. Current version published April 17, 2009. This work was supported in part by the Natural Science and Engineering Research Council of Canada and by the Canadian Institute for Photonic Innovation.

The authors are with the Department of Engineering Physics, McMaster University, Hamilton, Ontario, Canada L8S 4L7 (e-mail: logand@mcmaster.ca; pjessop@mcmaster.ca; aknight@mcmaster.ca).

Digital Object Identifier 10.1109/JLT.2008.927752

0733-8724/$25.00 © 2009 IEEE

TABLE I
SUMMARY OF FEATURES OF REPORTED IMPLANTED INTEGRATED PHOTODETECTORS

Device origin	MM [8]	HK [9]	LL [10]
Waveguide width (w)	3μm*	3.8μm	0.52μm
Waveguide height (H)	5μm	4.3μm	0.22μm
Waveguide etch depth (h)	1.7μm	1.5μm	0.17μm
Doping separation (x)	5-50μm†	>8μm	0.42μm
Device length (L)	6mm	17mm	0.25-3mm†
Substrate doping type and concentration	n, < 1x10^{15} cm^{-3}	p,‡ ~ 1x10^{14} cm^{-3}‡	p, ~ 1x10^{14} cm^{-3}
Defect implantation species	Si^+	He^+	Si^+
Defect implantation energy	1.2MeV	800keV	190keV
Defect implantation dose	1x10^{12}cm^{-2}	1x10$^{10-14}$cm^{-2}†	1x10^{13}cm^{-2}
Post-implantation anneal range	RT-350 °C†	RT-350 °C†	RT-450 °C†
Maximum responsivity around1550nm (device bias given in brackets)	59 mA/W (5V)	38 mA/W (20V)	800 mA/W (20V)
Excess optical loss at maximum responsivity	3.33 dB/cm	0.16 dB/cm	80-100 dB/cm

*The MM device was fabricated using a KOH wet etch process, producing non-vertical walls and thus W is measured at the top of the waveguide.
†A quoted range of values represents the experimental matrix employed by the authors.
‡For the HK device, the background doping type and concentration were not provided. We have assumed common values used in the fabrication of silicon waveguides.

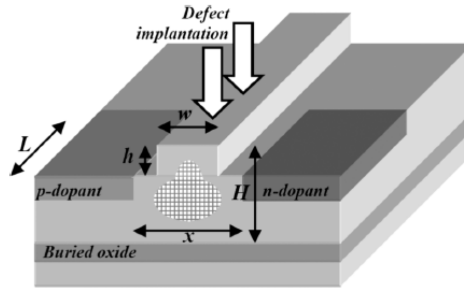

Fig. 1. Schematic representation of the generic defect mediated photodetector. The most relevant dimensions are labeled and described in Table I. The hashed area indicates the approximate position of the fundamental mode.

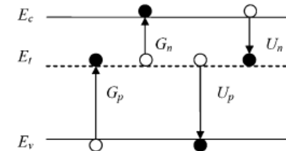

Fig. 2. Illustration of extrinsic transitions involving defect state at energy E_t, partway between the conduction band energy E_c and the valence band energy E_v (G_n, U_n, G_p, and U_p defined in text).

that there exists an optimum concentration of defects at which the highest responsivity is obtained). It also correctly describes trends in device performance as a function of device dimension. Deficiencies in the model are discussed and the need for fundamental measurements with regard to defect type, concentration, position in the bandgap, and response to thermal and optical agitation are highlighted.

B. Defect Mediated Waveguide Detectors for Silicon Photonics

Three research groups have thus far reported the fabrication of defect mediated detectors suitable for integration with SOI waveguides. These groups are based at McMaster University, The Chinese University of Hong Kong, and the MIT Lincoln Laboratories [7]–[10]. Hereafter, these groups will be referred to as MM, HK, and LL, respectively. Although using the same principle of operation, the devices from the groups were fabricated in substantially different processes with a variation in waveguide dimension, defect implantation and postimplantation thermal treatment in particular. The nature of the devices is however, the same, based upon the $p-i-n$ diode previously used in silicon photonic circuits for carrier injection into the waveguide. A schematic layout of the design is provided in Fig. 1 with the most important device parameters labeled. Table I provides the specific dimensions and critical processing conditions for the devices reported by the groups at MM, HK, and LL.

II. MODELING DEFECT ENHANCED DETECTION

A. Physical Basis of Defect Enhanced Detection

Carrier generation and recombination mediated by crystal defects are well described by the Shockley-Read-Hall (SRH) process [13]. Its extension to optical generation by subbandgap photons has been described also, for example by Keevers and Green [14]. Despite the comprehensive literature on this subject, we believe it is instructive to review these generation/recombination processes with a view to elucidate the defect mediated detection process.

From SRH theory, in steady state with no optical generation

$$U_n - G_n = U_p - G_p \quad (1)$$

where

$$G_n = C_n n_t n' = C_n n_t n_i e^{(E_t - E_i)/kT} \quad (2)$$

represents the rate of promotion of electrons from the defect to the conduction band

$$U_n = C_n(N_t - n_t)n \quad (3)$$

represents the rate of capture of electrons from the conduction band to the defect

$$G_p = C_p(N_t - n_t)p' = C_p(N_t - n_t)n_i e^{(E_i - E_t)/kT} \quad (4)$$

represents the rate of promotion of electrons from the valence band to the defect, and

$$U_p = C_p n_t p \quad (5)$$

represents the rate of capture of electrons from the defect to the valence band, as shown in Fig. 2 [15]. In this formulation we consider a single, deep defect state which lies closer to the conduction band than the valence band. This is the case for the silicon divacancy which has been identified to play a dominant role in optical absorption at wavelengths around 1550 nm [16].

The values n and p represent the concentration of electrons and holes, respectively. The intrinsic carrier concentration is given by n_i; E_i is the intrinsic position of the Fermi level; k is the Boltzmann constant, and T is the temperature; N_t is the total density of defects and n_t is the density of defects that are occupied by an electron; C_n and C_p are the coefficients of electron and hole thermal recombination, and are related to the capture cross section of electrons σ_n and holes σ_p by

$$C_n = \sigma_n v_{\text{th}} \quad C_p = \sigma_p v_{\text{th}} \quad (6)$$

where vth is the thermal velocity of electrons (approximately 10^7 cm/s) [15].

Since the defect level is closer to the conduction band, it is expected from (2) and (4) that n$'$ be much larger than p$'$. In fact, we can calculate that $\mathrm{n}' = 7.75 \times 10^{13}/\mathrm{cm}^3$ and $\mathrm{p}' = 3.30 \times 10^8/\mathrm{cm}^3$. Solving (1), the occupancy of the traps in thermal equilibrium (n_t^*) is

$$n_t^* = N_t \frac{(C_n n + C_p p')}{(C_n(n + n') + C_p(p + p'))}. \quad (7)$$

Also, for charge neutrality and assuming a device lightly doped with N_D donors (concentration $< 1 \times 10^{15}$ cm^{-3})

$$N_D + p = n + n_t* \quad (8)$$

and under bias V

$$np = n_i^2 e^{qV/kT}. \quad (9)$$

Solving (7)–(9) yields that for $N_t = 1 \times 10^{16} - 1 \times 10^{18}$ cm^{-3}

$$n_t* = N_D \quad (10)$$

with virtually all of the electrons trapped at defect sites.

This result illustrates the effects of background doping on the amount of depletion in the device and, therefore, its capacitance. For a lightly n-doped material, the negative charge of the occupied defects balances the positive charge of the ionized donors. Therefore, the presence of the defects enhances the depletion and lowers the capacitance. For the case of the divacancy defect in lightly p-doped material, the analysis is more straightforward—provided the Fermi-level stays above that needed to activate the single positively charged divacancy state, the defect will accept virtually no carriers, and therefore have a very small occupancy. In this case, there is no mechanism to balance the charge of ionized acceptors, so depletion is smaller (and capacitance is larger) than in n-type material.

Since $n' \gg p$ (and C_n and C_p are similar in magnitude) [16], it follows that

$$C_n n' \gg C_p p \ldots \quad \text{and hence } G_n \gg U_p. \quad (11).$$

An occupied defect is therefore more likely to promote its electron to the conduction band than have it fall to the valence band. Similarly, we can compare the relative values of $C_n n$ and $C_p p'$ to assess the dominant of the two processes G_p and U_n. This is more complex than for (11) though and is dependent on whether the semiconductor region is depleted, the doping type of the material, and the defect concentration N_t.

The defect mediated detectors under consideration here function through an additional hole generation term G_P^{opt}, a direct result of optical excitation of electrons from the valence band to the trap level. The cut-off wavelength associated with this mechanism is then determined by the level of the trap, i.e., E_t-E_v. In order to ensure the defect levels behave as generating centers it is necessary to induce a total hole generation rate $G_p' = G_P^{\text{opt}} + G_p$ which is larger than the electron recombination rate U_n. Therefore, we require

$$\begin{aligned} &G_P^{\text{opt}} + C_p(N_t - n_t)p' > C_n(N_t - n_t)n \\ &G_P^{\text{opt}} > (N_t - n_t)(C_n n - C_p p'). \end{aligned} \quad (12)$$

From (12), it is seen that the minimum G_P^{opt} required may be positive or negative. If it is negative, the defect center (divacancy) acts as a weak generating center in equilibrium, and any nonzero optical excitation will enhance this generation. If G_P^{opt} is positive, the divacancy acts as a weak electron trap in equilibrium and a minimum optical excitation is required to generate electron hole pairs.

The form of G_P^{opt} is taken to be [17]

$$G_P^{\text{opt}} = I(x, y) \frac{\lambda}{hc} \alpha \, e^{-\alpha z} \quad (13)$$

where $I(x, y)$ is the intensity of the optical mode, λ is the wavelength of light, h is Planck's constant, c is the speed of light, z is the distance along the length of the device, and α for the silicon divacancy can be approximated as [18]

$$\alpha = \frac{N_t}{\beta}, \text{where } \beta = 7.7 \times 10^{16} \text{ cm}^{-2}. \quad (14)$$

The upper limit to the detecting ability of such a device is the point where the optical generation rate becomes comparable to G_n. When G_P^{opt} exceeds G_n, carrier generation is no longer proportional to the incident light intensity.

B. Implementation of the Model

The model is implemented using the commercial semiconductor simulation platform ATLAS by Silvaco [12]. The various detector structures outlined in Section I-B are constructed in the Deckbuild environment, and acceptor traps are introduced in a uniform concentration throughout the volume of the device. The trap energy level E_t and thermal electron capture cross section σ_n are selected to correspond to the singly, negative charged

state of the divacancy defect such that E_c-E_t = 0.4 eV [16], [19], whereas σ_p is taken to be 3.6×10^{-14} cm^2 [16], and σ_n is given by the average of the two most commonly reported values, 5.3×10^{-15} cm^2 [16], 2×10^{-15} cm^2 [19], such that in our model $\sigma_n = 3.65 \times 10^{-15}$ cm^2.

The additional generation term is simulated by adding a spatially dependent electron-hole pair (*ehp*) generation rate to the device, in the form of G_p^{opt}. The model then assumes the process of promoting the electron from the valence band to the defect level, and instantaneously promoting it to the conduction band (since G_n is much larger than G_p). This also implies that the optical generation term has a minimal effect on the occupancy, and the change in occupancy with incident light intensity is negligible. This is justified by the calculation of n_t^* for low-doped (carrier concentration $\sim 1 \times 10^{15}$ cm^{-3}) samples with N_t in the range $1 \times 10^{16} - 10^{18}$ cm^{-3}, in which case the majority of defects are unoccupied, and the electrons promoted from the valence band to the defect level via G_p^{opt} are too small in number to cause a significant increase in occupation fraction (for the optical power under consideration here).

The spatial dependence of G_p^{opt}, determined by the mode profile, is calculated using the commercial software BeamPROP by RSoft [20]. In order to extend the use of the model to account for the variation in optical generation along the device length, the optical generation rate was integrated over the length L of the device, taking into account the exponential decay of the absorbed power, such that

$$\int_0^L G_p^{\text{opt}} dz = I(x,y)\frac{\lambda}{hc}\frac{\alpha_d}{\alpha_d+\alpha_i}\left(1-e^{-(\alpha_d+\alpha_i)L}\right) \quad (15)$$

where α_d is the loss corresponding to hole generation via the defect level, and α_i is waveguide loss that does not contribute to photocurrent (such as the free carrier loss caused by overlap between the mode and heavily doped regions). The α_i term was determined using BeamPROP simulations and experimental results for unimplanted devices. As expected, for large defect concentrations, the α_d term becomes very large and the integrated generation saturates.

The program ATLAS is then used to determine the photogenerated electron and hole concentrations, taking into account the input power, defect profile, and depletion width. The photocurrent is measured as the bias and light intensity are varied. Its magnitude changes according to the overlap integral of the electric field distribution, optical mode, and defect profile. This permits the quantification of the change in device response with respect to a variation in properties such as the p^+ and n^+ doped region separation (x), defect implant depth, and waveguide geometry.

C. The Silicon Divacancy

It is appropriate, at this point, to consider briefly the determination of the nature and concentration of the optically active defects present following ion implantation of silicon. The introduction of deep-levels associated with defects in silicon has been studied extensively and many different optically active defect types have been identified [21]. The model presented here, however, assumes a single optical defect center- in Section II-A, we state our choice of defect with the characteristics closest to those used in the model as the silicon divacancy. The divacancy is a primary defect induced by the irradiation of silicon and forms from the mobile vacancies caused by the nuclear interaction of implanted ions, primary atoms and target knock-ons. More complex damage, and ultimately amorphous silicon, is formed for high implantation doses (typically $> 10^{15}$ cm^{-2} for implanted Si^+ ions) [22], however for the doses used in the fabrication of defect mediated detectors (typically equivalent to $\sim 10^{12} - 10^{13}$ cm^{-2} implanted Si^+ ions) it seems reasonable to assume that the damage is dominated by primary point defects such as the divacancy. We note that other types of point defect may be introduced such as vacancy-impurity complexes and interstitials, and each defect type will have properties specific to the model described here. For instance, although vacancy-oxygen (V-O) pairs are often present following ion implantation, they will not contribute to carrier generation using 1550 nm wavelengths, as the negative charge state lays only 0.16 eV below the conduction band (photons of energy 0.96 eV or greater are required for the excitation from the valence band to this state) [23]. This defect does however have a larger capture cross-section than the divacancy, and therefore may dominate carrier recombination in a detector containing both V-O and divacancy defects. Concomitant with vacancy production during ion implantation is the generation of silicon interstitials, however these would seem to have less impact on the SRH processes important to these detectors. Hence, although conceding that damage production (and thermal evolution) is far more complex than implied by the current model (for example see [11] for a description of the complex thermal evolution of defect mediated detectors for annealing temperatures $> 300°$ C), the value of the properties associated with the divacancy (such as carrier recombination) should provide results relevant for comparison with those reported in [7]–[10]. Future development of the model will endeavor to account for a range of defect types.

The determination of the concentration of defects in ion implanted silicon is far from straightforward for such small irradiation doses. Deep-level-transient spectroscopy (DLTS) is a powerful method which provides information on defect concentration for a limited range of implantation conditions while accurately determining the energy level of carrier traps [24]. Specifically sensitive to silicon vacancy defects is Positron Annihilations Spectroscopy (PAS). An extremely useful empirical model for the determination of vacancy concentration, based upon PAS measurements, which may be applied to a wide range of implantation conditions, was proposed by Coleman *et al.* [25]. Further, this model, when combined with infrared loss data, was shown by Foster *et al.* to be able to predict the excess optical loss at 1550 nm induced in SOI waveguides by ion implantation [17]. That work thus provided experimental evidence for the assumption that the divacancy was the dominant implantation induced defect with regard to subbandgap optical loss in silicon. Further, it demonstrated that defect concentration in SOI waveguides could be inferred from excess optical loss using (14). In the present work then, we have deduced defect concentration from [7], [8] and [10] in this way using the loss data reported together with the photocurrent.

Authorized licensed use limited to: IEEE Xplore. Downloaded on April 26, 2009 at 13:04 from IEEE Xplore. Restrictions apply.

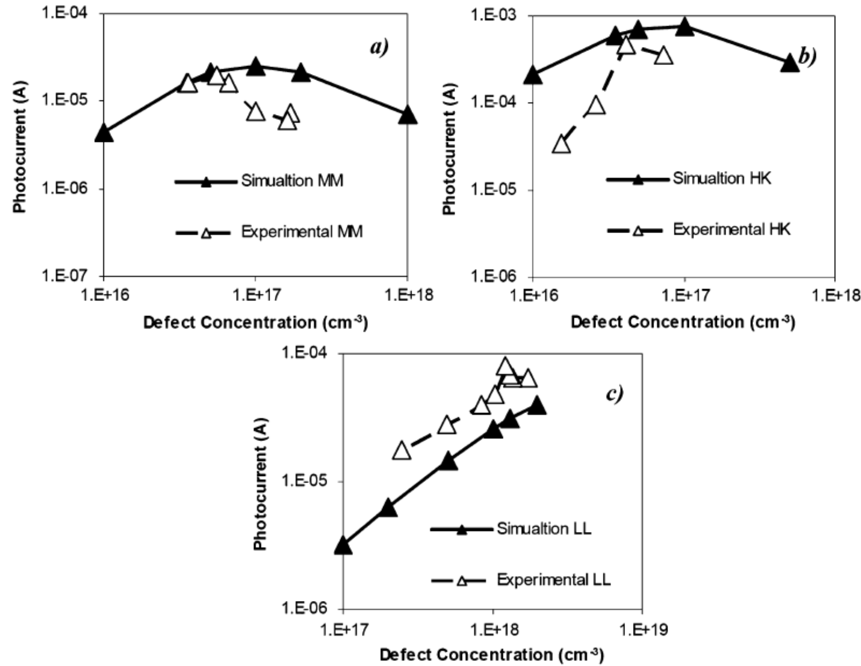

Fig. 3. Simulated and measured photocurrent versus divacancy concentration for the: (a) MM (2 V bias, 1 mW input, $x = 18\ \mu$m, this specific experimental data is from unpublished results); (b) HK (20 V bias, 25 mW input) [9]; and (c) LL (5 V bias, 1 mW input, $L = 0.25$ mm, where the 5 V data is obtained by converting data for 20 V reverse bias presented in [10] using the bias dependence of responsivity reported in the same devices described in Section I-A). Note that the defect observed after high temperature (> 400 °C) anneals, reported in [11], is not considered here.

It was found that all defect concentrations providing useful photocurrent were in the range $N_t = 10^{16} - 10^{18}$ cm^{-3}.

III. Results From the Atlas Model

A. Influence of Defect Concentration (N_t) on Photocurrent

The absolute photocurrent generated in the three devices described in Section I-A was simulated as a function of defect concentration (N_t), and plotted, along with the previously reported results, in Fig. 3. The defect concentration for the experimental data was calculated with (14), using the reported loss values.

In all of the devices, the photocurrent initially increases with defect concentration N_t, due to the increase in the generation rate G_p^{opt}. The response then peaks at a defect concentration which is characteristic of the device, and begins to decrease with further addition of defects. Two factors are responsible for this decrease.

1) The recombination rate provided by the defects increases linearly with N_t, while the generation rate becomes saturated over the device length L (as absorption α_d becomes large) as described by (15).
2) The depletion region at a given bias is reduced at larger defect concentrations. For lightly n doped material (such as MM), a negative charge from defect occupation nearly balances the positive charge from the ionized donors. The occupation fraction is perturbed when electrons are generated by optical excitation, causing the net static charge to become negative. The magnitude of this net charge will increase as defect concentration increases, reducing the depletion region and consequently providing less photocurrent. For a lightly p-doped device, the electron occupation of defects adds to the static charge of the ionized acceptors, so less depletion (and smaller responsivity) is typically observed for p-doped devices. For the LL device, because the contact separation is so small, this effect is not observed until the introduction of very large defect concentrations. Therefore, the peak response of the LL device is observed for defect concentrations much greater than the MM or HK devices.

The disparity between experiment and simulation in Fig. 3 has several potential sources. First, the assumption that the sole, optically active defect present is the silicon divacancy is likely a simplified description of the devices following implantation. Thus there must be some error in the values of assumed capture cross-sections and lifetime due to surface recombination. Second, the assumption that all optical absorption contributes to the generation of carriers is an upper-most estimate, in turn fixing the carrier generation rate used in the simulation to a maximum. Finally, the calculation of defect concentration from the

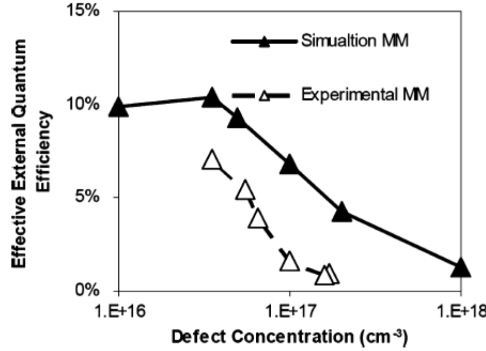

Fig. 4. Effective external quantum efficiency (η_{eff}) versus Defect concentration for MM (n^+/p^+ separation (x) = 6 μm).

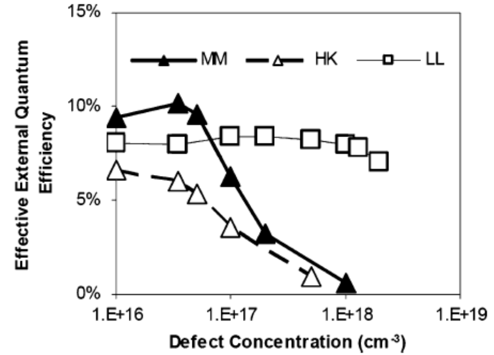

Fig. 5. Simulated effective external quantum efficiency (η_{eff}) of MM (2 V bias, $x = 6$ μm); (b) HK (20 V bias) [9]; and (c) LL (5 V bias, $L = 0.25$ mm) as a function of defect concentration N_t.

experimental absorption results does not reflect any measurement error (systematic or random) and is reliant on the use of the scaling value provided in [17]. However, this model correctly predicts the general trend of device responsivity as a function of varying defect concentration, and closely reproduces the absolute photocurrents observed for each device without recourse to parameter fitting. Therefore, it is extremely useful in evaluating changes in performance due to device structure in terms of photocurrent, and, thus, quantum efficiency.

B. *Influence of Defect Concentration on Effective External Quantum Efficiency*

In addition to the absolute photocurrent, it is also useful to observe the change in effective external quantum efficiency (η_{eff}) with respect to defect concentration. The η_{eff} is defined as follows:

$$\eta_{\text{eff}} = \frac{hc}{\lambda q}\frac{I}{P_{\text{abs}}} \tag{16}$$

where I is the photocurrent, P_{abs} is the optical power absorbed in the waveguide and $q = 1.6 \times 10^{-19}$ C. Fig. 4 shows such a plot for MM, indicating that the peak η_{eff} and the peak photocurrent do not occur for the same defect concentration. The overall decrease in η_{eff} with increasing defect concentration is a result of the increased recombination rate, i.e., the fraction of the electron-hole pairs generated that contribute to photocurrent is reduced when more defects are present.

Fig. 5 shows a similar plot of the simulated η_{eff} for all three devices, illustrating that although much higher absolute photocurrent may be achieved in the relatively smaller devices, the large absorption of the device limits the achievable effective quantum efficiency.

C. *Influence of Reverse Bias on Responsivity*

In addition to the work described in Section III-A, the devices were also simulated assuming operation in an unbiased condition with results showing that considerable photocurrent is still generated (typically 60%–80% of that found with a 5 V reverse bias). The major influence on the photocurrent reduction between these two bias conditions is the overlap of the depleted volume and the optical mode. This overlap is enhanced when the reverse bias is increased. The effect of increasing the reverse bias becomes negligible when the overlap is very large, for instance the simulation for the LL device showed relatively small (< 1 %/V) change in photocurrent when the bias was increased beyond 5 V. In that specific case we note that the experimental results did yield an increase in photocurrent for large reverse bias (> 10 V), which were attributed to a carrier multiplication process [10] not simulated here.

D. *Capacitance Limited Bandwidth*

We have determined that carrier transit time limits the theoretical maximum speed of operation of the MM device to approximately 1 GHz and the LL device to approximately 500 GHz. Since these values are significantly larger than the experimentally determined bandwidths, we conclude the *RC* product is the actual limiting factor with regard to speed of operation in both cases. The model described here is capable of solving for the capacitance of the device during operation. The MM device had an experimentally observed bandwidth of 2–3 MHz, and a simulated capacitance of 10–20 pF (at a measurement frequency of 1 MHz and 0.5 V reverse bias), which is consistent with measured values. The experimental speed of LL is vastly superior to the larger devices (MM and HK), due to its significantly reduced capacitance. By combining the value of simulated capacitance for LL of 0.1–1.5 pF (which is close to that reported by the authors) with the value for the load resistor of 50 Ω used during the measurement of bandwidth in [10], we calculate an upper limit of device bandwidth in excess of 30 GHz. We have already described the impact of defect concentration on depletion width and thus capacitance. In general we find that for very low defect concentrations, n-type devices offer the highest bandwidth, however for defect concentrations in excess of 5×10^{16} cm^{-3}, p-type devices are found to be superior.

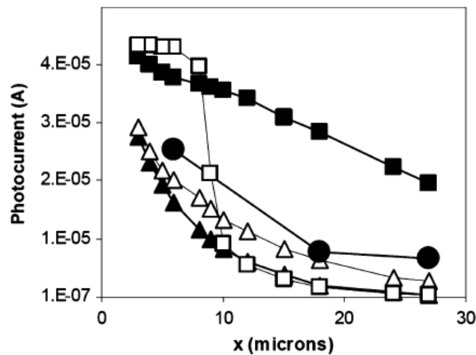

Fig. 6. Simulated photocurrent versus x *(contact separation)* for MM for both n and p substrate doping and 5 μm and 50 μm implant widths centered on the rib. Closed squares-n-type substrate, 50 μm implantation window width; Open squares- n-type substrate, 5 μm implantation window width; Closed triangles- p-type substrate, 50 μm implantation window width; Open triangles- p-type substrate, 5 μm implantation window width; Closed circles- Experimental data for MM, n-type substrate, 50 μm implantation window width.

E. Effect on Responsivity of n^+/p^+ Contact Separation (x) and Defect Volume

The importance of the overlap of the depletion width with the optical mode in achieving high responsivity suggests that one method for optimizing this property in the relatively large devices (MM and HK) is to narrow the distance between the n^+ and p^+ regions (labeled x in Fig. 1). However, the exact nature of the relationship between responsivity and x is complicated—although reducing x will indeed increase the overlap between the depleted region and the optical mode, it will also increase optical loss caused by overlap of the mode with the heavily doped p^+ and n^+ regions as x approaches zero. Further, it is reasonable to assume that responsivity for all devices may be improved by restricting the introduction of defects via restricting the area of the inert ion implantation to a narrow section centered on the ridge. If the minimum implantation window width is made commensurate with the p^+ and n^+ separation, this masked defect implantation should not strongly affect the overlap between the optical mode and implantation induced defects, but will reduce the carrier recombination in regions where the optical mode profile approaches zero. Fig. 6 shows the effects of varying n^+ and p^+ separation and the implantation window width during the introduction of the defects, for the MM device.

Fig. 6 illustrates the enhanced performance achieved by reducing x, both in the experimental case for the MM device and the simulated case. Further, for the n-type devices, the response is improved when the defect implantation window width is larger than x. This is due to the effects on depletion particular to n-type material addressed above: an area can be better depleted if it contains defects. Therefore, the edges of the p^+ and n^+ regions must contain defects in order to cause large overlap between the depletion region and the optical mode. For the p-type devices, narrowing the defect implantation window improves the responsivity regardless of x, as the defects do not affect the depletion in this case.

IV. Summary and Conclusions

We have presented a model which simulates the response to sub-bandgap photons of defected mediated silicon waveguide detectors. It is assumed that deliberately introduced, inert ion implantation damage causes the creation of a single defect level (the single negatively charged divacancy) which interacts with carriers as predicted by SRH theory. The nature of this interaction is perturbed when sub-bandgap light is guided within the waveguide, such that net carrier generation is achieved. This is modeled using an intensity dependent carrier generation term. We have compared the results of this model with experimental data published previously (in [8]–[10]) and found that the absolute photocurrent and its dependence on defect density and structure geometry were in reasonable agreement.

The model is capable of assessing potential device designs in terms of responsivity, effective external quantum efficiency, and capacitance limited bandwidth. Increasing the defect concentration will initially improve the detector responsivity by increasing carrier generation, but excessive defect concentration degrades responsivity due to the simultaneous increase in carrier trapping and recombination. The value of the optimum defect concentration is determined by the device structure. Those detectors facilitating strong overlap between the depletion widths (associated with the n^+ and p^+ contacts), optical mode and defect profile (while minimizing the effects of recombination) will have an optimum value at larger defect concentrations, and thus have superior responsivity. This does not, however, imply that the effective external quantum efficiency is greatest in such devices, where optical absorption is significantly greater than for waveguides with fewer defects. For these capacitance limited bandwidth devices it is possible also to predict the speed of operation using the present model, which may be many GHz for waveguide cross-sections $< 1\ \mu\text{m}^2$.

It is suggested that models such as that described here will be invaluable in designing integrated silicon waveguide detectors with properties suitable for a variety of applications such as terminal detection and power monitoring.

References

[1] R. G. Hunsperger, *Integrated Optics: Theory and Technology*. New York: Springer-Verlag, 1991.
[2] T. D. Bestwick, "Active silicon integrated optical circuits," in *Materials and Devices for Silicon-Based Optoelectronics Symposium*, Boston, MA, 1998, pp. 57–65.
[3] H. Park *et al.*, "Hybrid AlGaInAs-silicon evanescent preamplifier and photodetector," *Opt. Exp.*, vol. 15, pp. 13539–13546, May 2007.
[4] L. Colace *et al.*, "Ge on Si $p-i-n$ photodiodes operating at 10 Gbit/s," *Appl. Phys. Lett.*, vol. 88, pp. 101111-1–101111-3, Mar. 2006.
[5] J. Liu *et al.*, "High-performance, tensile-strained Ge $p-i-n$ photodetectors on a Si platform," *Appl. Phys. Lett.*, vol. 87, pp. 103501-1–103501-3, Aug. 2005.
[6] M. Morse *et al.*, "Performance of Ge-on-Si $p-i-n$ photodetectors for standard receiver modules," *IEEE Photon. Technol. Lett.*, vol. 18, pp. 2442–2444, Dec. 2006.
[7] A. P. Knights *et al.*, "Silicon-on-insulator waveguide photodetector with self-ion-implantation engineered-enhanced infrared response," *J. Vac. Sci. Technol.*, vol. A24, pp. 783–786, Jun. 2006.
[8] A. P. Knights *et al.*, "Monolithically integrated photodetectors for optical signal monitoring in silicon waveguides," in *Proc. SPIE*, 2006, vol. 6125, pp. 61250J-1–61250J-12.

[9] Y. Liu *et al.*, "In-line channel power monitor based on Helium ion implantation in silicon-on-insulator waveguides," *IEEE Photon. Technol. Lett.*, vol. 18, pp. 1882–1884, Sep. 2006.
[10] M. W. Geis *et al.*, "CMOS-compatible all-Si high-speed waveguide photodiodes with high responsivity in near-infrared communication band," *IEEE Photon. Technol. Lett.*, vol. 19, pp. 152–154, Feb. 2007.
[11] M. W. Geis *et al.*, "All silicon infrared photodiodes: Photo response and effects of processing temperature," *Opt. Exp.*, vol. 15, pp. 16886–16895, Dec. 2007.
[12] Silvaco Data Systems Inc. © 1984–2008. [Online]. Available: www.silvaco.com
[13] W. Schockley and W. T. Read, "Statistics of the recombination of holes and electrons," *Phys. Rev.*, vol. 87, pp. 835–842, Sep. 1952.
[14] M. J. Keevers and M. A. Green, "Efficiency improvements of silicon solar cells by the impurity photovoltaic effect," *J. Appl. Phys.*, vol. 75, pp. 4022–4031, Apr. 1994.
[15] S. Wang, "Transport and Recombination of Excess Carriers," in *Fundamentals of Semiconductor Theory and Device Physics.*. Englewood Cliffs, NJ: Prentice-Hall, 1989, pp. 277–83, ch. 7.
[16] E. Simoen *et al.*, "Impact of the divacancy on the generation-recombination properties of 10 MeV proton irradiated float-zone silicon diodes," *Nucl. Instrum. Methods in Phys. Res. A*, vol. 439, pp. 310–318, Jan. 2000.
[17] S. M. Sze and K. K. Ng, "Photodetectors and Solar Cells," in *Physics of Semiconductor Devices*, 3rd ed. Hoboken, NJ : Wiley, 2007, pp. 674–, ch. 13.
[18] P. J. Foster, "Optical attenuation in defect-engineered silicon rib waveguides," *J. Appl. Phys.*, vol. 99, pp. 073101-1–073101-7, Apr. 2006.
[19] S. D. Brotherton and P. Bradley, "Defect production and lifetime control in electron and γ-irradiated silicon," *J. Appl. Phys.*, vol. 53, pp. 5720–5732, Aug. 1982.
[20] RSoft Design Group, Inc. © 2002. [Online]. Available: www.rsoftdesign.com
[21] R. Harding *et al.*, "Identification by photoluminescence and positron annihilation of vacancy and interstitial intrinsic defects in ion-implanted silicon," *J. Appl. Phys.*, vol. 100, pp. 1–4, Oct. 2006.
[22] L. Pelaz *et al.*, "Ion-beam amorphized and recrystallization in silicon," *l. Appl. Phys.*, vol. 96, pp. 5947–5976, Nov. 2004.
[23] P. Hazdra *et al.*, "Effect of defects produced by MeV H and He ion implantation on characteristics of power silicon p-i-n diodes," in *Proc. IEEE Conf. Ion Implant. Technol.*, Sep. 2000, pp. 135–137.
[24] J. L. Benton *et al.*, "Evolution from point to extended defects in ion implanted silicon," *J. Appl. Phys.*, vol. 82, pp. 120–125, Jun. 1997.
[25] P. G. Coleman *et al.*, "Simple expression for vacancy concentrations at half ion range following MeV ion implantation of silicon," *Appl. Phys. Lett.*, vol. 80, pp. 946–949, Feb. 2002.

Dylan F. Logan received the B.Eng. degree in engineering physics from McMaster University, Hamilton, Ontario, Canada, in 2007.

He is currently pursuing the M.A.Sc. degree with the silicon photonics research group at McMaster University.

Paul E. Jessop received the B.Sc. degree in physics from the University of Waterloo, Canada, and the A.M. and Ph.D. (1978) degrees in physics from Harvard University, Cambridge, MA.

In 1978, he joined the Electrical Engineering Division of the National Research Council of Canada (Ottawa), where he worked in the area of laser spectroscopy of solids. Since 1981, he has been with McMaster University, Hamilton, Ontario, Canada, where he is currently a Professor with the Department of Engineering Physics and Chair of the department. His principal research interests are in the area of integrated optics and semiconductor optoelectronic devices. He heads an active research group of about eight people, both graduate students and full-time research professionals.

Andrew Knights received the Ph.D. degree from the University of East Anglia in 1994 in the area of surface and subsurface material characterization.

His subsequent work took him first to the University of Western Ontario, Canada, where he performed research on the generation and evolution of implant induced defects in silicon, and then to the University of Surrey, U.K., as part of the U.K. National Ion Beam Centre, researching novel fabrication processes for micro and optoelectronic materials. In 2000, he joined Bookham Technology and worked on a range of silicon-based, highly integrated photonic devices. In 2003, he moved to McMaster University, Hamilton, Canada, where he holds a faculty position with the Department of Engineering Physics. He currently leads a research group working on the interaction of optical and electrical functionality in silicon-based structures.

B.2 D. F. Logan, P. E. Jessop, A. P. Knights, "Design of Integrated LOCOS Waveguide Photodetector on SOI," Proc. SPIE, vol. 6898, p. 68981J, 2008; presented at Photonics West – Silicon Photonics III, San Jose, California, Jan. 21-24, 2008.

This manuscript is a proceedings paper describing the design of a LOCOS-based photodetector, presented as a poster at Photonics West in January 2008. It utilizes the modeling summarized in the paper of *B.1*. Its contents have been reproduced in the early portions of chapter 4. It is not included in full, due to repetition with the publications *B.1* and *B.6*.

B.3 D. F. Logan, P. E. Jessop, A. P. Knights, R. Gwilliam, and M. Halsall, "The Effect of Doping Type and Concentration on Optical Absorption via Implantation Induced Defects in Silicon-On-Insulator Waveguides," Proc. IEEE A-MRS; presented at Australian MRS meeting 2008.

This is a peer-reviewed proceedings paper summarizing work regarding the charge-state dependence of divacancy absorption. This work was supplemental to that completed towards the Ph. D. degree, and is not covered in the body of the thesis. It is included in full in the following pages.

© 2008 IEEE. Reprinted, with permission, from D. F. Logan, P. E. Jessop, A. P. Knights, R. Gwilliam, and M. Halsall, "The Effect of Doping Type and Concentration on Optical Absorption via Implantation Induced Defects in Silicon-On-Insulator Waveguides, " Proc. IEEE A-MRS, 2008.

This material is posted here with permission of the IEEE. Such permission of the IEEE does not in any way imply IEEE endorsement of any of McMaster University's products or services. Internal or personal use of this material is permitted. However, permission to reprint/republish this material for advertising or promotional purposes or for creating new collective works for resale or redistribution must be obtained from the IEEE by writing to pubs-permissions@ieee.org .By choosing to view this material, you agree to all provisions of the copyright laws protecting it.

The Effect of Doping Type and Concentration on Optical Absorption via Implantation Induced Defects in Silicon-on-Insulator Waveguides

D F Logan*, P E Jessop*, A P Knights*, R M Gwilliam†, and M P Halsall‡
*Department of Engineering Physics, McMaster University, 1280 Main Street West, Hamilton, Ontario L8S4L7, Canada.
Email: aknight@mcmaster.ca
†Surrey Ion Beam Centre, Advanced Technology Institute, University of Surrey, Guildford, GU2 5XH, United Kingdom.
Email: r.gwilliam@surrey.ac.uk
‡School of Electrical and Electronic Engineering, University of Manchester, Manchester, M13 9PL, United Kingdom.
Email: matthew.halsall@manchester.ac.uk

***Abstract*— The influence of the charge state of ion implantation induced defects in SOI waveguides on the absorption of sub-bandgap wavelengths is described. It is found that waveguides pre-doped with boron absorb with significantly greater efficiency than those pre-doped with phosphorus. Following annealing at 300°C this difference is approximately 8dBcm^{-1}, while the intrinsic loss of the waveguides is limited to 2dBcm^{-1}. These results have significant ramifications for a number of integrated optical devices fabricated in silicon.**

***Keywords-** silicon; waveguides; integrated optics; ion implantation; absorption.*

I. Introduction

Silicon photonics continues to receive a great deal of attention as a route to the monolithic integration of the performance of silicon microelectronics with optoelectronic functionality [1]. A range of devices has been demonstrated including sub-micron waveguides, optical detectors and those with complex diffractive elements [2]. Of some significance, optical source integration using hybridization [3] is well-advanced, although a monolithic, electrically pumped silicon optical source remains elusive.

Defect engineering is playing an increasingly important role in silicon photonic device development and has been shown to be useful in the fabrication of sub-bandgap detectors [4] and for the control of carrier lifetime [5]. In a recent work, Foster et al. looked in particular at the influence of vacancy-type defects on absorption in waveguide structures [6]. They showed that significant absorption exceeding 1000dBcm^{-1} could be induced using modest silicon ion implantation doses, thus demonstrating the potential of 'defect isolation' for passive optical attenuation and reducing optical cross-talk in integrated circuits. In this paper we describe the effects of doping type and concentration of the waveguide on the optical absorption of sub-bandgap wavelengths around 1550nm. We show that there is a significant difference between *p*-type doped waveguides containing vacancy defects and those doped *n*-type. We ascribe this difference primarily to the charge state of the defects, and thus the occupancy which either denies or permits optical transitions between the defect level, the conduction band or the valence band.

II. Experimental

A. Sample Fabrication

Silicon waveguides were formed in four separate chips of 5μm thick silicon-on-insulator. The fabrication followed standard photolithography and plasma-etch protocols with up to twenty-two waveguides being formed on each chip. The dimensions of the waveguides were such that only the fundamental mode could propagate for a coupled wavelength of 1550nm. The chips were subsequently doped either *n*- or *p*-type via phosphorus or boron implantation respectively, with the implantation energy being 80keV in all cases and the dose being either 5x10^{13}cm^{-2} (low-doped) or 5x10^{14}cm^{-2} (high doped). Following implantation the dopant was driven in at 1100°C for 5 hours in dry oxygen ambient. Doping levels for all chips were in excess of the background, *p*-type concentration of 1x10^{15}cm^{-3} to depths >2μm, accounting for >50% of the volume of the waveguide. Optical quality end-facets were prepared using a chip thinning and edge cleaving process. Fabry-Perot cavity determination of the loss introduced to the waveguides via free carrier absorption was determined to be ~2dBcm^{-1} for both the low-doped *p* and *n*-samples, in line with expectation [7].

The chips were masked to reveal differing lengths (this window length is subsequently labeled *L*) of the waveguide and then implanted using 1.5MeV Si^{+} ions to a dose of 1x10^{13}cm^{-2}.

B. Measurement of Optical Loss

Measurement of optical loss proceeded in a manner similar to that described by Foster et al. [6]. There are two sources of propagation loss in these structures: free-carrier absorption due to the dopants and enhanced absorption due to the defects introduced by Si^{+} implantation. The total loss may then be written as:

$$\alpha_d L + \alpha_i W + c \quad (1)$$

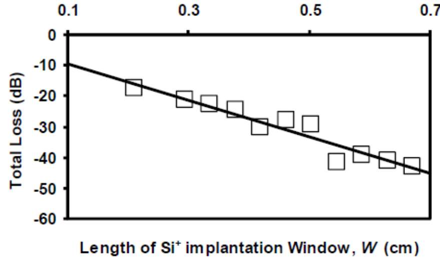

Figure 1 – Example of measured loss data analysis for the n-doped sample annealed at 250°C. The solid line is a fit of the form given by equation 1. The excess loss due to the defects is determined to be 60dBcm^{-1}.

where α_d is the absorption coefficient due to defects, L is the length of the implant window, α_i is the intrinsic absorption coefficient (which includes enhanced free carrier absorption consequent from doping), W is the entire length of the waveguide, and c is the coupling loss.

Laser output at a wavelength close to 1550 nm was butt-coupled into each waveguide via a tapered fiber. The output was collected by a lens and measured using a free-space detector and power meter. Measurements were repeated after annealing the chip for various temperatures up to 325°C.

Fig. 1 shows a typical plot (here for the low-doped n-type chip annealed at 250°C) of measured total loss as a function of L for a single chip (i.e. constant W). The slope extracted from a linear fit to this data provides the value α_d, in this case = 60dBcm^{-1}.

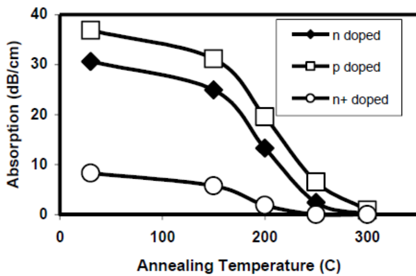

Figure 2 – Modeled optical loss for differently doped silicon waveguides following equation (2). The solid line is a guide to the eye only.

III. RESULTS

A. Modeling of Optical Loss

It is established that irradiation of silicon introduces a 1.8μm absorption band, attributed to optical transitions related to the divacancy point defect [8]. The mechanism for this absorption is the ionization of a neutral divacancy (causing it to acquire a single negative charge) through the excitation of an electron from the valence band to the singly negative charge state. This charge state is located approximately 0.4eV below the conduction band [9]. Therefore, in samples with Fermi levels below this energy level, the divacancy will be neutral, and thus be capable of absorption through this mechanism. As the Fermi level is raised higher, more divacancies become negatively charged in equilibrium, and therefore less are available to be ionized via optical absorption. This is supported by previous absorption studies of irradiated silicon, where it was shown that n-doped silicon has a lower absorption coefficient at 1.8μm than does p-doped material [8, 10]. Assuming the tail of the 1.8μm absorption band is primarily responsible for the enhanced absorption at 1550nm, this effect can be reasonably expected to dominate the propagation loss measured in this experiment.

The absorption via the 1.8μm band can be summarized as:

$$\alpha_d = \sigma_p{}^{opt} \int_{x,y} \Phi(x,y)(N_t(x,y) - n_t(x,y))dxdy \qquad (2);$$

where, $\sigma_p{}^{opt}$ is the cross-section for optical absorption;
$\Phi(x,y)$ is the normalized optical mode profile;
$N_t(x,y)$ is the profile of the divacancy concentration;
$n_t(x,y)$ is the profile of the ionized (negatively charged) divacancy.

The profile of divacancy concentration ($N_t(x, y)$) and the profile of dopant concentration ($N_D(x, y)$ or $N_A(x, y)$) were extracted from the commercial modeler ATHENA. The divacancy concentration and its evolution during high temperature anneals were approximated using the results of Foster *et al.* [6]. From both profiles, the ionized divacancy profile $n_t(x, y)$ was calculated using Fermi statistics. The mode profile $\Phi(x,y)$ was approximated using a beam propagation algorithm. Using equation (2) to consider the influence of the 1.8μm absorption band alone, the modeled propagation loss is shown in Fig. 2.

B. Experimental Results

Measurements of optical loss were carried out on the implanted material for the low-doped samples, and for all samples following several isochronal (10 minute) anneals between 175 °C and 325°C. The values from α_d were extracted for all chips following each annealing stage as in Fig. 1, and are summarized in Fig. 3.

The results reported here are consistent with the annealing behavior of the divacancy observed previously for silicon waveguides [6]. Of particular interest to this study, the results indicate a significant dependence of divacancy mediated, optical absorption on dopant type and concentration.

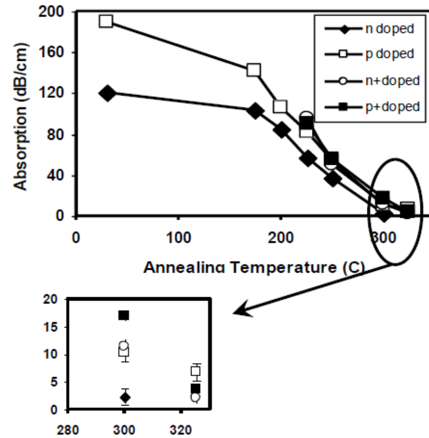

Figure 3 – Measured optical loss in the variously doped waveguides. For the upper panel, the solid lines are a guide to the eye only.

For all annealing temperatures, the lightly *p*-doped sample has stronger divacancy mediated absorption than the lightly *n*-doped sample. Following a 10 minute anneal at 300°C, for example, this excess loss mechanism was measured to be 2 ±1.5 dBcm^{-1} for the *n*-doped sample, while it was 10 ±1.6 dBcm^{-1} for the *p*-doped sample.

C. Comparison of Experimental and Modeled Results

Comparison of the modeled data of Fig. 2 to the experimental results of Fig. 3 shows agreement for the general trend of a stronger absorption in *p*-doped samples than for *n*-doped samples. Also, the Fermi statistics predicts that $n_t(x, y) = 0$ for both high and low-doped *p*-samples regardless of concentration, since the Fermi level is very far below the single negative charge level of the divacancy. As a result, the absorption is maximized for *p*-doped samples, independent of dopant concentration. This is confirmed by the results shown in Fig. 3.

We note a significant discrepancy between the modeled and measured highly *n*-doped sample. From a consideration of the 1.8μm absorption band alone, it would be expected that this sample would have complete ionization of divacancies, and thus have very low absorption (as predicted by equation 2). However, in Fig. 3 the absorption for this sample is larger than that from the lightly *n*-doped sample. This disparity exists because the 1.8μm band is not the only means of mediating optical absorption by the divacancy. For example the 3.3μm absorption band permits excitation of an electron from a single negatively charged divacancy into the conduction band. This band also has tails which extend into the 1550nm region of the optical absorption spectrum [8]. This absorption is weaker, and does not become comparable to that of the 1.8μm band until high donor concentrations are present, as in the case for highly-doped, *n*-type silicon.

A second discrepancy between modeled and experimental data is found in the absolute values of α_d, which were underestimated by the model in Fig. 2. This may be explained through the presence of additional loss via modal radiation which is not accounted for in the model [6]. This is a direct result of the perturbation of refractive index introduced by the silicon irradiation damage, which is not uniform throughout the volume of the waveguide. Complete irradiation of the whole waveguide via higher energy silicon implantation should negate this loss mechanism in further planned studies. This effect is independent of doping type and thus the conclusions regarding the difference in absorption between *n*- and *p*-doped samples remains intact.

IV. SUMMARY AND CONCLUSIONS

This report describes the effect of doping type and concentration on the attenuation of optical propagation in silicon waveguides at wavelengths within the telecommunications window. Following modeling of optical absorption which assigns the 1.8μm band as that which mediates the dominant transition (and hence provides the strongest absorption effect) it was shown that absorption in *p*-type silicon waveguides should be significantly enhanced when compared to those doped *n*-type. This behavior was confirmed by experimental measurement. For example, following annealing at 300°C of Si^+ implanted waveguides, attenuation in *n*-type samples was almost 10dBcm^{-1} less than that for *p*-doped waveguides. However, for heavily doped *n*-type material, absorption is comparable with *p*-doped waveguides- a result of the availability of additional absorption bands in n^+ silicon. A discrepancy between absolute attenuation predicted by the model and that measured is thought to be due to modal radiation. In addition to the importance of these results for those wishing to predict optical absorption in silicon waveguides we suggest that the variation in attenuation measured here may allow the design and realization of novel modulator devices suitable for silicon phonic applications.

ACKNOWLEDGMENTS

The authors would like to acknowledge the assistance with fabrication of the devices provided by Mr. D Thomson and Mr. A Royal, both of the University of Surrey, UK.

REFERENCES

[1] G.T.Reed "Device physics – the optical age of silicon", Nature, vol. 427, pp. 595-596, Feb. 2004.

[2] G.T.Reed, Silicon photonics – the state of the art, John Wiley, Chichester, England, 2008.

[3] A.W. Fang *et al.* "Hybrid silicon evanescent devices." Materials Today vol. 10, pp. 28-35, July 2007.

[4] J.D.B. Bradley, P.E. Jessop amd A.P.Knights "Silicon waveguide-integrated optical power monitor with enhanced sensitivity at 1550 nm" Appl. Phys. Lett. vol.86, 241103, June 2005.

B.4 D. F. Logan, P. E. Jessop, A. P. Knights, G. Wojcik, and A. Goebel, "Optical Modulation in Silicon Waveguides via Charge State Control of Deep Levels," Optics Express, vol. 17, p. 18571, 2009.

This results presented in this publication builds upon the work presented in *B.3*, and is similarly supplemental to the principle work of the Ph. D. and not presented within the body of this thesis. It investigates the dependence of charge state on indium-center optical absorption at 1550 nm. It is shown that control of the charge state can be used to control the absorption level, thus forming a novel method of light modulation in silicon. Several device implementations are described, and their performance is simulated using ATLAS. It is included in full in the following pages.

A patent was filed based on this work, with myself as the principle inventor. This work was also presented at the IPNRA (Integrated Photonics and Nanophotonics Research and Applications) meeting in Honolulu, HI in July 2009, and has an associated publication in the OSA Technical Digest.

© 2009 OSA. Reprinted with permission.

Optical modulation in silicon waveguides via charge state control of deep levels

D F Logan[1*], P E Jessop[1], A P Knights[1], G Wojcik[2], and A Goebel[2]

[1]*Department of Engineering Physics, McMaster University, 1280 Main Street West, Hamilton, Ontario, L8S4L7, Canada.*
[2]*Innolume Inc., 3333 Bowers Ave, Suite 190, 95054 Santa Clara, CA, USA*
** logand@mcmaster.ca*

Abstract: The control of defect mediated optical absorption at a wavelength of 1550nm via charge state manipulation is demonstrated using optical absorption measurements of indium doped Silicon-On-Insulator (SOI) rib waveguides. These measurements introduce the potential for modulation of waveguide transmission by using the local depletion and injection of free-carriers to change deep-level occupancy. The extinction ratio and modulating speed are simulated for a proposed device structure. A 'normally-off' depletion modulator is described with an extinction coefficient limited to 5 dB/cm and switching speeds in excess of 1 GHz. For a carrier injection modulator a fourfold enhancement in extinction ratio is provided relative to free carrier absorption alone. This significant improvement in performance is achieved with negligible increase in driving power but slightly degraded switching speed.

©2009 Optical Society of America

OCIS codes: (230.2090) Electro-optical devices; (250.4110) Modulators.

References and links

1. A. P. Knights, J. D. B. Bradley, S. H. Gou, and P. E. Jessop, "Silicon-on-insulator waveguide photodetector with self-ion-implantation engineered-enhanced infrared response," J. Vac. Sci. Technol. A **24**(3), 783–786 (2006).
2. M. W. Geis, S. J. Spector, M. E. Grein, R. T. Schulein, J. U. Yoon, D. M. Lennon, S. Deneault, F. Gan, F. X. Kaertner, and T. M. Lyszczarz, "CMOS-compatible all-Si high-speed waveguide photodiodes with high responsivity in near-infrared communication band," IEEE Photon. Technol. Lett. **19**(3), 152–154 (2007).
3. Y. Liu, C. W. Chow, W. Y. Cheung, and H. K. Tsang, "In-line channel power monitor based on Helium ion implantation in silicon-on-insulator waveguides," IEEE Photon. Technol. Lett. **18**(17), 1882–1884 (2006).
4. H. Y. Fan, and A. K. Ramdas, "Infrared absorption and photoconductivity in irradiated silicon," J. Appl. Phys. **30**(8), 1127–1134 (1959).
5. C. S. Chen, and J. C. Corelli, "Infrared spectroscopy of divacancy-associated radiation-induced absorption bands in silicon," Phys. Rev. B **5**(4), 1505–1517 (1972).
6. D. Logan, P. E. Jessop, A. P. Knights, R. M. Gwilliam, and M. P. Halsall, "The effect of doping type and concentration on optical absorption via implantation induced defects in silicon-on-insulator waveguides." in *COMMAD 2008 IEEE Proc. Conf. on Optoelectronic and Microelectronic Materials and Devices.* (Sydney, Australia, 2008). pp. 152–5.
7. E. Simoen, C. Claeys, E. Gaubas, and H. Ohyama, "Impact of the divacancy on the generation-recombination properties of 10 MeV proton irradiated Float-Zone silicon diodes," Nucl. Instrum. Methods Phys. Res. A **439**(2-3), 310–318 (2000).
8. M. J. Keevers, and M. A. Green, "Efficiency improvements of silicon solar cells by the Impurity photovoltaic effect," J. Appl. Phys. **75**(8), 4022–4031 (1994).
9. G. J. Parker, S. D. Brotherton, I. Gale, and A. Gill, "Measurement of concentration and photoionization cross section of indium in silicon," J. Appl. Phys. **54**(7), 3926–3929 (1983).
10. P. J. Foster, J. K. Doylend, P. Mascher, A. P. Knights, and P. G. Coleman, "Optical attenuation in defect-engineered silicon rib waveguides," J. Appl. Phys. **99**(7), 073101 (2006).
11. Silvaco Data Systems Inc, © 1984–2008. [online]. Available: www.silvaco.com.
12. RSoft Design Group, Inc., © 2002. [online]. Available: www.rsoftdesign.com.
13. K. Dieter, Schroder, *Semiconductor Material and Device Characterization.* (John Wiley & Sons, 2006). p. 255–8.

#114991 - $15.00 USD Received 29 Jul 2009; revised 23 Sep 2009; accepted 25 Sep 2009; published 30 Sep 2009
(C) 2009 OSA 12 October 2009 / Vol. 17, No. 21 / OPTICS EXPRESS 18571

14. A. Sato, K. Suzuki, H. Horie, and T. Sugii, "Determination of Solid Solubility Limit of In and Sb in Si using Bonded Silicon-On-Insulator (SOI) Substrate." in *Proc. IEEE 1995 Int. Conf. on Microelectronic Test Structures*. (Nara, Japan, vol. 8, 1995) pp. 259–263.
15. J. Liu, U. Jeong, S. Mehta, J. Sherbondy, A. Lo, K. Ha Shim, and J. Eun Lim, "Investigation of Indium Activation by C-V Measurement." in *Proc. IEEE Int. Conf. on Ion Implantation Technology*, H. Ryssel et al., ed. (Alpbach, Austria, 2000) pp. 66–69.

1. Introduction

Optical detection via defect-enhanced carrier generation in SOI ridge waveguides is now established as a viable method for sub-bandgap optical to electrical conversion [1–3]. In the previously reported work defects are introduced into the waveguide through ion implantation (with or without a post-implantation thermal anneal), which increases the optical absorption for wavelengths around 1550 nm through the (essentially) mid-gap divacancy or interstitial cluster level [4]. Integrated *p-i-n* diode structures are used to extract the optically generated carriers from the device volume supporting the optical mode, thus allowing for signal detection directly from the waveguide. The degree of absorption may be changed by varying the concentration of defects, and thus the amount of signal that is sampled may be varied from a few per cent to virtually the entire signal. As a result, defect-enhanced photodetectors may be implemented as both in-line power monitors and as end-of-line signal detectors. Their potential advantages over competing technologies rely on the fact that they are fabricated entirely using standard silicon processing methods and do not involve hybrid integration or the hetero-growth of germanium.

The photodetectors reported to date are fabricated in the intrinsic (or low-doped) silicon overlayer of a silicon-on-insulator (SOI) structure, and therefore the influence of background dopant concentration on device performance has not been studied. In the case of carrier generation via the divacancy defect, the background dopant concentration will affect the charge state of the divacancies, which in turn will influence the defect mediated absorption. Evidence consistent with this postulate has been reported previously [5], and has recently been demonstrated using a waveguide geometry [6].

The divacancy has a deep-level situated in the band gap 0.4 eV below the conduction band and as such, light at a wavelength of 1550 nm may cause charge excitation from the valence band or from the deep-level to the conduction band, albeit at significantly different rates [7]. The variation in cross-section for these two processes results in a measurable difference in absorption coefficient as background doping type and concentration is changed, but there is no doping concentration at which the absorption coefficient related to the defect is reduced to zero [6]. In contrast, a deep level which is positioned in the bandgap such that either the valence band to deep-level, or the deep-level to the conduction band transition is greater than 0.8 eV provides an absorption mechanism which may be reduced to a negligible amount via variation of the deep-level charge state. Doping silicon with indium provides just such a deep-level because indium is well known to have a single acceptor level at 157 meV above the valence band [8]. Strong absorption may be expected when in the neutral charge state (through hole generation), but not when the associated level is in the negative charge state (the threshold wavelength equivalent for such a transition is approximately 1320 nm). Of significance, a large shift in absorption in response to a change in defect charge state is potentially relevant to active devices, where the occupancy may be altered by injecting or removing carriers. In this work we present results which confirm the strong variation in absorption of 1550 nm light via indium doping in SOI waveguides through the variation of background *n*-type doping. We suggest device structures in which such a mechanism may be used to provide broadband, polarization independent variable attenuation and demonstrate that such devices are significantly more efficient than those of equivalent dimension which rely on free carrier absorption effects alone.

#114991 - $15.00 USD Received 29 Jul 2009; revised 23 Sep 2009; accepted 25 Sep 2009; published 30 Sep 2009
(C) 2009 OSA

2. Background to charge state mediated absorption

A 4 µm optical absorption resonance exists in indium doped silicon [9]. This absorption results from the excitation of an electron from the valence band onto a neutral indium center where it occupies the single negatively charged state lying 157 meV above the valence band. The cross-section for this optically excited transition is approximately 1.7×10^{-17} cm^2 for photons with an energy equivalent 1550 nm wavelengths [8]. The excitation of an electron from the indium into the conduction band requires a photon energy of 0.94 eV, and therefore has a negligible optical cross-section for 1550 nm photons. The absorption strength for this wavelength is then proportional to the concentration of neutral (unoccupied) indium, which is dependent on the position of the Fermi level. The absorption coefficient of the 4 µm resonant band for 1550nm can be described as follows:

$$\alpha_d = \sigma_p^{opt} \int_{x,y} \Phi(x,y)(N_t(x,y) - n_t(x,y))dxdy \tag{1}$$

where σ_p^{opt} is the cross-section for optical absorption at 1.55 µm wavelength; $\Phi(x,y)$ is the normalized (unit power) optical mode profile of the waveguide; $N_t(x,y)$ is the profile of the indium concentration; $n_t(x,y)$ is the profile of the ionized (negatively charged) indium.

For indium doping alone, the device is *p*-type and the indium acceptors are partially occupied (n_t is a fraction of N_t) and the optical absorption for 1550 nm is maximized, as depicted in the left of Fig. 1. Whereas, for background doping which is *n*-type the indium acceptors are compensated and thus have an occupation n_t which approaches N_t, which reduces the absorption coefficient.

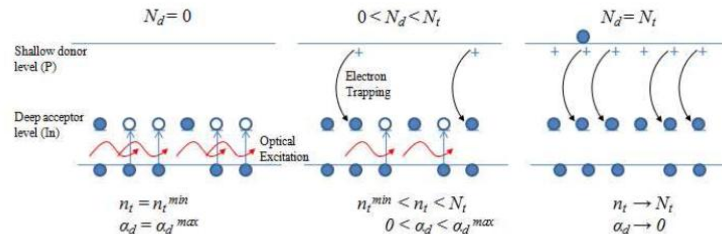

Fig. 1. The band diagram of silicon containing a constant concentration of deep acceptors N_t and varying concentrations of shallow donor levels N_d. Without the presence of shallow donors (left), many deep acceptors are unoccupied (n_t takes its minimum value n_t^{min}) and therefore electrons are capable of being optically excited from the valence band. Moving to the right, shallow donors are added in increasing concentrations. These donors supply free electrons that are trapped by the vacant deep level acceptors, thus decreasing the number of sites available for electrons to be optically excited into. On the far right, the shallow donor concentration is large enough to completely compensate the deep levels, making the optical excitation process impossible.

3. Experimental and modelled absorption

Rib waveguides of 4 µm width were fabricated on eleven samples cleaved from 2.5 µm thick silicon overlayer SOI, using a KOH wet etching technique described elsewhere [10]. The etch depth was chosen to ensure the resulting waveguide supported single-mode propagation for 1550 nm light. Windows of varying length *L* (up to a maximum length of 4 mm), centered on each rib, were defined using 4 µm thick photoresist, and used as a mask during ion implantation of indium at 500 keV for doses varying from 10^{13} to 6×10^{14}cm^{-2}. The samples were then cleaned of the resist mask and annealed at 1000 C in dry O_2 for 50 minutes. Eight of the unmasked samples were subsequently ion implanted with phosphorus at an energy of

#114991 - $15.00 USD Received 29 Jul 2009; revised 23 Sep 2009; accepted 25 Sep 2009; published 30 Sep 2009
(C) 2009 OSA

175 keV at doses ranging from $6x10^{12}$ to $2x10^{14}cm^{-2}$, and annealed at 1000 C in dry O_2 for a further 150 minutes. These implantation and thermal processes were designed to position the resulting indium and phosphorus concentration profiles coincidently, with a peak concentration at ~1 µm. The concentration of the indium and phosphorus doping at their peak of the profiles are provided in Table 1.

The unmasked phosphorus implantation contributes to free-carrier absorption over the entire waveguide length W, while the masked indium implant contributes to absorption over the window length L, only. Therefore, the total loss measured for each waveguide has the following form:

$$Total\ Loss\ (dB) = \alpha_d L + \alpha_i W + c \quad (2)$$

where α_d is the absorption coefficient of the indium center from Eq. (1); L is the length of the indium implantation window; α_i is the intrinsic absorption coefficient, which includes the effects of enhanced free carrier absorption consequent from phosphorus doping; W is the entire length of the waveguide; and c is the coupling loss.

Laser light close to 1550 nm in wavelength was coupled into each waveguide through a tapered optical fibre, and the transmitted light collected by an objective lens and focused onto a free-space InGaAs photodetector.

The measured variation in the total loss between waveguides on a single sample is due to the variation in L (the waveguides have constant length W). The value of α_d can be extracted from a fit to the total loss vs. L, examples of which are shown in Fig. 2. The summary of variation in indium and phosphorus doping for each sample and the measured α_d is provided in Table 1 and plotted as Fig. 3.

Table 1: Summary of Measured and Simulated Loss for Fabricated Waveguide Chips

Indium		Phosphorus		Measured Excess Loss (dB/cm)	Modelled Excess Loss (dB/cm)
Implanted Dose (cm^{-2})	Peak Concentration (cm^{-3})	Implanted Dose (cm^{-2})	Peak Concentration (cm^{-3})		
10^{13}	1.7×10^{17}	6×10^{13}	1.3×10^{18}	−0.17 +/− 3.87	−0.38
10^{13}	1.7×10^{17}	6×10^{12}	1.4×10^{17}	1.86 +/− 0.93	0.45
10^{13}	1.7×10^{17}	-	-	2.58 +/− 0.62	1.09
6×10^{13}	10^{18}	2×10^{14}	3.7×10^{18}	1.18 +/− 0.33	−4.84
6×10^{13}	10^{18}	6×10^{13}	1.3×10^{18}	5.28 +/− 2.03	−2.47
6×10^{13}	10^{18}	6×10^{12}	1.4×10^{17}	13.09 +/− 1.03	9.16
6×10^{13}	10^{18}	-	-	11.56 +/− 1.06	9.91
6×10^{14}	1.5×10^{18}	2×10^{14}	3.7×10^{18}	10.37 +/− 3.18	1.04
6×10^{14}	1.5×10^{18}	6×10^{13}	1.3×10^{18}	24.77 +/− 3.67	22.16
6×10^{14}	1.5×10^{18}	6×10^{12}	1.4×10^{17}	29.41 +/− 4.11	32.26
6×10^{14}	1.5×10^{18}	-	-	33.51 +/− 4.07	33.04

#114991 - $15.00 USD Received 29 Jul 2009; revised 23 Sep 2009; accepted 25 Sep 2009; published 30 Sep 2009
(C) 2009 OSA

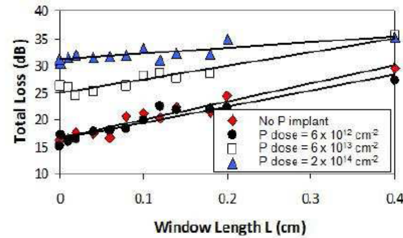

Fig. 2. Example plots of total loss measured for each waveguide for the chip with indium implanted at a dose of 6x10^{14}cm^{-2}, while the various phosphorus doses are also indicated. A fit to the data using Eq. (2) provides the excess loss due to the indium doping, α_d (the slope of the line, which is observed to decrease with increasing phosphorus dose).

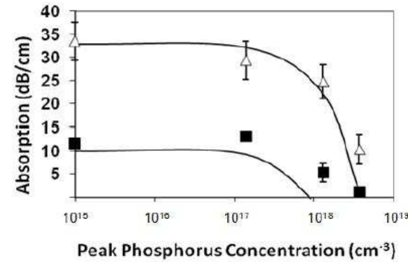

Fig. 3. Extracted values of α_d vs. peak phosphorus concentration for all samples with indium implanted to a dose of 6x10^{13} cm^{-2} (black squares) and 6x10^{14} cm^{-2} (white triangles), illustrating the significant decrease of α_d resulting from co-doping with phosphorus. The solid lines are fits to the data derived from Eqs. (1) and (3).

The modelled excess optical loss due to the presence of indium doping is shown in the far right column of Table 1. Using the implantation conditions given above the dopant concentration profiles were simulated using the software code ATHENA [11]. The optical cross-section for excitation of an electron from the valence band to the unoccupied indium level, σ_p^{opt}, was assumed to be 1.7x10^{-17} cm^2 [8]. The optical mode profile $\Phi(x,y)$ was obtained from commercial Beam Propagation software [12].

The indium occupation $n_t(x, y)$ was calculated by assuming 100% activation of phosphorus (with a concentration N_d), and numerically solving

$$e + n_t = \frac{n_i^2}{e} + N_d, \qquad \frac{n_t}{N_t} = \frac{c_n e + c_p p'}{c_n(n'+e) + c_p(p'+ n_i^2/e)} \tag{3}$$

for n_t and e at each point (x, y), where: e is electron concentration, c_n and c_p are capture rates of electrons and holes for indium, n' and p' are related to the indium level's position in the band gap) [13].

For example, the calculated n_t/N_t is plotted in Fig. 4 for N_t = 10^{17} cm^{-3} and 10^{18} cm^{-3} for varying values of N_d.

#114991 - $15.00 USD Received 29 Jul 2009; revised 23 Sep 2009; accepted 25 Sep 2009; published 30 Sep 2009
(C) 2009 OSA

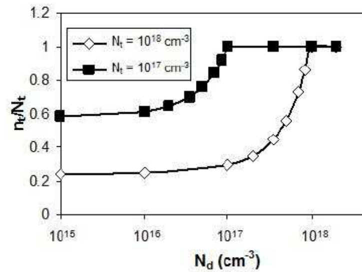

Fig. 4. Occupation fraction of indium vs. donor concentration N_d for N_t = 10^{17} cm^{-3} and 10^{18} cm^{-3}.

The results in Table 1 indicate that the variation in occupation of the indium dopant caused by the presence of shallow donor atoms manifests as a variation in optical absorption. We note that while the largest indium implantation dose would be expected to produce a peak indium concentration of 6x10^{18} cm^{-3}, and therefore an absorption in the region of 130 dB/cm, the activated indium concentration is limited by the solid solubility of indium in silicon. This solid solubility has been determined previously to be 1.4 – 1.5x10^{18} cm^{-3}, for an activation temperature of 1000 C which limits the accessible absorption [14,15]. This effect has been taken into account also in the modelling. Implicit is that indium which is not activated does not support electronic excitation.

The modelling also takes into account the decrease of free-carrier absorption within the implantation window as a consequence of electron trapping by indium centers. This is manifest as an added component to Eq. (1) that in certain cases causes α_d to take on apparent negative values, as shown in the far-right column of Table 1. A revision to Eq. (1) accounting for this effect yields:

$$\alpha_d = \sigma_p^{opt} \int_{x,y} \Phi(x,y)(N_t(x,y) - n_t(x,y))dxdy - \sigma_e^{opt} \int_{x,y} \Phi(x,y)e'(x,y)dxdy \quad (4)$$

where e' is the electron density supplied by phosphorus atoms which has been trapped by indium (i.e. the difference in indium occupation n_t between a phosphorus doped sample and a sample without phosphorus doping); $\sigma_e^{\ opt}$ is the cross-section for free electron absorption in silicon at 1550 nm, 6 x 10^{-18} cm^{-3} .

4. Potential designs for a modulator structure

It is of interest to consider how the phenomenon described in sections II and III (specifically for the case of indium doping) might be used to produce a modulation effect in a silicon waveguide. It is envisaged that a modulator may function by varying n_t (the number of occupied indium acceptors) over a large range to vary α_d as described in Eq. (1). For example, if a concentration of indium centres, N_t, is introduced into a waveguide with negligible background doping, n_t will be a small fraction of N_t (controlled by the electrical activation of indium) and α_d will be a maximum. Subsequent application of an electric field to the waveguide would then cause a depletion effect with the result that holes would be emitted from the indium centres, increasing n_t and decreasing the absorption to a minimum level. Alternatively, if N_t indium centers are introduced into a waveguide which is co-doped with shallow donors (such as phosphorus atoms) to a concentration of N_d, such that $N_d \geq N_t$, the indium dopant will be fully compensated with the result that $n_t = N_t$ (as in Fig. 3) so that minimum absorption occurs. An application of a forward bias causes n_t to decrease and

#114991 - $15.00 USD Received 29 Jul 2009; revised 23 Sep 2009; accepted 25 Sep 2009; published 30 Sep 2009
(C) 2009 OSA

thereby enhance absorption. Investigation of these two alternative device designs is the focus of the remainder of this paper. Each design is subsequently referred to as the *depletion* or *injection* methods.

Simulations were performed using the commercial software ATLAS [11]. A silicon waveguide structure shown schematically in Fig. 5 was described in the Deckbuild environment and electronic levels, having the characteristics of the indium center, were added into the entire overlayer region of the SOI. The structure was subsequently modelled for electrical performance using ATLAS. For each bias condition, the two-dimensional profile of the ionized acceptor trap density, $n_t(x, y)$, was determined. The normalized optical mode profile $\Phi(x,y)$, obtained from the waveguide propagation simulator BeamPROP, was used to calculate the overlap integral of Eq. (1). As a result, it was possible to acquire α_d as a function of electrical bias applied to the device. In addition, free carrier concentration distributions were simulated and used to calculate their absorption contribution. This was also incorporated into a transient simulation, whereby the total absorption was computed at various time intervals following bias application in order to determine the bandwidth of the device.

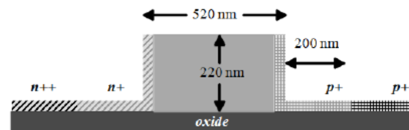

Fig. 5. Cross-sectional view of the device modelled in this study, described previously by Geis et al. The p + and n + regions correspond to doping levels of 10^{18} cm^{-3}, and the p + + and n + + correspond to doping levels of 10^{19} cm^{-3} [2].

The device used for this study, shown in Fig. 5, utilises a sub-micron sized structure used previously, for example, to form waveguide photodetectors as described by Geis *et al.* [2]. Both contact regions are in close proximity to the optical mode, which is beneficial in that any carrier depleted volume or injected hole distribution overlaps strongly with the optical mode.

Depletion Method: A limitation of the depletion method when applied to the device structure shown in Fig. 5 is that it is restricted to relatively small values of indium concentration, N_t. The use of high concentrations of indium severely limits the volume of the waveguide that could be depleted. For instance, α_d increases with N_t at a rate given by Eq. (1), but the bias required to achieve $n_t = N_t$ increases also. To demonstrate this effect Fig. 6 plots simulated optical absorption as a function of reverse bias for two values of N_t. The achievable modulation depth is limited to ~5 dB/cm for a relatively large bias of –20 V, while it is difficult to achieve zero loss using the depletion method, even for $N_t = 2\text{x}10^{17}\text{cm}^{-3}$. Although the large insertion loss and limited modulation depth limits its applicability, this 'normally off' device can provide substantially reduced power consumption over traditional optical modulators, particularly in the case of multiple channel devices where the majority of the channels are required to be in the 'off' state for a given time interval.

A transient study was also performed using the depletion method. For the case of N_t = 2x10^{17} cm^{-3} the results are shown in Fig. 7. The turn-on time is 0.6 ns, and becomes larger as N_t is increased. The turn-off time is 0.3 ns, and was found to be independent of the value of N_t (for the two values in Fig. 6). There is no significant impact of the magnitude of the reverse bias on the turn-on and turn-off times.

#114991 - $15.00 USD Received 29 Jul 2009; revised 23 Sep 2009; accepted 25 Sep 2009; published 30 Sep 2009
(C) 2009 OSA

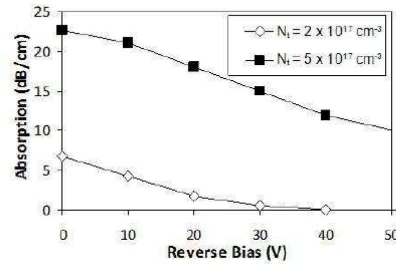

Fig. 6. Absorption coefficient α_d plotted as a function of applied reverse bias, for two uniform indium concentrations, N_t.

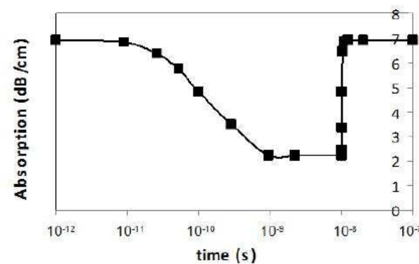

Fig. 7. Simulated absorption coefficient following the application of a −20 V bias, and following the removal of the bias after 10 ns.

Injection Method: Relative to the depletion method, the modulation achievable via carrier injection is considerable. The ability of ionized acceptors to decrease n_t via hole capture is largely dependent on the difference between the capture rates for electrons and holes. For indium the capture cross-section of holes (8×10^{-15} cm^2) is much larger than the capture cross-section for electrons (2×10^{-22} cm^2) [8]. As a result, the injected holes will be preferentially captured over the injected electrons in a bipolar device. This disparity in carrier trapping rates can be enhanced by placing the *p*-type contact in a closer proximity to the optical mode than the *n*-type contact, allowing more holes in the modal volume than electrons. This injection method then can be used as an enhancement to a variable optical attenuator (VOA) which relies on free carrier absorption alone, achieving a significantly larger extinction ratio with a negligible increase in dissipated power.

In the simulation results that follow the value of the *n*-type background doping N_d of the waveguide were fixed such that $N_d = N_t$. The extinction ratio of the modulator will increase with increasing N_t. Figure 8 plots this increase as a function of N_t, showing the seemingly unbounded improvement over a modulator without indium and with a background doping concentration of 10^{15}cm^{-3} (this is equivalent to a device using free-carrier injection alone to achieve modulation). The limit on modulation improvement will in fact be determined by the solid solubility of indium in the silicon waveguide. For larger devices (on the order of 10 μm^2 cross-section), the large donor concentrations will limit the penetration of holes into the device cross-section.

In practice, N_d is unlikely to be matched to N_t, which may lead to an excess insertion loss. If $N_d > N_t$, the insertion loss will increase due to free carrier absorption; while if $N_t > N_d$, the insertion loss will increase due to absorption from uncompensated indium. Since the optical

#114991 - $15.00 USD Received 29 Jul 2009; revised 23 Sep 2009; accepted 25 Sep 2009; published 30 Sep 2009
(C) 2009 OSA

cross-section for indium absorption is approximately double that for absorption of free electrons, it is preferred to overcompensate the background doping such that $N_d > N_t$, as is the case in the passive loss data described in section III. For example, overcompensating such that $N_d = 1.1 \times 10^{18}$ cm^{-3} while $N_t = 10^{18}$ cm^{-3}, an insertion loss of 2.6 dB/cm will be present.

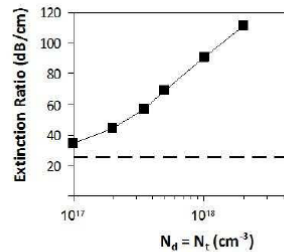

Fig. 8. Simulated α_d following application of 1 V forward bias as a function of $N_t = N_d$ (dotted line: performance of free-carrier absorption alone).

The turn-on and turn-off times for the injection modulator are plotted as a function of $N_t = N_d$ in Fig. 9. The horizontal lines indicate the turn-on and turn-off times for a device containing no indium and again represents the performance of a device relying on free-carrier absorption alone. It is possible to improve the turn-on time (t_{on}) by applying a reverse bias rather than a zero bias to switch to the non-absorbing state. However, this decreases the modulation depth because the electric fields not only sweep out free-carriers but also decrease the indium occupancy. Regardless, t_{on} cannot be reduced below t_{off}, which is related to the capture and emission rate of free carriers at the indium centers and represents the fundamental limit in the speed of these devices. Compared to the case of free carrier absorption alone then, the modulation bandwidth is degraded by the introduction of indium. We note though that for indium doping levels < 3×10^{17}cm^{-3} the speed of the device remains close to 1 GHz.

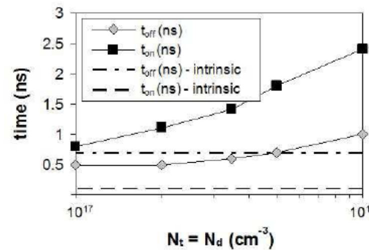

Fig. 9. Turn-off time (t_{off}) and turn-on time (t_{on}) plotted as a function of $N_t = N_d$, showing the decrease in device speed concurrent with the increase in absorption.

The Extinction Ratio vs. Dissipated Power for two indium doping concentrations, one having $N_t = N_d = 10^{18}$ cm^{-3} and a second having $N_t = N_d = 10^{17}$ cm^{-3}, is plotted as Fig. 10, together with that for a device without enhancement from indium absorption.

At $N_t = N_d = 10^{17}$ cm^{-3}, the enhancement in modulation relative to the undoped device is such that the addition of indium barely compensates for the degradation in absorption from free holes. For $N_t = N_d = 10^{18}$ cm^{-3}, the increase in absorption is however significant. For example, a device of 1 mm in length would require 40 mW of power to achieve an extinction

#114991 - $15.00 USD Received 29 Jul 2009; revised 23 Sep 2009; accepted 25 Sep 2009; published 30 Sep 2009
(C) 2009 OSA

ratio of 10 dB. Alternatively, a 1 mm VOA using only free-carrier absorption would require approximately 400 mW to achieve a 10 dB extinction ratio.

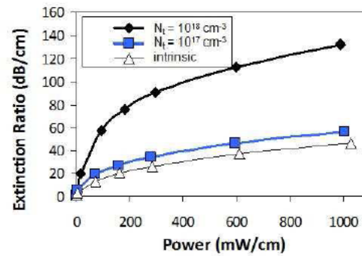

Fig. 10. Extinction ratio vs. Power (both normalized to length) for the enhanced VOA for two levels of indium doping, plotted with the performance of an undoped device operating solely by free-carrier absorption.

Assuming the device is sufficiently small, the limiting factor on both extinction ratio and speed is the deep level characteristics, specifically the optical cross-section for excitation of electrons from the valence band to the defect level, σ_p^{opt}, and the relative capture cross-sections of electrons and holes at the defect level. For instance, the larger the difference in hole and electron cross-sections, the more effective the current injection for changing the occupancy. The speed of the device could be increased by selecting a defect level with larger capture cross-sections of both electrons and holes, while maintaining a significant superiority of holes over electrons for the reasons outlined above.

5. Conclusion

We have investigated the effects of doping type and concentration on the absorption of deep level defects in silicon waveguides using the indium center as an example. The dependence has been shown to be correlated with the defect occupancy, which in turn depends on the location of the Fermi level, and can be changed by depleting or injecting a device with charge carriers. This presents a novel means for fabricating a "normally off" VOA device or enhancing more traditional forms of carrier injection VOA operation. We have shown that both the speed and modulation depth of a sub-micron cross-sectional device depends primarily on the defect characteristics.

#114991 - $15.00 USD Received 29 Jul 2009; revised 23 Sep 2009; accepted 25 Sep 2009; published 30 Sep 2009
(C) 2009 OSA
12 October 2009 / Vol. 17, No. 21 / OPTICS EXPRESS 18580

B.5 D. F. Logan, P. Velha, M. Sorel, R. M. De La Rue, A. P. Knights, and P. E. Jessop, "Defect-enhanced Silicon-on-insulator Waveguide Resonant Photodetector with High Sensitivity at 1.55 µm," Photonics Technology Letters, vol. 22, p. 1530, 2010.

This letter summarizes the early work in sub-micron photodetector structures, with emphasis on the resonant photodetectors described in chapter 6. It is included in full in the following pages.

This work was also presented at the IPR (Integrated Photonics Research) meeting in Monterey, CA in July 2010, and has an associated publication in the OSA Technical Digest.

© 2010 IEEE. Reprinted, with permission, from D. F. Logan, P. Velha, M. Sorel, R. M. De La Rue, A. P. Knights, and P. E. Jessop, "Defect-enhanced Silicon-on-insulator Waveguide Resonant Photodetector with High Sensitivity at 1.55 µm," IEEE Photonics Technology Letters, October 2010.

This material is posted here with permission of the IEEE. Such permission of the IEEE does not in any way imply IEEE endorsement of any of McMaster University's products or services. Internal or personal use of this material is permitted. However, permission to reprint/republish this material for advertising or promotional purposes or for creating new collective works for resale or redistribution must be obtained from the IEEE by writing to pubs-permissions@ieee.org .By choosing to view this material, you agree to all provisions of the copyright laws protecting it.

1530 IEEE PHOTONICS TECHNOLOGY LETTERS, VOL. 22, NO. 20, OCTOBER 15, 2010

Defect-Enhanced Silicon-on-Insulator Waveguide Resonant Photodetector With High Sensitivity at 1.55 μm

Dylan F. Logan, Philippe Velha, Marc Sorel, Richard. M. De La Rue, Andrew P. Knights, and Paul E. Jessop

***Abstract*—We describe the fabrication and characterization of a silicon waveguide resonant photodetector compatible with the optical-to-electrical conversion of wavelengths at, or around, 1550 nm. Sub-band responsivity is provided through the introduction of defects via inert self-implantation and subsequent annealing. The detector is located within a 20-μm radius silicon microring resonator. An 18-dB resonant enhancement in absorption coefficient and 12-dB enhancement in photocurrent were measured, leading to a resonant responsivity of approximately 39 mA/W at 20-V reverse bias.**

***Index Terms*—Integrated optics, optical resonators, p-i-n photodiodes, semiconductor defects.**

I. Introduction

THE integration of electrical and photonic functionality in silicon continues to drive a large volume of research, with the aim of realizing optoelectronic devices that are compatible with a complementary metal–oxide–semiconductor (CMOS) process flow and able to perform fundamental functions such as emission, waveguiding, multiplexing, modulation, and detection [1]. In the case of integration of a sub-bandgap detector, there is the challenge of efficient optical-to-electrical conversion of optical wavelengths for which silicon is normally transparent. In addition to the hybrid integration of silicon and III–V semiconductors [2] and/or Germanium [3], the technique of selective ion-implantation to generate mid-gap defects has been utilized in p-i-n waveguide photodiodes [4], [5]. The flexibility of this process has been shown to produce devices suitable for terminal detection and optical monitoring capability (so that a small fraction of the light is sampled, while the majority passes unmolested) [6], [7]. The carrier-trapping behavior of defects leads to limited charge extraction, and thus limited responsivity, with large cross-section ($>1\ \mu$m^2) waveguide photodiodes [4]. However, large responsivity approaching 10 A/W has been reported in submicrometer channel waveguides with doped sidewalls, where an applied electric field may penetrate sufficiently far into the waveguide to efficiently extract charge [8], [9]. One disadvantage of this approach is that the optical absorption is on the order of 100 dB/cm, and therefore, the device size must be several hundred micrometers in length to absorb the majority of the propagating light.

In order to reduce the length of these devices, while maintaining high absorption, a resonant structure may be incorporated. The optical loss of such a device scales proportionally with the accumulation of intensity in the resonator, thereby increasing the effective absorption length. The absorption coefficient may be written as

$$\alpha = \alpha_0 \times \text{BUF} = \alpha_0 \frac{2}{\pi} \frac{\lambda_{\text{FSR}}}{\Delta\lambda} \quad (1)$$

where α is the enhanced absorption in the resonator; α_0 is the waveguide absorption (in this case dominated by the defects introduced by the implantation process); BUF is the build-up factor; λ_{FSR} is the free-spectral range of the resonance; and $\Delta\lambda_0$ is the full-width at half-maximum of a single resonance [10].

This resonant enhancement of absorption and modest detection in monolithic silicon devices has been demonstrated recently by Chen *et al.* [11], using a microring resonator architecture that did not receive a defect-inducing ion implantation step. In their devices, the detection mechanism was assumed to be mediated by an interface state and the two-photon absorption of the propagating sub-bandgap signal. They reported that the photocurrent from a reverse-biased p-i-n junction integrated with the ring increased by 20 times on resonance, leading to a responsivity of 0.25 mA/W at -15-V bias. Also of relevance to the current work is that recently reported by Doylend *et al.* [12], in which a sub-bandgap ring resonant detector structure was defined using the LETI CMOS fabrication facility. In the current work, we show that, through the use of electron beam lithography and the incorporation of defects by Si^+ ion-implantation, the absorption can be further significantly increased (significantly) to achieve much higher resonant responsivity.

II. Fabrication and Experiment

A schematic of the devices fabricated in this experiment is shown in Fig. 1(a). A Leica VB-6 electron-beam writer was used to define 500-nm-wide waveguides in 300-nm-thick HSQ resist on a lowly p-doped ($\sim 10^{15}$ cm^{-3}) 220-nm-thick Si-overlayer, silicon-on-insulator (SOI) substrate. The waveguides were etched to a depth of 150 nm using an SF_6–C_4F_8–O_2 inductively coupled plasma. After a subsequent dry thermal growth of a 50-nm oxide layer at 1000 °C, a 50-nm silicon slab remained in the regions surrounding the waveguide. The microrings were 20 μm in radius—and were coupled to the drop waveguide by an evanescent point coupler with a gap

Manuscript received April 07, 2010; revised July 02, 2010; accepted August 08, 2010. Date of publication August 12, 2010; date of current version September 24, 2010.

D. F. Logan, A. P. Knights, and P. E. Jessop are with the Department of Engineering Physics, McMaster University, Hamilton, ON, L8S 4L8, Canada (e-mail: logand@mcmaster.ca; aknight@mcmaster.ca; pjessop@mcmaster.ca).

P. Velha, M. Sorel, and R. M. De La Rue are with the Department of Electronics and Electrical Engineering, University of Glasgow, Glasgow, G12 8LT, U.K. (e-mail: velhap@elec.gla.ac.uk; sorel@elec.gla.ac.uk; r.delarue@elec.gla.ac.uk).

Digital Object Identifier 10.1109/LPT.2010.2066963

1041-1135/$26.00 © 2010 IEEE

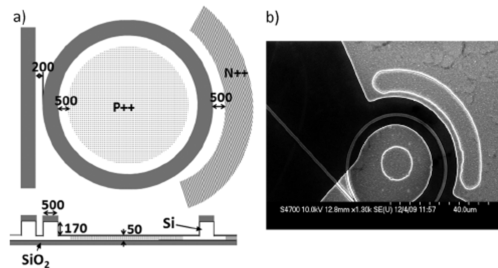

Fig. 1. (a) Schematic of the device structure from above (top) and cross-sectional view (below) (all dimensions in nanometers). (b) SEM image of final device.

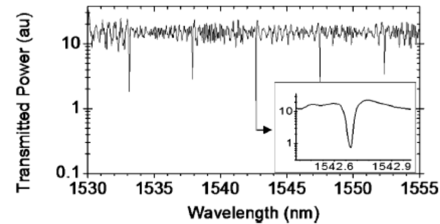

Fig. 2. Transmitted power measured on bus waveguide; resonant drops in transmission due to the 20-μm ring are spaced at 4.83 nm, and have a linewidth of 0.06 nm (inset shows the drop at 1542.7 nm).

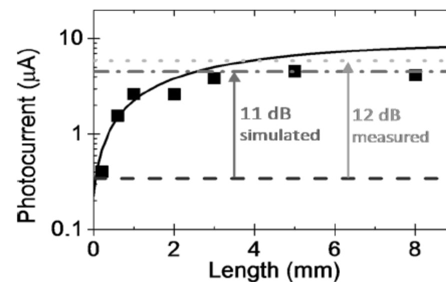

Fig. 3. Simulated (solid black curve) and measured (solid square points) performance of straight photodiode sections of varying length. Also indicated is the simulated response of a 50-μm-long straight photodiode section (bottom dark dashed line), as well as the simulated (gray dashed–dotted line) and measured (gray dotted line) resonant response of a 50-μm-long photodiode integrated with a microring, showing a photocurrent enhancement of 12 dB. All measurements and simulations use a 20-V reverse bias and an on-chip optical power of 115 μW.

of 200 nm. Boron was implanted to a peak concentration of 5×10^{19} cm^{-3} to form a p-type region in the slab in the center of the ring, at a distance of 500 nm from the inner edge of the waveguide. Phosphorus was implanted to a peak concentration of 5×10^{19} cm^{-3} to form an n-type region over a 140° (50 μm long) arc—and also at a distance of 500 nm from the outer edge of the ring. The device was then annealed at 1000 °C for one minute, in order to activate the dopants. Subsequent deposition of 400-nm silicon dioxide and dry etching in a CHF_3 plasma was used to form contact vias to the doped regions—which was followed by a patterned aluminum lift-off process, in order to form electrical contacts to the p- and n-doped regions of the slab. A scanning electron microscope (SEM) surface image of the resulting device is shown as Fig. 1(b). Windows were opened over the entire ring as well as a 50 μm of the bus waveguide in 1.8-μm-thick photoresist, and implanted with 190-keV Si^+ ions to a dose of 1×10^{13} cm^{-2}, to form sufficient damage to increase the optical absorption. In addition to those located within the rings, p-i-n diodes were also formed on straight waveguide sections with lengths varying from 0.2 to 8 mm. From measurement of the transmission loss of the straight photodiode sections, the extracted excess loss was approximately 170 dB/cm. A subsequent 5-min anneal, at 325 °C in N_2, removed/modified the implantation induced defects to reduce the excess optical absorption to 10.8 ± 2.3 dB/cm.

Light was butt-coupled into the bus waveguide from a wavelength tunable laser diode source via a tapered fiber and collected by an objective lens and directed to a free-space InGaAs amplified detector. The coupling loss for unimplanted waveguides was measured to be $14.8+/-3.2$ dB. Fig. 2 plots the transmission of the bus waveguide as a function of wavelength, featuring resonant drops in transmission with a free spectral range of $4.83 + / - 0.03$ nm. The linewidth of the resonant peaks is $0.060 + / - 0.006$ nm. Using (1), one may calculate an absorption enhancement by a factor of 51.

III. Results and Discussion

Previous modeling of defect-enhanced detection in silicon waveguides predicts photodetector performance by assuming that the implantation damage leads to the formation of a single deep-level in the silicon bandgap [7]. The previously measured optical [13] and electrical [14] characteristics of the silicon divacancy were used to simulate the effect of this single level in [7]. Using the following relationship between the excess optical absorption α (in units of cm^{-1}) and the concentration of divacancies $N_{\rm Div}$ [13]:

$$N_{\rm Div} = \alpha \times \left[7.7 \times 10^{16}\ {\rm cm}^{-2}\right] \tag{2}$$

a loss of $\alpha = 10.8$ dB/cm corresponds to the presence of approximately $N_{\rm Div} = 2 \times 10^{17}$ cm^{-3} mid-gap defects in the waveguide. The detectors in the straight waveguide sections (i.e., those not in a resonant structure) were modeled with the assumption of this defect concentration, following the method described in [7]. An on-chip optical power of 115 μW was assumed, with an applied reverse bias of 20 V. The results are presented as the solid curve in Fig. 3. For comparison, the photocurrent measurements of the straight devices are plotted as data points, and suggest good agreement with the model. We note that the simulated photocurrent for a 50-μm-long device is 0.37 μA. The resonant photodiode current (for detectors integrated with the rings) may be approximated by assuming an absorption enhancement factor of 51; giving a value of 4.53 μA, representing an enhancement in the photocurrent of 11 dB.

The measured resonant photocurrent is indicated as the light dotted line on Fig. 3, and represents a 12-dB enhancement over a straight (nonresonant) defect-enhanced photodiode of the same dimensions. The resonant photodiode produces a photocurrent that is larger than that measured for straight devices of all lengths—and an equivalent simulated photodiode

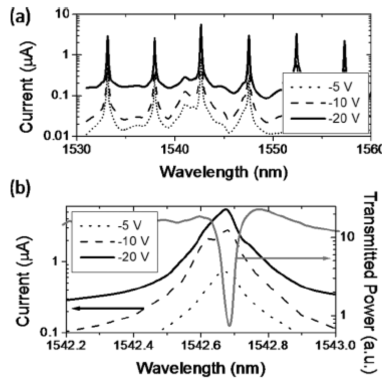

Fig. 4. Measured current versus wavelength of the tunable laser: (a) over a large range of resonances, (b) on the 1542.65-nm resonance with the measured waveguide transmission on the right axis (gray curve).

length of 3 mm. Therefore, the 50-μm microring integrated detector has an absorption that is enhanced by a factor of 60 by the resonant build-up of optical intensity. It should be stressed that the enhancement produced is in the absorption coefficient, rather than in the photocurrent, since the absorption coefficient and photocurrent are nonlinearly related, as indicated by Fig. 3. As a result, this 18-dB increase in the absorption leads to a 12-dB enhancement of the photocurrent.

Measured resonant photocurrent versus optical wavelength for several applied bias voltages is shown in Fig. 4(a) for the wavelength range of 1530–1560 nm—and in Fig. 4(b) for the range 1542.2–1543 nm. A linear relationship between the measured photocurrent and the estimated on-chip optical power allows calculation of the responsivity for the detectors of $1.0+/-0.3$ mA/W at 0-V bias and $39+/-13$ mA/W at 20-V reverse bias. This performance represents a more than 100-fold improvement in responsivity over the ring-resonator devices fabricated by Chen *et al.*, which utilized optical-to-electrical conversion that was not mediated by ion-implantation induced defects [11]. The dark current of the detectors integrated with the microring is 1.1 nA at 20 V reverse bias, but increases to 175 nA when off-resonant wavelength light is present, indicating some detection of light propagating in the waveguide bus. This likely accounts for the wider spectral response of the detectors compared to the drop spectrum measured at the output of the bus [shown in Fig. 4(b)]. Coupling of light at resonant wavelengths causes the photocurrent to increase to measured values as high as 5.9 μA, a 15-dB resonant enhancement that is measured consistently for all reverse bias values.

IV. Conclusion

We have demonstrated resonant detection of sub-bandgap light in defect mediated photodiodes incorporated in a microring waveguide structure. In addition to suitability for applications in wavelength-division multiplexing, they provide a significant advantage in that the detector size may be reduced by the enhancement factor, with equivalent performance to detectors previously described in a straight waveguide geometry.

Acknowledgment

The authors would like to acknowledge useful discussions with J. Doylend with regard to results obtained from ring resonant detectors fabricated during the 2009 LETI ePIXfab shuttle run.

References

[1] L. Chen, K. Preston, S. Manipatruni, and M. Lipson, "Integrated GHz silicon photonic interconnect with micrometer-scale modulators and detectors," *Opt. Express*, vol. 17, pp. 15248–15256, 2009.
[2] L. Liu, G. Roelkens, J. Van Campenhout, J. Brouckaert, D. Van Thourhout, and R. Baets, "III–V/silicon-on-insulator nanophotonic cavities for optical network-on-chip," *J. Nanosci. Nanotechnol.*, vol. 10, pp. 1461–1472, 2010.
[3] L. Vivien, J. Osmond, J.-M. Fédéli, D. Marris-Morini, P. Crozat, J.-F. Damlencourt, E. Cassan, Y. Lecunff, and S. Laval, "42 GHz p.i.n Germanium photodetector in a silicon-on-insulator waveguide," *Opt. Express*, vol. 17, pp. 6252–6257, 2009.
[4] A. P. Knights, J. D. B. Bradley, S. H. Gou, and P. E. Jessop, "Silicon-on-insulator waveguide photodetector with self-ion-implantation engineered-enhanced infrared response," *J. Vac. Sci. Technol.*, vol. A24, pp. 783–786, 2006.
[5] Y. Liu, C. W. Chow, W. Y. Cheung, and H. K. Tsang, "In-line channel power monitor based on Helium ion implantation in silicon-on-insulator waveguides," *IEEE Photon. Technol. Lett.*, vol. 18, no. 17, pp. 1882–1884, Sep. 1, 2006.
[6] J. K. Doylend, A. P. Knights, B. J. Luff, R. Shafiiha, M. Asghari, and R. M. Gwilliam, "Modifying functionality of variable optical attenuator to signal monitoring through defect engineering," *Electron. Lett.*, vol. 4, pp. 234–6, 2010.
[7] D. Logan, P. E. Jessop, and A. P. Knights, "Modeling defect enhanced detection at 1550 nm in integrated silicon waveguide photodetectors," *J. Lightw. Technol.*, vol. 27, no. 7, pp. 930–937, Apr. 1, 2009.
[8] M. W. Geis, S. J. Spector, M. E. Grein, R. T. Schulein, J. U. Yoon, D. M. Lennon, S. Deneault, F. Gan, F. X. Kaertner, and T. M. Lyszczarz, "CMOS-compatible all-Si high-speed waveguide photodiodes with high responsivity innear-infrared communication band," *IEEE Photon. Technol. Lett.*, vol. 19, no. 3, pp. 152–154, Feb. 1, 2007.
[9] M. W. Geis, S. J. Spector, M. E. Grein, J. U. Yoon, D. M. Lennon, and T. M. Lyszczarz, "Silicon waveguide infrared photodiodes with > 35 GHz bandwidth and phototransistors with 50 AW^{-1} response," *Opt. Express*, vol. 17, pp. 5193–5204, 2009.
[10] J. E. Heebner, R. W. Boyd, and Q.-H. Park, "Slow light, induced dispersion, enhanced nonlinearity, and optical solitons in a resonator-array waveguide," *Phys. Rev. E*, vol. 65, p. 036619, 2002.
[11] H. Chen, X. Luo, and A. Poon, "Cavity-enhanced photocurrent generation by 1.55 μm wavelengths linear absorption in a p-i-n diode embedded silicon microring resonator," *Appl. Phys. Lett.*, vol. 95, p. 171111, 2009.
[12] J. K. Doylend, P. E. Jessop, and A. P. Knights, "Silicon photonic resonator-enhanced defect-mediated photodiode for sub-bandgap detection," *Opt. Express*, vol. 18, p. 14671, 2010.
[13] P. J. Foster, J. K. Doylend, P. Mascher, A. P. Knights, and P. G. Coleman, "Optical attenuation in defect-engineered silicon rib waveguides," *J. Appl. Phys.*, vol. 99, p. 073101, 2006.
[14] E. Simoen, C. Claeys, E. Gaubas, and H. Ohyama, "Impact of the divacancy on the generation-recombination properties of 10 MeV proton irradiated float-zone silicon diodes," *Nucl. Instrum. Methods Phys. Res. A*, vol. 439, pp. 310–318, 2000.

B.6 D. F. Logan, A. P. Knights, P. E. Jessop, and N. G. Tarr, "Defect-Enhanced Photo-detection at 1550 nm in a Silicon Waveguide Formed via LOCOS," Semiconductor Science and Technology, vol. 22, p. 045009, 2011.

This publication summarizes the fabrication and characterization of the LOCOS-based photodetectors described in *B.2*. The majority of this paper is reproduced as chapter 4 of this thesis. It is included in full in the following pages.

© 2011 IOP. Reprinted with permission.

IOP PUBLISHING SEMICONDUCTOR SCIENCE AND TECHNOLOGY
Semicond. Sci. Technol. **26** (2011) 045009 (7pp) doi:10.1088/0268-1242/26/4/045009

Defect-enhanced photo-detection at 1550 nm in a silicon waveguide formed via LOCOS

D F Logan[1], A P Knights[1], P E Jessop[1] and N G Tarr[2]

[1] Department of Engineering Physics, McMaster University, Hamilton, ON, Canada
[2] Department of Electronics, Carleton University, Ottawa, ON, Canada

E-mail: logand@mcmaster.ca

Received 2 August 2010, in final form 7 December 2010
Published 21 February 2011
Online at stacks.iop.org/SST/26/045009

Abstract
We present the integration of a defect-enhanced photodiode with high sensitivity at 1550 nm with a silicon waveguide structure formed by the LOCOS (LOCal Oxidation of Silicon) process. The defects are introduced through a 4 MeV Si^+ implantation followed by thermal treatment at 200–500 °C to form a sub-bandgap photo-response. A 100 nm polycrystalline silicon layer forms a self-aligned contact to the top of the ridge waveguide and provides efficient extraction of generated carriers. Processing conditions and device structure design have been varied to determine their influence on responsivity, insertion loss and leakage current. A 6 mm long optical power monitor is presented with responsivity of approximately 47 mA W^{-1} at −5 V bias for an absorption of 12 dB (∼0.003 A W^{-1} dB^{-1}).

1. Introduction

1.1. Defect-enhanced photodetection

A necessary component for the continual development towards silicon-based chip-level optical integration is the silicon waveguide photodetector [1]. A complementary metal oxide semiconductor (CMOS) compatible process that selectively increases the sub-bandgap absorption in a silicon waveguide is required in devices which use light at a wavelength at or around 1550 nm. Ideally, that process technology should provide control in the degree of optical mode absorption, so that both power monitoring [2] and end-line detection [3] can be achieved. For broad-band detection (for example across the entire *C* and *L* bands), the photodetector should be integrated onto the transmission waveguide itself.

One method to achieve sub-bandgap response is to introduce defects into the silicon lattice by inert ion implantation to facilitate carrier generation. By incorporating a p-i-n junction laterally onto an implanted waveguide, an integrated photodiode sensitive to wavelengths near 1550 nm may be formed [4]. An attractive feature of this method is that the implantation and subsequent annealing conditions can be varied to engineer the optical absorption and therefore the responsivity of the detector. This control over defect concentration and distribution has been shown to produce efficient power monitors [2, 5].

1.2. Modelling the photodetection process and device structures

A model of the performance of photodiode structures using the commercially available ATLAS software has been presented in [6]. This model assumes that a single-defect level is responsible for the enhanced sensitivity. The optical and electronic properties of the silicon divacancy point defect were utilized in this previous work. This approach is justified by close agreement between the observed variation of ion implantation-induced excess waveguide absorption with thermal treatment and the behaviour of the 1.8 μm divacancy absorption band [7]. An electron hole generation rate is introduced into the simulation, having the spatial dependence of the waveguide mode. This generation rate includes a dependence on the length of the photodiode, input power, intrinsic loss, and the excess loss due to defects. The latter is related to the defect concentration through the optical cross-section for absorption of the divacancy, which has been reported as 1.3×10^{-17} cm^2 [7]. The electronic trap characteristics are introduced separately into ATLAS using the capture cross-section of the silicon divacancy [8]. This

 © 2011 IOP Publishing Ltd Printed in the UK & the USA

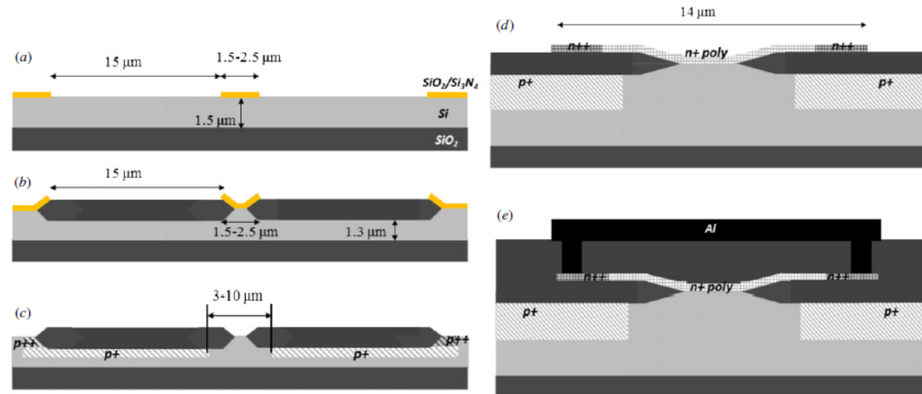

Figure 1. Cross-section of photodiode at selected points in the process flow: (*a*) following patterning of 50 nm $SiO_2/80$ nm Si_3N_4; (*b*) following wet oxidation at 1100 C; (*c*) following masked boron implant at 110 keV and 30 keV; (*d*) following patterning and phosphorus implantation of LPCVD amorphous silicon and (*e*) final device with aluminum contacts.

provides a means of evaluating photodetector geometries and optimizing the responsivity as a function of the introduced defect concentration. This approach and single defect state model were used in the design of the photodiode reported here. The present experimental results serve to further validate the general applicability of this model.

1.3. LOCOS waveguides

The LOCOS method (LOCal Oxidation of Silicon) is a standard CMOS electrical isolation process, whereby patterned silicon nitride prevents the thermal oxidation of silicon beneath it, creating smooth trenches on the silicon surface, filled with thermally grown SiO_2. The utilization of this process to form rib waveguides in silicon-on-insulator (SOI) material is attractive in that sidewalls formed by oxidation have low roughness and therefore provide low propagation loss [9]. The process has been optimized to produce losses of 0.36 dB cm^{-1} (for TE modes) [10] and modified to produce submicron isolated photonic wire waveguides [11].

An additional benefit of the LOCOS structure is that it forms a planarized surface ideal for electronic integration. In this paper, we describe the integration of an optical power monitor with a LOCOS waveguide through a self-aligned polysilicon junction above the guiding ridge, as depicted in figure 1. Forming a 'through' p-i-n junction in an etched waveguide ridge would require a deposition step as well as a critical photolithography alignment stage. Using a LOCOS waveguide alleviates the alignment requirement, and the trench oxide effectively isolates the contact metal (Al) from the region of the optical mode. This provides carrier depletion in the region of the optical mode that is enhanced over devices where depletion is provided by doped regions placed on either side of the ridge, leading to improved generated carrier extraction efficiency. Using the aforementioned model, it is anticipated that this structure will produce a response approximately 40 times more sensitive than previous large area ($>\mu m^2$) devices [4], approaching that of recent sub-micron photodetectors [5].

2. Experimental details

2.1. Design and fabrication

The waveguides were fabricated using 1.5 μm thick Si overlayer SOI wafers with a buried oxide (BOX) thickness of 1 μm, provided by SOITEC through the SmartCut process. Individual samples of approximately 250 cm^2 were oxidized to form a 50 nm SiO_2 layer, followed by a deposition of 80 nm Si_3N_4 via low pressure chemical vapour deposition (LPCVD). This dielectric stack was patterned into strips of 1.5, 2 and 2.5 μm width and etched back to the Si surface using a combination of a CF_4/O_2 plasma and hydrofluoric acid (HF) wet etch, forming the structure shown in figure 1(*a*). A wet oxidation at 1100 °C followed in which a 430 nm oxide layer was grown, providing a ridge height of approximately 190 nm. The patterned strip widths determined the bottom ridge width as illustrated in figure 1(*b*), and the height was chosen such that all widths exhibited single-mode behaviour. The Si_3N_4 layer above the ridge was removed using hot phosphoric acid, and the 50 nm oxide layer was removed using 10:1 buffered HF acid etch.

The width of the thermal oxide surrounding the ridge was required to be 15 μm to ensure negligible optical mode leakage. The waveguides were then patterned with photoresist to form windows for boron ion implantation, extending over the thermal oxide into the regions on either side, as illustrated in figure 1(*c*). A boron ion implantation at 110 keV and 4×10^{13} cm^{-2} dose was used to dope the silicon beneath

Table 1. Summary of device structure variations within wafer design.

Waveguide width (μm)	1.5, 2, 2.5
p-i-n junction length (mm)	3, 6
p+ region separation (μm)	3, 5, 10
Si^+ defect implant window width (μm)	3, 5, 10

the thermal oxide to a peak concentration of 10^{18} cm^{-3}, and another implantation at 30 keV and 10^{16} cm^{-2} dose was used to dope the sides of the trench to a peak concentration of $\sim 10^{20}$ cm^{-3}.

A 100 nm amorphous silicon layer was then deposited using either LPCVD on selected devices or by plasma-enhanced chemical vapour deposition (PECVD) as noted explicitly in the following text. This was followed by a phosphorus ion implantation at 25 keV and 3×10^{12} cm^{-2} dose. The deposited silicon was then selectively masked with the photoresist and dry etched in an SF_6 plasma to form 14 μm wide strips centred on the waveguide. Another masked phosphorus implant of 25 keV and 5×10^{14} cm^{-2} dose provided a peak doping concentration of 5×10^{19} cm^{-3} on the edges of the strips for electrical contact, as shown in figure 1(*d*).

The devices were then capped with a 300 nm thick PECVD SiO_2 layer and annealed in nitrogen to crystallize the amorphous silicon and to break down the native oxide at the interface between the deposited silicon and the ridge. The cap oxide prevents the out-diffusion of phosphorus during annealing [12], and the annealing temperatures were selected following reported work on the development of polysilicon-emitter bipolar junction transistors [13]. It was found that an anneal process at 900 °C for 30 min in an N_2 ambient was sufficient to electrically activate the majority of the implanted phosphorus. At higher temperatures, increased segregation of phosphorus into the silicon limits the activated concentration, and an increased reverse saturation current (attributed to epitaxial re-alignment of polysilicon grains near the polysilicon–silicon interface [14] and/or increased number of grain boundaries) is observed.

The devices were then masked for contact formation and the oxide cap was dry etched using a CHF_3/Ar plasma. A 200 nm aluminum film was deposited and selectively etched to form contacts, which were sintered at 450 °C for 1 min, forming the final device structure shown in figure 1(*e*). A final mask of 4 μm photoresist defined windows centred on the waveguide for a 4 MeV Si^+ ion implantation with a dose of 10^{13}–5×10^{13} cm^{-2}. This final implantation introduced the defects necessary to mediate sub-bandgap detection.

2.2. Summary of fabricated device structures

The LOCOS waveguide photodetectors were fabricated with a varied waveguide width, p-i-n junction length, p+ region separation, and Si^+ defect implant window width as summarized in table 1.

In addition, the amorphous silicon deposition method for the top contact and the Si^+ implant dose was varied between fabrication runs. The three processed wafers are identified in table 2.

Table 2. Summary of variations in the amorphous silicon deposition method and the Si^+ implant dose between fabrication runs.

Wafer no	Amorphous silicon layer deposition method	Si^+ implant dose (in cm^{-2}), at 4 MeV
1	LPCVD	10^{13} cm^{-2}
2	PECVD	10^{13} cm^{-2}
3	LPCVD	5×10^{13} cm^{-2}

2.3. Characterization

The devices were characterized using an ILX Lightwave laser (FOM system) operating at 1550 nm, end-fire coupled into the waveguide via a tapered fibre. The transmitted power was collected by a 40× objective and focused onto a Newport fibre-optic detector. From an analysis of the Fabry–Perot fringes of an un-implanted waveguide using a tunable laser source, the transmission loss was measured to be 2.9 ± 1.1 dB cm^{-1} (for the 2 μm waveguide width). Using measurements from several undoped waveguides, the insertion loss was estimated to be 10.2 ± 3.5 dB. The 50 × 50 μm Al pads were probed by 1 μm tip radius tungsten probes connected in series to a variable voltage supply and ammeter, which were used to measure the photocurrent as a function of device bias.

This characterization process was completed following 5 min anneals in N_2 at temperatures ranging from 200 to 450 °C. At each annealing stage, the defect concentration N_t is approximated using the measured excess optical absorption α_{ex} (in units of cm^{-1}) by [6]

$$N_t = \frac{\alpha_{ex}}{1.3 \times 10^{-17}\ \text{cm}^2}. \quad (1)$$

This facilitates a direct comparison between *measured photocurrent* versus α_{ex} curves and *simulated photocurrent* versus N_t curves.

3. Results and discussion

3.1. Behaviour of photocurrent and dark current with post-implant annealing

Figure 2 compares the simulated and measured photocurrent for wafer 1 under a 5 V reverse bias as a function of excess absorption α_{ex} or, equivalently, estimated defect concentration N_t. The data points were obtained from measurements following successive anneals at 200–425 °C. Following the final inert silicon ion implantation of 10^{13} cm^{-2} dose, the device is in a high optical absorption state, owing to the large number of defects in the waveguide. This leads to both a large recombination rate of carriers and a small optical absorption length ($1/\alpha_{ex}$) in the device relative to the total device length. As a result, the responsivity is low for this configuration, as shown in the right-most data point of figure 2 (corresponding to a post-implantation annealing temperature of only 200 °C, the lowest used in this study). Following low-temperature annealing, the defects are progressively removed and α_{ex} is decreased, causing the photocurrent to increase. Following anneals at temperatures beyond 350 °C, the lowered α_{ex} leads to a lower carrier generation rate, and so the

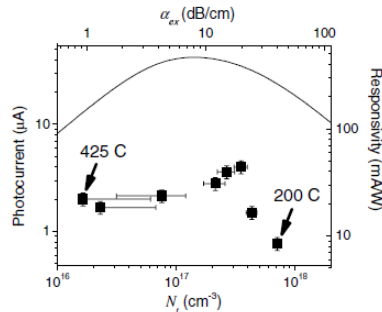

Figure 2. Measured (square points) and simulated (curve) photocurrent (left axis) and responsivity (right axis) versus excess absorption α_{ex} (top axis) and estimated defect concentration N_t (bottom axis); plotted for 1.5 μm waveguide width, 10 μm p$^+$ region separation, 5 μm (final silicon) implantation window width and 6 mm length; the data points were measured following 5 min anneals at (from right to left) 200, 250, 275, 300, 350, 375, 400 and 425 °C, with the two points corresponding to the extreme anneal temperatures of 200 and 425 °C indicated on the plot; the defect concentration was calculated from the excess loss using the optical absorption cross-section as in equation (1).

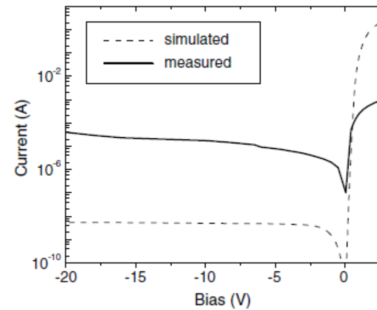

Figure 3. Measured *IV* curve of the LOCOS device prior to damage implantation, and the *IV* curve simulated by ATLAS.

photocurrent decreases once more. Using the approximate coupling loss of 10.2 dB to calculate an on-chip optical power of 95 μW, the peak responsivity of the photodiode in figure 2 is 47 mA W^{-1}, and occurs for an excess loss of $\alpha_{ex} = 20$ dB cm^{-1} (or 12 dB).

There is general agreement between the simulation and the experiment on the location of maximum response as a function of defect concentration, although the magnitude of photocurrent is lower by nearly an order of magnitude. This disparity is likely caused by the use of the polycrystalline silicon top contact. There exist a large number of defect states within the polysilicon grain boundaries and at its interface with the guiding ridge [14]. These defects have carrier capture properties that could not be simulated in a straightforward manner using the model reported in [6]. Further evidence for the impact of these additional defect states on the electrical properties of the device is exhibited through a softened forward bias characteristic and larger leakage current than expected for a crystalline diode of the same dimensions. This is illustrated in the measured and simulated current–voltage (*IV*) curves shown in figure 3. The defects present in the polysilicon are clearly detrimental and limit the dynamic range of the photodetector by setting the minimum dark current to a value of >1 μA.

Photodetectors utilizing implanted junctions do not suffer from high dark current, as evidenced by recently reported small-area enhanced photodetectors with dark currents of 1 nA at 20 V reverse bias [15]. Therefore, in order to fully realize the advantages of LOCOS photodetectors, it is necessary to further adjust processing conditions to reduce this dark current. It should be noted that photodetectors formed from silicon/germanium p-i-n heterojunctions exhibit similar magnitudes of dark current to those observed here, albeit with a much higher responsivity [16]. In this case, the dark current and the photocurrent are of the same order of magnitude for on-chip optical powers of 10–100 μW. In order to become suitable for telecommunication applications, for example, it would be necessary to decrease this value through either an increase in sensitivity or a decrease in dark current. Different fabrication approaches were utilized to achieve both, as will presently be described.

3.2. Evaluation of PECVD versus LPCVD polysilicon

The variation in the silicon deposition method used for the top contact layer is useful in determining its influence on the dark current. Using Hall effect measurements, it was found that the ion-implanted phosphorus dose in the PECVD devices needed to be a factor of 10 greater over that used for the LPCVD devices to activate the same concentration of dopant. All other stages of the fabrication process were performed identically to those of the LPCVD samples. Both final device sets (PECVD and LPCVD) produced similar photo-responsivities and had measured excess optical loss that was equal within experimental error. The largest difference between the two device types was the reverse saturation current, which was much larger in the PECVD sample. This feature is illustrated in figure 4, which plots the dark current (at −5 V bias) for two identical device designs (3 mm length, 10 μm p$^+$ region separation, 2.5 μm waveguide width) after each annealing stage. In all devices, the dark current was initially reduced after Si$^+$ ion implantation and increased to its pre-implanted value after anneals at temperatures approaching 450 °C. The initial reduction observed in the PECVD device is stronger than for the LPCVD device, likely due to a larger influence of ion damage on the polysilicon structures. Above the 300 °C anneal, the observed trend in dark current with annealing temperature is similar in the two devices. In the LPCVD sample the pre-implanted value was 11.8 μA, while in the PECVD sample it was 900 μA. The polysilicon layer formed using each deposition method differs in defect content. In addition to the differences in grain boundary density, the

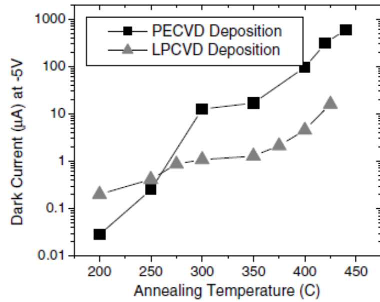

Figure 4. Dark current measured at −5 V bias for samples prepared using amorphous silicon deposited by PECVD and LPCVD methods, plotted as a function of annealing temperature following an implantation of Si^+ at 4 MeV and 10^{13} cm^{-2} dose.

PECVD film will have a much higher hydrogen content, which is retained in the crystallized film [17]. Deposition techniques clearly have a significant impact on the resulting diode properties, and further investigation is necessary in order to achieve optimization. For instance, *in situ* phosphorus doping may provide a significant improvement in dopant activation, and a hydrogenation step could help passivate a significant fraction of the defects [18,19].

3.3. Evaluation of the impact of the Si^+ implantation dose

The limiting nature of the dark current on the dynamic range provides incentive for the investigation of the impact of higher inert implantation doses in order to reduce the dark current to below its pre-implanted values. It is postulated here that a relatively high implantation dose of 5×10^{13} cm^{-2} introduces complex defects such as tetravacancies and agglomerated interstitial-type defects, which remain after anneals at 400–500 °C [20, 5].

Following a 4 MeV Si^+ implantation at a 5×10^{13} cm^{-2} dose and a subsequent anneal at 400 °C, the dark current in the LPCVD device is reduced over its value when implanted with a dose of 1×10^{13} cm^{-2} (corresponding to the LPCVD data points plotted in figure 4) for all annealing temperatures. With further annealing, the photocurrent is found to increase, along with a relatively modest increase in dark current, as shown in figure 5. Similar to the devices implanted with the 1×10^{13} cm^{-2} dose, the excess loss was found to decrease with annealing temperature, as shown in the lower portion of figure 5. In this case, however, the optimum photocurrent has lower corresponding excess loss values of ⩽4 dB, indicating an improved efficiency of the defects formed using this dose over those described in section 3.1.

Following the 450 °C anneal, the responsivity reaches a value of approximately 18 mA W^{-1} (at −20 V bias), while the excess absorption is at a level of 2.3 ± 1.5 dB. Thus, the dramatic improvement in dark current over that described in figure 4 is gained at the expense of the responsivity.

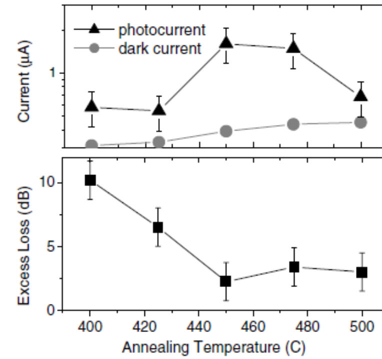

Figure 5. Photocurrent and dark current at −20 V bias following anneals from 400 to 500 °C, for a waveguide of width 1.5 μm, p^+ separation of 10 μm and implant window width of 10 μm.

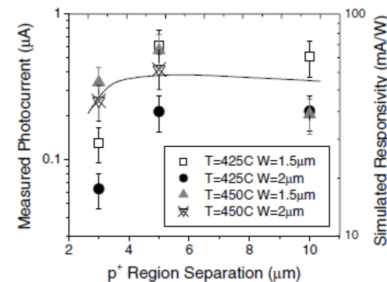

Figure 6. Measured photocurrent versus p+ region separation for 1.5 and 2 μm waveguide widths following 425 and 450 °C anneals (data points, left axis), and simulated responsivity of a 1.5 μm waveguide width assuming $N_t = 10^{17}$ cm^{-3} (curve, right axis).

3.4. Variation of p^+ implantation separation and Si^+ implantation window width

A careful consideration of the device structure is needed to facilitate the efficient removal of generated carriers. Here we illustrate the effects of changing the proximity of the p^+ regions to the optical mode and the width of the window for the defect-inducing Si^+ implantation.

Figure 6 plots the measured photocurrent for waveguide widths of 1.5 and 2 μm versus p^+ separation, along with a simulated curve assuming $N_t = 10^{17}$ cm^{-3}. The photocurrent was found to increase only slightly when the p^+ region separation was reduced from the 10 μm value for the device whose results are reported in figure 2. Further, figure 6 shows that the photocurrent *decreases* as this separation is reduced below 5 μm. This feature illustrates the trade-off between the enhanced carrier extraction and the increased free-carrier-induced optical absorption that occurs when the p^+ regions and

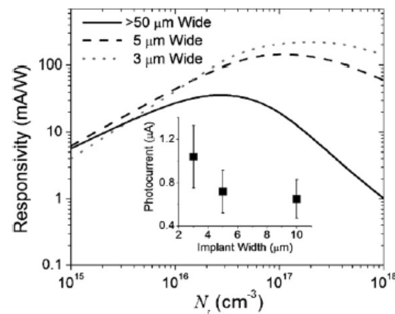

Figure 7. Simulated responsivity versus defect concentration N_t for implant window widths of 3 , 5 and >50 μm; inset: measured photocurrent of a sample of length = 6 mm, 10 μm p+ region separation and bias = −10 V.

the optical mode begin to overlap significantly. The modelling predicts an optimal electric field in the region of the poly–bulk silicon interface, and therefore both simulated and measured points indicate a minimal benefit in decreasing the p^+ region separation for moderate defect concentrations. For separations of less than 5 μm, however, the photocurrent is degraded by the excess loss.

The photocurrent may also be enhanced by a narrowing of the inert Si^+ implantation region, determined by the width of the window in the photoresist used to mask the implantation. The simulated responsivity is plotted as a function of defect concentration in figure 7, for three implant window widths. The confinement of defects to the region of the optical mode limits the recombination centres that do not contribute to carrier generation, and therefore enhances photocurrent, shifting the peak efficiency to higher defect concentrations. The inset of figure 7 illustrates the enhancement observed in narrowing the implant window width for three nominally identical photodiodes at a single annealing stage. These geometry changes were not observed to change the dark current of the device.

4. Conclusion

We have demonstrated the design and fabrication of a defect-enhanced photodetector integrated with a LOCOS silicon waveguide, the first active device to be integrated with waveguides formed in this way. While responsivities of 47 mA W^{-1} can be achieved, it is noted that performance is limited by the quality of the polysilicon and its electronic contact to the top of the guiding ridge, which has been shown to lead to excessive dark current (several μA). We have analysed the influence of processing conditions on the device leakage current and shown that it can be partially mediated by selecting higher dose inert ion implantation, although there is a concomitant decrease in responsivity. Finally, changes in implantation geometry were shown to greatly impact the efficiency of the device, in good agreement with simulations.

References

[1] Reed G T 2004 The optical age of silicon *Nature* **427** 595–6

[2] Doylend J K, Knights A P, Luff B J, Shafiiha R, Asghari M and Gwilliam R M 2010 Modifying functionality of variable optical attenuator to signal monitoring through defect engineering *Electron. Lett.* **4** 234–6

[3] Masini G, Sahni S, Capellini G, Witzens J and Gunn C 2008 High-speed near infrared optical receivers based on Ge waveguide photodetectors integrated in a CMOS process *Adv. Opt. Technol.* **2008** 196572

[4] Knights A P, Bradley J D B, Gou S H and Jessop P E 2006 Silicon-on-insulator waveguide photodetector with self-ion-implantation engineered-enhanced infrared response *J. Vac. Sci. Technol.* A **24** 783–6

[5] Geis M W *et al* 2007 All silicon infrared photodiodes: photo response and effects of processing temperature *Opt. Express* **15** 16886–95

[6] Logan D F, Jessop P E and Knights A P 2009 Modeling defect enhanced detection at 1550 nm in integrated silicon waveguide photodetectors *J. Lightwave Technol.* **27** 930–7

[7] Foster P J, Doylend J K, Mascher P, Knights A P and Coleman P G 2006 Optical attenuation in defect-engineered silicon rib waveguides *J. Appl. Phys.* **99** 073101

[8] Simoen E, Claeys C, Gaubas E and Ohyama H 2000 Impact of the divacancy on the generation-recombination properties of 10 MeV proton irradiated float-zone silicon diodes *Nucl. Instrum. Methods Phys. Res.* A **439** 310–8

[9] Rowe L K, Elsey M, Tarr N G, Knights A P and Post E 2007 CMOS-compatible optical rib waveguides defined by local oxidation of silicon *Electron. Lett.* **43** 392–3

[10] Pafchek R, Tummidi R, Li J, Webster M A, Chen E and Koch T L 2009 Low-loss silicon-on-insulator shallow-ridge TE and TM waveguides formed using thermal oxidation *Appl. Opt.* **48** 958–63

[11] Sherwood-Droz Nicolás, Gondarenko Alexander and Lipson Michal 2010 Oxidized silicon-on-insulator (OxSOI) from bulk silicon: a new photonic platform *Opt. Express* **18** 5785–90

[12] Murarka S P 1984 Phosphorus out-diffusion during high temperature anneal of phosphorus-doped polycrystalline silicon SiO_2 *J. Appl. Phys.* **56** 2225–30

[13] MacKay G F, Manning B M and Tarr N G 1992 Rapid thermal annealing of *in situ* phosphorus-doped polysilicon emitters *Can. J. Phys.* **70** 1109–11

[14] Patton G L, Bravman J C and Plummer J D 1986 Physics, technology and modeling of polysilicon emitter contacts for VLSI bipolar transistors *IEEE Trans. Electron Devices* **33** 1754–68

[15] Logan D F, Velha P, Sorel M, De La Rue R M, Knights A P and Jessop P E 2010 Defect-enhanced silicon-on-insulator waveguide resonant photodetector with high sensitivity at 1.55 μm *IEEE Photonics Technol. Lett.* **22** 1530–2

[16] Yin T, Cohen R, Morse M M, Sarid G, Chetrit Y, Rubin D and Paniccia M J 2007 31 GHz Ge *n-i-p* waveguide photodetectors on silicon-on-insulator substrate *Opt. Express* **15** 13965–71

[17] Brodsky M H, Cardona M and Cuomo J J 1977 Infrared and Raman spectra of the silicon–hydrogen bonds in amorphous silicon prepared by glow discharge and sputtering *Phys. Rev.* B **16** 3556–71

[18] Briand D, Sarret M, Le Bihan F, Bonnaud O and Pichon L 1995 Polysilicon *in situ* phosphorus doping control over

large concentration range using low temperature, low pressure chemical vapour deposition growth process *Mater. Sci. Technol.* **11** 1207–9

[19] Wu I-W, Huang T-Y, Jackson W B, Lewis A G and Chiang A 1991 Passivation kinetics of two types of defects in polysilicon TFT by plasma hydrogenation *IEEE Electron Device Lett.* **12** 181–3

[20] Vavilov V S and Chelyadinskii A R 1995 Impurity ion implantation into silicon single crystals: efficiency and radiation damage *Phys.—Usp.* **38** 333–44

B.7 D. F. Logan, P. Velha, R. M. De La Rue, G. Wojcik, A. Goebel, P. E. Jessop, and A. P. Knights, "Charge State Switching of Deep-Levels For Low Power Optical Modulation in Silicon Waveguides."

This manuscript has been accepted for publication in Optics Letters, and summarizes the fabrication and characterization of the devices proposed in *B.4.* The active *p-i-n* diodes, fabricated at the University of Glasgow, were shown to provide normally-off modulation (with a modulation depth of 16.3 dB/cm) by the application of a reverse bias.

B.8 D. F. Logan, P. Velha, M. Sorel, R. M. De La Rue, P. E. Jessop, and A. P. Knights, "Monitoring and Tuning Micro-ring Properties using Defect-enhanced Silicon Photodiodes at 1550 nm."

This manuscript has been submitted for publication in Photonics Technology Letters, and summarizes the work contained in chapter 7 of this thesis.

This work was also presented at the IPR (Integrated Photonics Research) meeting in Toronto, ON in June 2011, and has an associated publication in the OSA Technical Digest.